Smart Sensors, Measurement and Instrumentation 1

Series Editor

Subhas Chandra Mukhopadhyay
School of Engineering and Advanced Technology (SEAT)
Massey University (Turitea)
Palmerston North
New Zealand
E-mail: S.C.Mukhopadhyay@massey.ac.nz

For further volumes:
http://www.springer.com/series/10617

Subhas C. Mukhopadhyay,
Krishanthi P. Jayasundera,
and Anton Fuchs (Eds.)

Advancement in Sensing Technology

New Developments and Practical Applications

Springer

Editors
Subhas C. Mukhopadhyay
(Guest Editor)
School of Engineering and Advanced
Technology (SEAT)
Massey University (Manawatu Campus)
Palmerston North
New Zealand

Anton Fuchs (Guest Editor)
Institute of Electrical Measurement
and Measurement Signal Processing
Graz University of Technology
Graz
Austria

Krishanthi P. Jayasundera
(Guest Editor)
Institute of Fundamental Sciences (IFS)
Massey University (Manawatu Campus)
Palmerston North
New Zealand

ISSN 2194-8402 e-ISSN 2194-8410
ISBN 978-3-642-32179-5 e-ISBN 978-3-642-32180-1
DOI 10.1007/978-3-642-32180-1
Springer Heidelberg New York Dordrecht London

Library of Congress Control Number: 2012942955

Printed on acid-free paper

Springer is part of Springer Science+Business Media (www.springer.com)

Guest Editorial

This book titled "Advancement in Sensing Technology: New Developments and Practical Applications" in the new book series "Smart Sensors, Measurement and Instrumentation" contains the extended version of the papers selected from those that were presented at the Fifth International Conference on Sensing Technology (ICST 2011) which was held in November 28 to December 1, 2011 at Massey University, New Zealand. A total of 153 papers were presented at ICST 2011, of which 18 papers have been selected for this book.

This book has focussed on the recent advancements of the different aspects of sensors and sensing technology, i.e. information processing, adaptability, recalibration, data fusion, validation, high reliability and integration of novel and high performance sensors. The advancements are in the areas of wireless sensors and network, environmental monitoring, structural health monitoring, dielectric, magnetic, electrochemical, ultrasonic, microfluidic, flow, surface acoustic wave, gas, cloud computing and bio-medical. While future interest in this field is ensured by the constant supply of emerging modalities, techniques and engineering solutions, many of the basic concepts and strategies have already matured and now offer opportunities to build upon.

We do sincerely hope that the readers will find this book interesting and useful in their research as well as in practical engineering work in the area of sensing technology. We are very happy to be able to offer the readers such a diverse special issue, both in terms of its topical coverage and geographic representation.

Finally, we would like to whole-heartedly thank all the authors for their contribution to this book.

Subhas Chandra Mukhopadhyay, Guest Editor
School of Engineering and Advanced Technology (SEAT),
Massey University (Manawatu Campus)
Palmerston North, New Zealand
S.C.Mukhopadhyay@massey.ac.nz

Krishanthi Padmarani Jayasundera, Guest Editor
Institute of Fundamental Sciences (IFS)
Massey University (Manawatu Campus)
Palmerston North, New Zealand
K.P.Jayasundera@massey.ac.nz

Anton Fuchs, Guest Editor
Institute of Electrical Measurement and Measurement Signal Processing,
Graz University of Technology
Graz, Austria
anton.fuchs@tugraz.at

Dr. Subhas Chandra Mukhopadhyay graduated from the Department of Electrical Engineering, Jadavpur University, Calcutta, India in 1987 with a Gold medal and received the Master of Electrical Engineering degree from Indian Institute of Science, Bangalore, India in 1989. He obtained the PhD (Eng.) degree from Jadavpur University, India in 1994 and Doctor of Engineering degree from Kanazawa University, Japan in 2000.

Currently, He is working as a Professor of Sensing Technology with the School of Engineering and Advanced Technology, Massey University, Palmerston North, New Zealand. His fields of interest include Smart Sensors and Sensing Technology, Wireless Sensors Network, Electromagnetics, control, electrical machines and numerical field calculation etc.

He has authored/co-authored over 270 papers in different international journals and conferences, edited nine conference proceedings. He has also edited ten special issues of international journals and twelve books with Springer-Verlag as guest editor.

He is a **Fellow** of **IEEE**, a **Fellow** of **IET** (UK), an associate editor of IEEE Sensors journal and IEEE Transactions on Instrumentation and Measurements. He is also a Technical Editor of IEEE Transactions on Mechatronics. He is a Distinguished Lecturer of IEEE Sensors council. He is in the editorial board of many international journals. He has organized many international conferences either a General Chair or Technical programme chair.

Dr. Krishanthi P. Jayasundera graduated from Faculty of science specialized in Chemistry, from University of Peradeniya, Kandy, Sri Lanka and obtained her Master and PhD in Organic Chemistry from Kanazawa University, Japan. She worked as a Post-doctoral researcher, Research scientist with the Institute of Fundamental Sciences, Massey University, New Zealand. Currently, she is an independent research consultant. She specialised in Organic chemistry, Bio-sciences, sensitivity analysis using NMR, HPLC, SPM machines and so on. She has published over 30 papers in different international journals and conference proceedings.

Anton Fuchs was born in Graz, Austria, in 1977. He received the Dipl.Eng. degree in telematics from Graz University of Technology in 2001 and joint the Institute of Electrical Measurement and Measurement Signal Processing, Graz University of Technology in 2002. He worked as a researcher, project manager, and lecturer and received the Doctoral degree in technical science in 2006 from Graz University of Technology. He was Visiting Researcher and Research Fellow at the Centre for Bulk Solids and Particulate Technologies, University of Wollongong, Australia in 2004 and in 2007/2008 respectively.

In 2009 he received the venia docendi for "Process Instrumentation and Sensor Technology" from Graz University of Technology and became Associate Professor.

Anton Fuchs is now with the Virtual Vehicle Competence Center in Graz, Austria. He is Associate Professor and Distinguished Lecturer at Graz University of Technology. His main research interests include capacitive sensors and the measurement of transported material in industrial conveying processes. Anton Fuchs is author and co-author of more than 90 scientific papers and patents.

Contents

Ecological Monitoring Using Wireless Sensor Networks—Overview, Challenges, and Opportunities 1
Chia-Pang Chen, Cheng-Long Chuang, Joe-Air Jiang

Development of an Embedded System-Based Gateway for Environmental Monitoring in Wild Fields 23
Xiang-Yao Zheng, Chun-Yi Liu, Po-Tang Chen, Cheng-Long Chuang, Chia-Pang Chen, Joe-Air Jiang

Experimental Research Platform for Structural Health Monitoring 43
Benjamin Babjak, Sandor Szilvasi, Alex Pedchenko, Mark Hofacker, Eric J. Barth, Peter Volgyesi, Akos Ledeczi

A Review of Cooperative Spectrum Sensing in Cognitive Radios 69
Babak Ahsant, Ramanarayanan Viswanathan

Dielectric Characterisation of Lipid Droplet Suspensions Using the Small Perturbation Technique 81
R.T. Blakey, A. Mason, A. Al-Shamma'a, C.E. Rolph, G. Bond

Dielectric Properties of Wood for Improved Internal Imaging 93
W.S. Holmes, S.C. Mukhopadhyay, S.G. Riley

Laser-Induced Breakdown Spectroscopy Measurements for Dielectric Materials and Metals 105
S. Ikezawa, M. Wakamatsu, T. Ueda

Microdevice with Half-Ring Shaped GMR Sensors for Magnetic Bead Manipulation and Detection 121
C.P. Gooneratne, I. Giouroudi, J. Kosel

Design of Induction Gradiometer for MCG Measurement 139
Kunihisa Tashiro, Shin-ichiro Inoue, Hiroyuki Wakiwaka

Electroacoustic Model Based Pneumatic Fill-Level Measurement for Fluids and Bulk Solids 165
R. Brunnader, G. Holler

New Developments in Electrode Materials for Electrochemical Sensors 181
U. Guth, J. Zosel, J. Riedel, T.N. Tran, M. Berthold, C. Vonau, U. Sasum, P. Shuk, M. Paramasivam, V. Vashook

Optical Fiber Sensors Based on Lossy Mode Resonances 191
Miguel Hernáez, Carlos R. Zamarreño, Ignacio Del Villar, Francisco J. Arregui, Ignacio R. Matias

Ultrasonic Thermometry for Temperature Profiling of Heated Materials 211
Ikuo Ihara, Takuya Tomomatsu, Manabu Takahashi, Akira Kosugi, Iwao Matsuya, Hiroyuki Yamada

Non-invasive Measurement of Blood Components: Sensors for an In-Vivo Haemoglobin Measurement 237
J. Kraitl, D. Klinger, D. Fricke, U. Timm, H. Ewald

Homeland Security and Cloud: Challenges and On-Going Developments 263
M. Fazio, M. Paone, A. Puliafito, M. Villari

Formulation, Characterization and LPG-Sensing Properties of CuO-Doped ZnO Thick Film Resistor 283
M.K. Deore, V.B. Gaikwad, R.M. Chaudhari, N.U. Patil, P.D. Hire, S.B. Deshmukh, G.E. Patil, V.G. Wagh, G.H. Jain

Synthesis of Cu-Doped SnO_2 Thin Films by Spray Pyrolysis for Gas Sensor Application 299
G.E. Patil, D.D. Kajale, S.D. Shinde, V.G. Wagh, V.B. Gaikwad, G.H. Jain

Nanocystalline In_2O_3 Thick Film Sensor 313
D.N. Chavan, R.H. Bari, G.E. Patil, D.D. Kajale, V.B. Gaikwad, D.V. Ahire, G.H. Jain

Author Index 323

Ecological Monitoring Using Wireless Sensor Networks—Overview, Challenges, and Opportunities

Chia-Pang Chen, Cheng-Long Chuang, and Joe-Air Jiang

National Taiwan University,
Taipei, Taiwan

Abstract. Wireless sensor networks (WSNs) offer a powerful feasible integration of distributed sensing capability, real-time data analysis, and remote surveillance due to the combined result of miniaturization of electronic devices and availability of powerful computational capability, larger information storage, and ubiquitous Internet connection. With these advances, WSNs are starting to be translated into a new ecological knowledge. They are providing a new insight into the observation of the world in new ways of extended spatial and temporal scales. Through WSNs, more unexpected phenomena can be obtained, and new paradigms can be developed. Recently, more and more ecological WSNs have been established, and lagre WSNs are deployed to monitor habitats with different scales. The research in the temporal scale ranges from the evaluation of soil moisture dynamics at several minutes to daily precipitation. Spatial measurements, on the other hand, range from the evaluation of global climate change to those related to the monitoring of forest and riparian environments in the range of a few meters. Although we are seeing more use of ecological WSNs, opportunities and challenges begin to be realized, including newly better design of software and hardware, formulation of new questions, discovery of previously unobservable phenomena, and development of new sensors, etc.

1 Introduction

Before 1980s, the scientist must deploy sensors such as thermometers, hygrometers, precipitation collectors to record in situ measurement. And they periodically visit the places where the instruments were set up to manually record sensed data [1]. With the advent of microprocessors and the advanced technology of very large scale integration (VLSI) on IC design in the 1980s, sensors were then connected to a microprocessor-based data logger through which the sensed data could be recorded electronically and an observation with a much frequent sampling rate would be achieved. The sensed data could be obtained with a lower frequent manual visiting. Meanwhile, some data loggers were connected to the modems with the remote communication capability based on phone wire. By doing so, the

S.C. Mukhopadhyay et al. (Eds.): Advancement in Sensing Technology, SSMI 1, pp. 1–21.
springerlink.com

sensed data could be retrieved by the remote control center automatically. Recently, because wireless transmission technologies began to revolutionize personal communication networks, brand-new applications have rapidly developed to this point such as weather information update on cellular phones, GPS navigation in vehicles and cellular phones, file share in Internet cloud services, and wireless Internet access at hotspots in modern cities. Therefore, there is a growing trend of applications involving with connecting humans to the surrounding environment, plants or animals, such as landslide detection [2], pest population detection [3-4], structural health monitoring of bridges [5] using wireless remote monitoring technologies, and animal tracking using Radio Frequency Identification (RFID) technologies. A key to the advances is the development of cyberinfrastructure presented by National Science Foundation (NSF), U.S. [6], which is a technological solution that support advanced data storage, access, inquiry, mining, visual representation, and computing over the Internet.

New ways of processing and recording collected data, new types of sensor, and new methods of data communication are leading to the growing use of WSNs [7]. With new sensing technologies, the measurement is not restricted within a few variables, such as general meteorological variables, but is extended to a variety of variables, such as the concentration of carbon dioxide (CO_2) and nitrogen dioxide (NO_2) in air, soil moisture, and other types of chemical materials [8-9]. Coupled with cyberinfrastructure, WSNs provide a powerful combination of distributed computing capability, sensing capability, Internet connection, wireless access, and self-configuration that can be applied to countless various ecological applications. The scientific imperative of multi-point observation also drives the adoption of advanced WSNs by biologists. Moreover, WSNs allow an near-real-time observation based on the incoming sensed data stream from remote fileds. With the characteristics of high-frequency and large spatial scale sampling, the use of WSNs is offering a better understanding of ecological systems by showing the previously unobservable phenomenon. Hart and Martinez [10] have concluded that WSNs will become a standard research tool by reviewing more than 50 examples of WSN applications.

To date, the environmental science community, which is supported by the National Science Foundation (NSF, U.S.), National Oceanographic Partnership Program (NOPP, U.S.), etc., has begun designing and implementing some new observing systems, including the National Ecological Observatory Network (NEON) [11], the Collaborative Large-scale Engineering Analysis Network for Environmental Research Network (CLEANER) [12], and Global Lake Ecological Observatory Network (GLEON) [13]. For example, the mission of NEON is to increase the understanding of how ecosystems and organisms respond to the variation in climate and changes in the use of land in US. Figure 1 demonstrates the infrastructure regarding the regional distribution of sensors and data transmission nodes in the NEON program. Through the combination of WSNs and wireless/cable communication technologies, the important feedbacks related to the change of territorial use among atmosphere, geosphere and biosphere could be

Fig. 1. The NEON's infrastructure to advance ecological monitoring (created by Nicolle Rager-Fuller, National Science Foundation, 2007) [11]

measured, and a further investigation could also be conducted. Similarly, Rundel et al. [14] have indicated that Southern California faces many challenges in managing the environment, so examining how the ecosystem is affected by human activities, e.g. change of land use, is crucial. On the other hand, how the human living is influenced by the ecosystem structure and climate also needs to be investigated. The researchers concluded that the combination of new sensing and communication technologies as the NEON program did is a promising way to explore such information. Furthermore, NASA has developed the Integrated Earth Observation System (IEOS) [15] to integrate the data from ocean buoys, satellites, weather stations and in-situ earth observing instruments into advanced decision support tools and science numerical models that will offer new outcome benefiting worldwide science research. In addition, the research team of Texas Environmental Observatory (TEO) [16] aims at providing near-realtime data of environmental conditions in the state of Texas based on the wired/wireless ground sensors, which were built by other research teams or governmental organizations. The data includes rainfall, water quality, weather information, and soil moisture. The ecologists expect to build the hydrologic model by analyzing and synthesizing the valuable sensed data provided by TEO. More importantly, TEO also offers cyberinfrastructure to make the data available to the public.

Because the automated WSN-based systems could extend the scales of observation, they could cooperate with the ecological models and theories. A better understanding of ecology would be achieved when spatial, temporal, quantitative data could be easily compared. If the data is collected daily at a few

monitoring sites, but the ecological model is built resting on the hourly scale of a large range observation, it does not make sense to perform the analysis. In general, WSNs provide an appropriate scale and accuracy of observation that is sufficient to build an ecological model, thus allowing a wider and detailed verification. However, although WSNs offer a improved capability of performing automatic ecological observation, they generate a vast amount of data needs to be further identified, mined, and analyzed. In order to deal with such a data richness problem, Collins et al. [17] have presented a conceptual strategy to reduce the scale of WSNs and their associated cyberinfrastructure to three main components that are common to the field ecological experiment: 1) the sensors which are specific for unique measurements; 2) a WSN that gathers and transfers the sensed data; and 3) the end user analyzes and interprets the data with a particular question. The sensors and end users were problem-specific, whereas WSNs are generalized across different applications. Understanding the relations among the three components would lead to more efficient WSNs. Practically, there have been many existing studies developing the potential ability of WSNs to function beyond the acquisition of large amount of complex sensed data. That is, the WSN itself is able to produce and transmit the particularly important information in a usual form from the sensed data rather than directly transmitting the raw data [18-20]. On the other hand, a technology called Sensor Web Enablement (SWE) [21], developed by OGC based on the notion of Sensor Web first proposed by NASA's Jet Propulsion Laboratory [22-23], allows more end users to manipulate the sensed data from WSNs and control data quality via Internet.

Although employing the WSN technology could facilitate the ecological observation, there have been many challenges that need to be overcome, including the issues of data gaps caused by sensor failure or energy depletion of sensor nodes, stability of operation, housing process in a wild environment, constrained energy source, reliability of wireless communication, etc. Fortunately, more and more ecologists, scientists, and engineers have presented new solutions of hardwares and approaches to deal with these issues in order to optimize sensor fidelity, data completeness, and system operating performance.

In this article, we will investigate the characteristics of ecological WSNs by reviewing and summarizing the existing studies involved with terrestrial, soil, and aquatic surveillance, etc. Meanwhile, combing with our more than five years experience of implementing the near-real-time WSN-based pest monitoring system [3-4], we also address the possible challenges and opportunities for using ecological WSNs.

2 New Advanced Sensors Allowing New Ways to Conduct Ecological Monitoring

Due to the advance of Microelectromechanical Systems (MEMS), a variety of sensors with a very small size have been well developed. Theses sensors are capable of converting real world physical/analog values such as temperature,

stress, strain, pressure, etc, into an electrical signal. In general, sensor modalities can be categorized into three types, 1) physical sensors; 2) chemical sensors; and 3) biological sensors [24]. Firstly, physical sensors are common ones and may include the sensors used to measure temperature, relative humidity, lead wetness, wind speed, wind direction, cup anemometer, 2-D/3-D sonic anemometer, and soil moisture. These physical sensors are usually, reliable and with low power consumption, but not expensive. Secondly, chemical sensors may be used to measure soil carbon dioxide, soil nitrate, phosphorus, but they are expensive and deployed under a reliable environment. Finally, the minirhizotron image sensor, sap flow sensors, and acoustic sensors belong to the biological sensors, which are expensive and need a control system.

Coupled with a communication component and a microprocessor, sensors are able to carry out a unobtrusively successive observation at a distant place where people cannot easily arrive at. These individual entities with capabilities of sensing and communicating are called sensor nodes in this article. Further, through the data received from the network configured by these sensor nodes, ecologists can study animals behavior, oceans, and rare dangerous events that cannot be directly observed. In some cases, the rates of ecosystem processes can be estimated as coupled with ecological models. In Table 1, we will show the examples of utilization of advanced sensors in ecological observation ranging from ecology surveillance of pests to in-stream temperature monitoring, we also provide some discussions regarding the insights drawn from ecological observation.

In addition to these sensors mentioned above, the advent of low power digital cameras allows automatic in-situ photography. The in-situ images could be captured and then compressed into a digital file with a smaller size by a compression IC chip. These images are wirelessly transmitted to a remote control center to be restored into a database. Further, due to the smaller size of images, a series of images collected during a short time frame, i.e., a short film, could also be produced to achieve a complete and detailed record for complicated dynamic ecological behavior. For example, Chen et al. have deployed a solar-powered remote visual surveillance system to monitor the Chinese Crested Tern (*Thalasseus bernsteini*), which is one of the least known and possibly the rarest seabirds [34]. Through these images sent back to the remote base station every 30 minutes, ecologists could study the brooding and breeding activities of these seabirds, as well as the population dynamics. Wawerla et al. [35] have used solar panels, a battery, and a camera to build a ecological monitoring system for grizzly bears at the Ni'iinlii Njik (Fishing Branch) Park in Canada. The captured video was periodically forwarded to the control center/base station and was stored in hard drives via a radio signal. Such a visual system aids ecologists in investigating the behavior of grizzly bears. Due to the observation was conducted in an arctic region, how to maintain an normal operation under such a severe climate and environment is crucial for the remote visual surveillance. Figure 2 shows some practical photos of these ecological applications.

Table 1. Summary of ecological monitoring using various advanced sensors

Example	Sensor modality/ technology	Property	Insights or comments
Landslide detection [2]	Geologic sensors (geophone and dielectric moisture sensor)	C, G	Studying the relations between the occurrence of landslide and the environment
Ecological monitoring for pests [3-4], Figure 1(a)	Pest number (detected by a particular sensor) meteorological parameters	A, C, G, H	Studying the population dynamics and distribution of pests and its ecology, and providing pest outbreak forecast
Hydrologic monitoring [25], Figure 1(b)	Soil moisture, meteorological parameters	C, H	Understanding the vegetation distribution and response to flooding
Cattle trajectory tracking [26], Figure 1(c)	GPS devices affixed to WSN motes	A, B, F	Discovering animal-landscape interaction
Avian activity around the entrance to burrow [27], Figure 1(e)	RFID, temperature/ humidity sensor, PIR (Passive Infrared) sensors	C, E, F	Understanding the bird's breeding, arrival/departure to burrow activities
Desert shrub microclimate [28]	Air/soil temperature, light sensor	C, F	Finding the relation of shrub species and microclimate
Carp tracking in a lake [29]	Robotic sensor, radio tag	C, F	Studying carp migration behavior and distribution in the lake
Diurnal fluctuations of pH, dissolved oxygen, and temperature by photosynthesis nia lake[30]	Water quality sensors (pH, dissolved oxygen, water temperature)	C, F	Exploring how an aquatic environment is influenced by the algal blooms
Dynamics of phytoplankton in a lake [31-32]	Water temperature, in situ chlorophyll fluorescence, robotic mobile sensing boat	C, G	Studying the seasonal changes in structure of the lake and phytoplankton assemblage

Table 1. *(continued)*

Example	Sensor Modality/ technology	Property	Insights or comments
Predict a increase of peak stream temperature under various riparian covers [33], Figure 1(d)	In-stream temperature (distributed temperature sensing, DTS), meteorological parameters	C, F	Investigating the impact of various riparian covers on stream temperature, higher stram temperature that causes a kidney disease of fish

Note: A: a wide range observatoin; B: an extra-high frequency observation (second level); C: a high frequency observation (minute level); D: a mediate frequenct observation (hour level); E: an event-driven observation; F: a low-frequency radio (MHz); G: a high-frequency radio (GHz); H: a deployment with a larger amount of sensor nodes (> 100).

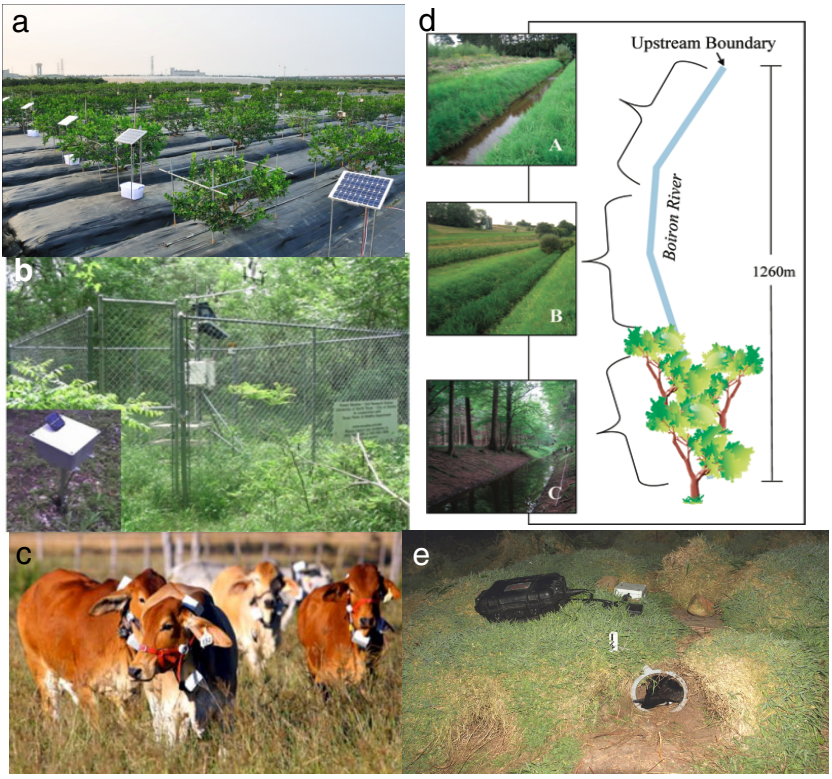

Fig. 2. Illustration of several WSN-based ecological systems. (a) Ecological monitoring system targeting pests in Taiwan [3-4]; (b) Environmental monitoring station and installed waterproof box of WSN mote in Texas [25]; (c) Cattle wearing GPS receivers and motes in Australia [26]; (d) In-stream temperature monitoring and environmental parameter measurement under three kinds of riparian covers (A, B, C) along of the Boiron de Morges Rive in Switzerland [33]; (e) Habitat monitoring using RFID and WSN technology on Skomer Island, UK [27].

On the other hands, acoustic sensors have also been developed nowadays. Acoustic sensor network can offer a non-intrusive approach to observe animal behavior by passively listening to the animals' vocalizations [36-37]. In the domain of ecological observation, microphone is one kind of the pervasive means in acoustic sensor networks. Through the collection of acoustic data, ecologists and biologists can determine the occurrence of specified animal species [38] using feature extraction methods. In addition, ecologists have been pursuing the goal of passive acoustic acoustic localization because of its merit of non-intrusiveness. For example, a study [39] has presented a localization approach coupled with some signal processing technologies that can simultaneously estimate the localizations of acorn woodpeckers using the acoustic sensor networks equipped with microphone arrays. Further, with the utilization of acoustic WSNs, the interaction of multiple individuals can be simultaneously observed. In practice, although we can benefit from the acoustic sensor networks in ecological observation, it is inevitable to involve more complicated front-end (sensor nodes) pre-processing to deal with the larger amount of collected data [36-37] (e.g. data compression and feature extraction) due to the limited wireless communication bandwidth. Thus, both the difficulty and cost to implement the acoustic sensor networks in ecological monitoring may rise because of the processing requirement.

3 Extending Spatial and Temporal Sacles of Ecological Observation

Distributed embedded sensing devices, including imaging devices, can provide a high-resolution spatio-temporal data of observation to complement the conventional sensing products that are very coarse in spatial and temporal scale. WSN technologies drive the ecological observation to a new domain in which researchers can explore new model of ecosystems, and the technologies also can support them to resolve compelling scientific questions related to ecology, biology, and nature. Despite ecological research benefits from WSN technologies, there is barrier emerging in the extending spatio-temporal scale.

Due to the expensive high cost of installations and maintenance of WSN devices, most of WSN-based ecological studies merely deployed the sensing instruments at specific points. Moreover, a successive observation is required for ecological monitoring, because modeling the ecological behavior or phenomenon may face some problems if a large amount of data is missing. Energy-harvesting instruments are adopted in the practical monitoring field in order to last a longer system lifetime. Such a requirement of energy harvesting is often a necessity in the visual surveillance systems because of the power-hungry image processing and wireless data transmission [34-35]. One of the pervasive schemes satisfying the requirement is the solar energy harvesting technology, which is utilized in the ecological studies [25-26, 34-35, 37]. Solar energy is the cleanest, most abundant,

renewable energy source, and it can be conveniently transformed into electricity through solar cells. In many studies involved with ecological monitoring [27, 29-32], the research results indicated that a better way to charge the batteries and power the instruments is to use solar panels. More importantly, redundant electricity can be stored into batteries so that the system can maintain normal operation when sun lights are unavailable, such as in the night. These energy-harvesting devices usually have an installation location contraint, e.g. it is best to place the solar-harvesting system in an open space without any veils like trees. Therefore, for automatic ecological monitoring systems deployed in a remote field, some constraints that obstruct any extension of a spatial scale may still exist.

Much early WSN-related literature claimed that wireless sensor nodes could be randomly scattered into an interest of area for monitoring purposes, even can be dispersed from an aircraft [40-41]. Such a statement or assumption cannot be easily applied to the WSN-based ecological monitoring applications because only some of ecological phenomena that take place in certain areas need to be observed. The location-specific observation also has similar constraints on extension of spatial scales. Although freely deploying WSNs in ecological monitoring is not feasible, an appropriate location arrangement for sensor node deployment that takes network connectivity into account can offer a better quality of service.

In general, the deployment of WSNs mainly considers as a 2-D deployment. Although the physical environment where the WSN is settled is a 3-D space (i.e., sensor nodes can be regarded as the different points in a 3-D coordinate), most studies still took a more simple 2-D horizontal plane model into consideration for convenience. A typical application of 3-D WSNs in ecological monitoring is underwater WSNs [42-43]. In addition to the networks formed by the sensor nodes floating on the water, there is another type of networks formed by the sensor nodes located under water. By a connecting bridge or gateway, both of the networks can be integrated into a underwater WSN. More specifically, the sensor nodes locate at different depths under water can be viewed as the third vertical axis of a 3-D WSN deployment. For example, Bondarenko et al. have proposed a underwater WSN coupled with the Niskin bottle method [42], which aims at monitoring the sea temperature at various depths and collecting the plankton (e.g., *Trichodesmium* cyanobacteria), to examine the interaction between cold water intrusions, originating from the coral sea and upwelled on the reef, and coral growth in the Great Barrier Reef Australia (GBR). In this study, each sensor node is composed several temperature sensors and Niskin bottles, which are fixed in a hydraulic cable. The signal between each sensor and the mote (Unode) that is in charge of managing the sensed data and transmitting them to the base station, is propagated in a wireline. Figure 3(a) displays the study sites at Nelly Bay, Magnetic Island, Australia. Moreover, Figer 3(b) shows the system architecture of another 3D scale underwater observation system [43]. A observation result regarding the sea surface temperature is shown in Figure 3(c) [43].

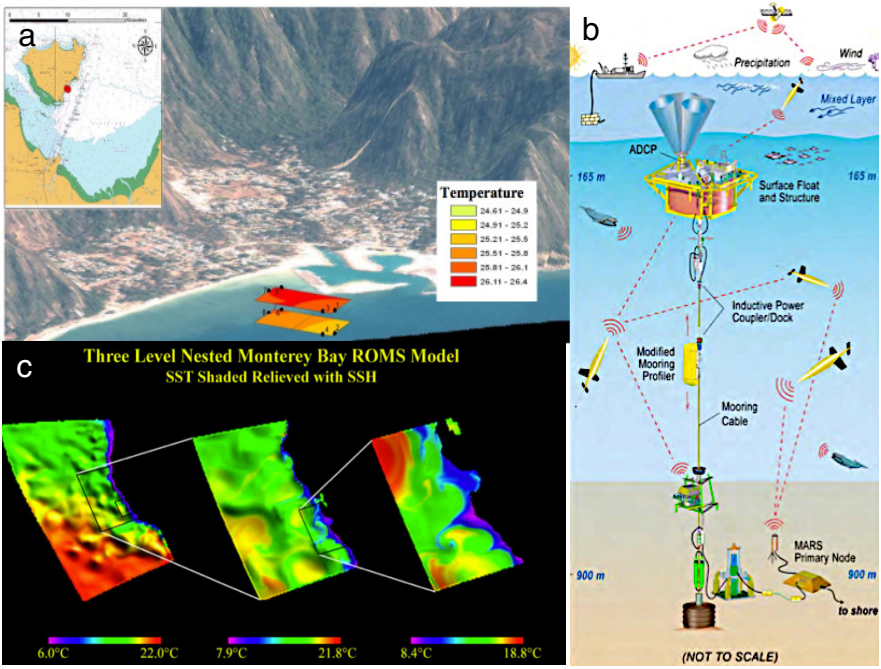

Fig. 3. Illustartion of 3-D WSNs. (a) Observation sites at Nelly Bay, Magnetic Island, Australia [42]; (b) A underwater mooring WSN system based on the acoustic communication technology [43]; (c) The simulated sea surface temperature distribution using nested ROMS models [43].

In the past, ecological/biological observation was conducted in manual ways, which may lead to a high cost and could not provide a better sensing fidelity as well as a high-resolution observation. Fortunately, WSNs can fill in the areas of spatio-temporal continuos sampling in ways that could not be done in the past. In terms of the scalability of a temporal scale, depending on various ecological phenomena to be observed, the sampling rate of WSNs can be flexibly adjusted to satisfy different requirements. According to the survey result as shown in Table 1, it is obvious that most of ecological studies using WSN technologies have a minute-level temporal scale of observation. Note that the temporal scale of sampling/observation refers to the practical frequency of sensed data sent to a database (i.e., the sampling rate of WSNs) rather than the physical sampling rate of sensors. In general, the sampling rate of WSNs are smaller than that of sensors, because of the limited transmission bandwidth and energy. In order to realize the spatio-temporal characteristics of WSN-based ecological applications, we show the distribution of spatio-temporal characteristics of ecological research in Figure 4, based on Porter et al.'s analysis results in 2005 [44]. After adding several recent ecological studies mentioned in this article to the research outcome provided by Porter et al., we create a new statistical result. Figure 4 shows that the temporal scale ranges from seconds to several hours, and the spatial scale ranges from

several meters to 100 km. The spatio-temporal sampling of most WSN-based ecological applications falls within such ranges. For temporal scales, obviously, it appears that the minute scale observation is widely adopted by many studies. On the contrary, the conventional methods usually offer a larger temporal scale observation ranging from several hours to years. Specifically specking, the new observation methods using WSN technologies have a smaller temporal scale that cannot be applied to the conventional methods.

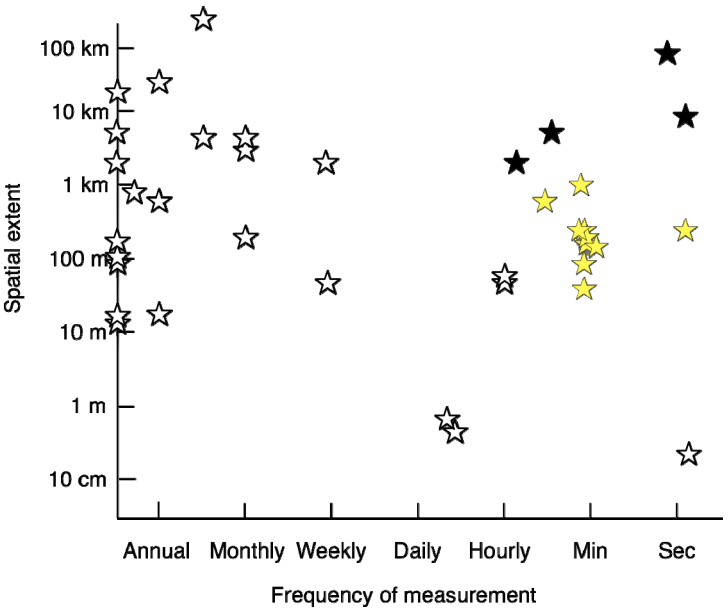

Fig. 4. A distribution of spatio-temporal scales of ecological observation based on the analysis result [44], and which is comuped with several recent ecological studies mentioned in this article. Conventional monitoring methods are marked by open stars, and WSN-based monitoring approaches are marked by black filled stars (surveyed by Porter et al. [44]) and yellow ones (surveyed by this article).

On the other hand, a new paradigm of designing WSNs is multi-scale sensing that can be used to spatially and temporally dynamic phenomena. The basic concept of multi-scale sensing is to employ low-resolution sensor nodes to carry out a wide-range observation. Thus, by doing so, the points (areas) of interest can be identified and then higher-resolution sensor nodes will be used to replace original lower-resolution ones at these points of interest. Our research team has developed an ecological monitoring system for pests using the WSN technology for a long period of time while deploying hundreds of sensor nodes into the fileds [3-4]. Each sensor node can provide the number of its captured pests through an specifically designed pest deciton sensor, and the micro-climate parameters are collected every 30

minutes. The practical deployment sites of our developed system are shown in Figure 5(a). Figure 5(b) illustrates the predicted plane of pest distribution in a monitored orchard using a hot spot analysis approach. After the areas of interest are found, the pest population dynamics and the interaction between pest's behavior and micro-climate (or micro-environmental) variables can be further studied by deploying higher-resolution sensor nodes in the areas. Meanwhile, the cost of providing infrastructure to perform monitoring tasks can be drastically reduced. Hence, indeed, there is a great promise when using WSNs in ecological studies. Nevertheless, there are a number of challenges in developing ecological WSNs. We will discuss this in the following section according to our practical experience of designing and implementing a long-term ecological monitoring system for pests.

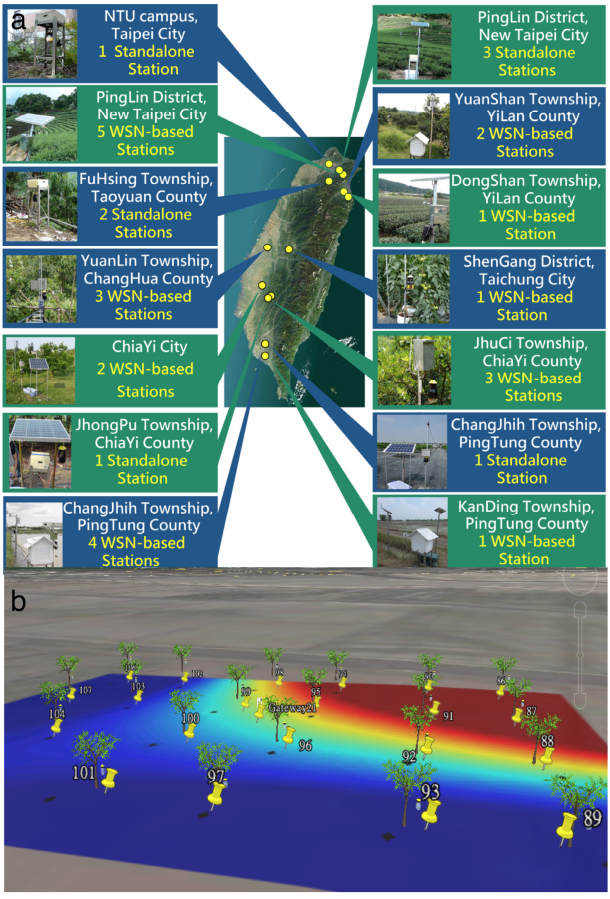

Fig. 5. An illustration of multi-scale sensing. (a) WSN-based ecolgocial monitoing system for pests in Taiwan [3-4]; (b) Red region indicates the hot spot of trapped pest distribution, which suggests that this area of interest should be monitored.

4 Challenges and Opportunity for Sensor Network Development in Ecological Monitoring

4.1 Data Management and Preservation

Ecological WSNs are able to generate a large amount of data due to the characteristics of high-resolution and wide-range sensing. However, the challenging problem is to preserve the fidelity of sensed data while reducing the size of data and transmit it to the remote base station using an energy-efficient way. A larger amount of sensed data to be transmitted will rapidly consume the energy of sensor nodes, and this problem should be addressed especially in ecological monitoring. To overcome such a problem, the data aggregation technology is a prevalent approach [45-48]. The main idea of the data aggregation technology is gathering the sensed data from a number of sensor nodes and sending it to a head node. The gathered data is pruned, compressed, or fused. Thus, the data amount can be reduced. Meanwhile, the fidelity of data can also be retained. For example, video/image sensor networks applied to ecological observation use the image compression technology in order to decrease the data amount to be transmitted [35].

For ecological WSNs, gaps in data flow present a serious and pervasive problem, which will influence the ecological modeling — such as time series analysis — if such observed data is used. In general, data gaps may be caused by many factors, such as outage of power, device failures, poor communication quality, animal destruction, harsh climate, etc. Figure 6 shows some practical photos regarding the problem that WSNs may encounter in a wild environment according to our actual field experience in building the ecological monitoring systems for pests [3-4]. Thus, maintaing a successive observation seems to be a difficult goal to achieve. Even in some sophisticated WSNs, only 50–83% of measurements can be accepted [49-50]. Moreover, a wireless visual surveillance system established by our research team shows that 76% of images have pixel loss rates below 20% in the best case [34]. To date, there are many related schemes proposed to avoid data gaps and guarantee the survival and persistence of sensed data, e.g., energy-harvesting approaches, optimal energy-efficient routing protocols, etc. Among these methods, robust in-network distributed storage mechanisms are a new feasible ones [51-53]. Previous studies generally rely on external storage devices. However, in-network distributed storage mechanisms are more efficient for ecological WSNs, because the sampling rate of sensor nodes may be much higher than the rate that the sensor nodes can upload data to the external storage drive in some high duty cycle observation applications. Furthermore, when the connectivity of sensor nodes breaks down, the sensor nodes with the in-network storage capability can ensure a complete recording. For example, the research team of Light Under Shrub Thicket for Environmental Research (LUSTER) [51] has developed an automatic sensor node with in-network storage capability using SD/MMC flash storage cards affixed to the sensor nodes. The designed sensor nodes support that both redundant in-network storage of data to eliminate data loss and an online query mechanism to recover the missing data. Figure 7 shows the physical photos of the sensor node with a

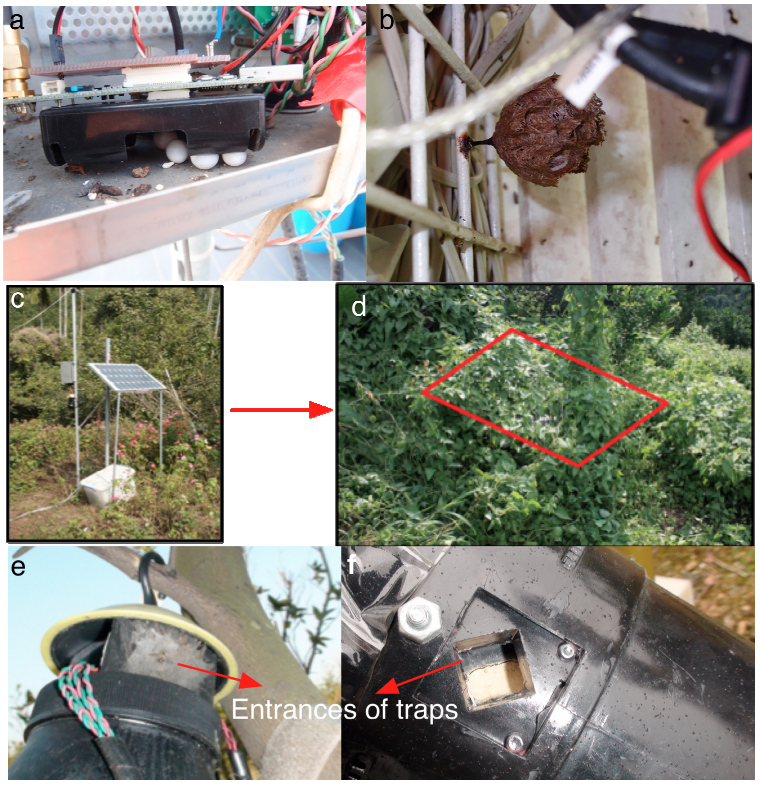

Fig. 6. The problems that WSNs encounter in wild areas [3-4]. (a) the intrusion of geckos, and they laid eggs near the sensor nodes inside the waterproof protection case; (b) a beehive is built inside the waterproof protection case, which implies that the activity of wild bees is present in the case; (c) The initial deployment scene of the solar panel used to power the sensor node; (d) The scene after the monitoring system has been deployed for one year, and the solar panel was covered by these thick leaves; (e) Entrance of the pest trap equpped with automatic infrared sensors is cobwebbed, whcih prohibits the pests (for the oriental fruit fly) from being attractted into the trap; (f) Entrance of the pest trap for the tobacco cutworm is jammed with the beehive.

Fig. 7. The sensor nodes capable of in-network storage using an external SD/MMC storage device, which is implemented based on the MICAz mote [51]

in-network storage device, which is developed by the team of LUSTER[51]. Hence, it is obvious that ecological WSNs have an urgent need of developing preservation strategies to avoid data loss or missing, because they face many challenging problems in wild environment than in a stable indoor environment.

4.2 Energy-Efficient Operation and Energy-Harvesting

Many investigation locations of ecological WSNs are difficult to arrive at, which suggests that the battery change (batteries are the power source for most WSN systems) is not easy to do. Therefore, another challenging problem is to allow ecological WSNs operate normally for a very long time with sufficient electrical power. Two main approches are 1) energy-efficient operation and management of WSNs; and 2) enrichment of power. The majority of existing literature focuses on how to design an energy-efficient WSN. The possible strategies include developing optimal routing protocols, using optimal scheduling strategies for sensor node (i.e., determination of turning-off or turning-on for all sensor nodes), employing the above-mentioned aggregation methods, etc. We will not discuss these strategies in this article due to their prevalence. The second way to prolong network lifetime is to provide additional power to WSNs using energy-harvesting technologies. Energy harvesting is a technique that capture or harvest unused ambient energy (such as thermal, wind, solar, etc.) and convert the harvested energy into the usable electrical energy that can be stored and used for performing sensing tasks. Thus, energy harvesting is increasingly gaining notice in ecological WSNs since it is a potential solution to maximize the system lifetime.

Some energy harvesting prototypes that harvest various energy have been developed. In this article, we focus on discussing the energy-harvesting technologies suitable for the ecological WSNs deployed in wild areas. Generally, energy harvesting can be categorized into three types depending on various sources, including 1) thermal energy; 2) radiant energy; and 3) mechanical energy. Thermal energy can be derived from animal heat and some external heat. Radiant energy can be generated from solar energy and RF waves, and mechanical energy can be derived from vibration, air flow, or heel strikes. Although there are many existing ways to harvest ambient energy, the gathered energy is general small. For example, the power density produced by thermoelectric generators ranges from 100 $\mu W/cm^2$ (at 5℃ gradient) to 3.5 mW/cm^2 (at 30• gradient). The power density produced by vibrational generators, by contrast, is very small ranging from 4 to 800 $\mu W/cm^2$. The power density produced by wind turbine generators vary from 35 $\mu W/cm^2$ (< 1m/s) to 3.5 m W/cm^2 (at 8.4 m/s) [54-56]. However, the power density yielded by solar radiant generators is quite high, reaching 100 mW/cm^3 (exposure to direct sunlight). In addition to the energy-harvesting methods mentioned above, scientists have developed sound energy harvesting systems. When noise comes into an acoustic collector, electrical power will be produced. For example, the noise of a jet plane of 160 dB can produce up to 100 kW power. Recently, they have also devised a prototype of magnetic energy harvesters to collect magnetic energy everywhere on the earth. We expect these technologies can be practically applied to the domain of WSNs in the future.

After surveying the literure related to automatic ecological observation systems, we found that the majority of these observation systems adopted solar energy as their primary power source [25-26, 34-35, 37]. This is because that the solar energy harvesting has a better performance in generating higher electrical power, which matches the demand of long-term ecological monitoring. Although solar energy harvesting systems offer a good way to power WSN-based ecological observation systems, not all of the applications involved with ecological observation need such a energy harvesting system. For example, for cattle behavior observation systems [26], placing solar panels and batteries on cattle to maintain the operation of monitoring systems does not make sense. Thermal energy harvesting systems exploiting natural temperature difference between different materials may be a better solution in this case. In summary, it is worth noting that the selection and design of energy harvesting systems for ecological WSNs may vary due to different requirements of deployment locations and system loading. There is no doubt that energy harvesting systems will become an important component of self-powered ecological WSNs.

4.3 Fault Detection Technology

Because sensor nodes are often deployed in an uncontrolled or even a harsh environment, they are prone to have faults. Thus, it is important to identify the faulty sensor node, locate them, and exclude them from a normally-operating WSN. If available, they can only serve as relaying nodes in charge of transferring sensed data after they are identified as faulty ones. Since ten years ago, fault detection and fault tolerance in WSNs have began to be investigated. Basically, they used the concepts in data mining to discover the necessary information among neighboring nodes and then compared the information with the possible faulty node to determine the abnormal condition. Related to the SOM technology, a number of studies have applied the technology to anomaly detection [57-60]. Siripanadorn et al. [60], for example, have proposed an anomaly detection algorithm using self-organizing map (SOM) coupled with the discrete wavelet transform (DWT) to accurately detect anomalies. By employing DWT, the size of input data to SOM can be efficiently reduced. Moreover, Sharma et al. have employed four anormal detection technologies to detect different types of faults [61]. The Bayesian fault recognition algorithm was also presented to solve the fault-event identification problem in WSNs [62]. In addition to fault detection, some research has further proposed some self-healing strategies for the faulty sensor nodes to recover from the malfunction [63–64]. In addition, Bokareva et al. have proposed a hybrid sensor network structure [64], which is capable of recognizing various types of faults and responding to these possible faults. The basic concept is to use another monitoring node to supervise a number of sensor nodes in a local area. The monitoring nodes are able to survey sensor readings and ensure their correctness. When faults are detected, they can notify the faulty nodes to take an appropriate action.

In a wild field, ecological WSNs are much susceptible to the faults from overheating, low power battery, chemical fouling of sensors, or physical damage, which will result in degradation of sensor accuracy. Furthermore, given that the quality of wireless links easily vary, fault detection or and healing technologies pose an opportunity to improve the effectiveness of ecological WSNs. With such technologies, the invalid sensed data can be found, even be modified or interpolated in advance to ensure that the sensed data is complete. This will be a promising way for ecological WSNs, because ecologists can get a reliable, accurate, and useful data for further analysis.

5 Conclusion

Wireless sensor networks have great potential in ecological and environmental monitoring. Ecologists can use WSNs to collect multiple-point sensed data related to ecological variables at a high temporal scale across broad geographical areas. Sensor nodes equipped with different kinds of sensors are able to monitor various parameters in real world. Ecologists can conduct comparative analysis on some unexplored phenomena based on high spatio-temporal resolution data, if they use WSNs as their research tool. Nevertheless, many challenging questions are emerging from the implementation of the WSN technology in ecological monitoring, including limited energy, inevitable data gaps, sensor degradation, faulty sensors, etc. To date, these issues could be addressed by developing new hardware/software suitable for ecological observation. For example, energy-harvesting technologies have been employed to power WSNs. Some anomaly detection algorithms have been used to identify and locate sensor faults. Ecological WSNs, therefore, have benefitted from the useful technologies.

Although the development of ecological WSNs is promising, ecological WSNs are not insufficient to have a quick answer to some complicated scientific questions in nature. We need to increase the cooperation among research areas including biology, ecology, electrical engineering, information technology, statistics, etc. Only making an effective integration of these research areas can facilitate studies aiming to explore the unobservable and unexpected phenomena in the past.

References

1. Porter, J.H., Nagy, E., Kratz, T.K., Hanson, P., Collins, S.L., Arzberger, P.: New eyes on the world: advanced sensors for ecology. BioScience 59(5), 385–397 (2009)
2. Ramesh, M.V.: Real-time wireless sensor network for landslide detection. In: Proceedings of Third International Conference on Sensor Technologies and Applications, pp. 405–409 (2009)
3. Jiang, J.-A., Tseng, C.-L., Lu, F.-M., Yang, E.-C., Wu, Z.-S., Chen, C.-P., Lin, S.-H., Lin, K.-C., Liao, C.S.: A GSM-based remote wireless automatic monitoring system for field information: A case study for ecological monitoring of the oriental fruit fly, Bactrocera dorsalis (Hendel). Computers and Electronics in Agriculture 62(2), 243–259 (2008)

4. Okuyama, T., Yang, E.-C., Chen, C.-P., Lin, T.-S., Chuang, C.-L., Jiang, J.-A.: Using automated monitoring systems to uncover pest population dynamics in agricultural fields. Agricultural Systems 104(9), 666–670 (2011)
5. Federici, F., Graziosi, F., Faccio, M., Colarieti, A., Gattulli, V., Lepidi, M., Potenza, F.: An integrated approach to the design of wireless sensor networks for structural health monitoring. International Journal of Distributed Sensor Networks, Article ID 594842 (2012)
6. Cybreinfrastructure Vision for 21st Century Discovery, Tech. Rep. Cyberinfrastructure Council, National Science Foundation (March 2007)
7. Porter, J.H., Nagy, E., Kratz, T.K., Hanson, P., Collins, S.L., Arzberger, P.: New eyes on the world: advanced sensors for ecology. BioScience 59(5), 385–397 (2009)
8. Ho, C.K., Itamura, M.T., Kelley, M., Hughes, R.C.: Review of chemical Sensors for in-situ monitoring of volatile contaminants. Tech. report, Sandia National Laboratories (March 2001)
9. Hierlemann, A., Gutierrez-Osuna, R.: Higher-order chemical sensing. Chemical Reviews 108, 563–613 (2008)
10. Hart, J.K., Martinez, K.: Environmental sensor networks: A revolution in earth system science? Earth-Science Reviews 78, 177–191 (2006)
11. Website of National Ecological Observatory Network, http://www.neoninc.org/ (accessed May 15, 2012)
12. Website of CLEANER program, http://www.nsf.gov/pubs/2003/nsf03607/nsf03607.html (accessed May 15, 2012)
13. Website of GLEON, http://www.gleon.org/ (accessed May 15, 2012)
14. Rundel, P., Estrin, D., Kaiser, W.: Innovations in Environmental Monitoring. Sourthern California Environmental Report Card, pp. 31–37 (2006)
15. Website of IEOS, http://eospso.gsfc.nasa.gov/ (accessed May 15, 2012)
16. Website of TEO, http://www.teo.unt.edu/ (accessed May 18, 2012)
17. Collins, S.L., Bettencourt, L.M.A., Hagberg, A., Brown, R.F., Moore, D.I., Bonito, G., Delin, K.A., Jackson, S.P., Johnson, D.W., Burleigh, S.C., Woodrow, R.R., McAuley, J.M.: New opportunities in ecological sensing using wireless sensor networks. Frontiers in Ecology and the Environment 4(8), 402–407 (2006)
18. Faso, E., Rossi, M., Widmer, J., Zeros, M.: In-network aggregation techniques for wireless sensor networks: a survey. IEEE Wireless Communication Magazine, 70–87 (April 2007)
19. Shaikh, F.K., Khelil, A., Ali, A., Suri, N.: Reliable congestion-aware information transport in wireless sensor networks. International Journal of Communication Networks and Distributed Systems 7(1/2), 135–152 (2011)
20. Maraiya, K., Kant, K., Gupta, N.: Wireless sensor network: a review on data aggregation. International Journal of Scientific & Engineering Research 2(4), 1–7 (2011)
21. Website of Sensor Web Enablement, http://www.opengeospatial.org/projects/groups/sensorwebdwg/ (accessed May 16, 2012)
22. Delin, K.A.: The sensor web: a macro-instrument for coordinated sensing. Sensors 2, 70–85 (2002)
23. Delin, K.A., Jackson, S.P., Johnson, D.W., Burleigh, S.C., Woodrow, R.R., McAuley, J.M., Dohm, J.M., Ip, F., Ferré, T.P.A., Rucker, D.F., Baker, V.R.: Environmental studies with the sensor web: principles and practice. Sensors 5(1-2), 103–117 (2005)
24. Rundel, P.W., Graham, E.A., Allen, M.F., Fisher, J.C., Harmon, T.C.: Environmental sensor networks in ecological research. New Phytologist 182(3), 589–607 (2009)

25. Yang, J., Zhang, C., Li, X., Huang, Y., Fu, S., Acevedo, M.F.: Integration of wireless sensor networks in environmental monitoring cyber infrastructure. Wireless Networks 16(4), 1091–1108 (2009)
26. Handcock, R.N., Swain, D.L., Bishop-Hurley, G.J., Patison, K.P., Wark, T., Valencia, P., Corke, P., O'Neill, C.J.: Monitoring animal behaviour and environmental interactions using wireless sensor networks, GPS collars and satellite remote sensing. Sensors 9(5), 3586–3603 (2009)
27. Naumowicz, T., Freeman, R., Kirk, H., Dean, B., Calsyn, M., Liers, A., Braendle, A., Guilford, T., Schiller, J.: Wireless sensor network for habitat monitoring on Skomer Island. In: Proceedings of the 5th IEEE International Workshop on Practical Issues in Building Sensor Network Applications, pp. 882–889 (2010)
28. Collins, S.L., Bettencourt, L.M.A., Hagberg, A., Brown, R.F., Moore, D.I., Bonito, G., Delin, K.A., Jackson, S.P., Johnson, D.W., Burleigh, S.C., Woodrow, R.R., McAllen, J.M.: New opportunities in ecological sensing using wireless sensor networks. Frontiers in Ecology and the Environment 4(8), 402–407 (2006)
29. Bhadauria, D., Isler, V., Studenski, A., Tokekar, P.: A robotic sensor network for monitoring carp in Minnesota lakes. In: Proceedings of the 2010 IEEE International Conference on Robotics and Automation (ICRA), pp. 3837–3842 (2010)
30. Seders, L.A., Shea, C.A., Lemmon, M.D., Maurice, P.A., Talley, J.W.: LakeNet: an integrated sensor network for environmental sensing in lakes. Environmental Engineering Science 24, 183–191 (2007)
31. Caron, D.A., Stauffer, B., Moorthi, S., Singh, A., Battalion, M., Graham, E.A., Hansen, M., Kaiser, W.J., Das, J., Pereira, A.: Macro-to fine-scale spatial and temporal distributions and dynamics of phytoplankton and their environmental driving forces in a small montane lake in southern California, USA. Limnology and Oceanography, pp. 2333–2349 (2008)
32. Sukhatme, G.S., Dhariwal, A., Zhang, B., Oberg, C., Stauffer, B., Caron, D.A.: Design and development of a wireless robotic networked aquatic microbial observing system. Environmental Engineering Science 24, 205–215 (2007)
33. Roth, T.R., Westhoff, M.C., Howard, H., Huff, J.A., Rubin, J.F., Barrenetxea, G., Vetterli, M., Pariah, A., Sekler, J.S., Parlange, M.B.: Stream temperature response to three riparian vegetation scenarios by use of a distributed temperature validated model. Environmental Science & Technology 44, 2072–2078 (2010)
34. Chen, C.-P., Chuang, C.-L., Lin, T.-S., Liu, C.-Y., Jiang, J.-A., Yuan, H.-W., Chiou, C.-R., Hong, C.-H.: TernCam: an automated energy-efficient visual surveillance system. International Journal of Computational Science and Engineering (accepted to be published, 2012)
35. Wawerla, J., Marshall, S., Mori, G., Rothley, K., Sabzmeydani, P.: Bearcam: Automated wildlife monitoring at the arctic circle. Journal of Machine Vision Applications 20(5), 303–317 (2009)
36. Wang, H., Elson, J., Girod, L., Estrin, D., Yao, K.: Target classification and localization in habitat monitoring. In: Proceedings of the International Conference on Acoustics, Speech, and Signal Processing (ICASSP), pp. 844–847 (April 2003)
37. Hu, W., Bulusu, N., Chou, C.T., Jha, S., Taylor, A., Tran, V.N.: Design and evaluation of a hybrid sensor network for cane toad monitoring. ACM Transactions on Sensor Networks 5, 1–28 (2009)
38. Butler, R., Servilla, M., Gage, S., Basney, J., Welch, V., Baker, B., Fleury, T., Duda, P., Gehrig, D., Bletzinger, M.: Cyberinfrastructure for the analysis of ecological acoustic sensor data: a use case study in grid deployment. Cluster Computing 10, 301–310 (2007)

39. Wang, H., Chen, C.E., Ali, A.M., Asgari, S., Hudson, R.E., Yao, K., Estrin, D., Taylor, C.: Acoustic sensor networks for woodpecker localization. In: Proceedings of SPIE, vol. 5910, pp. 591009-1–591009-12 (2005)
40. Lach, J., Evans, D., McCune, J., Brandon, J.: Power-efficient adaptable wireless sensor networks. In: Proceedings of International Conference on Military and Aerospace Programmable Logic Devices, MAPLD (2003)
41. Brazil, M., Ras, C.J., Thomas, D.A.: Deterministic deployment of wireless sensor networks. In: Proceedings of the 2009 World Congress on Engineering, vol. 1, pp. 863–868 (2009)
42. Bondarenko, O., Kininmonth, S., Kingsford, M.: Underwater Sensor Networks, Oceanography and Plankton Assemblages. In: Proceedings of the International Conference on Intelligent Sensors, Sensor Networks and Information, pp. 657–662 (2007)
43. Howe, B.M., Chao, Y., Arabshahi, P., Roy, S., McGinnis, T., Gray, A.: A Smart Sensor Web for Ocean Observation: Fixed and Mobile Platforms, Integrated Acoustics, Satellites and Predictive Modeling. IEEE Journal of Selected Topics in Applied Earth Observations and Remote Sensing 3, 507–521 (2010)
44. Porter, J., Arzberger, P., Braun, H.-W., Bryant, P., Gage, S., Hansen, T., Hanson, P., Lin, C.-C., Lin, F.-P., Kratz, T., Michener, W., Shapiro, S., Williams, T.: Wireless Sensor Networks for Ecology. BioScience 55(7), 561–572 (2005)
45. Jiang, X., Huang, L., Zhang, J., Li, Y., Kai, Y.: Application of Data Fusion in Ecological Environment Monitoring System. In: Hou, Z. (ed.) Measuring Technology and Mechatronics Automation in Electrical Engineering. LNEE, vol. 135, pp. 109–117. Springer, Heidelberg (2012)
46. Yoon, S., Sahib, C.: The Clustered AGgregation (CAG) technique leveraging spatial and temporal correlations in wireless sensor networks. ACM Trans. Sen. Netw. 3(1), Article 3
47. Meng, X., Wang, C.: Application of data fusion technology in greenhouse environment monitoring and control system. Computer and Computing Technologies in Agriculture 3, 293–299 (2011)
48. Gupta, V., Pandey, R.: Data fusion and topology control in wireless sensor networks. WSEAS Transactions on Signal Processing 4(4), 150–172 (2008)
49. Richardson, A.D., Hollinger, D.Y.: A method to estimate the additional uncertainty in gap-filled NEE resulting from long gaps in the CO2 flux record. Agricultural and Forest Meteorology 147, 719–729 (2007)
50. Xing, Z.S., Bourque, C.P.A., Meng, F.R., Cox, R.M., Swift, D.E., Hza, T.S., Chow, L.: A process-based model designed for filling of large data gaps in tower-based measurements of net ecosystem productivity. Ecological Modeling 213, 165–179 (2008)
51. Slavo, L., Wood, A., Cao, Q., Sookoor, T., Liu, H., Srinivasan, A., Wu, Y., Kang, W., Stankovic, J., Young, D., Porter, J.: LUSTER: wireless sensor network for environmental research. In: Proceedings of the 5th ACM Conference on Embedded Networked Sensor Systems, SenSys (2007)
52. Khan, M.I., Gansterer, W.N., Haring, G.: In-network storage model for data persistence under congestion in wireless sensor network. In: The First International Conference on Complex, Intelligent and Software Intensive Systems (CISIS), pp. 221–228 (2007)
53. Luo, L., Huang, C., Abdelzaher, T.F., Stankovic, J.: EnviroStore: a cooperative storage system for disconnected operation in sensor networks. In: Proceedings of INFOCOM 2007, pp. 1802–1810 (2007)

54. Roundy, S., Steingart, D., Frechette, L., Wright, P., Rabaey, J.: Power Sources for Wireless Sensor Networks. In: Karl, H., Wolisz, A., Willig, A. (eds.) EWSN 2004. LNCS, vol. 2920, pp. 1–17. Springer, Heidelberg (2004)
55. Tan, Y.K., Panda, S.K.: Review of energy harvesting technologies for sustainable wireless sensor network. In: Tan, Y.K. (ed.) Sustainable Wireless Sensor Networks, pp. 1–30. InTech
56. Wan, Z., Tan, Y., Yuen, C.: Review on energy harvesting and energy management for sustainable wireless sensor networks. In: Proceedings of the IEEE 13th International Conference on Communication Technology (ICCT), pp. 362–367 (2011)
57. Barreto, G.A., Mota, J.C., Souza, L.G., Frota, R.A., Aguaya, L.: Condition monitoring of 3G cellular network through. IEEE Trans. Neural Networks 16(5), 1064–1075 (2006)
58. Sukkhawatchani, P., Usaha, W.: Performance evaluation of anomaly detection in cellular core networks using self-organizing map. In: Proceedings of ECTI-CON 2008, vol. 1, pp. 361–364 (2008)
59. Paladina, L., Paone, M., Jellamo, G., Puliafito, A.: Self organizing maps for distributed localization in wireless sensor networks. In: Proceedings of the 12th IEEE Symposium on Computers and Communications, pp. 1113–1118 (2007)
60. Siripanadorn, S., Hattagam, W., Teaumroong, N.: Anomaly detection in wireless sensor networks using self-organizing map and wavelets. International Journal of Communications 4(3), 74–83 (2010)
61. Sharma, A.B., Golubchik, L., Govindan, R.: Sensor faults: detection methods and prevalence in real-world datasets. Trans. on Sensor Networks 5, 1–34 (2010)
62. Luo, X., Dong, M., Huang, Y.: On distributed fault-tolerant detection in wireless sensor networks. IEEE Trans. Comput. 55(1), 58–70
63. Bein, D.: Self-Organizing and Self-Healing Schemes in Wireless Sensor Networks. In: Misra, S., Woungang, I., Misra, S.C. (eds.) Guide to Wireless Sensor Networks, pp. 293–304. Springer (2009)
64. Bokareva, T., Bulusu, N., Jha, S.: SASHA: toward a self-healing hybrid sensor network architecture. In: Proceedings of the 2nd IEEE Workshop on Embedded Networked Sensors (EmNets 2005), pp. 71–78 (2005)

Development of an Embedded System-Based Gateway for Environmental Monitoring in Wild Fields

Xiang-Yao Zheng, Chun-Yi Liu, Po-Tang Chen, Cheng-Long Chuang, Chia-Pang Chen, and Joe-Air Jiang

National Taiwan University
Taipei, Taiwan

Abstract. Acquiring continuous observation results is an essential demand for environmental monitoring. Wireless sensor networks (WSNs), encompassed of many tiny sensing devices, give a good solution when collecting continuously temporal and spatial data. Because WSNs have no long-range communication capabilities, a gateway is needed to collect sensing data from wild fields and transmit the data to a backend server. The gateway has to handle all sensor nodes in a network, so both stability and processing capability have higher priorities. Thus, to achieve these goals, an embedded system-based field gateway with an energy-efficient design that includes a suitable graphical user interface for system maintenance and a touch screen is proposed. The touch screen provides users with gateway information, so that the users can take action when facing unexpected situations. The operation of the gateway is self-sustained by a lead-acid battery and a solar cell.

1 Introduction

Wireless sensor networks (WSNs) have been widely applied to environmental monitoring in recent years [1-11]. Small-sized wireless sensors not only consume less power but also enable wireless communication, so they can be used in high density and high frequency monitoring [2-11]. The overview of conventional WSN architecture is shown in Figure 1. In this figure, sensor nodes are deployed in an area of interest. A gateway manages the whole network, collects and transmits the sensed data to a backend server via the communication network. The communication network can use different types of communication technologies such as Ethernet (wired or wireless) and Global System for Mobile Communications (GSM). Based on the GSM communication technology, Short Message Service (SMS) and General Packet Radio Service (GPRS) are also available for data transmission between the gateway and the WSN. Administration personnel can manage the WSN through an access to a backend server, and other users (clients) can browse the webpages that provide monitoring information.

S.C. Mukhopadhyay et al. (Eds.): Advancement in Sensing Technology, SSMI 1, pp. 23–42.
springerlink.com

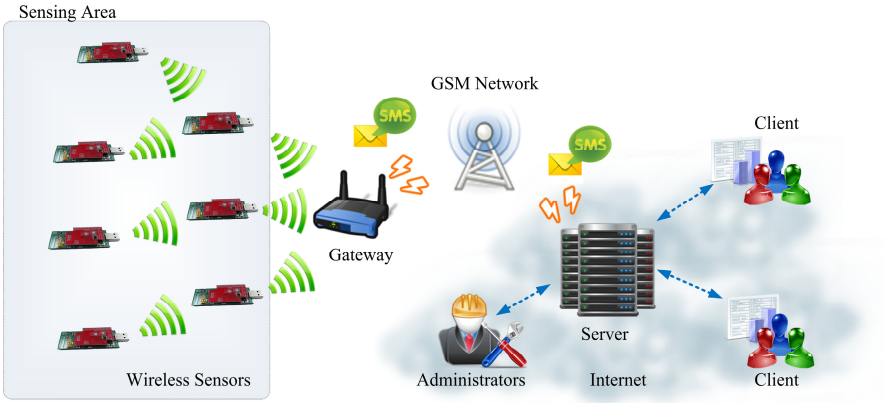

Fig. 1. Overview of conventional WSN architecture

In WSNs, a gateway plays an important role as it performs data-gathering, data-transmission, and network-management tasks. To process a great amount of continuously spatial-temporal data acquired from sensor nodes that perform environmental monitoring task, the gateway must have a high computing capability, consume lower energy, and survive in a wild environment for longer period of time. For example, Song et al. [12] proposed an embedded system based gateway that provided both high computing and maintenance capabilities designed for WSNs. This gateway was built on a well-designed embedded board controlled by the embedded Linux, and it was able to transmit the data through Ethernet. Users were allowed to control the gateway via the website provided by the built-in Linux web server. However, this design was not suitable for long-term monitoring in a wild field, since it did not take energy consumption and gateway durability into account. Aiming at lower power consumption, on the other hand, Alippi et al. built a solar-powered WSN framework for environmental monitoring [13]. A better integration of software and hardware in their proposed system led to a successful long-term environmental monitoring. The researchers also introduced an activity management scheme to ensure that the system could operate as long as possible. Moreover, in order to extend the lifetime of WSNs, some studies focused on the energy-efficient communication techniques and tools of communication. For instance, Zarrabi et al conducted a case study on a ZigBee-based WSN [14], and found that the ZigBee-based WSN was a good solution for solving the problem of limited power supply when a proper activity management program was also employed. Some researchers tried to develop energy-efficient protocols for WSNs. Zabin and Ren proposed two different protocols [15-16]. Zabin focused on the routing protocol that tackled the problem of limited power supply and successfully combined diffusion-based and data centric methods to save energy. Ren also took energy efficiency into account by emphasizing the balance of energy consumption through the routing table in the network. In this paper, an energy-efficient gateway based on an embedded system was developed, and the gateway is powered by a battery recharged by a solar cell to prolong the system operational time. The gateway can also perform heavy computation tasks.

1.1 Recent Development of Field Gateways

Recently, due to the miniaturization and cost reduction of electronic products, field gateways based on the embedded system are starting to be employed in WSN applications. According to the literature mentioned above, the embedded gateway is able to provide the capability of front-end processing and sensor information analyse. With a powerful computation capability, the embedded gateway could efficiently manage a large number of sensor nodes multi-tasking operations, and file and data fusion systems. Moreover, the embedded system can be easily powered by a battery recharged by a solar panel, as it is deployed in an outdoor environment without electricity supply. The embedded system also provides a variety of communication interfaces. In an indoor environment, for example, the embedded system can transmit the data through the wired Ethernet device. Otherwise, the embedded system uses a wireless transmission module such as the GSM/GPRS/3G/4G communication modem to complete the communication task in the field where physical wiring is difficult.

Some researchers have used a variety of embedded system based gateways ecological monitoring. Song et al [12], for example, proposed an embedded system based gateway for field observation. Their study results showed that the computing capability of the proposed gateways outperformed that of the microprocessor-based gateway, because the latter may not be able to deal with a large amount of data collected from monitoring area. Consequently, the data was not transmitted to the destination. Sensor nodes may have to resend the data, and this would make the transmission flow dramatically increase and finally cause the whole sensing network crash. Therefore, it is necessary to develop a high performance and reliable gateway to maintain the operation of the entire system. The gateway proposed by Song et al. [12], however, may not be applied to large-scale ecological monitoring, because the computing capability of the gateway is not sufficient to manage the large quantity of data gathered during large-scale monitoring.

Some studies did propose embedded gateways designed for agricultural monitoring systems. Li et al. [17], for example, established a WSN system using an embedded gateway for vegetable greenhouses monitoring. This study presented a graphical user interface (GUI) for the gateway deployed in the greenhouse, and users are allowed to send commands to manage sensor nodes through the GUI. In addition to the GUI, this study also proposed a mechanism that dealt with data loss and a delay processing mechanism to avoid sensing data loss. Yoo et al. [18], developed a WSN system using an embedded gateway for melon greenhouses monitoring. The proposed WSN system allowed users to use hand-hold devices – such as a PDA – to show the greenhouse related information and directly manage sensor nodes.

For ecological monitoring, the monitoring network generally includes many sensor nodes, so the embedded gateway is expected to manage a large number of sensor nodes. Vana et al. [19], for example, developed a wireless sensor network that includes an embedded system gateway to monitor an olive grove. The gateway that they proposed combined an embedded system and a GPS module, and it forwarded the monitoring information from the WSN to a central server through the TCP/IP protocol. This gateway could get access to the WSN through the Internet. In addition, a camera node was used to observe the olive grove.

In this study, proposed gateway managed three nodes, so the number of nodes that the gateway controlled was very small for ecological monitoring. This embedded gateway, thus, may not be used in large-scaled ecological monitoring.

Some studies did proposed embedded gateways designed for the large-scaled habitat monitoring. Mainwaring et al. [20], for instance, used an embedded gateway to monitor the nesting environment of seabirds and observe their behavior. This study deployed a network of 32 nodes and a StrongArm-based embedded field gateway on a small island off the coast of Maine streaming. In addition to supporting remote interactions via the Internet, the embedded gateway enabled the in-situ interactions between users and the WSN. During the initial deployment of the WSN, on-site users required to examine the connections among sensor nodes and the gateway and set the operational parameters. A small sized PDA was used to assist the on-site users to perform these tasks. To achieve long-term ecological monitoring, the sensor nodes and the gateway in this study were all powered by a solar system. Table 1 shows a detailed comparison of different

Table 1. Comparison of different embedded gateways

Research Institute	National Taiwan University (the proposed system)	Beijing Science and Engineering Technology Institute [12]	Croatia Zagreb University [19]	USA California Berkeley University [20]	South China Agricultural University [21]
Processor	Texas Instrument Cortex A8 1 GHz	Intel Xscale PXA270 624 MHz	Actel Cortex M1 350 MHz	Intel PXA255 400 MHz	Samsung S3C2410X 200 MHz
Memory	Micron 4 Gb MDDR SDRAM	64 MB SDRAM and 32 MB NOR Flash	N/A	32 MB SDARM and 32 MB Flash	64 MB SDRAM and 64 MB NAND Flash.
Ethernet (Mbps)	10/100	10/100	No Ethernet	10/100	10/100
Power Connector	5 V	5 V	N/A	5 V	N/A
The size of WSN (ideal state)	About 40 nodes	N/A	3 nodes	32 nodes	20 nodes
Unit Price	US$149	US$599	~US$124	N/A	N/A
Communication way to the back-end server	GSM	Ethernet	GPRS	Ethernet	Ethernet
GUI Availability	Yes	Yes	No	No	No

embedded gateways proposed in recent years. All of these studies proposed an embedded based gateway to be the gateway in an entire WSN for ecology monitoring, but they had to overcome the drawbacks mentioned above.

With the merits of better capabilities in computing and data-storage, the embedded system based field gateway devised in our study acts as a control center to gather, store, and transmit data to a backend server. Additionally, it also determines the best transmission route for each sensor node in order to maintain the stability of the network. Different from sensor nodes being characterized by the feature of low power consumption, field gateways inevitably consume much energy, because the latter have to manage all of the information in a WSN. Thus, it is necessary to allow filed gateway to have sufficient power supply when they are deployed in wild environments. In our previous study, for example, the integration of a chargeable battery and a solar cell has served as a good solution to extend the lifetime of a field gateway. An energy-efficient protocol also helps reduce the power consumption of the gateways so as to extend the lifetime of the gateways. Thus, in this study the proposed embedded system-based gateway has a self-powered capability. In addition, a friendly graphical user interface designed for the gateway is also developed for improving in-situ management. Moreover, the proposed gateway involves two important mechanisms that allow sensor nodes entering a sleep mode and network rerouting. With the sleep mechanism, wireless sensor nodes could save energy when the network does not need to collect sensing data. The rerouting mechanism is used to improve data delivery rates. These proposed mechanisms will be discussed in detail later.

The remainder of this chapter is organized as follows. In the Section 2, we present the system architecture of the proposed gateway. In the Section 3, the design of the administrative program is described in detail. System verification is presented in the Section 4. Finally, conclusions and future research plans are provided in the Section 5.

2 Architecture of the Propsoed Gateway

The proposed embedded system-based gateway is composed of an embedded board and a number of external devices. Figure 2 shows the embedded board and a number of external devices. As Figure 2 shows, the proposed gateway can connect with different input and output interfaces. For regular users, the gateway can connect with a HDMI monitor to obtain the gateway information, and administrators can use a RS232 cable to connect to the embedded system to manage gateway data or change some parameters of the proposed gateway. Figure 3 shows the block diagram of the proposed gateway in which the principal parts of the gateway are represented. The embedded board is the main part of the gateway and is responsible for basic computation. The board provides four Universal Serial Bus (USB) connectors, which are used to connect to other external devices, e.g. the weather module, the ZigBee communication module, and the GSM modem. By connecting it with the external devices, the gateway is capable of retrieving meteorological information and communicating with sensor nodes in the WSN and the back-end server.

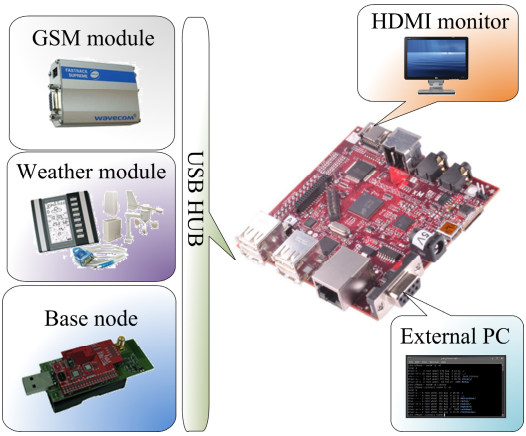

Fig. 2. Architecture of the proposed gateway that consists of an embedded board and externally connected devices

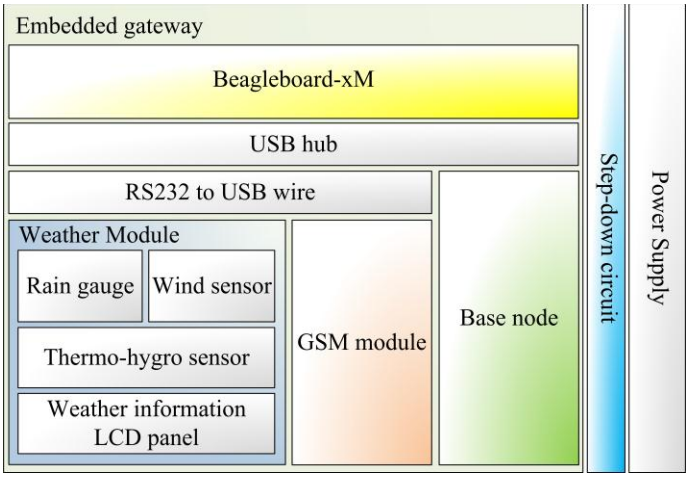

Fig. 3. Block diagram of the proposed gateway

Figure 4 shows the block diagram of the architecture of the embedded board. As the figure shows, the hardware part of the embedded board has a RS-232 interface which is used to communicate with a personal computer when system adjustment or maintenance is required. The Beagleboard-xM embedded board designed by the Beagleboard company [22-23] is adopted in this study, and it is composed of an ARM architecture-based CPU with a NAND flash, a synchronous dynamic random access memory (SDRAM) and a memory management unit (MMU) designed by Texas Instruments. The configuration of the Beagleboard-xM is shown in Figure 5. Due to its energy-efficient feature, the ARM-based embedded system is widely utilized to develop many tiny devices such as mobile phones, printers, and watches. Thus, the proposed WSN gateway also uses the Beagleboard-xM for long-term ecological monitoring. The detail hardware

information of Beagleboard-xM is shown in Table 2. The CPU of Beagleboard-xM has 1GHz operating frequency, and such processing capability is enough for the gateway deployed in a wild field. In addition, the Beagleboard-xM has an overvoltage protect mechanism, and this mechanism can protect the embedded system if an overvoltage situation occurs. Some popular Linux distributions supported by Beagleboard-xM are: Debian, Ubuntu, and Angstorm. In this study, Angstorm was included in our gateway program.

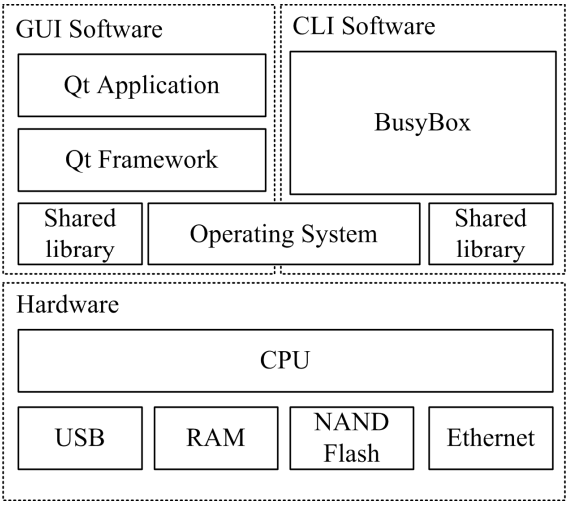

Fig. 4. Block diagram of the architecture of the embedded board

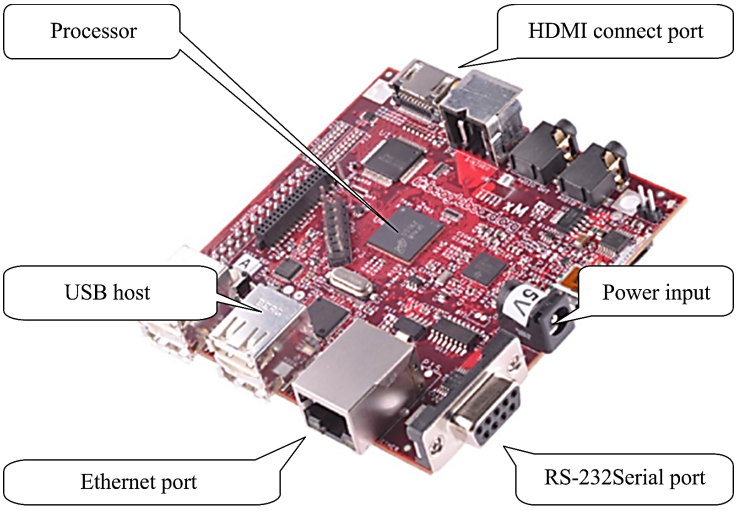

Fig. 5. Configuration of the Beagleboard-xM

Table 2. Detailed hardware information of the Beagleboard-xM [23]

Component	Specification
Processor	Texas Instruments Cortex A8 1 GHz processor
Memory	Micron 4Gb MDDR SDRAM 200 MHz
Debug Support	14-pin JTAG, GPIO Pins, UART, and 3 LEDs
PCB	3.1" × 3.0" (78.74 × 76.2 mm); 6 layers
Ethernet	10/100 Mbps
SD Connector	Micro SD
User Interface	1-User defined button and reset button
Video	DVI-D and S-Video
Overvoltage Protection	Shutdown @ Over voltage
Power Connector	USB power and external DC power (5V)

The operation system of the embedded board is the Linux kernel. Two interfaces -command-line interface (CLI) and a – graphical user interface (GUI) – are controlled by BusyBox shell [24] program under the Linux system and Qt, respectively Qt is a cross platform program language based on C++, and it can be executed on different operating systems like Windows, Linux and Mac. Qt also has many shared libraries regarding the design of the GUI program. In this study, the GUI is developed for users to get gateway information and control the gateway through input devices like mouse or keyboard. The work flow of the gateway program will introduce in Section 6 in detail.

The proposed gateway is also able to temporarily store the sensing data received from sensor nodes and its own operational information. Compared to the microprocessor-based field gateway, the embedded system-based gateway is more flexible. And it is also more energy efficient than the computer-based gateway. In this study, the Beagleboard-xM based gateway is equipped with a base node (Zigbee communication module with a CC2420 RFIC [25] controlled by a MSP microprocessor [26]) and a GSM modem by which the gateway is able to communicate with a WSN and a backend server. In addition, a monitor connected to the gateway is used to show instant information regarding the operational status of the WSN and the gateway, and the signal quality of the GSM network. The monitor is generally turned off to save energy during the operational period of the gateway. Moreover, the gateway is equipped with a weather module designed by the LA CROSSEE technology company [27]. The weather module is composed of a thermo-hygro sensor, a wind sensor, a rain gauge and a LCD display that shows the instant weather information. Table 3 summarizes the specification of each meteorological sensor connected to the weather module. The weather module provides the weather parameters at the sensing area, and the gateway transmits the weather parameters to the back-end server further analysis

3 Design of the Management Software Used in the Proposed Gateway

The gateway software program includes two parts; one focuses on the program associated with the WSN auto-management that controls network initiation and operation, and the other concentrates on developing a GUI. This study introduces another Qt-based program to perform auto-management tasks. Through the RS232 interface, the auto-management program is able to communicate with the base node and the GSM modem through which the gateway can get the sensing data and transmit it to the backend server. Moreover, the auto-management program is responsible for automatically retrieving the data from the weather station according to a predetermined time period. Using a duplex processor, these tasks can be performed by the gateway at the same time. The detailed flowchart of the auto-management program is shown in Figure 6. There are three kinds of stages that the proposed gateway will experience: system initialization, data collecting, and data receiving. First kind of events is system initialization. When the gateway starts, it will broadcast an initialization command to initialize the whole sensors network. After the initialization stage, the gateway will start to deploy the network through broadcasting 10 deployment commands. Then, the gateway will wait for acknowledgement (ACK) signal from sensor nodes. If no sensor nodes respond to the ACK signal, this means that the deployment of this round fails and the gateway will reboot to redeploy the sensor network again. If the deployment stage is successful, the gateway will calculate the data delivery rate of the successful round. If the data delivery rate is lower than a predetermined threshold, then the gateway will broadcast a redeployment command to redeploy the whole sensor network. On the other hand, if the data delivery rate is acceptable, then the gateway will save the routing results and send these results to the back-end server so that administrators can monitor the routing status of the network. The following stage after the successful deployment is the data collecting stage. In this stage, the gateway broadcasts an update command and a data collecting command to sensor nodes in the sensing area, and these commands will allow the nodes to collect sensing data. If sensor nodes receive these commands, they will update their status and transmit the sensing data collected by them to the gateway. When the base node that connects to the gateway receives the sensing data from

Table 3. Specification of each sensor connected to the weather module [28]

Type of sensor	Unit	Range	Resolution
Temperature	°C	−29.88 ~ 69.88	0.1111
Relative Humidity	%RH	1 ~ 99	1
Rainfall	mm	0 ~ 999.99	0.254
Wind Speed	m/s	0 ~ 49.97	0.044
Wind Direction	degrees	0 ~ 337.5	22.5
Air Pressure	hPa	300.03 ~ 1098.88	0.34

sensor nodes, the data receiving stage is initiated. The base node will broadcast an ACK command to sensing nodes, because the gateway will record the information regarding how many nodes are in the sensing area. If some of the nodes do not transmit sensing data this round, the gateway will broadcast a retransmitting command to these nodes and ask them to retransmit the sensing data again. For the purpose of energy saving, after sending the retransmitting command, the base node will broadcast a sleep command to the whole sensing network and ask sensing nodes to enter a sleep mode and the sensing nodes will be awaken in the next round to transmit the sensing data.

Figure 7 shows the block diagram of the gateway programs in detail. As this figure shows, the proposed gateway programs include different parts. The controller and the serial node controller perform the main tasks of the proposed gateway. The controller includes different slot functions and other gateway programs could activate these functions through sending corresponding signals. The serial node controller is designed to handle the data packets from the base node. When a data packet is received by the base node, the serial node controller will send out a signal of receiving the packet to the controller, and then the controller will deal with the data packet.

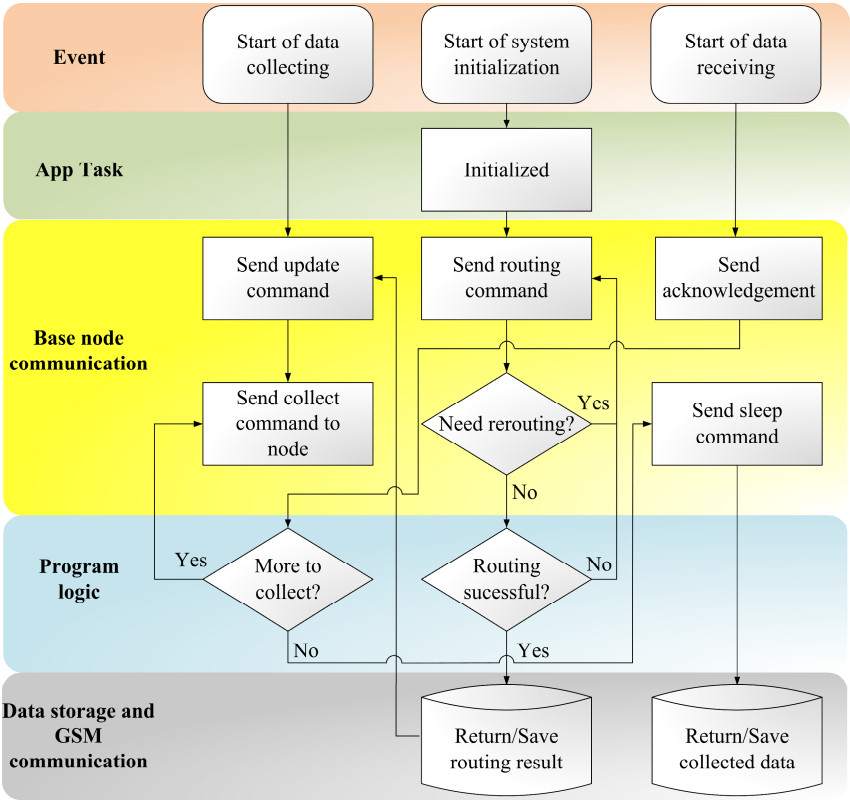

Fig. 6. Flowchart of the gateway auto-management program

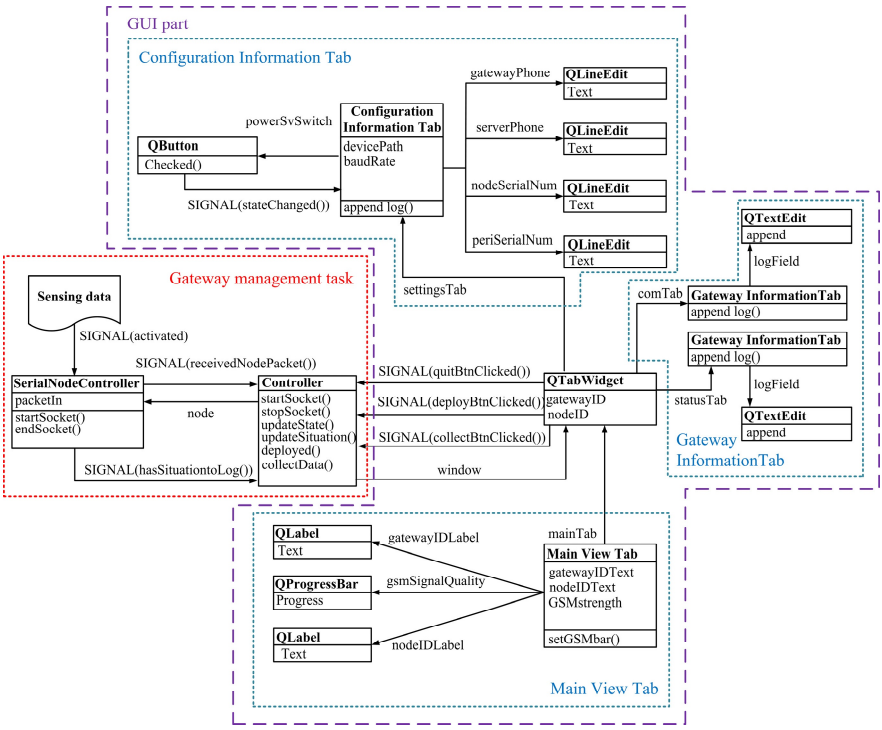

Fig. 7. Data signal flowchart of the gateway auto-management program

The rest parts of the gateway programs are related to GUI. The main purpose of the GUI is to visually provide administration personnel useful information such as sensor network status and GSM signal quality. In this research the GUI is a multi-dialog interface that has three sub-frames: 1) Main View, 2) Gateway Information, and 3) Configuration Information. The Main View frame, as shown in Figure 8, demonstrates how strong the GSM signal is, how many nodes are deployed, and how many nodes are working properly. The Gateway Information frame, as shown in Figure 9, provides event logs during the program execution, so users are able to know whether the gateway operates normally. Two control buttons are designed for users to rebuild the entire network or to immediately acquire real-time information. In addition, the Configuration Information frame, as shown in Figure 10, allows users to set/change the phone number of administration personnel for emergency notification when the system fails. The administration personnel can also change some parameter settings through this GUI. As Figure 10 shows, for example, administrators can use the serial port settings on the Configuration Information frame to change the serial port number connected to the GSM modem.

The gateway program is implemented on the Qt framework [29], which is a type of object-oriented programming architecture and uses an event-based programming language. Qt is based on C++, and it is a powerful tool when designing GUIs. After the initialization, the gateway monitors the network and shows the network status on the GUI.

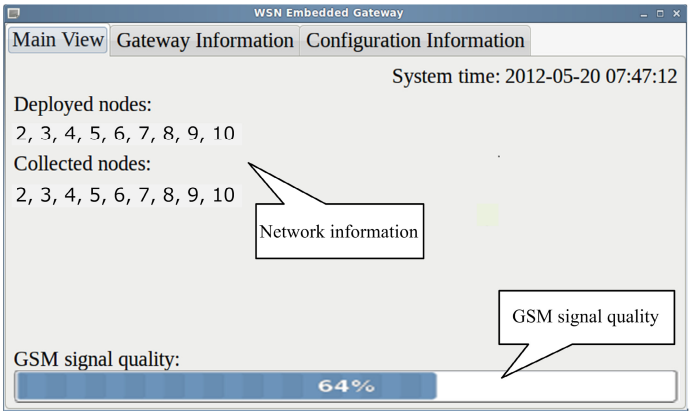

Fig. 8. Main View frame of the gateway GUI

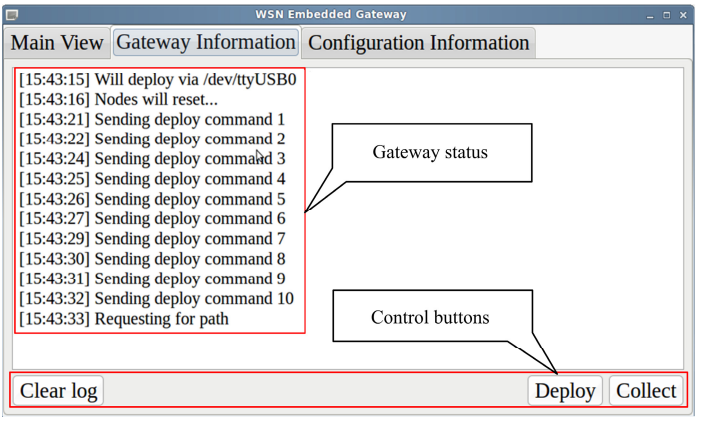

Fig. 9. Gateway Information frame of the gateway GUI

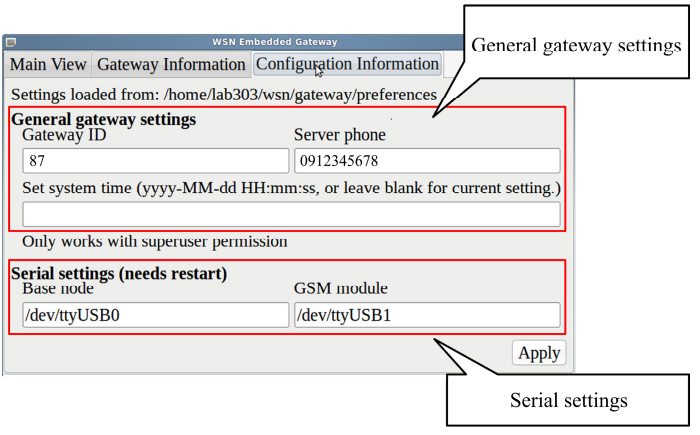

Fig. 10. Configuration Information frame of the gateway GUI

4 System Verification

To verify the robustness and stability of the proposed gateway, a series of field experiments were conducted in this research. First, a data delivery rate was measured to verify the robustness of the proposed gateway. The data delivery rate is defined by the following formula:

$$\theta = \frac{D_r}{D_t} \times 100\%, \tag{1}$$

where D_r is the actual number of sets of data that the gateway received, and D_t is the number of sets of data that the gateway should receive. To verify the robustness of the proposed gateway, a large number of sensor nodes were evenly deployed in an indoor room. The size of the experimental site was about 6 m × 1 m.

4.1 Indoor Experiments

To test whether the proposed gateway could still work properly after connecting to a large number of sensor nodes, a series of experiments with different numbers of sensor nodes were conducted, ranging from 20 to 40. Every experiment lasted a week, and all the sensor nodes collected the sensing data every 30 minutes. Figure 11 shows the data delivery rate under three experimental scenarios. As Figure 11 shows, the proposed gateway rather stably gather the sensing data from the sensor nodes in the cases of 20, 30, and 40 nodes, but the data delivery rate decreases to about 62% when 30 nodes were deployed. It is possibly because the packet collision often occurs when a large number of sensor nodes are deployed in an indoor environment even if a simple mechanism is adopted to prevent packet collision.

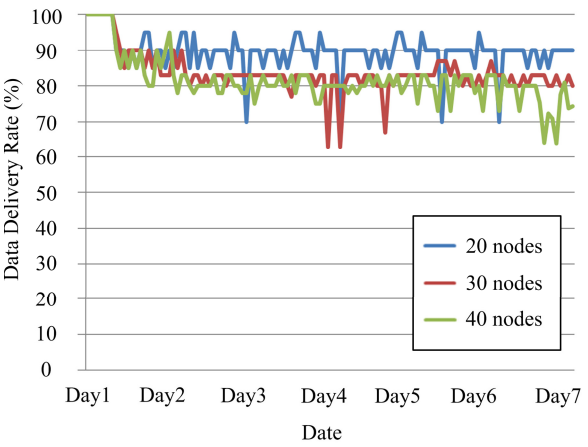

Fig. 11. Data delivery rate when different numbers of nodes (20, 30, and 40) are considered

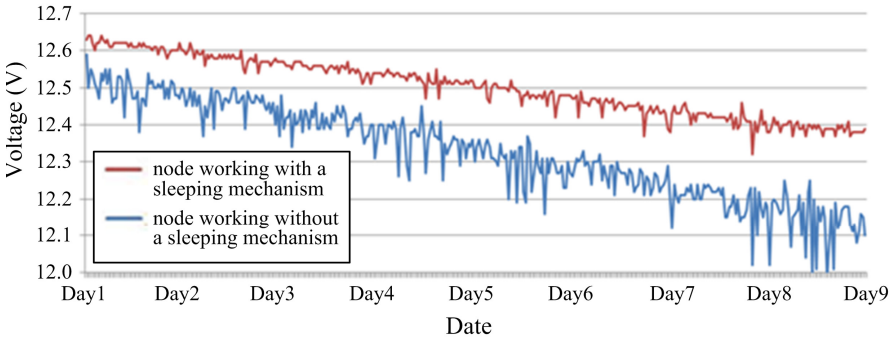

Fig. 12. Voltage readings from two sensor nodes (operating with/without a sleeping mechanism)

Another experiment was conducted to evaluate the effect of auto-management on energy saving. In this experiment, the battery voltages of two sensor nodes (working with/without a sleeping mechanism control by the gateway) were measured. During the experiment, the gateway sent a sleeping command to one of the two sensor nodes and awakened it when necessary. The experimental results are shown in Figure 12. It is obvious that the voltages dropped faster when no sleeping mechanism was used. These results suggest that the proposed gateway can prolong the lifetime of the WSN through the auto-management program of the gateway.

4.2 Outdoor Experiments

For improving the data delivery rate of the sensor network, we designed a rerouting mechanism to reach this goal. The proposed gateway checked the data delivery rate of the sensor network every round after the data was collected. A threshold of the data delivery rate was set by the administrator. If the rate was lower than the threshold, the rerouting mechanism would be activated, and the whole sensor network will be redeployed again. To verify the availability of the rerouting mechanism that we designed, we deployed a WSN in a wood in the hallway of a building. Ten sensor nodes were deployed, and the distance between each sensor node and the gateway was about 5m. Three thresholds that represented three different scenarios (i.e., the data deliver rate of 30%, 50%, and 70% under the first, second, and third scenario, respectively) were set, and the experiment under each scenario lasted five days to examine the rerouting mechanism. If the data delivery rate was lower than the threshold, the rerouting mechanism would be activated. Figures 13, 14, and 15 show the results of the experiments. As Figure 13 shows, the data delivery rate decreased to 20% on the 4th day. The proposed gateway detected the data delivery rate was lower than the threshold of 30%, so the rerouting mechanism was activated to redeploy the sensor network. The Figures 14 and 15 show the data delivery rate charts in which the thresholds were set at 50% and 70%.

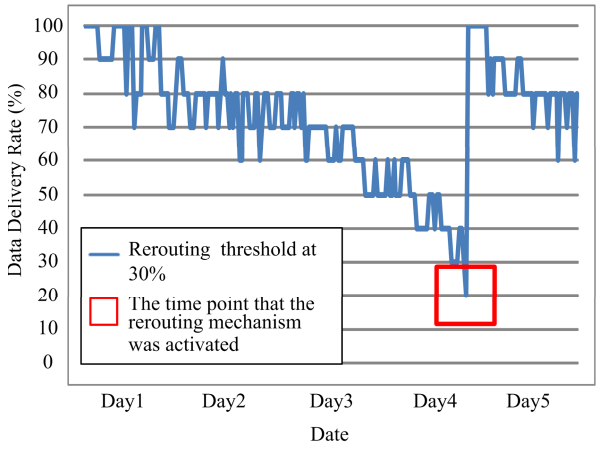

Fig. 13. Results of the rerouting mechanism experiment in which the threshold of the data delivery rate was set at 30%

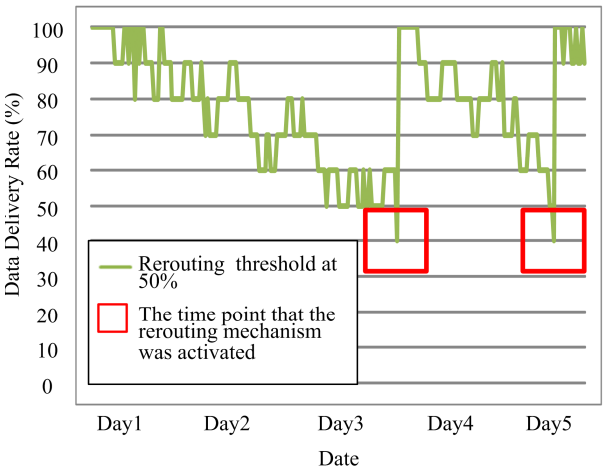

Fig. 14. Results of the rerouting mechanism experiment in which the threshold of the data delivery rate was set at 50%

Given that the gateway would automatically redeploy the whole sensor network if the data delivery rate was lower than the threshold, the data delivery rate of the sensor network remained at a high level. The average data delivery rate under the three scenarios was 73.25%, 77.625% and 86.08%. These experimental results show that the rerouting mechanism is useful in the WSN system. In addition, the proposed mechanism can also be used in the MSP based gateway, but the embedded system based gateway can handle more sensor nodes than MSP based gateway, since the memory capacity of the embedded based gateway is much larger than that of the

MSP based gateway. In this research, the proposed gateway employs rerouting mechanism that simply uses data delivery rates to determine whether the network redeployment is required. In some cases, however, the low data delivery rates were caused by temporary communication failure, and the delivery rate may back to the original level later. From a perspective of energy consumption, more energy would be consumed, if the network had to be redeployed each time when the data delivery rate was lower than the pre-set threshold. In our future work, thus, add an algorithm will be developed to find a proper way to determine when the network requires redeployment.

In order to verify the feasibility of the proposed gateway in the wild area, a WSN were deployed in a tea garden located on a hill in Pingling District were deployed, New Taipei City, which is the northern Taiwan. Figure 16 shows the layout of the WSN. In this figure, the red dots represent the locations of the sensor nodes, while the router icon represents the gateway's location. The longest distance between a sensor node and the gateway was about 150 m. The embedded board was placed in a Stevenson screen. A lead-acid battery served as the power supply for the gateway, and the battery was recharged by two solar cells. The practical deployment of the proposed gateway is shown in Figure 17.

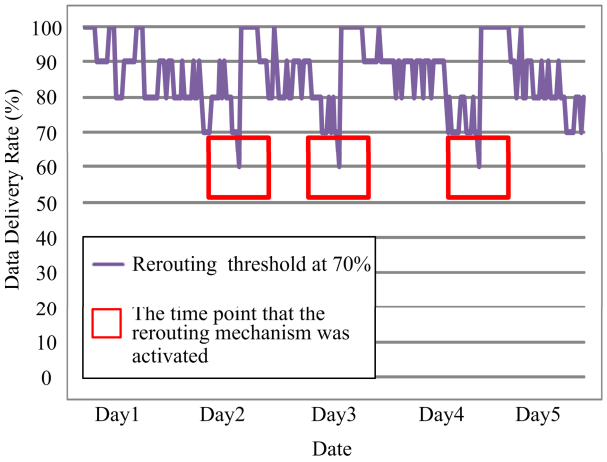

Fig. 15. Results of the rerouting mechanism experiment in which the threshold of the data delivery rate was set at 70%

Using a 1 kW solar cell, the solar power generated in the northern, central and southern Taiwan was 1.9 kWh, 2.3 kWh and 2.7 kWh per day, respectively [30]. Therefore, a self-powered system composed of two 20 W solar cells could generate 76 Wh per day (1.9 kWh × 0.02 kW × 2 = 76 Wh) in the northern Taiwan. With a full 12 V-100 Ah lead-acid battery, the proposed gateway could be expected to normally work up to 8.4 days (12 V × 100 Ah ÷ 142.8 Wh/day) without additional electricity supplied by the solar cells. Note that the field

gateway connecting with a GSM modem, a base node, and a digital weather station would consume 142.8 Wh (5.95 Wh × 24 h). Hence, after integrating with a self-powered system, the proposed gateway would be suitable for operating in a wild environment for a longer period of time.

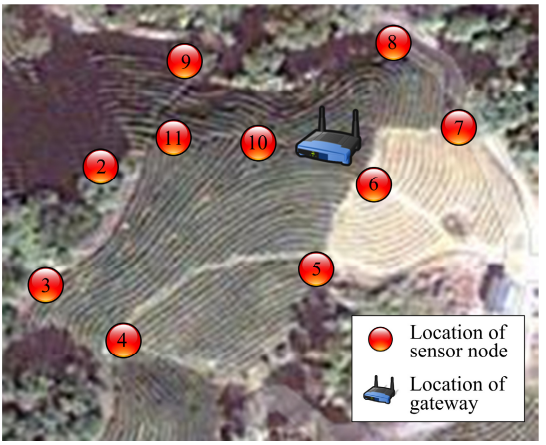

Fig. 16. Layout of the sensor nodes in the experimental field (the tea garden at Pingling District, New Taipei City, Taiwan)

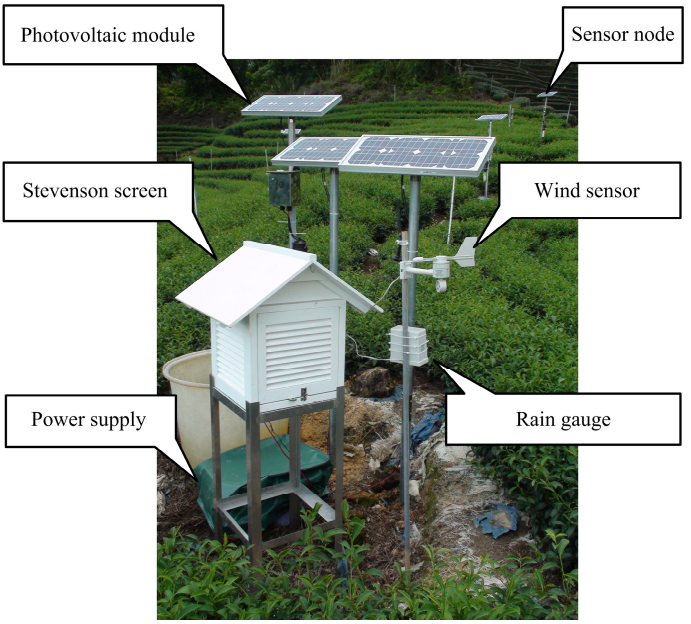

Fig. 17. Practical deployment of the proposed gateway

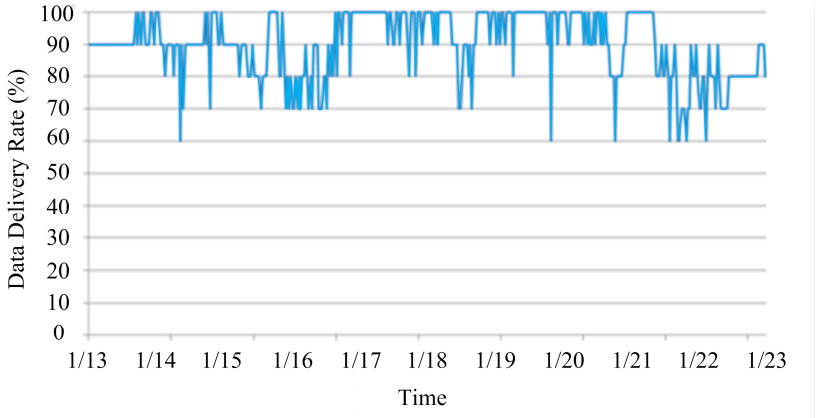

Fig. 18. Data delivery rate of the proposed field gateway deployed in Pingling from January 13 to 23, 2012

The field experiment was conducted from January 13 to 23, 2012. The averaged data delivery rate of the gateway was calculated every half hour as shown in Figure 18. The averaged data delivery rate was about 85.41%. At some specific moments, the data delivery rate dropped to 60%. This was because of the harsh weather in the monitored area. Especially from November to March, the high humidity strongly influenced the quality of wireless communication. In addition, the rugged hill terrain where the WSN was deployed also worsened the quality of wireless communication.

5 Conclusion and Future Work

This research focuses on the software and hardware development for an embedded system-based gateway. The proposed gateway is powered by a lead-acid battery, which is recharged by a photovoltaic module, so the gateway is suitable for long-term environmental monitoring. Both of the indoor experimental results or real field testing results show that the proposed gateway not only could effectively collect and transmit data and sent it to the back-end server but also could save energy by employing a sleep mechanism to extend sensor network lifetime. In addition, the proposed gateway has a rerouting mechanism that allows the gateway to prevent sensing data loss intelligently. In the future, the proposed gateway will be allowed to perform other tasks, such as data recording and data retransmission. A more powerful and intelligent rerouting mechanism will also be developed to increase the date delivery rate. An algorithm will be designed to make a better determination when the rerouting mechanism should be activated for the purpose of energy saving. The gateway will be applied to large-scale monitoring with some improvements. In addition, the self-powered gateway will be examined under different weather conditions in order to improve its durability.

References

1. Oliveira, L., Rodrigues, J.: Wireless sensor networks: a survey on environmental monitoring. Journal of Communications 6(2), 143–151 (2011)
2. Barrenetxea, G., Ingelrest, F., Schaefer, G., Vetterli, M., Couach, O., Parlange, M.: SensorScope: out-of-the-box environmental monitoring. In: Proceedings of 7th International Conference in Information Processing in Sensor Networks, pp. 332–343 (2008)
3. Yang, J., Zhang, C., Li, X., Huang, Y., Fu, S., Acevedo, M.F.: Integration of wireless sensor networks in environmental monitoring cyber infrastructure. Wireless Networks 16(4), 1091–1108 (2009)
4. Okuyama, T., Yang, E.-C., Chen, C.-P., Lin, T.-S., Chuang, C.-L., Jiang, J.-A.: Using automated monitoring systems to uncover pest population dynamics in agricultural fields. Agricultural Systems 104(9), 666–670 (2011)
5. Bhadauria, D., Isler, V., Studenski, A., Tokekar, P.: A robotic sensor network for monitoring carp in Minnesota lakes. In: Proceedings of the 2010 IEEE International Conference on Robotics and Automation (ICRA), pp. 3837–3842 (2010)
6. Collins, S.L., Bettencourt, L.M.A., Hagberg, A., Brown, R.F., Moore, D.I., Bonito, G., Delin, K.A., Jackson, S.P., Johnson, D.W., Burleigh, S.C., Woodrow, R.R., McAllen, J.M.: New opportunities in ecological sensing using wireless sensor networks. Frontiers in Ecology and the Environment 4(8), 402–407 (2006)
7. Naumowicz, T., Freeman, R., Kirk, H., Dean, B., Calsyn, M., Liers, A., Braendle, A., Guilford, T., Schiller, J.: Wireless sensor network for habitat monitoring on Skomer Island. In: Proceedings of the 5th IEEE International Workshop on Practical Issues in Sensor Network Applications, pp. 882–889 (2010)
8. Caron, D.A., Stauffer, B., Moorthi, S., Singh, A., Battalion, M., Graham, E.A., Hansen, M., Kaiser, W.J., Das, J., Pereira, A.: Macro-to fine-scale spatial and temporal distributions and dynamics of phytoplankton and their environmental driving forces in a small montane lake in southern California, USA. Limnology and Oceanography, 2333–2349 (2008)
9. Seders, L.A., Shea, C.A., Lemmon, M.D., Maurice, P.A., Talley, J.W.: LakeNet: an integrated sensor network for environmental sensing in lakes. Environmental Engineering Science 24, 183–191 (2007)
10. Sukhatme, G.S., Dhariwal, A., Zhang, B., Oberg, C., Stauffer, B., Caron, D.A.: Design and development of a wireless robotic networked aquatic microbial observing system. Environmental Engineering Science 24, 205–215 (2007)
11. Handcock, R.N., Swain, D.L., Bishop-Hurley, G.J., Patison, K.P., Wark, T., Valencia, P., Corke, P., O'Neill, C.J.: Monitoring animal behaviour and environmental interactions using wireless sensor networks, GPS collars and satellite remote sensing. Sensors 9(5), 3586–3603 (2009)
12. Song, P., Chen, C., Li, K., Sui, L.: The design and realization of embedded gateway based on WSN. In: Proceedings of 2008 International Conference on Computing Science and Software Engineering, vol. 4, pp. 32–36 (2008)
13. Alippi, C., Camplani, R., Galperti, C., Roveri, M.: A robust, adaptive, solar-powered WSN framework for aquatic environmental monitoring. IEEE Sensors Journal 11, 45–55 (2011)

14. Zarrabi, H., Al-Khalili, A.J., Savaria, Y.: Activity management in battery-powered embedded systems: a case study of ZigBee® WSN. In: Proceedings of 18th IEEE Internatioal Conference on Electronics, Circuits, and Systems, pp. 727–731 (2011)
15. Zabin, F., Misra, S., Woungang, I., Rashvand, H.F., Ma, N.-W., Ali, M.A.: REEP: data-centric, energy-efficient and reliable routing protocol for wreless sensor networks. IET Communications 2(8), 995–1008 (2008)
16. Ren, F., Zhang, J., He, T., Lin, C., Das, S.K.: EBRP: energy-balanced routing protocol for data gathering in wireless sensor networks. IEEE Transactions on Parallel and Distributed Systems 22(12), 2108–2125 (2011)
17. Li, X., Cheng, X., Yen, K., Gong, P.: A monitoring system for vegetable greenhouses based on a wireless sensor network. Sensors, 8963–8980 (2010)
18. Yoo, S., Kim, J., Kim, T., Ahn, S., Sung, J., Kim, D.: A^2S: Automated agriculture system based on WSN. In: IEEE International Symposium on Consumer Electronics, pp. 1–5 (2007)
19. Jelicic, V., Razov, T., Oletic, D., Kuri, M., Bilas, V.: MasliNET: A wireless sensor network based environmental monitoring system. In: Proceedings of the 34th International Convention on Information and Communication Technology, Electronics and Microelectronics, pp. 150–155 (2011)
20. Mainwaring, A., Polastre, J., Szewxzyk, R., Culler, D., Anderson, J.: Wireless sensor networks for habitat monitoring. In: The ACM International Workshop on Wireless Sensor Networks and Application, pp. 88–97 (2002)
21. Sun, D., Wang, W., Lu, J., Lin, Z.: Design of WSN nodes and network performance analysis in a tea plantation. In: IET International Conference on Wireless Sensor Network, IET-WSN, pp. 144–147 (2010)
22. Website of Beagleboard technology, `http://beagleboard.org/` (accessed at: May 24, 2012)
23. Website of Beagleboard-xM datasheet, `http://beagleboard.org/static/BBxMSRM_latest.pdf` (accessed at: April 30, 2012)
24. Website of BusyBox specifiation, `http://www.busybox.net/` (accessed at: April 30, 2012)
25. Website of CC2420 datasheet, `http://inst.eecs.berkeley.edu/~cs150/Documents/CC2420.pdf` (accessed at: April 30, 2012)
26. Website of MSP430F1611 datasheet, `http://www.ti.com/product/msp430f1611` (accessed at: April 30, 2012)
27. Website of La Crosse Technology, `http://www.lacrossetechnology.com/2310twc/index.php` (accessed at: April 30, 2012)
28. Website of La Crosse Technology, `http://www.lacrossetechnology.com/2310/manual.pdf` (accessed at: April 30, 2012)
29. Website of Qt Framework, `http://qt.nokia.com/` (accessed at: April 30, 2012)
30. Ou, W.-S., Ho, M.-C., Chen, J.-L., Chen, J.F., Lo, S.-C.: The study on the typical radiation for solar architecture design of Taiwan. Journal of Architecture (64), 103–118 (2006)

Experimental Research Platform for Structural Health Monitoring

Benjamin Babjak[1], Sandor Szilvasi[1], Alex Pedchenko[2], Mark Hofacker[2], Eric J. Barth[2], Peter Volgyesi[1], and Akos Ledeczi[1]

[1] Institute for Software Integrated Systems, 1025 16th Ave S, Nashville, TN 37212
{benjamin.babjak,sandor.szilvasi,peter.volgyesi,akos.ledeczi}@vanderbilt.edu

[2] Vanderbilt University Department of Mechanical Engineering, 2400 Highland Ave, Olin Hall, Nashville, TN, 37212
{alexander.v.pedchenko,mark.e.hofacker,eric.j.barth}@vanderbilt.edu

1 Introduction

Non-destructive structural testing aims to characterize material and detect failures without damaging the structure in any way. Detection historically meant some form of a visual assessment combined with auditory tests carried out by trained personnel. Inspectors well prepared to identify various types of deterioration would conduct periodic evaluations comparing the current state with previous reports. The problem with this was not only that most likely damage locations had to be known a priori and had to be readily accessible but also that the whole approach had a strong subjective aspect to it. This latter issue was somewhat alleviated with the introduction of more advanced inspection methods and instruments, such as X-ray and ultrasonic techniques, but the main problem of inspections being cumbersome, slow, and superficial still remained untouched.

Major improvement came with the first deployments of permanent, on-site sensor networks providing remote monitoring capability, with the important advantages of real-time data analysis and the ability to generate alerts. The main objectives became to perpetually observe some set of state parameters, follow them as they change with time, and look for indications of detrimental processes.

As for the hardware itself, early networks would typically consist of several data acquisition sensors wired to data processing stations and power sources. Actual deployment of such extensively wired systems, proved to be inconvenient, especially because monitored structures were not constructed with easy sensor installation in mind. To reduce the cost of deployment, node communication became wireless where application methods permitted. The evolution of sensors has also led to more and more capable devices, and consequently to a wide variety of structural health monitoring techniques.

S.C. Mukhopadhyay et al. (Eds.): Advancement in Sensing Technology, SSMI 1, pp. 43–68.
springerlink.com

According to [16, 1], besides sensing environmental conditions, such as temperature, humidity, pressure, and wind, the main purpose of any sensor is to provide information on the structural state or more precisely, material deformation, presence of structural damage or fatigue, and material composition. For this, several categories of non-destructive methods can be distinguished [3], some of which are more widely used in the industry than others. As an example, strain, displacement, and acceleration measurements give information on *material deformation*, shifts in resonant frequencies or changes in structural mode shapes are indicators of *structural damage or fatigue*, measuring the presence of chloride ions or corrosion of reinforcing steel will give insight into *material composition*.

Acoustic Emission

Vibration based methods represent a widespread category among measurement techniques. Their advantage compared to X-ray, radar, or lidar is that they don't necessarily require a separate device for active signal generation. Vibrations will naturally occur in structures for several reasons. A bridge, for example, will experience vibrations to some degree when traffic is present. Material failure can also be a cause. However, if active signal generation is preferred, that is also much easier to generate. Historically inspectors would employ chain dragging and impact sounding, while modern approaches induce application-specific acoustic signals into the structure and reflections are interpreted in the search for defects.

Acoustic emission, a subset of vibration based techniques, can be used to monitor melting, solidification, ferromagnetic domain wall motion, surface friction, among others, but predominantly it is applied to locate material failures such as fatigue cracks. In that context the term describes both the technique and the phenomenon itself [22]. The underlying mechanism is the sudden internal stress redistribution at failure spots, which generates ultrasonic signals. Generally speaking AE methods are not limited to ultrasonic signals (greater than 20 kHz), but ambient noise tends to be higher at low frequencies, thus high frequency signals are easier to process in that regard. AE is applicable in diverse conditions; steel, concrete, and composite materials can be tested alike given one takes different material properties, such as signal attenuation, into consideration.

The flexibility and the non-destructive nature of this comparatively simple method made it possible to utilize it in as early as 1964 for testing rocket-motor casings, and ever since then it has found its way into the nuclear industry to locate incipient defects, into the petrochemical industry to test pressurized components, and even into the aerospace industry to perform in-flight monitoring, among others.

A system performing AE measurements would record acoustic signals propagating in the structure and perform some form of analysis. The microphones

have to be uniquely designed to handle ultrasonic signals up to a few MHz wide and typically significantly attenuated by the measured structure. Optical or capacitive devices can be used as well, but the prevalent approach is a piezoelectric solution directly mounted to the surface. Grease or other non-attenuating fluid is added for better contact. These devices usually have a resonant frequency range whose bandwidth varies depending on the purpose of the device. High bandwidth is not always beneficial, because it introduces high levels of noise and requires higher sampling rates on the processing side. The situation is further complicated since AE measurements usually employ several sensors concurrently for localization purposes, and AE events are transient occurring randomly leaving the system no choice but to process (or at least store) all the data continuously in real-time. Further signal processing can also be equally resource intensive, thus special care is required when designing a processing platform.

AE can be used to locate and identify damage spots, but just as any other method, it has its shortcomings. Obviously it can only report damages as they happen, hence, applying an AE sensor network will not give information on pre-existing conditions instantly. Furthermore, foresight is required to pick the right instruments for any given deployment. Even then, if deterioration is slow enough and material stress is not released in the form of sudden energy bursts, AE will fail to warn. The remedy is to use several SHM techniques at the same time, so that the shortcoming of one method may be compensated by another. These factors underline the need for a versatile, high performance sensor platform.

Towards a Research Platform

Research on Wireless Sensor Networks (WSN) goes back as far as the nineties with many noteworthy accomplishments. Both industry and academia proposed an impressive array of wireless sensor prototypes [9, 12, 13, 10, 20, 14, 25, 6]. Solutions for process monitoring and control, data center monitoring, home security, traffic monitoring, automatic meter reading, and soil monitoring, to name a few, have already been successfully deployed. However, the still unsolved, true challenge lies in the development of low-power and high data rate deployments with long lifetimes. The typical wireless sensor node combines an integrated radio transceiver circuit with a microcontroller providing a low-cost flexible platform. However, microcontrollers are not powerful enough for high speed digital signal processing. Their performance has been steadily increasing, but they are still not capable of processing sensor data at high rates and/or on multiple channels.

Both DSP processors and FPGAs offer the capability to process at higher data rates than microcontrollers can. Both solutions have their advantages and disadvantages, while hybrid approaches are also not uncommon.

DSP processors are more easily configured and programmed, but their clock rates tend to be much higher – even as high as several hundred MHz – resulting in an overall higher power consumption. FPGAs can be more efficient in that regard offering better parallel processing capabilities with lower clock rates and moderate active power draw. It is, however, hardware duty cycling that ultimately determines the lifetime of a battery-operated radio node. Unfortunately the inrush currents associated with these SRAM-based devices turning on are too high, resulting in FPGAs consuming too much power as well. Flash based FPGA technology, on the other hand, is a promising recent alternative, which seems to mitigate not only the active power draw but the inrush current problem during duty cycling as well by incorporating flash memory in the fabric configuration.

Flash-based FPGA platforms can outperform microcontroller-based ones in terms of raw parallel computational power and hardware flexibility, but the life-time on a single charge of such a device strongly depends on the actual application. Unfortunately the above described multi-channel, high sampling rate utilization in combination with frequent node communication will inevitably deplete any battery source within a short period of time. Duty cycling will of course improve on the situation to a certain degree, but if a lifespan of more than a couple of weeks is desired, alternative energy sources have to be exploited. Having wired power for the sensors defeats the purpose of the whole WSN concept, thus some form of local energy harvesting is unavoidable. Hence, part of this chapter discusses efficient vibration based energy harvesting in detail.

With the guidelines and pitfalls outlined above, we introduce a novel, versatile *experimental research platform for structural health monitoring* built around a highly integrated system-on-chip solution. The target audience for the sensor is the academic community, hence our goal is to provide a platform facilitating experimentation and offering a unique level of insight and accessibility. This low-power node is modular by design and incorporates everything necessary to work as a stand alone unit. The main component is a SoC including flash FPGA fabric, a microcontroller unit, and even some analog processing. Multi-channel, high speed analog to digital signal conversion is supported, communication is covered by a general purpose radio front-end chip carefully selected to impose as few limitations on the system as possible. The complete node enables tight coordination between hardware and software components. Users have the ability to experiment which parts of their design get implemented as algorithms running on the MCU, and which parts become hardware implementations in the FPGA fabric. This approach enables timing-critical, low latency, and low jitter design on a tightly integrated platform with only a handful of components.

2 Sensor Platform

2.1 Background and Related Work

SRAM FPGA-Based Prototype

Our pilot project – a cooperation between Vanderbilt University, ISIS, and WINS LLC, a company specializing in the inspection of civil structures –, was launched in 2006 with the goal to develop a wireless 4-channel acoustic emission (AE) sensor node that is comparable in performance to the wired AE testing system used at that time. The feasibility of wireless structural health monitoring with the developed AE sensor nodes was successfully demonstrated during an actual bridge inspection with the wireless and wired systems working side by side[11]. This early SRAM FPGA-based prototype was designed to prove the feasibility of bridge inspection, thus, it was primarily optimized for processing power, rather than long-term monitoring. At the heart of the prototype board was a Xilinx Spartan-3 XC3S1000L SRAM FPGA with hardware multipliers and programmable logic resources sufficient to process the AE signals sampled at a 1 MSPS rate on 4 channels simultaneously. Alongside the FPGA, there was an integrated low-power radio chip utilized for low data rate wireless communication. Due to the energy requirements of the FPGA, however, the design was limited to short-term monitoring (few weeks).

Towards Low-Power Operation

Careful power analysis of the first prototype board revealed that longer term (months) deployment could be achieved by utilizing advanced power management techniques, by eliminating the (re)configuration phase and by lowering the static power consumption associated with SRAM FPGAs. This recognition led to a second prototype, "AEPod", where power management has been separated into an independent low-power microcontroller and the SRAM FPGA has been replaced with a flash FPGA [11].

Flash FPGAs, such as the Actel Igloo AGL600, consume significantly less static power, offer clock-scaling and instantaneous power-on options, which, in conjunction with the newly separated power manager, can lead to significant energy saving. Even though the low-power features of the flash FPGA came at the price of certain resources (e.g. hardware multipliers), the programmable resources of the IGLOO flash FPGA still proved to be sufficient for processing 4 parallel signal channels at ∼4MSPS simultaneously.

Although these improvements significantly extended the battery life of the new prototype, it has been concluded that a truly long-term deployment with several years of autonomous operation would not be feasible on a single charge battery. Thus, the use of alternative (renewable) energy sources should be considered.

Modular Low-Power Research Platform

Experiences learned through the second prototype board suggested that flash FPGAs offer sufficient processing horsepower at an affordable performance per energy ratio and come with truly desirable power saving features, but long-term on-site node deployment is limited by the battery capacity. In order to combat energy scarcity, various energy harvesting options were considered, such as solar, wind and vibrational energy of the monitored structure.

Thus, our third prototype ("Marmote") was designed with a similar flash FPGA-based approach and a separated power management module that allows for experimentation with the above power sources. Compared to the previous "AEPod" design where a flash FPGA and a microcontroller were discrete components on the board, the FPGA fabric became part of an integrated system-on-chip infrastructure with a capable microcontroller core and several peripheral modules. The single-board approach of previous designs has been dropped in favor of a more general 3-layer modular platform, where the flash FPGA based processing module was kept as a main board but both the power management and the analog front-end modules have been separated to simplify experimentation with various power sources and analog signal conditioning approaches.

The design of the Marmote platform enables experimentation in a wide range of wireless sensor applications in the sensing, processing and communication domains. To leverage our previous experiences and to demonstrate the capabilities of this platform, we implemented an AE-based wireless SHM first with a vibrational energy harvester presented in Section 3.

2.2 The Marmote Platform

The primary motivation behind the Marmote SHM was to eliminate the need for expensive cycles of site visits and bridge instrumentation each time its health assessment is required. For a new semi-permanent wireless monitoring infrastrucutre to succeed it must meet the following requirements:

1. maintenance free autonomous operation for years (long-term deployment)
2. accurately sensing, pre-processing and reporting critical structural health parameters

The above goals are addressed by designing sensor nodes using low-power components backed up with advanced power management techniques, and energy harvesting and storage capabilities.

The physical size of a "Marmote" node is $90 \times 56 \times 45$ mm not including actual AE sensor-heads and the energy harvester. The three different layers are separated into a power management module, a mixed-signal processing module, and an analog and radio front-end module – according to these distinct tasks.

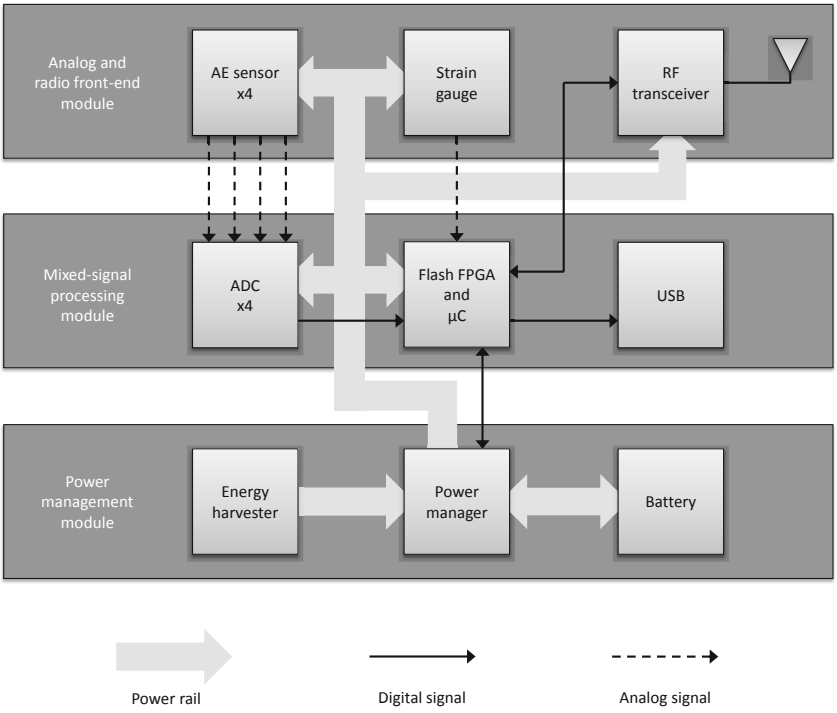

Fig. 1. Block diagram showing the layered architecture of the Marmote platform for structural health monitoring

Power Management Module

The bottom layer of the Marmote platform is the power management module responsible for energy harvesting, storage and distribution among the other components of the platform. The current design treats the prototype energy harvester as an external module and provides a convenient interface to connect it to the Marmote platform. Note, however, that the modular partitioning shown in Figure 1 allows for seamless integration of the harvester into the power management module – without the need to redesign any of the other modules.

The prototype energy harvester extracts power from the vibrational movement of the bridge it is attached to. Mechanical energy is converted into electrical energy by an actively controlled electromechanical generator based on the maximum transfer theorem described in Section 3 in details. A BEI LA15-33-000A type linear actuator acts as the actual energy harvester, while an Analog Devices ADXL330 accelerometer and a U.S. Digital EM1 optical

encoder provide feedback for the control logic on the acceleration and position (and indirectly the velocity) of the harvester, respectively.

The power manager supervises the energy being received from the harvester and charges the attached Li-Ion battery using a CC/CV source. It also distributes power among the other modules based on its availability from the harvester, the battery and on the actual power-mode being active. Furthermore, the power manager monitors power consumption on each power rail and logs it on a removable memory card.

Mixed-Signal Processing Module

The middle layer of the Marmote platform, shown in Figure 1, is a mixed-signal processing module built around a Microsemi (formerly Actel) customizable system on chip (cSoC) and two external analog front-ends that allow to digitize the incoming analog AE sensor inputs and efficiently process them in the digital domain. Analog to digital (A/D) conversion is supported in four channels simultaneously by two Maxim MAX19706 low-power analog front-ends, each containing two separate A/D converters. The fully differential analog inputs are sampled with seven-stage pipeline architecture A/D converters of 10-bit precision and an adjustable sampling rate up to 22 MSPS. The sample values of the two A/D converters of each analog front-end are output with 5 and 5.5 clock cycle delay, respectively, through a 10-bit parallel dual data rate (DDR) interface.

Processing of the samples takes place primarily on a Microsemi SmartFusion A2F500 cSoC, shown in Figure 2, comprising a programmable analog interface, a flash-based FPGA and a Cortex-M3 microcontroller subsystem. The 500 KSPS successive approximation (SAR) A/D converters of the integrated analog interface are primarily used to connect strain gauge sensors, which allows the Marmote platform to save energy by spending most of the time in a deep sleep mode and waking the system up only when the structure is under stress (e.g. traffic is present on the bridge). Supporting low-power operation was as important design goal as finding an adequate architecture for simultaneous processing of the high-data-rate signals. These goals were primarily met by exploiting the flash FPGA fabric of the cSoC device.

The SmartFusion A2F500 FPGA fabric comprises 24 4,608-bit block RAMs and 11,520 logic elements (VersaTiles), which roughly equals to 500,000 system gates, the latter built with firm-error immune, 130 nm, flash-based CMOS process. This amount of logic resources is sufficient to interface with the DDR buses of the MAX19706 analog front-ends and to implement low-level, high-speed, parallel, processing datapath for the digitized AE signals. Advanced power saving techniques also benefit from the SmartFusion FPGA fabric as it retains its configuration when powered off and offers true live-at-power-up (LAPU) functionality. Unlike SRAM FPGAs, where the configuration for programmable interconnects and look-up-tables (LUT)

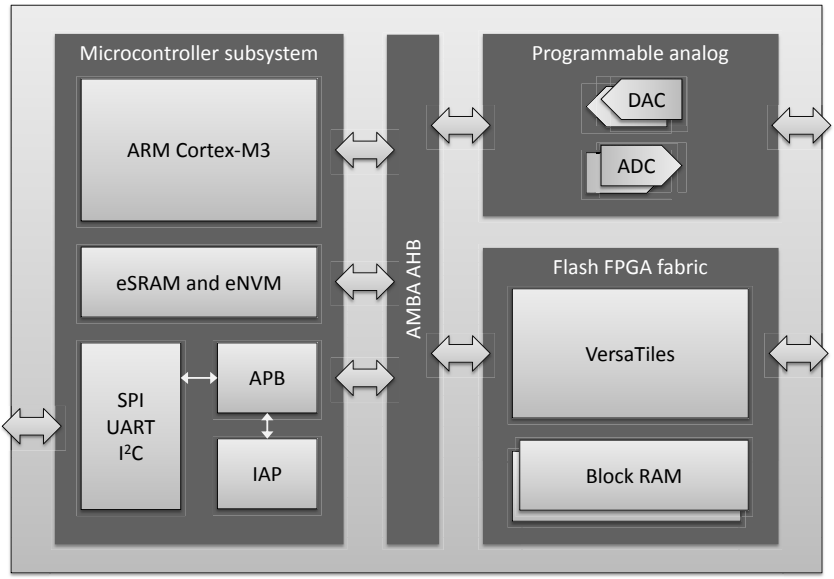

Fig. 2. Block diagram of the SmartFusion customizable system-on-chip comprising a Cortex-M3 based microcontroller subsystem, a programmable analog interface and a flash FPGA fabric

are stored in SRAM cells that need to be configured on every power-up, flash FPGAs store their configuration in non-volatile flash cells directly, which has several advantages. First, there is no need for an external flash memory to store the configuration file, effectively reducing board complexity and saving board space. Second, there is no need to reconfigure the FPGA when applying supply voltage to the fabric, therefore, enabling efficient duty cycling operation as the energy waste associated with power-on inrush current and configuration bitstream load are virtually eliminated, as depicted in Figure 3. This saves not only energy, but also wake-up time rendering the device immediately live at power up and, thus, more responsive in duty cycling mode. Figure 3 compares the power consumption of SRAM and non-volatile flash FPGA devices with duty cycle operation and illustrates the energy and time saved by the flash fabric due to the absence of the (re)configuration phase. Flash FPGAs are also claimed to have lower static current consumption than sram FPGAs, making them a preferable choice for low-power WSN applications (not shown in Figure 3).

The SmartFusion chip also contains a *hard IP* microcontroller subsystem (MSS) comprising an ARM Cortex-M3 based 32-bit microprocessor, 64 kB embedded SRAM memory , 512 kB embedded nonvolatile memory (NVM),

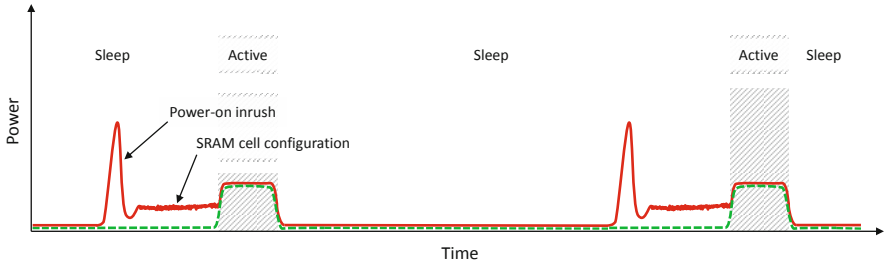

Fig. 3. Power consumption comparison of sram (red solid) and flash (green dashed) FPGAs during duty cycle operation with the sram FPGA power-on effects exaggerated for better visibility

a set of communication peripherals and an ARM Advanced Microcontroller Bus Architecture (AMBA) Advanced High-performance Bus (AHB) as shown in Figure 2. The MSS, therefore, offers a complete low-power embedded solution to interface with external peripherals via SPI, I2C and UART, and to the FPGA fabric via the AMBA AHB. Furthermore, the MSS provides means for secure in-application programming (IAP) of the NVM and the FPGA fabric through the dedicated IAP and AES decryption logic. The Cortex-M3 manages communication through these interfaces and runs background signal processing tasks that would be uneconomic to implement in Versatiles of the FPGA fabric.

For signal processing the current Marmote platform offers two options: one for rapid processing algorithm development and one for the actual long-term deployment. Algorithm prototyping is supported by the mixed-signal processing module via a streaming data path that enables transfer of the raw digitized samples of the four channels to a PC through the analog front-ends, the SmartFusion FPGA fabric and a high-speed USB connection. The streamed samples can either be recorded and then processed off-line, or processed directly on-line. Both ways make it possible to develop the signal processing algorithm initially on the PC, then to port it to the embedded FPGA and microcontroller.

Embedded signal processing takes place entirely on the mixed-signal module. The data path comprises the A/D converters and both the FPGA and microcontroller parts of the SoC. The analog AE signals are digitized by the four A/D converters simultaneously. Parallel processing (e.g. simultaneous FIR filtering) is applied to the samples in the FPGA part, while further processing, compression and feature extraction take place in the microcontroller. These extracted parameters are logged by the microcontroller and transferred thourgh the radio front-end, found on the top layer, for transmission to the off-site diagnostic facility.

Analog and Radio Front-End Module

The top layer of the Marmote platform consists of a set of analog circuitry for various sensing applications, and a low-power RF transceiver for communication with the on-site data storage and forwarding unit.

The four high speed analog channels on this module interface with the four AE sensor heads attached to the bridge structure. The signals received through this single-ended analog interface are amplified with a variable gain and bandwidth and are filtered with band-pass filters. For better noise rejection the single-ended analog signals are also converted into differential pairs before they reach the mixed-signal processing module.

Independent from the four wide band sensor interfaces – handling for example the above mentioned AE signals – optional low band interfaces are available as well to connect for example strain gauges to the analog and radio front-end module. The analog output of the strain gauge is driven through a passive low-pass filter then to the SmartFusion analog front-end A/D converter on the mixed-signal module.

The top layer module also incorporates an integrated low-power RF transceiver. This radio chip is directly accessible from the MCU of the mixed-signal processing module and is used to communicate with the on-site unit in the 2.4 GHz band.

2.3 Sensing and Measurement Philosophy

The above described hardware platform combined with the software defined functionality concept gives sensors the unique ability to adapt. To give an impression as to how a system based on our experimental research platform could work, let's take an example in the field of acoustic emissions as discussed in the introduction.

Example Measurements

The pencil lead break test is a widely used method to test AE measurement equipment before actual field deployment. For our own tests we have used a VS375-RIC high sensitivity AE sensor with integrated preamplifier. The structure under test was a simple metal file cabinet, signals were sampled at 4 MSPS.

Our test results seen in Fig. 4. indicate that signal spectra are rather similar for a given measurement setup, but looking at other reported measurements [19, 8, 21, 4, 18] it is obvious that AE signals can be vastly different depending on the examined material, structure, and microphone.

Depending on where the actual measurement evaluation takes places, one can differentiate between a few approaches. The more of the signal processing is done on the sensor itself the lighter the burden on the communication side.

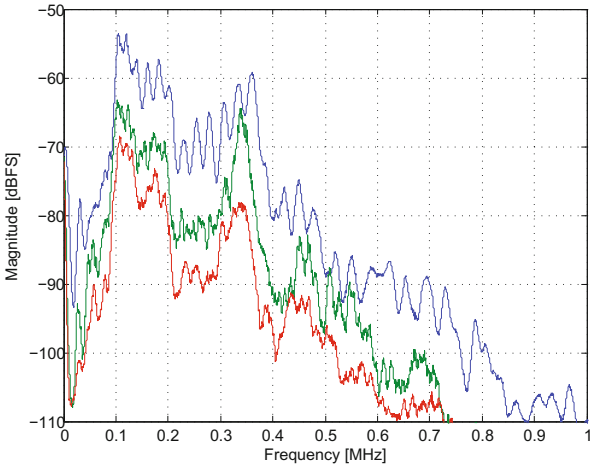

Fig. 4. Pencil lead break test spectrum results measured with one sensor subsequently at three different places on a metal file cabinet sampled at 4 MSPS

Evaluation on the sensor. On the one side there are methods where basically all of the evaluation is executed by the sensor, and only the final results are transmitted. An example for that can be some sort of a time difference of arrival (TDOA) approach, where a single sensor would analyze signals from separate channels. Knowing the monitored structure, the exact location of the sensors, and the time differences one could relatively easily locate crack positions. In this case we can look for rising edges to estimate signal arrival times, or we can also use cross-correlation with reduced sample rates or perhaps random sampling to figure out arrival time differences.

Feature extraction on the sensor. The sensor's job here is to process the signal just enough to find the relevant information and transmit that to the diagnostic centers where the rest of the analysis takes place. As an example one could also make assumptions on the structure's state by examining signal nonlinearity, meaning that in this case high frequency components and harmonics would be of primary concern.

Lossless data transmission. As an extreme the sensor may only transmit recorded data without performing any processing at all. An example for this could be a more sophisticated method where one would model the monitored structure and the effects of failures with Lamb waves. In this case not only arrival times but entire recorded signals are of interest.

If the complete detected signal has to be transmitted, and minimal information loss is allowed, DSP techniques like undersampling, mixing, and decimation can be applied in order to stay low-power. These methods can easily decrease the effective sampling frequency (and thus the communication) without loosing information given the signal is narrow band limited.

In conclusion AE signals can be differently analyzed based on the evaluation method, and simple, microcontroller based hardware platforms are very likely unable to process these ultrasonic signals measured simultaneously on several channels. However a more flexible sensor, like our experimental hardware platform, where one can decide on the evaluation method later on and make changes at the implementation phase, seams a feasible way doing this while still achieving high power efficiency and increasing life cycle.

3 Vibration Energy Harvester

3.1 Introduction

Whatever method is chosen to monitor the health of a bridge, sensing and transmitting the bridge's condition requires electrical power. Wiring the bridge health monitoring device(s) to power and data networks would be difficult and expensive [13], so ideally data would be transmitted wirelessly and power would be generated locally. Power generation is preferable to using batteries, as the latter would require regular replacement. Solar and wind power should be avoided, as both are not guaranteed to generate power when it is most needed, i.e., during heavy traffic conditions; additionally, mounting options would be limited depending on bridge configuration.

In the following several sections, an electromechanical generator that harvests power from bridge vibrations will be investigated. This device will circumvent the costs associated with having to wire the sensors to an external power source. The investigated device will have the additional goal of requiring minimum maintenance during long periods of operation. The three most commonly used techniques for electromechanical generation are electrostatic, piezoelectric, and electromagnetic [2, 5, 15]. Out of these three options, an electromagnetic generator was chosen for this application due to its robustness and controllability properties (for an in depth explanation of the advantages of electromagnetic generation in bridge vibration energy harvesting please refer to [17]).

Electromagnetic generators operate in a similar manner to a mass-spring-damper system, where power is extracted from the damping element. The drawback of these devices is that they are only able to collect an appreciable amount of power when the bridge oscillates at or close to the generator's natural frequency [2]. This poses a significant problem because different bridges oscillate at different frequencies [7], a particular bridge will oscillate differently depending on traffic [24], and the oscillation of any given point on a bridge usually contains multiple frequencies [23].

The following sections describe a method of overcoming these challenges by actively controlling the motion of the harvester to maximize the amount of

net power (i.e., power harvested reduced by power supplied to the harvester to alter its motion) generated. A controller is derived utilizing the maximum power transfer theorem. This control methodology is validated using a low-friction prototype electromechanical harvester and the results are presented.

3.2 Derivation of Control Law

The motivation behind the controller is to extract the maximum amount of power for any given frequency of bridge oscillation. This concept has been fully explored in the electrical domain with the maximum power transfer theorem, which dictates the necessary load to transfer the most power from a specific source to the said load. To apply this theorem to the vibrational energy harvester, the mechanical system is converted to its dynamic equivalent in the electrical domain as shown in Figure 5. The bond graph shown in Figure 5-ii is an intermediate step used to preserve the system's dynamics during this conversion. The electrical equivalent circuit (Figure 5-iii) is then converted to its Thevenin form (Figure 5-iv) so that the maximum power transfer theorem can be easily applied.

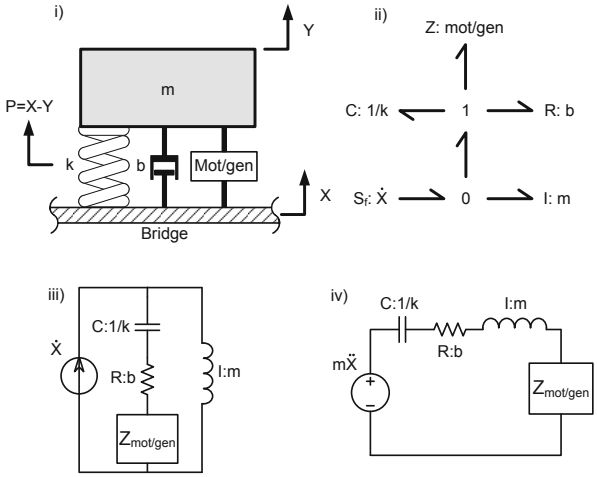

Fig. 5. Transformation of bridge energy harvester into electrical domain: i) mechanical representation; ii) bond graph representation; iii) electrical equivalent of bond graph; iv) Thevenin equivalent circuit

In the mechanical domain, the vibrational bridge energy harvester can be represented by a conventional mass-spring-damper with an additional element in parallel with the spring and the damper components (see Figure 5-i). In passive electromagnetic harvesters, this component is a generator that harvests power by siphoning kinetic energy from the mass, m. In an actively controlled harvester, this component functions as both a generator

and a motor. In casting the system from Figure 5-i into bond graph form, as shown in Figure 5-ii, the motor/generator is represented by a component of impedance, $Z_{\text{mot/gen}}$. In the circuits shown in Figure 5-iii and Figure 5-iv, according to standard bond graph convention, the current flowing through a component is equivalent to the velocity of the component and the voltage across a component is equivalent to the force exerted by said component. Although all of the representations of the system have identical dynamic behaviors, the Thevenin equivalent circuit allows direct application of the maximum power transfer theorem. Additionally, it allows to clearly see the relationship between current and voltage of the harvester as described by the transfer function shown in (1),

$$\frac{P(s)s}{ms^2X(s)} = \frac{1}{\frac{k}{s} + b + ms + Z_{\text{mot/gen}}} \tag{1}$$

where $ms^2X(s)$ is the voltage source, $P(s)s$ is the current running through the circuit components, $\frac{k}{s}$, b, and ms are the impedances of the capacitor, resistor and inductor respectively.

In applying the maximum power transfer theorem to the electrical system depicted in Figure 5-iv, we note that parameters k, m, and b cannot be changed as they represent the physical characteristics of the energy harvester. Since in the Thevenin equivalent circuit, the component $Z_{\text{mot/gen}}$ is analogous to the load, the sum of the impedances of the mass, the spring, and the damper can be defined as the source impedance. The frequency-dependent behavior of this complex impedance, Z_{SRC}, can be described by:

$$Z_{\text{SRC}} = \frac{k}{s} + b + ms\Big|_{s=j\omega} = b + j(m\omega - \frac{k}{\omega}) \tag{2}$$

Knowledge of the source impedance, Z_{SRC}, in (2) and the dynamic response of the system (1) allows the designer to formulate a controller capable of satisfying the maximum power transfer theorem. The theorem states that maximum power transfer to the load occurs when the load impedance is the complex conjugate of the source impedance as shown in (3).

$$Z_{\text{LOAD}} = Z_{\text{mot/gen}} = Z^*_{\text{SRC}} \tag{3}$$

When this condition is satisfied, the sum of the load and source impedance contains double the resistance/damping of the source and no complex component. Successful load matching defined by (3) reduces (1) to

$$\frac{P(s)s}{ms^2X(s)} = \frac{1}{Z_{\text{SRC}} + Z_{\text{mot/gen}}} = \frac{1}{2b} \tag{4}$$

The electrical and mechanical equivalents of the above transfer function are shown in Figure 6.

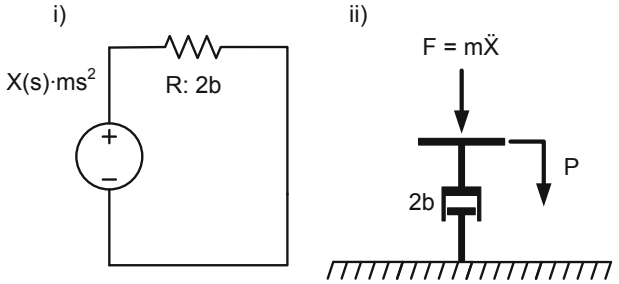

Fig. 6. Electrical circuit (i) and mechanical system (ii) representations of ideal energy harvester behavior

This ideal behavior is logical because both systems depicted above are composed of only a resistive element, which is sole component capable of drawing (harvesting) power from the system. Physically, inertial components (masses) and capacitive elements (springs) are necessary only because they generate the kinetic energy from which power is extracted. This behavior can also be shown to be ideal by noting that it is equivalent to a mass-spring-damper system excited at a frequency which is equal to the system's natural frequency. Explicitly,

$$\frac{P(s)s}{ms^2X(s)} = \frac{1}{\frac{k}{j\omega} + 2b + mj\omega}\bigg|_{\omega=\omega_n=\sqrt{\frac{k}{m}}} = \frac{1}{2b} \tag{5}$$

This can also be seen in (2), when the forcing frequency (ω) is equal to the system's natural frequency (ω_n), only the real component remains.

To achieve the modeled behavior shown in (4), a control signal must be applied to the motor/generator. The equation of motion derived from Figure 5-i with the motor/generator applying a force $u(t)$ on the proof mass m in the direction pointed towards the bridge is:

$$m\ddot{y} = b(\dot{x} - \dot{y}) + k(x - y) - u(t) \tag{6}$$

Reorganizing the equation, letting $p = x - y$, and performing a Laplace transformation, yields:

$$P(s)(ms^2 + bs + k) = mX(s)s^2 + U(s) \tag{7}$$

In order to obtain the desired transfer function shown in (4), $U(s)$ must be set equal to the following:

$$U(s) = P(s)(ms^2 - bs + k) \tag{8}$$

which is the controller which satisfies the maximum power transfer theorem as it applies to the vibration energy harvester.

3.3 Simulation Results

Let us compare the frequency behavior of (9) to that of the transfer function of the same system operating passively. The system shown in Figure 6 behaves according to the transfer function shown below

$$\frac{P(s)s}{ms^2X(s)} = \frac{P(s)}{F(s)} = \frac{1}{2bs} \tag{9}$$

where $F(s)$ is used to replace $ms^2X(s)$, which is the force imposed on the mass by the vibration of the bridge. If the system shown in Figure 5 -i was operating as a passive vibration energy harvester, $Z_{\mathrm{mot/gen}}$ would be tuned such that it doubles the parasitic damping (i.e., acts like another damper b [7]). This type of system would have the transfer function:

$$\frac{P(s)}{F(s)} = \frac{1}{ms^2 + bs + k + Z_{\mathrm{mot/gen}}}\bigg|_{Z_{\mathrm{mot/gen}}=bs} = \frac{1}{ms^2 + 2bs + k} \tag{10}$$

where inputs and outputs are the same as those for (9). Figure 7 shows the behaviors defined by (10) for several passive energy harvesters with different natural frequencies ($f_n = 4\,\mathrm{Hz}, 6\,\mathrm{Hz}, 8\,\mathrm{Hz}, 10\,\mathrm{Hz}$) as well as the behavior of the controlled system defined by (9).

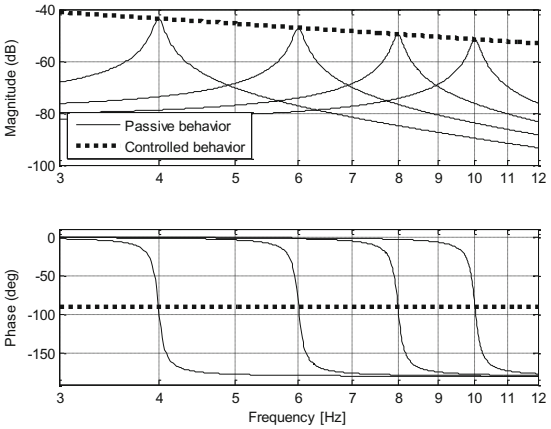

Fig. 7. Magnitude and phase behavior of several passive, tuned, energy harvesters and that of the controlled impedance matched energy harvester to a force input

The power generated by a vibrational energy harvester was described by [2] as follows:

$$P_d = \left. \frac{m\delta Y^2 \left(\frac{\omega}{\omega_n}\right)^3 \omega^3}{\left(1 - \left(\frac{\omega}{\omega_n}\right)^2\right)^2 + \left(2\delta\frac{\omega}{\omega_n}\right)^2} \right|_{\delta=\frac{b}{2\sqrt{km}}} \tag{11}$$

where m represents the magnitude of the proof mass, δ is the harvesters damping ratio, ω is the bridge vibration frequency, and ω_n is the natural frequency of the harvester. Figure 8 shows the net power that the harvester demonstrated in Figure 5-i would generate, given that the bridge vibrates sinusoidally at an amplitude of 0.25 mm and each harvester has a mass of 0.55 kg and a damping ratio of 0.013.

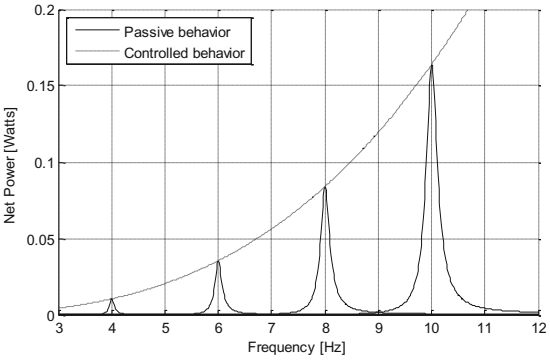

Fig. 8. The power generated by passive and controlled harvesters vs. frequency

As seen in Fig 8, the controlled device is capable of extracting as much power as a properly tuned passive device when the bridge operates at the passive device's natural frequency, yet the controlled device has much higher bandwidth than any single passive system. Another advantage of having no single natural frequency is that the controller is able to respond intelligently to bridge oscillations that contain more than one frequency component. Bridge vibration data from Shahabadi [23] containing 6 Hz, 7 Hz, and 12 Hz components was reproduced in simulation and used to excite a passive harvester, and an identical harvester with active control. Again, the simulation harvesters had a mass of 0.55 kg and a damping ratio of 0.013. The spring stiffness was chosen to be $975\,\mathrm{N\,m^{-1}}$ for a natural frequency of 6.7 Hz. The bridge's position and corresponding simulated responses of the two harvesters are shown in Fig 9.

From the figure it can be seen that amplitude of oscillation of the controlled harvester is far greater than that of the uncontrolled. For increased clarity, the amplitude of the bridge is shown as opposed to the force exerted on the harvester as used in Figure 7. From the figure, we see that the bridge has 90°

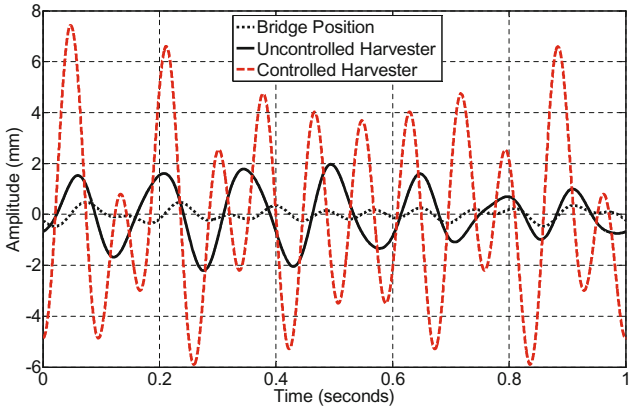

Fig. 9. Passive and controlled responses of the energy harvester to a force input

phase lag on the harvester. Since we know that input force has 180° phase lead on the bridge position, we can infer that the harvester position has 90° phase lag on the input force, as previously demonstrated in Figure 7. This is to say that the controlled harvester behavior shown in Figure 9 exhibits the harvester's ability to maintain 90° phase lag on the incoming force, even when excited by several different frequencies.

The ability to increase amplitude and maintain phase lag increases the power output of the device. Calculations from the simulation show that if the motor and generator were both 100% efficient, the controlled device would generate a net 13.3 mW (this value takes into account the amount of power required to alter the motion of the proof mass as required by the control law), while the uncontrolled device would harvest 4.37 mW when both are exposed to the bridge vibrations shown in Figure 9. Even with a more realistic estimate of 70% efficiency of regeneration and actuation, the controlled device would still yield 9 mW net power. It is important to note that these simulation results were obtained using a device having the parameters of the small scale setup discussed in the next section. Thus, the net power output serves only as a performance metric to gauge the benefits of controlled behavior against traditional, passive energy harvesting.

3.4 Experimental Setup and Results

A small scale harvester was constructed so that the derived controller based on the maximum power transfer theorem could be tested on a physical device. In this prototype, a linear motor was used as both the proof mass and the motor/generator. Compliant mechanisms were arranged into self-aligning spring elements to eliminate the need of bearing surfaces. During the design process, it was vital to decrease parasitic losses because the total amount

of power available from bridge vibrations is in the sub-watt range. To create this self-aligning spring structure, 16 guided-beam compliant mechanisms were arranged in such a way as to be extremely stiff in translational and rotational modes yet have an appropriate amount of compliance along the axis of the linear motor. As previously mentioned in the simulated results section, the compliant structure was made to have a stiffness of $975\,\mathrm{N\,m^{-1}}$. Also, in keeping with the simulated data, an effective mass of 0.55 kg was used to yield a natural frequency of 6.7 Hz. Using frequency response data of the prototype, its damping ratio was calculated to be 0.013.

A second, larger linear motor was used to simulate actual bridge motion.Acceleration and position of the proof mass and simulated bridge were collected using accelerometers, a potentiometer, and an encoder.

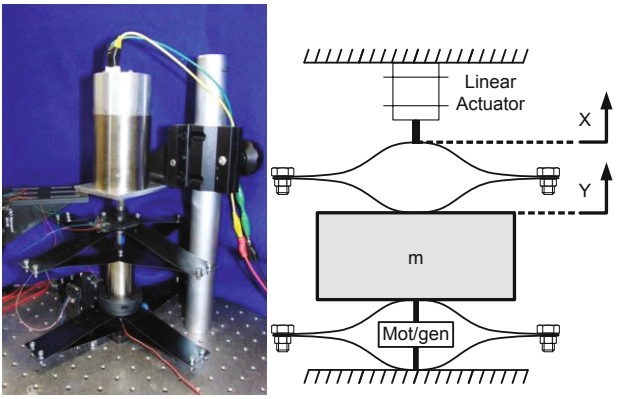

Fig. 10. Experimental setup photograph and schematic NOTE: the large linear motor at the top of the setup in the photograph is used simply to provide a mechanical input for testing, and therefore its power draw does not explicitly factor into energy cost/output calculations

There is a notable difference between the experimental device, shown in Figure 10, and a device that could be used on a bridge for energy harvesting. The device shown in Figure 10 is connected to a stationary ground through a spring element, which is not practical with a real bridge. For the device in Figure 10 to be used on a bridge, a stiff, strong structure needs to be built to connect the top spring to the bottom spring. Mounting such a structure on a bridge would not pose a problem, but in the current setup, the linear motor used to simulate bridge motion was not powerful enough to move such a structure precisely, thus the setup shown in 10 was used.

By converting the experimental setup shown in Figure 10 (represented schematically in Figure 11-i) to its Thevenin equivalent shown in Figure 11-iv, it is seen that the dynamic elements of the experimental apparatus are

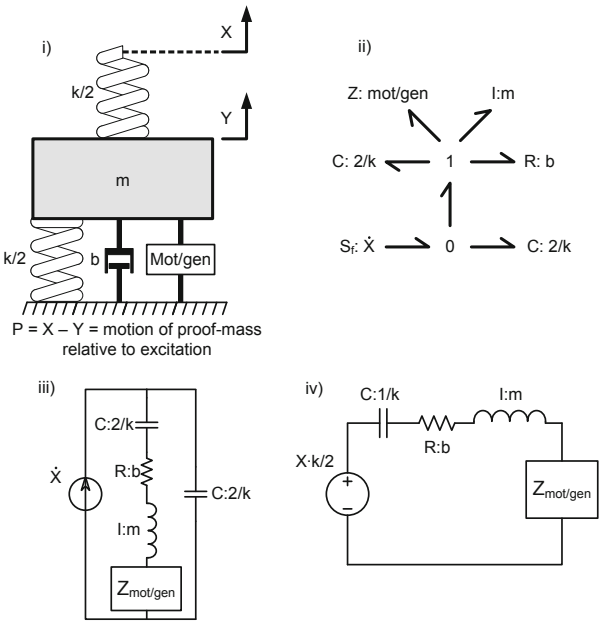

Fig. 11. Transformation of prototype harvester into electrical domain: i) mechanical representation; ii) bond graph representation; iii) electrical equivalent of bond graph; iv) Thevenin equivalent circuit

identical to the elements of the practical device shown in Figure 5. The only difference lies in the way the power from the bridge is transmitted to the harvester.

The transfer function of the system depicted in Figure 11, shown below in (12), has the same characteristic equation as that of the original system shown in (10).

$$\frac{Y(s)}{X(s)} = \frac{\frac{k}{2}}{ms^2 + bs + k + Z_{\mathrm{mot/gen}}} \tag{12}$$

In other words, (10) and (12) only differ in their forcing functions.

Controlling this apparatus to satisfy the requirements of maximum power transfer theorem is therefore quite similar to controlling the device shown in Figure 5-i. It is only necessary to double the systems damping and eliminate the inertial and stiffness elements, which results in (12) reducing to the following ideal transfer function:

$$\frac{Y(s)}{X(s)} = \frac{\frac{k}{2}}{2bs} \tag{13}$$

This desired behavior is only marginally stable, which is problematic because when practically implemented it causes the proof mass to drift. To eliminate

this problem, the desired behavior needs to contain a filter that attenuates the lower frequencies. Combining such a filter with (13) yields the transfer function shown in (14), which exhibits stable desired behavior of the harvester.

$$\frac{Y(s)}{X(s)} = \frac{\frac{k}{2}}{2bs} \frac{\tau^2 s^2}{(\tau s + 1)^2} \tag{14}$$

In the above equation, τ is the time constant that determines which frequencies are attenuated. For the data shown in this paper $\tau = 0.57$ was used which gives a knee of 0.28 Hz. The desired transfer function shown in (14) can be achieved by implementing the following control law through the linear motor:

$$u(t) = \ddot{y}(m - 2b\tau^2) + \dot{y}(b - 4b\tau) + (k - 2b) + \dot{x}\frac{k}{2}\tau^2 - x\frac{k}{2} \tag{15}$$

where u(t) is the force exerted by the motor/generator upwards on the proof mass (away from ground). In the experimental data shown in Figure 12 and Figure 13, the artificial bridge was excited at several different frequencies. The control law shown in (15) was applied to the harvester and its experimental response was recorded and compared to the modeled responses of (12) where $Z_{\mathrm{mot/gen}}$=bs - Damping Only Control (conventional passive method), (13) - Unfiltered implementation of the maximum power transfer theorem (MPTT) controller, and (14) - Implementation of the MPTT controller with the discussed filter.

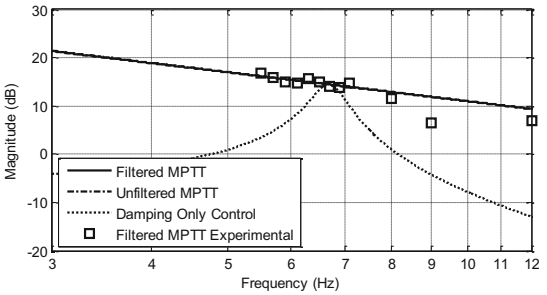

Fig. 12. Experimental response (in terms of gain in vibration amplitude) of the controlled harvesters proof mass compared to the ideal theoretical responses of the passive harvester and the controlled harvester

These figures show that applying the filter to the ideal behavior does not have a significant effect at the frequencies of interest. Also shown is that the actively controlled harvester closely follows the desired behavior in both magnitude and phase, which implies that it is capable of collecting power across a broad spectrum of frequencies. The controller also demonstrates its ability

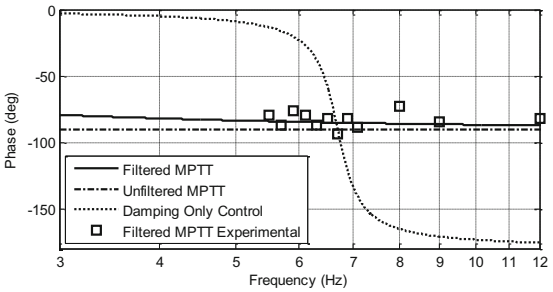

Fig. 13. Experimental frequency response of controlled harvesters proof mass to vibrations (in terms of phase shift) compared to the ideal theoretical responses of the passive harvester and the controlled harvester

to simultaneously harvest power from multiple frequencies. This is an important characteristic for a practical harvester because bridges usually move in multiple modes, which means there is potential for harvesting more power than can be contained in a single frequency component. To demonstrate this ability, the artificial bridge was driven with a forcing function which contained 6 Hz, 7 Hz, and 12 Hz components simultaneously. The displacement of the harvesters proof mass was recorded while the harvester was actively controlled as well as when the bridge was excited with the same frequencies without the controller altering the motion of the proof mass. The results of these tests are shown in Figure 14

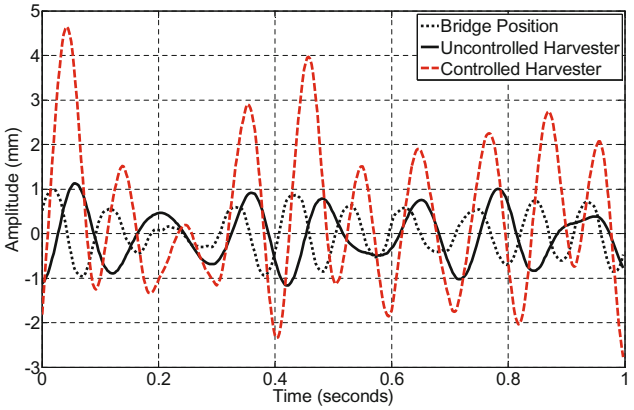

Fig. 14. Experimental response of the harvester's proof mass to vibrations with and without active control

Two of the harvester's important characteristics are demonstrated in Figure 14. First, even though the uncontrolled harvester (where uncontrolled is

taken to mean that the harvester is not siphoning energy from the motion of the proof mass meaning no additional damping is introduced)has only half of the damping of the actively controlled harvester, the controlled harvester has much higher amplitudes of oscillation. Secondly, the controller causes the harvester to have approximately 90° phase lag, which is evidence that the controller is performing as predicted in simulation, shown in Figure 9.

3.5 Discussion

Practical bridge health monitoring requires a self-contained power source to power sensors and transmit bridge health data wirelessly. It is possible to harvest power from bridge vibrations by connecting a mass to a bridge via a spring and converting some of the mass's kinetic energy into useful electrical power with a generator. In this section it was shown that by applying the principles of the maximum power transfer theorem to the control of the power extraction element, more power can be extracted from given bridge vibrations than is possible passively. By considering the Thevenin electrical equivalent of the harvester it becomes clear that in order to satisfy the maximum power transfer theorem, the controller must satisfy two criteria:

1. Complex impedance elements (the mass and spring components) of the source must be cancelled by the load, and
2. The real component of the impedance (the systems internal damping) must be matched by the load's damping for energy harvesting.

By accomplishing these goals, the harvester is able to maximize the magnitude of its proof masss motion and keep it 90° out of phase with the source motion across a wider range of vibration frequencies that is possible using conventional electromagnetic energy harvesting. Additionally, there is no single natural frequency of the controlled harvester, which allows for appreciable power to be extracted from multiple frequency components simultaneously. With the control methodology presented in this paper, the frequency of the bridge does not need to be computed, so there is no delay or computational overhead inherent to fast Fourier transforms. Moreover, because the controller is composed entirely of linear computations, it could be implemented using only analog circuitry. Further energetic analysis needs to be carried out to calculate the net power gains (additional harvested power reduced by the amount of power required to obtain the necessary actuation) that can be achieved.

4 Conclusion

This chapter presented a novel experimental research platform for multi-channel, high data rate SHM application. The new methods and solutions

provide an unprecedented level of flexibility. The two key factors that provide these benefits are the modular design and the SoC-based architecture that includes both a microcontroller for flexibility and ease of programming and a Flash-based FPGA for high computational power at a reasonable energy cost. The chapter also pointed out that the one of the main design drivers in this domain today is power efficiency, and that energy harvesting needs to be a major aspect of the system design. The characteristics of the novel vibration-based harvester presented provides higher power output than existing approaches. It has the potential to make locally powered bridge health monitoring systems based on acoustic emissions or other high bandwidth methods more viable.

References

1. Ahlborn, T.M., Shuchman, R., Sutter, L.L., Brooks, C.N., Harris, D.K., Burns, J.W., Endsley, K.A., Evans, D.C., Vaghefi, K., Oats, R.C.: The State-of-the-Practice of Modern Structural Health Monitoring for Bridges: A Comprehensive Review. Technical Report 734, Michigan Tech (2010)
2. Beeby, S.P., Tudor, M.J., White, N.M.: Energy harvesting vibration sources for microsystems applications. Measurement Science and Technology 17(12), R175–R195 (2006)
3. Chang, P.C., Chi Liu, S.: Recent Research in Nondestructive Evaluation of Civil Infrastructures. Journal of Materials in Civil Engineering 15(3), 298 (2003)
4. Chen, R., Fernando, G.F., Butler, T., Badcock, R.A.: A novel ultrasound fibre optic sensor based on a fused-tapered optical fibre coupler. Measurement Science and Technology 15(8), 1490–1495 (2004)
5. James, M.: Conrad. A survey of energy harvesting sources for embedded systems. In: IEEE SoutheastCon 2008, pp. 442–447. IEEE (April 2008)
6. Dondi, D., Pompeo, A.D., Tenti, C., Simuni, T.: Shimmer: a Wireless Harvesting Embedded System for Active Ultrasonic Structural Health Monitoring. Energy, 2325–2328 (2010)
7. Galchev, T., McCullagh, J., Peterson, R.L., Najafi, K.: Harvesting traffic-induced bridge vibrations. In: Solid-State Sensors, Actuators and Microsystems Conference (TRANSDUCERS), pp. 1661–1664 (2011)
8. Gorman, M.R.: Plate wave acoustic emission. The Journal of the Acoustical Society of America 90(1), 358 (1991)
9. Harms, T., Sedigh, S., Bastianini, F.: Structural Health Monitoring of Bridges Using Wireless Sensor Networks. IEEE Instrumentation & Measurement Magazine 13(6), 14–18 (2010)
10. Healy, M., Newe, T., Lewis, E.: Wireless Sensor Node hardware: A review. In: 2008 IEEE Sensors, pp. 621–624. IEEE (October 2008)
11. Ledeczi, A., Hay, T., Volgyesi, P., Hay, D.R., Nadas, A., Jayaraman, S.: Wireless Acoustic Emission Sensor Network for Structural Monitoring. IEEE Sensors Journal 9(11), 1370–1377 (2009)
12. Lynch, J.P.: A Summary Review of Wireless Sensors and Sensor Networks for Structural Health Monitoring. The Shock and Vibration Digest 38(2), 91–128 (2006)

13. Lynch, J.P., Law, K.H., Kiremidjian, A.S., Carryer, E., Farrar, C.R., Sohn, H., Allen, D.W., Nadler, B., Wait, J.R.: Design and performance validation of a wireless sensing unit for structural monitoring applications. Structural Engineering and Mechanics 17(3-4), 393–408 (2004)
14. Mascareñas, D., Flynn, E., Todd, M., San, C.: Wireless Sensor Technologies for Monitoring Civil Structures. Analysis, 16–20 (April 2008)
15. Moghe, R., Lambert, F., Divan, D.: A scoping study of electric and magnetic field energy harvesting for wireless sensor networks in power system applications. In: 2009 IEEE Energy Conversion Congress and Exposition, pp. 3550–3557. IEEE (2009)
16. Los Alamos National. A Review of Structural Health Monitoring Literature: 1996 - 2001. Structural Health Monitoring, LA-13976-M(LA-13976-MS):1996–2001 (2004)
17. Pedchenko, A.V., Hoke, J.W., Barth, E.J.: A Control Approach for Broadening the Operating Frequency Range of a Bridge Vibration Energy Harvester. In: 2011 Dynamic Systems and Control Conference (2011)
18. Qi, G., Barhorst, A., Hashemi, J., Kamala, G.: Discrete wavelet decomposition of acoustic emission signals from carbon-fiber-reinforced composites. Composites Science and Technology 57(4), 389–403 (1997)
19. Rippert, L., Wevers, M., Van Huffel, S.: Optical and acoustic damage detection in laminated CFRP composite materials. Composites Science and Technology 60(14), 2713–2724 (2000)
20. Russell-Minda, E., Jutai, J., Speechley, M., Bradley, K., Chudyk, A., Petrella, R.: Sensors and Technologies for Structural Health Monitoring: A Review. Journal of Diabetes Science and Technology 3(6), 1–14 (2011)
21. Sakamoto, W.K., Marin-Franch, P., Das-Gupta, D.K.: Characterization and application of PZT/PU and graphite doped PZT/PU composite. Sensors and Actuators A: Physical 100(2-3), 165–174 (2002)
22. Scruby, C.B.: An introduction to acoustic emission. Journal of Physics E: Scientific Instruments 20(8), 946–953 (1987)
23. Shahabadi, A.: Bridge Vibration Studies: Interim Report. Transportation Research, pp. 108–130 (1977)
24. Williams, C.B., Pavic, A., Crouch, R.S., Woods, R.C.: Feasibility study of vibration-electric generator for bridge vibration sensors. In: IMAC-Proceedings 16th International Modal Analysis Conference, pp. 1111–1117 (1998)
25. Xu, N., Rangwala, S., Chintalapudi, K.K., Ganesan, D., Broad, A., Govindan, R., Estrin, D.: A wireless sensor network For structural monitoring. In: Proceedings of the 2nd International Conference on Embedded Networked Sensor Systems - SenSys 2004, p. 13. ACM Press, New York (2004)

A Review of Cooperative Spectrum Sensing in Cognitive Radios

Babak Ahsant[1] and Ramanarayanan Viswanathan[2]

[1] Department of Electrical & Computer Engineering
Southern Illinois University, Carbondale, Illinois, USA
bahsant@siu.edu
[2] Department of Electrical Engineering, University of Mississippi,
University, MS 38677-1848
viswa@olemiss.edu

Abstract. Dramatically increasing requests for frequency bands in recent years, which has resulted in spectrum scarcity, lead us to examine the feasibility of dynamic spectrum access (DSA) technology. Cognitive radio (CR) has been considered as the key enabler of DSA because of its capability to perform spectrum sensing by using different detection techniques that guarantee acceptable probability of interference to primary users (PU), due to secondary user(s) (SU) access. Furthermore, cooperative spectrum sensing, which combines the observations/decision from a number of CR nodes, in order to determine the presence or absence of a PU signal, can yield better performance than that arrived by a single CR alone. This chapter provides a review of techniques and challenges encountered in cooperative spectrum sensing.

1 Introduction and a Summary of Sensing Methods

Cognitive Radio is built on the software defined radio (SDR) platform with an extra feature, "re-configurability." The idea behind CR is to identify "spectrum holes," performing real-time spectrum allocation and acquisition. This temporarily idle space, which is also known as "white space," is basically the absence of transmission of licensed users. Of course, this space should be vacated in case of re-appearance of primary user(s). For this purpose, following spectrum sensing techniques have been proposed and implemented [1]: matched filter (or pilot) detection (MFD), energy detection (ED), cyclostationary (or characterization) detection (CD), eigenvalue detection (EVD), autocorrelation (or covariance) detection (AD), wavelet detection (WD), and probability-based detection (PD); advantages and disadvantages of these strategies have been reviewed in [2]. Some of these techniques discussed are also presented here. All these techniques are suffering from hidden terminal problem, which could be caused by heavily multipath fading and shadowing effects. The cooperative spectrum sensing has been proposed in order to combat this critical issue [3]; in this work only the hard decision combining, i.e., one bit quantization of CR data has been considered. The soft decision, i.e., multiple bits quantization of CR data was investigated in [4].

S.C. Mukhopadhyay et al. (Eds.): Advancement in Sensing Technology, SSMI 1, pp. 69–80.
springerlink.com

Detection of any phenomenon, based on stochastic data, can lead to errors in decision. When a PU is present, the sensing device could declare that it is not present, leading to a miss, which is the complement of detection. Similarly, when a PU is absent (or spectral hole), the sensing device could declare that a PU is present, leading to a false alarm. If a sensing device is designed to control one type of error, say, the probability of miss P_m, which is One minus the probability of detection ($P_m = 1 - P_d$), below a specified value, the other probability of error, the probability of false alarm P_f, is determined by the quality of the received signal and the noise in the system. From a PU point of view, a larger probability of detection would provide it with better protection, as the chance of a SU transmitting while the PU is present will be less. From a SU point of view a low probability of false alarm is better, as it provides a SU with more access. It is interesting that, depending on the values of these probabilities, one can classify the sensing system in three different categories: *Conservative System* which has an opportunistic spectrum utilization rate less than or equal to 50% and a probability of interference less than 50% that is $P_d > 0.5, P_f \geq 0.5$. *Aggressive System* which expects to achieve more than 50% opportunistic spectrum utilization while maintaining less than 50% probability to interfere with the PU that gives the condition of $P_d > 0.5, P_f < 0.5$. *Hostile System* that targets more than 50% opportunistic spectrum utilization and is likely to cause interference to the PU with a probability greater than or equal to 50% that means $P_d \leq 0.5, P_f < 0.5$ [5].

Furthermore, according to the nature of sensing techniques we can divide the sensing systems into two major groups: Blind sensing that does not rely on any target signal features, like energy detection and autocorrelation detection or signal specific sensing that utilizes specific target signal features, like matched filter detection and cyclostationary detection. On the other hand, IEEE 802.22 standard proposal mentions that no specific spectrum sensing technique is mandatory in the standard and designers will be free to implement whatever spectrum sensing technique they choose as long as it meets the specified sensing requirements [6].

The MFD method provides coherent detection and gives the best performance in terms of signal power to noise power ratio (SNR) as the secondary user receiver assumes the exact knowledge of the signal arriving from the transmission of a primary user. This means necessity of having exact knowledge of the modulation scheme employed by the primary transmitter, time synchronization of arriving symbols, and the channel parameters and if this information is not correct, the MFD performs poorly. In many practical scenarios, such exact knowledge is unavailable and hence it may not be realizable. Of course, the main advantage of MFD is that it needs less time to determine the presence of a PU signal with acceptable probabilities of errors tolerance, when compared to other methods. However, a significant drawback of a matched filter is that a cognitive radio would need a dedicated receiver for every PU class [7].

If a signal exhibits cyclostationary properties, its presence could be detected even in low SNR because CD is capable of differentiating the primary signal from the interference and noise. A signal is cyclostationary, if its autocorrelation is a periodic function. By searching for the peak in the spectral correlation function, the presence of the signal can be identified. It is more robust as noise does not possess any cyclic property whereas different modulated signals have different unique cyclic frequencies. A drawback is that CD is more complex to implement

and requires the knowledge of modulation format [1]. We can say CD method, as well as MFD technique, are good to be used in high processing power systems. For more efficient and reliable performance, the enhanced feature detection scheme, combining cyclic spectral analysis with pattern recognition based on neural networks is proposed in [8].

Eigenvalues detection is not computationally complex and primary user waveform information is not required. EVD is based on random matrix theory and auto-correlations are applied on received signal samples thereby estimating the covariance matrix. Then, the maximum eigenvalue of the covariance matrix is compared with predetermined threshold value to determine primary user presence; it has been shown that at lower SNR, EVD has even better results compare to MFD, ED and CD [9].

The Wavelet Detection is based on wavelet transform, which is a multi-resolution method where an input signal is decomposed into different frequency components. By computing the wavelet transform of the power spectral density of received signal, the singularity in spectrum can be located and therefore vacant frequency bands can be found. Again, high sampling rate and computational complexity are the disadvantages. The covariance detection exploits the difference between the autocorrelation of a noise process and that of a signal process in order to sense a PU signal, this technique is suitable for low processing power systems.

The Energy Detection is also termed as a radiometer or a non-coherent detection method. An ED is simply base on Neyman-Pearson approach and computes the energy of a signal present in a certain bandwidth and compares it to certain threshold value to decide whether the desired signal is present or not. The main advantage of ED is that it does not require any knowledge of the signal, such as modulation format or symbol synchronization. When a PU is transmitting, a SU which is located within a reasonable distance from the PU receives the PU signal in noise. The nature of channel between the PU and the SU and hence the power of the received signal in relation to the noise level will impact the performance of the ED. The performance improves with increased signal sensing (observation) time, which, however, results in lapsed opportunity to exploit a significant portion of the duration of PU spectral hole for SU transmission. Moreover, accurate determination of noise level is needed in order to guarantee a certain false alarm probability; error in noise power estimation can result in performance loss. The energy detector shows poor performance in low SNR, because the noise variance is not accurately known at low SNR. Although ED has a simple algorithm when compared to other techniques, at values of SNR below certain threshold, the ED could become useless. Another drawback is the inability of ED to differentiate the interference from other SUs and a PU. There are some other spectrum sensing techniques like multi-tape spectrum estimation (MTSE), which is based on maximal energy concentration of the Fourier transform of Slepian vectors and filter bank spectrum estimation (FBSE), which is a simplified version of MTSE; more details about these methods and a comparison between different sensing techniques could be found in [6]. Also, there is a recently proposed scheme, which is called probability based detection (PD). This method is based on the assumption that the idle duration of the licensed spectrum band is exponentially distributed, so

that the probability model regarding the appearance of the primary signal at each sampling point of a CR user frame is established [10].

It is conceivable that the sensing performance of a CR network could be significantly improved, if two or more SUs, who want to opportunistically use the spectrum in a given band, cooperatively sense the presence or absence of a PU in their vicinities. The success of such a cooperative spectrum sensing depends on several factors: first, the SU's ability to cooperate and network among themselves; second, mobile SUs may necessitate dynamically configuring CR networks and third, establishment of a network coordinator or a fusion center, where a final determination based on the sensing data from several SUs could be made. The superiority of cooperative sensing results from the fact that multiple pieces of information from several SUs would be better than one piece of information at a single SU; this is especially true when one of the SU receivers is hidden from a nearby PU transmitter, whereas one or more of other SU receivers in the vicinity of the PU may pick up the transmitted signal. However, there may exists a scenario, where the determination of the presence of a PU by a set of SUs may not be relevant to another SU, simply because the particular PU sensed may really belong only to the "vicinity" of other SUs and not to the one SU under question. This brings up the question of vicinity determination before SUs could cooperatively sense. Hence, one could argue that the determination of a PU is not only with respect to time (present or absent) but also with respect to the location. A detailed discussion of this aspect with ensuing analysis is presented in a recent paper [11]. In this survey, we make the simplified assumption that an appropriate group of cooperative SUs has been determined in order to assess the presence of a PU in their vicinity. Cooperative sensing mechanism draws upon results from distributed detection and its application to wireless sensor networks.

Based upon the distributed detection concept, a cooperative CR system can either use data fusion or decision fusion rules for combining individual observations of CRs. According to the nature of CR networks and their common applications, bandwidth limitation of the reporting (control) channel still remains as a challenge and has been discussed in various literature. In [12], a censoring method for a hard decision scenario is proposed in which every cognitive users obtain an observation independently and determines the reliability of the information and only the users with reliable information were allowed to report their local binary decisions to a common receiver at the fusion center (FC). In that work, the authors studied the performance of spectrum sensing in perfect and imperfect reporting channels and their analytical results show that the average number of sensing bits can be decreased greatly without impacting a great loss of PU detection performance.

2 Cooperative Spectrum Sensing Algorithms and Challenges

Cooperative spectrum sensing, when implemented appropriately, would yield better sensing performance and better throughput in CR networks. Most of the works reviewed here, excluding very recent contributions, have also been included in [13]. In this section, the terms CR and sensor will be used interchangeably.

Different studies have considered different signal models, fusion rules, or performance issues such as, sensing throughput tradeoffs and SNR walls [5, 14-20]. We discuss below some of these results.

In [5], the authors consider energy detection and a large number of samples at the detector so that the ED output can be considered to be Gaussian under both the hypotheses. The mean and variance of the output under the PU present hypothesis are larger than the corresponding values for spectral holes hypothesis. The CRs transmit the ED outputs directly, without any quantization, to a FC over listening channels. After front-end processing at the FC, it is assumed that the received statistic from a CR is a zero-mean Gaussian corrupted version of the transmitted statistic. A LRT at the fusion center will be a linear quadratic statistic and will require computation of multidimensional Gaussian integrals in order to determine the test threshold that meets a specific detection probability at the FC. Because of this computational complexity, a linear combination of received observations was considered. Optimization of weighting vector, for different cases of *Conservative, Aggressive* and *Hostile* systems was considered. For small values of *N*, the LRT performance was also determined numerically and then compared with that of a linear combiner. The results show usefulness of the linear combiner. In [14], it is shown that the optimization of weights can be done without any approximation and without having to delineate three cases.

In [15], each CR uses identical energy detectors and transmits their binary decisions to the FC over error-free links. The power of the additive noise component in a sensor is assumed to have been estimated by the sensor, with the error in the estimate assumed to be distributed as log-normal with zero mean. Similarly, under the presence of a PU, each CR is assumed to receive a shadowed version of the transmitted PU signal in AWGN noise. For this condition, received power at a CR is modeled as a log-normal distribution with a mean value and a variance that depends on the shadowed-signal variance. Moreover, the signal powers in decibels at two CRs are assumed to have a correlation that decreases exponentially with distance between the receivers. With the assumed knowledge of a minimum value of the mean signal power level at the edge of a PU transmitter range and the goal of keeping the P_m (miss probability, termed as interference probability, the probability of wrongly deciding absence of PU and therefore transmitting SU signal) below a number, a Neyman-Pearson (NP) test was considered. Because of correlated sensor observations, the individual decisions made at the sensors will be dependent. Because of the dependence, a LRT at the FC would require complete joint probability calculations, which would be computationally cumbersome. A suboptimal test based on the sensor decisions, termed linear-quadratic (LQ), was formulated and was shown to provide better performance, i.e., higher probability of spectrum holes detection at a prescribed probability of interference level, than a simple counting rule.

The question of improvement attainable in sending multiple bits (soft decisions) from CRs to the FC, instead of single bits (hard decisions) was examined in [16]. The model assumes the detection of an OFDM signal with cyclic prefix at a CR and assumes a LRT statistic based on the computed autocorrelation coefficient [17]. Assuming the sensor signal observation interval

to be very large compared to one OFDM block and that the SNR is small, the distributions of the test statistic under both hypotheses are approximately Gaussian. This becomes a problem of testing two Gaussian distributions with known means and variances. For hard decision combining, the OR, AND, and majority logic (ML), in the class of fusion counting rules were considered. For soft decision combining, the quantizer at a CR was assumed to be a maximum output entropy quantizer and the fusion rule is the comparison of the sum of estimated quantized values against a threshold. The estimated quantized value of a sensor at the FC may differ from the quantized value at the sensor, due to noisiness of the sensor-fusion link. It was assumed the each sensor-fusion is link static and independent of each other, so each exhibits a constant bit error probability (BEP). The theoretical and simulation results show that the ML logic is more robust to bit error probability variations in sensor-fusion (listening channel) link when compared to both OR and AND.

The reference [16] also talks about a BEP wall. The basic idea is that, for the listening channel bit error rate above a certain limit, it is possible that no sensor quality could achieve certain prescribed fusion center performance, specified in terms of both required probabilities, probability of detection (P_{d0}) and probability of false alarm (P_{f0}). Another way to describe this is to calculate the SNR loss in dB defined as the difference between the minimum SNR required at the SUs to meet the constraints on P_{d0}, P_{f0} in the presence of reporting channel errors (P_b) and the minimum SNR required at the SUs in the ideal case of using exact log-likelihood ratio (LLR), an optimal fusion rule and error free reporting channels ($P_b = 0$). A plot of SNR loss against BEP (P_b) was done for soft decision and various hard decision fusion schemes. BEP wall is the point at which the SNR loss increases without bound. BEP wall close to "1" is desirable, since in that case, the cooperative sensing is robust for larger values of BEP. The soft decision combining with two or more bits provide better performance, both in terms of reduced SNR loss and the BEP wall, when compared to hard decision fusion. Among the counting rules examined, ML performs the best. In a related issue, [18] considers the upper bound on P_f (alternatively $1 - P_d$), for a given channel P_b and a specific *k*-out-of-*n* fusion rule (counting rule), so that a specified fusion center performance can be met. In other words, if P_f exceeds the bound, the specified fusion center performance cannot be attained. BEP wall basically points out the limitations imposed by the listening channel quality. In [19], the effect of the quality of listening channel on the sensor false alarm and detection probabilities, as seen at the FC, was examined. In that paper, minimum sensor SNR was computed for a prescribed fusion center performance and a given link P_b. Alternatively speaking, since only certain parameters can be controlled by devising a test, under a prevailing condition, certain demands on performance levels may never be met.

In [20], the authors consider a multiband detection procedure for detecting the presence or absence of PUs at the same time. The assumption is that multiple sub-bands within a wideband may be occupied by several PUs and that a simultaneous identification of spectral holes in these sub-bands would allow several SUs to opportunistically transmit their signals. Each sub-band detection is allowed to

have different false alarm probability, and hence different sensor detection threshold. By putting a bound on cost function for the interference caused to PUs, and by putting bounds on false alarm and miss probabilities for each sub-band, the authors address the problem of finding optimum sensor thresholds so that the aggregate throughput of all SUs is maximized. The authors show that this optimization problem can be recast into a convex optimization problem so that a computationally feasible solution can be sought. The problem was then extended to the situation of pooled data from all SUs (i.e., cooperative sensing). As in [5], a linear combination of ED sensor outputs was considered. The optimization is now with respect to the weighting vector of the linear combiner and the threshold vector for decisions at the FC (notice that, in this case, no individual decisions are made at a CR). The general optimization problem is not convex; however, by optimizing only the lower bound on the aggregate throughput, and not the exact throughput, the problem can be seen as a convex optimization problem. Simulation results show that cooperative sensing scheme proposed can significantly improve the system performance.

In [21], the authors proposed a cooperative wideband detection scheme with an optimal fusion based on a likelihood ratio test (LRT). In this scheme, which is independent of noise variance estimation, each SU detects the availability of spectrum hole, based on a robust Bayesian estimation algorithm, and then sends their decisions to the fusion center. The authors' simulation results show the effectiveness of the scheme in improving the probability of detection under log-normal shadow fading channel. As mentioned previously, gathering all participating radios data in one place may be very difficult under practical communication constraints [22].

Some distributed cooperative spectrum sensing methods based on consensus algorithms are proposed [23-25]. In [26] consensus schemes for decision fusion-based cooperative spectrum sensing, i.e., OR fusion, AND fusion, and k-out-of-n fusion is investigated. Theoretical analysis shows that by exchanging decision information among adjacent neighboring nodes in a distributed way, these algorithms will converge to the traditional optimal central decision fusion results, assuming that network topology does not change throughout the consensus process.

Another problem addressed is related to finding the optimal number of secondary users. In [27] it was shown that co-operating all secondary users in the network does not achieve the optimum P_d (probability of detection) or P_f (probability of false alarm). The optimum values are usually achieved by exploiting cooperation among a group of users that have higher primary user's signal to noise ratios (SNR). Also, numerical and simulation results provided in [28] show that there exists an optimum number of cooperating users, for a pair of fixed probabilities of detection and false alarm, and cooperating a certain number of users with highest reputation will achieve better sensing performance by accounting for network security.

In [29], the authors consider SNR walls for signal detection. Of specific interest is the spectrum sensing in CR. Given that there will be uncertainty in noise models (noise is never perfectly WGN, noise power measured is uncertain within some

non-zero interval), signal models, and transmission channel models (fading parameters can be known only within certain uncertain intervals), dictates of specific false alarm probability and miss probability may not be met, even if the number of independent samples received by a detector become infinitely large. When a radiometer (ED) is used to detect the presence of a weak (very small SNR) unknown signal in AWGN noise, with the noise variance assumed to lie over the uncertainty interval:$[\sigma^2/\rho, \rho\sigma^2]$ $\rho > 1$, the detector will be unable to meet specified constraints on both $P_f < \alpha < 0.5$ $P_m < \beta < 0$ if the SNR is below the SNR wall specified by $(\rho^2 - 1)/\rho$. That is, any amount of sensing time for the radiometer cannot provide the required accuracy. Drawbacks of ED can be clearly seen in this context. If certain information about PU signal, such as the presence of a pilot tone, is known to the radiometer, the SNR wall could be pushed back, but the noise uncertainty still poses a non-zero SNR wall. Thus, if a licensed PU is allowed to transmit any choice signals and at the same time, severe constraint on miss probability for a SU is imposed, the opportunistic spectrum access can yield only a very limited throughput for secondary users. But, if the rules mandate a PU to transmit a pilot at certain power, then SUs can operate more successfully at the cost of potentially lower performance for the PU. This general tradeoff can be seen as capacity-robustness tradeoff [29].

In [30], the authors consider optimizing sensing time in order to maximize secondary user throughput, subject to constraint on interference to PU. Assume a lower bound on the probability of detection (to protect primary user) and an available block of total time out of which a portion of time τ is allocated for sensing and the remaining time for secondary user data transmission, when a SU decides to transmit. Then the problem is to find an optimum τ so that the throughput R of the secondary user is maximized. Notice that R has two components: one when a spectrum hole truly exists, the SU correctly identifies it and the other when a PU is present, but the SU mistakenly considers it to be absent (sneak through case). For radiometer detection it was shown an optimum τ exists and that it can be numerically found. The paper also considers extension to distributed spectrum sensing with multiple SUs. Assuming the knowledge of sensing channels' coefficients, a maximal ratio combiner is considered at the FC. Performance of OR, AND, and ML were also studied.

We discuss now some of the recent contributions to spectrum sensing in CR. In [31] sensing efficiency of the AND, OR, and the *k*-out-of-*n* fusion rules has been discussed, where the authors focus on two important issues of spectrum sensing: the discovered spectrum opportunity and the overall sensing overhead and presented the cooperative spectrum sensing strategies for single and multiple licensed channels. In [32] the authors consider the combining of hard decisions from multiple energy detectors and compare the sensing efficiency for different fusion rules. The optimal decision threshold for the *k*-out-of-*n* rule that can maximize the sensing efficiency was determined and was shown that this rule is optimal in terms of sensing efficiency when compared to tow other rules, for a given false alarm probability. Also, it has been observed that if SU senses the channel over a longer duration, then a lower decision threshold will be required in spectrum sensing, because sensing accuracy will be higher.

In [33] the authors have studied the optimization of cooperative spectrum sensing when the local decisions of the CR users are correlated and a counting rule is employed at the fusion center. Also, the optimal number of users and the local sensing threshold that jointly minimize the probability of sensing error are obtained using the genetic algorithm (GA), when the correlation index is known. Detection performance analysis shows that the cooperative spectrum sensing scheme degrades with an increase in the correlation between CR local decisions for all fusion rules i.e. AND, OR, majority logic and any other counting rule.

In [34] the authors have considered an additional parameter of probability of interference along with the probability of missed detection in order to increase the performance of spectrum hole discovery. Their optimization formulation considers both single and cooperative sensing and the case of one primary user existence. When compared to conventional approaches, their "interference-aware" metric can result in a better utilization of the spectrum by allowing the secondary user to maximize its transmission opportunity, without sacrificing the desired degree of protection for primary users.

Knowing that the reporting channels are not error free in real implementation of CR, in [35] the authors designed a realistic cooperative spectrum sensing network, where the reporting channels from the cognitive radios to the fusion center are affected by AWGN and Rayleigh fading and an optimal minimum mean square error (MMSE) detector is used to improve the detection performance. It is observed that the performance of this detector converges to that of fusion center operating in an ideal (noise free) environment with increasing SNR.

In [36] the authors investigated the performance of cooperative spectrum sensing with cognitive radio users censored on the basis of the quality of Rayleigh-faded reporting channel connecting CR users to a FC. The authors observed that no further improvement in missed detection performance is obtained by increasing the number of CRs beyond a certain limit.

Many analyses presented dealt with cooperative spectrum sensing assuming one primary user. In fact, most of the detection techniques do not require the information about primary users, but in real environment, multiple primary users might exist. In [37] multi-antenna cooperative spectrum sensing in cognitive radio networks, when there may be multiple primary users, is considered. In this approach, sensing performance of a multiple primary users' detector, based on the spherical test (ST) is investigated and also the detection performance is analyzed by deriving closed-form approximations by matching the moments of the test statistics to the Beta distributions, under both hypotheses. Besides, the ST detector estimates whether the covariance matrix differs from a matrix proportional to the identity matrix. According to simulation results, the authors conclude that, in the presence of more than one primary user, some performance gain may be obtained via the spherical test, even without knowing the number of primary users.

3 Conclusion

In this chapter we provided a review of some of the research on cooperative spectrum sensing techniques. The review has not been complete, but an effort was

made to present some of the key results. Since the technology for implementation is at an early stage, the topic is of interest to many researchers and we can anticipate more results in the near future.

References

[1] Letaief, K.B., Zhang, W.: Cooperative communications for cognitive radio networks. Proceeding of the IEEE 97(5), 878–893 (2009)
[2] Viswanathan, R., Ahsant, B.: A review of sensing and distributed detection algorithms for cognitive radio systems. International Journal on Smart Sensing and Intelligent Systems 5(1), 177–190 (2012)
[3] Ghasemi, A., Sousa, E.S.: Collaborative spectrum sensing for opportunistic access in fading environments. In: Proceeding of IEEE International Symposium on New Frontiers in Dynamic Spectrum Access Networks, pp. 131–136 (November 2005)
[4] Ma, J., Zhao, G.D., Li, Y(G.): Soft combination and detection for cooperative spectrum sensing in cognitive radio networks. IEEE Transactions on Wireless Communications 7(11), 4502–4507 (2008)
[5] Quan, Z., Cui, S., Sayed, A.H.: Optimal linear cooperation for spectrum sensing in cognitive radio networks. IEEE Journal of Selected Topics in Signal Processing 2(1), 28–40 (2008)
[6] Shellhammer, S.J.: Spectrum Sensing in IEEE 802.22. In: IAPR Workshop on Cognitive Information Processing, pp. 1–6 (June 2008)
[7] Carbic, D., Mishra, S.M., Brodersen, R.W.: Implementation Issues in Spectrum Sensing for Cognitive Radios. In: Proceeding of the 38th Asilomar Conference on Signals, Systems and Computers, vol. 1, pp. 772–776 (November 2004)
[8] Fehske, A., Gaeddert, J., Reed, J.H.: A New Approach to Signal Classification Using Spectral Correlation and Neural Networks. In: Proceeding of IEEE International Symposium on Dynamic Spectrum Access Networks, pp. 144–150 (November 2005)
[9] Ziafat, S., Ejza, W., Jamal, H.: Spectrum Sensing Techniques for Cognitive Radio Networks: Performance Analysis. In: Proceeding of IEEE MTT-S Microwave Workshop Series on Intelligent Radio for Future Personal Terminals, p. 1 (August 2011)
[10] Ma, J., Li, Y.: A Probability-Based Spectrum Sensing Scheme for Cognitive Radio. In: Proceeding of IEEE International Conference on Communications, pp. 3416–3420 (May 2008)
[11] Tandra, R., Sahai, A., Veeravalli, V.V.: Space-Time Metrics for Spectrum Sensing. In: Proceeding of IEEE Symposium on New Frontiers in Dynamic Spectrum, pp. 1–12 (May 2010)
[12] Sun, C., Zhang, W., Letaief, K.B.: Cooperative spectrum sensing for cognitive radio under bandwidth constraints. In: IEEE Wireless Communications and Networking Conference, pp. 1–5 (March 2007)
[13] Viswanathan, R.: Cooperative Spectrum Sensing for Primary User Detection in Cognitive Radio. In: Proceedings International Conference on Sensing Technology, pp. 79–84 (November 2011)
[14] Taricco, G.: Optimization of linear cooperative spectrum sensing for cognitive radio networks. IEEE Journal of Selected Topics in Signal Processing 5(1), 77–86 (2011)

[15] Unnikrishnan, J., Veeravalli, V.V.: Cooperative sensing for primary detection in cognitive radio. IEEE Journal of Selected Topics in Signal Processing 2(1), 18–27 (2008)
[16] Chaudhari, S., Lunden, J., Koivunen, V., Poor, H.V.: Cooperative sensing with imperfect reporting channels: hard decisions or soft decisions? IEEE Transactions on Signal Processing 60(1) (January 2012)
[17] Chaudhari, S., Koivunen, V., Poor, H.V.: Autocorrelation-based decentralized sequential detection of OFDM signals in cognitive radios. IEEE Transactions on Signal Processing 57(7), 2690–2700 (2009)
[18] Chaudhari, S., Lunden, J., Koivunen, V.: BEP walls for collaborative spectrum sensing. In: Proceeding of IEEE International Conference on Acoustics, Speech and Signal Processing, pp. 2984–2987 (May 2011)
[19] Kanchumarthy, V.R., Viswanathan, R., Madishetty, M.: Impact of Channel Errors on Decentralized Detection Performance of Wireless Sensor Networks: A Study of Binary Modulations, Rayleigh-Fading and Non-Fading Channels, and Fusion-Combiners. IEEE Transactions on Signal Processing 56(5), 1761–1769 (2008)
[20] Quan, Z., Cui, S., Sayed, A.H., Poor, H.V.: Optimal multiband joint detection for spectrum sensing in cognitive radio networks. IEEE Transactions on Signal Processing 57(3), 1128–1140 (2009)
[21] Jamali, V., Sadegh Zadeh, R.A., Hamid Safavi, S., Salari, S.: Optimal cooperative wideband spectrum sensing in cognitive radio networks. In: Proceeding of International Conference on Ubiquitous and Future Networks, pp. 371–374 (June 2011)
[22] Mishra, S.M., Sahai, A., Brodersen, R.W.: Cooperative sensing among cognitive radios. In: Proceedings of IEEE International Conference on Communications, vol. 4, pp. 1658–1663 (June 2006)
[23] Saber, R.O., Fax, J.A., Murray, F.M.: Consensus and cooperation in networked multi-agent systems. Proceedings of the IEEE 95(1), 215–233 (2007)
[24] Yildizy, M.E., Aysaly, T.C., Barner, K.E.: In-network cooperative spectrum sensing. In: Proceeding of European Signal Processing Conference (August 2009)
[25] Zeng, F., Li, C., Tian, Z.: Distributed compressive spectrum sensing in cooperative multi-hop cognitive Networks. IEEE Journal of Selected Topics in Signal Processing 5(1), 37–48 (2011)
[26] Zheng, S., Yang, X., Lou, C.: Distributed consensus algorithms for decision fusion based cooperative spectrum sensing in cognitive radio. In: Proceeding of International Symposium on Communications and Information Technologies, pp. 217–221 (October 2011)
[27] Peh, E., Liang, Y.C.: Optimization for cooperative sensing in cognitive radio networks. In: Proceeding of IEEE Wireless Communications and Networking Conference, pp. 27–32 (March 2007)
[28] Zhang, L., Zhang, D., Huang, G.: "Optimal number of secondary users for cooperative sensing in cognitive radio networks. In: Proceeding of IEEE Conference on Information, Computing and Telecommunication, pp. 347–350 (September 2009)
[29] Tandra, R., Sahai, A.: SNR walls for signal detection. IEEE Journal of Selected Topics in Signal Processing 2(1), 4–17 (2008)
[30] Liang, Y.C., Zheng, Y., Peh, E.C.Y., Hoang, A.T.: Sensing-throughput tradeoff for cognitive radio networks. IEEE Transactions on Wireless Communications 7(4), 1326–1337 (2008)

[31] Song, J., Xue, J., Feng, Z., Zhang, P., Liu, Z.: Optimal cooperative spectrum sensing strategies in cognitive radio networks. In: Proceeding of the IEEE 71st Vehicular Technology Conference, pp. 1–6 (May 2010)
[32] Yang, L., Song, S.H., Letaief, K.B.: Optimizing spectrum sensing efficiency in Cognitive Radio networks. In: Proceeding of the Computing, Communications and Applications Conference, pp. 262–266 (January 2012)
[33] Khalid, L., Anpalagan, A.: Cooperative Sensing With Correlated Local Decisions in Cognitive Radio Networks. IEEE Transactions on Vehicular Technology 61(2), 843–849 (2012)
[34] Lin, Y., Liu, K., Hsieh, H.: On Using Interference-Aware Spectrum Sensing for Dynamic Spectrum Access in Cognitive Radio Networks. IEEE Transactions on Mobile Computing (accepted for Publication, 2012)
[35] Liza, J., Muthumeenakshi, K., Radha, S.: Cooperative Spectrum Sensing in a Realistic Cognitive Radio Environment. In: International Conference on Recent Trends in Information Technology, pp. 375–379 (June 2011)
[36] Nallagonda, S., Roy, S.D., Kundu, S.: Cooperative spectrum sensing with censoring of cognitive radios in Rayleigh fading channel. In: Proceeding of India National Conference on Communications, pp. 1–5 (February 2012)
[37] Wei, L., Tirkkonen, O.: Spectrum Sensing in the Presence of Multiple Primary Users. IEEE Transactions on Communications 60(5), 1268–1277 (2012)

Dielectric Characterisation of Lipid Droplet Suspensions Using the Small Perturbation Technique

R.T. Blakey[1,*], A. Mason[1], A. Al-Shamma'a[1], C.E. Rolph[2], and G. Bond[3]

[1] School of Built Environment, Liverpool John Moores University, Byrom Street, Liverpool, UK
[2] School of Pharmacy and Biomedical Science, University of Central Lancashire, Preston, UK
[3] School of Forensic and Investigative Sciences, University of Central Lancashire, Preston, UK
R.T.Blakey@2010.ljmu.ac.uk

Abstract. This work proposes a novel approach to differentiate biological cells based upon the total concentration of lipids. Lipid accumulation within cells is significant as it serves as a marker pertaining to the metabolism and oncologic state of the cell and organism. This is accomplished through dielectric characterisation of the sample. This chapter presents a preliminary proof of concept experiment using vegetable oils and cell culture media to model lipid droplets in biological cells. The experiment indicated that solutions of numerous different lipid suspensions at different concentrations can be differentiated based upon the dielectric characteristics of the sample. The dielectric constant of vegetable oils was calculated to be between 2.9 and 3.1. The dielectric constant of the suspensions reached up to 27 at a concentration of 0.5% (v/v).

Keywords: Cavity, dielectric spectroscopy, microwave, sensor, small perturbation, triacylglycerol.

1 Introduction

The incidence of malignant neoplasms has continued to rise for the past three decades and significantly contributes to population morbidity and mortality. Neoplasms occur when cell proliferation exceeds cell apoptosis (naturally initiated cell death) which results in the formation of a tumour or increased blood cell volume depending on the origin of the cancerous cell. Tumours can be difficult to identify in the early phase due to being asymptomatic with noticeable symptoms not arising until later development [1]. The earlier a neoplasm is identified the less invasive, simpler and cheaper treatments become resulting in increased patient comfort and prognosis [2-4]. Currently there are no quantitative or qualitative point-of-care diagnostic assays available to indicate neoplasmic growth. This

* Corresponding author.

S.C. Mukhopadhyay et al. (Eds.): Advancement in Sensing Technology, SSMI 1, pp. 81–91.
springerlink.com

paper proposes a novel method for assessing the lipid concentration of biological cells and a proof of concept experiment.

Under normal circumstances, most cells store small amounts of triacylglycerols (TAGs) in organelles called lipid droplets (lipid bodies, adiposomes). These are used to synthesise lipid membranes, other molecules of the lipid family and as a source of chemical energy and finally to synthesise signalling molecules [5, 6]. However, due to cellular mutations and/or abnormal cell to cell signalling, the metabolism of the cell is altered resulting in TAGs being accumulated in such lipid droplets [7, 8]. Depending on the genetic mutations that lead to neoplasm, a lipid droplet can constitute a significant sum of cell volume. Hence, the cell concentration of TAG is an excellent indicator or biomarker of cell metabolism and proliferative state.

The current methods for assessing the lipid profile of a cell or sample are lengthy, require specialised facilities and are subject to calculation induced error. The assay consists of hydrolysed fatty acids from the glycerol back bone employing lipase enzymes. The resulting glycerol is then quantified using colorimetric assays whereby an enzyme, usually glycerol kinase or glycerol triphosphate oxidase, reacts with the molecule producing hydrogen peroxide. This combined with a peroxidise results in a measurable colour change [9]. However, the drawbacks of this method are the inclusion of any free glycerol molecules already present and the patient must fast for up to 12 hours before the test [10]. It is currently employed as a marker of cardiovascular risk and metabolic diseases. Low density lipids (LDLs) and very low density lipids (VLDLs) can be calculated as a result of this and other tests. This test is currently the "gold standard" used in laboratories around the world and therefore is the benchmark to which the product of this research will be compared.

2 Characterisation Using Microwaves

Unlike chemical and fluorescent assessment methods of cellular lipid content, the dielectric characteristics of a cell may be used as a non-destructive indication of lipid accumulation. Biological samples, when exposed to radio and microwave frequencies of electromagnetic radiation, store an amount of electrical energy through an interaction with the molecular and structural properties of the sample [11]. The ability of the sample to store energy is described as the *permittivity*. Generally, the permittivity of a biological cell sample decreases in a series of stages known as dispersions: this phenomena is illustrated in Figure 1. Each step reflects the relaxation of a polarisation process.

Dielectric characterisation of cellular material is dependent upon polarisation processes that occur across a frequency range of Hz up to lower THz frequencies. Biological cells exhibit a characteristic decrease in permittivity as a function of increasing frequency known as α, β, δ and γ dispersions, details of which are noted briefly below.

- α dispersion is related to the adjacent flow of ions across the cell surface.

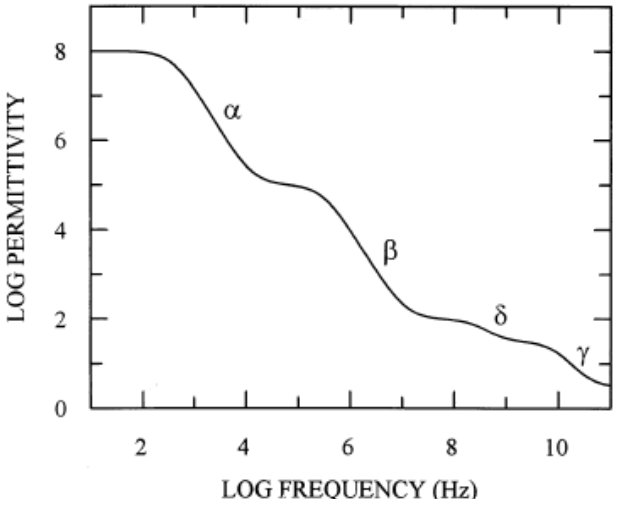

Fig. 1. Generalised dispersions of real permittivity associated with biological material

- β dispersion (also known as interfacial or Maxwell-Wagner interaction) is associated with the build-up of ions at the cell surface leading to polarisation across cell membranes.
- δ and γ dispersions are associated with molecular and sub-molecular rotations, predominantly bound and unbound water.

Neoplasmic processes alter biological characteristics, such as morphology and molecular composition consequently shifting the frequencies at which dispersions occur. Therefore, at a specific frequency the amount of energy stored will differ between normal and neoplasmic biological material. Many different dielectric spectroscopy techniques have been developed in an array of cancer diagnostic applications. The approach varies dependent on the site and type of cancer from characterising isolated individual cells to non-invasive in-vivo imaging techniques [12-14].

Dielectric spectroscopy may quantify permittivity of the material in the complex form. The complex permittivity is composed of the real and imaginary permittivity represented by the equation (1) where ε is the complex permittivity, ω is the angular frequency (ω = 2πf), σ the conductivity and j represents the imaginary unit (j = $\sqrt{-1}$) [15, 16].

$$\boldsymbol{\varepsilon}(\omega) = \varepsilon'(\omega) - j\varepsilon''(\omega) = \varepsilon_r + \frac{\boldsymbol{\sigma}}{j\omega} \tag{1}$$

$$\boldsymbol{\varepsilon_r} = \frac{\boldsymbol{\varepsilon}}{\varepsilon_0} = \frac{\varepsilon'(\omega) - j\varepsilon''(\omega)}{\varepsilon_0} = \varepsilon_r' - j\varepsilon_r'' \tag{2}$$

The permittivity of the sample under test is more commonly quantified as the relative permittivity whereby the permittivity of the material is calculated relative to

the permittivity of free space as in (2), where ε_r is the relative permittivity, ε0 is the permittivity of free space which is equal to 8.8541878×10^{-12} F/m , ε_r is the real part of the relative permittivity and ε_r is the imaginary part of the relative permittivity.

3 Experimental Methodology

The following experiment provides a simple preliminary proof of concept trial to determine if different conformations of vegetable oil and different concentrations of lipid droplets can be differentiated based on their dielectric properties at microwave frequencies. The oil suspensions serve as a cellular lipid droplet model whereby TAG is suspended in an ionic media similar to a lipid droplet within a neoplasmic cell. This method serves to validate the approach and technique to be implemented when assessing biological cells. The dielectric characteristics are calculated using the small perturbation method whereby a sample introduced to a resonating cavity shifts the frequency of resonant modes and decreases the quality factor dependant on the dielectric characteristics of the sample under test [17-19].

Samples of 100% grapeseed, groundnut, olive and sunflower oil (n=5) were prepared in sample tubes ready for dielectric measurement. Secondly, olive oil was suspended in YEPD media to yield concentrations of 50 to 0.5 (% v/v) oil (n=5). YEPD was prepared to the following protocol: 1 % (w/v) of yeast extract, 2 % (w/v) of bacto-peptone and 2 % (w/v) of dextrose diluted in de-ionised water. Before dielectric measurement, the sample would be thoroughly agitated for 15 seconds until a sufficient suspension was achieved.

Measurements were performed using an Agilent Technologies (Hewlett Packard) 8720 ET Vector Network Analyser (VNA) as illustrated in Fig. 2. The instrument was set to generate a signal between 1.5-1.8 GHz over 1601 data points for 10 linear frequency sweeps and calculate the S_{21} (transmission) parameters. Measurements were made through a custom cylindrical resonating cavity, designed and constructed to resonate at approximately 1.75 GHz at mode TM_{010} (see Fig. 3).

$$\varepsilon' = \frac{V_c\,(f_c - f_s)}{2V_s\,f_s} + 1 \tag{3}$$

$$\varepsilon'' = \frac{V_c}{4V_s}\left(\frac{1}{Q_s} - \frac{1}{Q_c}\right) \tag{4}$$

$$\tan\delta = \frac{\varepsilon''}{\varepsilon'} \tag{5}$$

The dielectric constant, dielectric loss and loss tangent of the sample were then calculated using equations (3-5) [19], where ε' and ε'' are the dielectric constant and dielectric loss respectively, f_c and f_s are the resonant frequencies of the empty cavity and loaded cavity respectively, V_s and V_c are the volumes of the sample and cavity respectively and Q_c and Q_s are the quality factors of the empty cavity and the loaded cavity respectively. Precise measurement and documentation of the frequency shift and Q-factor by the VNA and custom GUI software reduced measurement error.

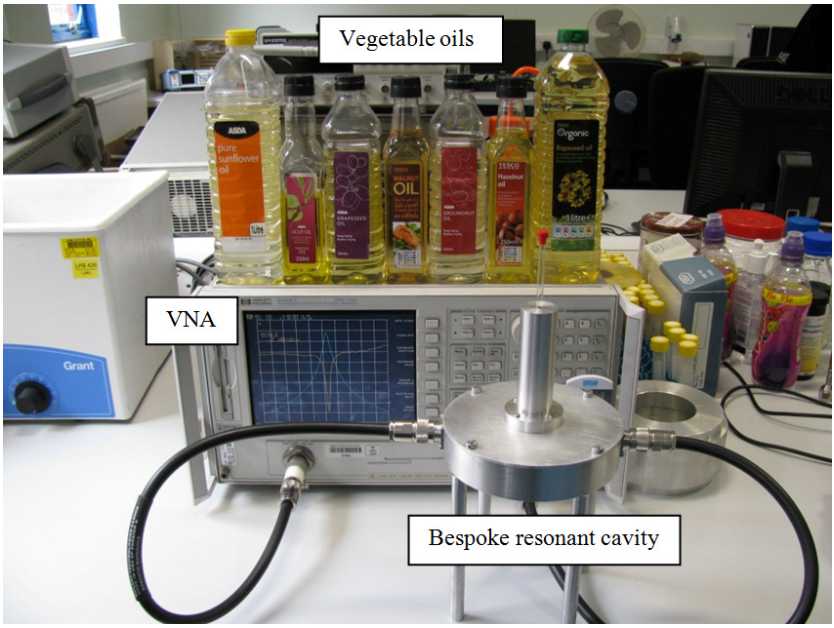

Fig. 2. Experimental setup, showing the range of oils used during experimentation, the microwave cavity and the VNA

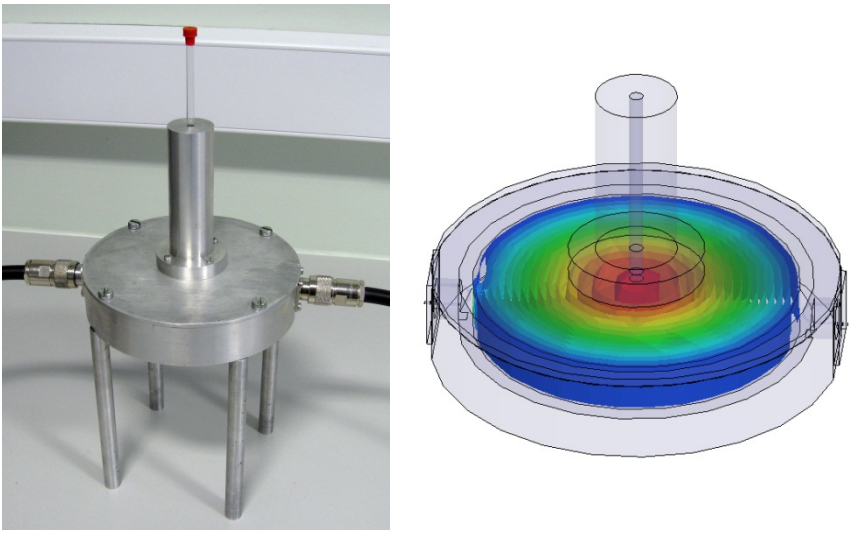

(a) (b)

Fig. 3. (a) The microwave cavity used to assess the dielectric characteristics of the lipids, and (b) a simulation of the cavity showing TM_{010} mode, where the electric field is centred in the cavity at approximately 1.75 GHz

4 Results

Fig. 4 shows the relative dielectric constant plotted against the dielectric loss to represent the complex permittivity of vegetable oils at approximately 1.75 GHz. This is in general agreement with previous research that calculates the dielectric constant of vegetable oils to be 3.05 to 4.6 [20].

Table 1. Dielectric characteristics of vegetable oil

Veg. Oil	ε' (ω)	Std. Deviation	ε'' (ω)	Std. Deviation	tan δ	Std. Deviation
Grapeseed	3.014	0.0121	0.073	0.0005	0.024	0.0002
Groundnut	2.991	0.0119	0.066	0.0017	0.022	0.0007
Olive	3.004	0.0038	0.063	0.0005	0.021	0.0002
Sunflower	3.005	0.0115	0.069	0.0009	0.023	0.0003

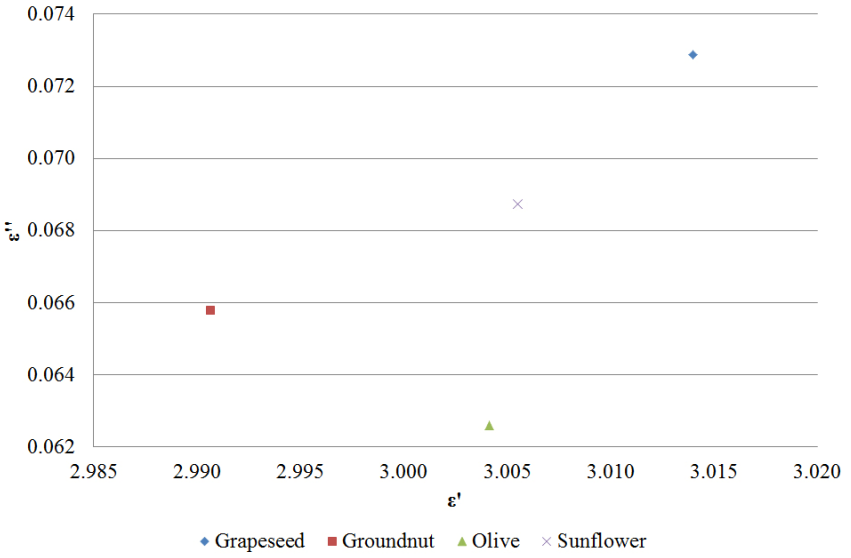

Fig. 4. Complex permittivity of Grapeseed, Groundnut, Olive and Sunflower Oil

Fig. 5 shows the relative dielectric constant and dielectric loss of olive oil suspensions. As the concentration of olive oil decreases within the suspension, both the dielectric constant and dielectric loss increase up to 27 and 2.5 respectively.

In Fig. 6 the dielectric loss was plotted against the relative dielectric constant representing the complex permittivity. As the concentration of lipid droplet increases and the YEPD media inversely decreases, the permittivity of the sample decreases. Detailed results are shown in Table 1 and 2.

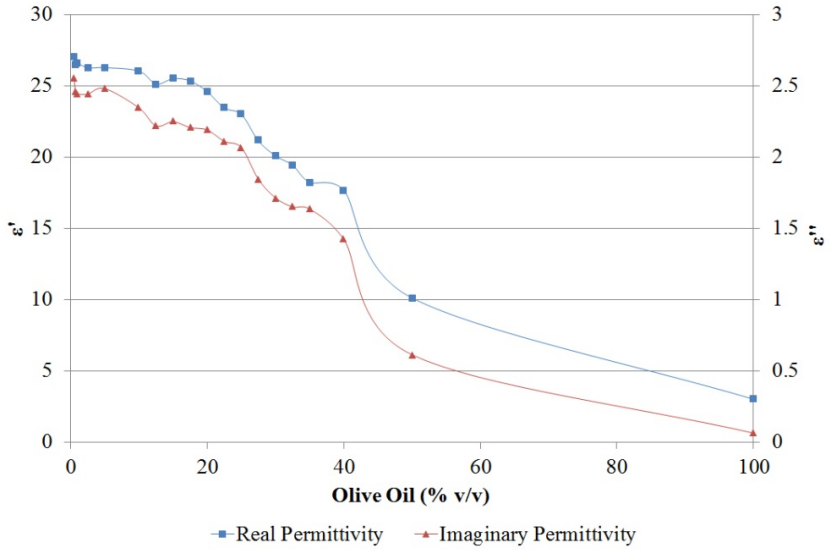

Fig. 5. Graph showing a decrease in relative dielectric constant and dielectric loss as the concentration of olive oil increases

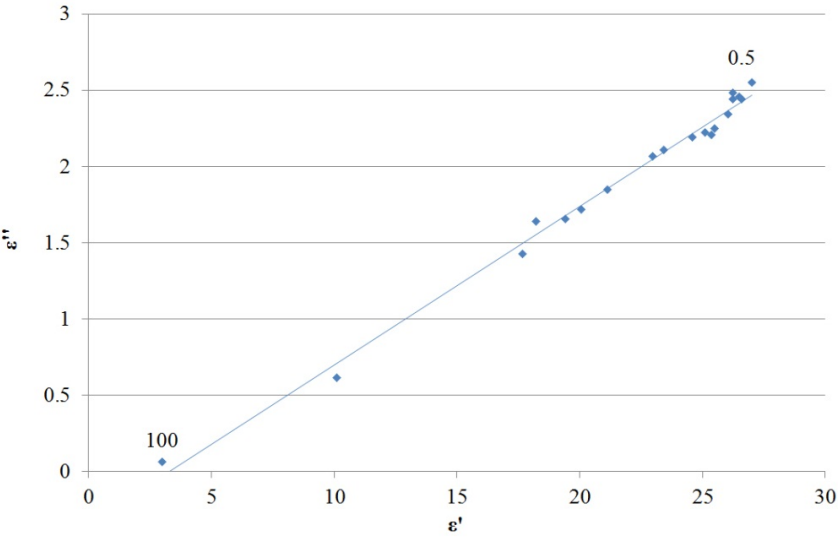

Fig. 6. Plot of relative dielectric constant against dielectric loss to represent complex permittivity. Each data point indicates a concentration of olive oil suspension with oil concentration decreasing as the complex permittivity increases

Table 2. Dielectric characteristics of lipid droplet samples

Olive Oil (% v/v)	ε' (ω)	Std. Deviation	ε'' (ω)	Std. Deviation	tan δ	Std. Deviation
100	3.004	0.0038	0.063	0.0005	0.021	0.0002
50	10.106	1.6102	0.612	0.1652	0.059	0.0054
40	17.658	1.5520	1.423	0.1675	0.080	0.0044
35	18.215	1.1339	1.635	0.0467	0.090	0.0031
32.5	19.423	1.0756	1.650	0.1395	0.085	0.0029
30	20.078	0.9285	1.714	0.1394	0.085	0.0032
27.5	21.138	0.0118	1.844	0.0017	0.087	0.0006
25	22.992	0.6427	2.066	0.0678	0.090	0.0020
22.5	23.434	0.9851	2.110	0.1027	0.090	0.0014
20	24.585	0.3151	2.190	0.0256	0.089	0.0016
17.5	25.336	0.4128	2.206	0.0606	0.087	0.0014
15	25.489	0.2968	2.247	0.0365	0.088	0.0005
12.5	25.118	0.2618	2.217	0.01400	0.088	0.0005
10	26.028	0.3046	2.345	0.0733	0.090	0.0034
5	26.269	0.2545	2.480	0.1030	0.094	0.0033
2.5	26.256	0.3081	2.441	0.0271	0.093	0.0018
1	26.588	0.4961	2.441	0.1034	0.093	0.0052
0.75	26.504	0.0118	2.453	0.0017	0.093	0.0006
0.5	27.024	0.3939	2.549	0.0343	0.094	0.0019

5 Discussion

This experiment has shown that differing conformations of TAG and different concentrations of lipid droplets can be distinguished based on the electromagnetic properties of the suspensions. The differing concentrations cause a frequency shift indicating a change in dielectric constant and losses of the samples at this frequency range. However, the molecular and structural composition, interactions between molecules, interfaces between substrates and the frequency employed must be considered as to the contribution to the dielectric qualities of the samples under test.

A range of vegetable oils were used to investigate how varying proportions of TAG species affected the dielectric characteristics. Groundnut oil, which is relatively low in mono-unsaturated TAGs (21%), has a relative dielectric constant of 2.991 while grapeseed oil with comparatively higher concentrations of mono-unsaturated TAGs (53%) has a dielectric constant of 3.014. This is in agreement

with literature that reports an increase in dielectric constant as the proportion of mono-unsaturated TAGs increases.

When the oil mixtures are agitated, the oil does not dissolve into the YEPD media. Instead the hydrophobic oil converges into lipid droplets resulting in a colloidal sample. At lower frequencies (MHz region) charge builds up at the interface of the separate phases known as the Maxwell-Wagner effect and is responsible for the β-dispersion. At the frequency of this experiment however it is likely that the major influence to relative complex permittivity is attributable to the organic and ionic content of the YEPD media. The media contains a combination of molecules necessary for yeast culture namely carbohydrates (sugars), amino acids (protein) and minerals (salt). Such molecules are well known to interact in aqueous solution, lowering the relaxation frequency of the water molecules into roughly the lower GHz frequency range [21]. This loss of polarisation is known as the δ dispersion attributable to the rotation of molecular side chains and bound water. Increasing the proportion of media increases the amount of material that can be polarised increasing the amount of energy that can be stored by the sample.

After agitation, as the sample is introduced to the cavity the lipid droplets begin to converge into larger droplets until the lipid begins to separate into a different phase resting on the YEPD media. This results in the lipid droplet surface area being lower than the newly agitated suspension. As this process occurred, a decrease in the perturbation frequency was noted signifying a decrease in permittivity. Therefore, it is probable that a change to the β dispersion, due to the decreasing lipid droplet surface area, may contribute to the complex permittivity of the sample at this frequency. Acquiring data periodically from agitation to phase separation could be carried out to investigate the consequence of a changing droplet surface area. Stabilisation of the lipid droplets using phospholipids would improve the homogeneity of the suspensions also improving measurement repeatability.

6 Conclusions

This research proposes a novel, non-invasive diagnostic approach for the detection of neoplasmic growth. The aim of the research has been to develop a microwave sensor and methodology to assess the lipid profile of yeast cultures. Experiments conducted so far have validated the applicability of the method for detecting lipid accumulation in biological cells using a lipid droplet model.

The technique may in the future be adapted for use with mammalian cell cultures and, finally, isolated cells from the body. The approach has the potential to be fast, safe and relatively inexpensive allowing a commercialised product to be easily rolled out across healthcare facilities.

As part of on-going work, a method has been devised to reliably insert a test sample into an EM field generated by a small microwave frequency sensor. The method utilises a platform with an engraved grid pattern into which a microtitre plate can be slotted. The microtitre plate can then be repositioned so each of the wells will be interacting with the sensor. The platform in Fig. 7 is designed for 24

well plates. The sensor mounting is composed of a recess cut into the platform. Realised sensors can be secured into the sensor mounting of the platform allowing the performance of different sensors to be evaluated under similar conditions. Further work may also consider the implication of environmental factors such as temperature and humidity which may influence sensor response.

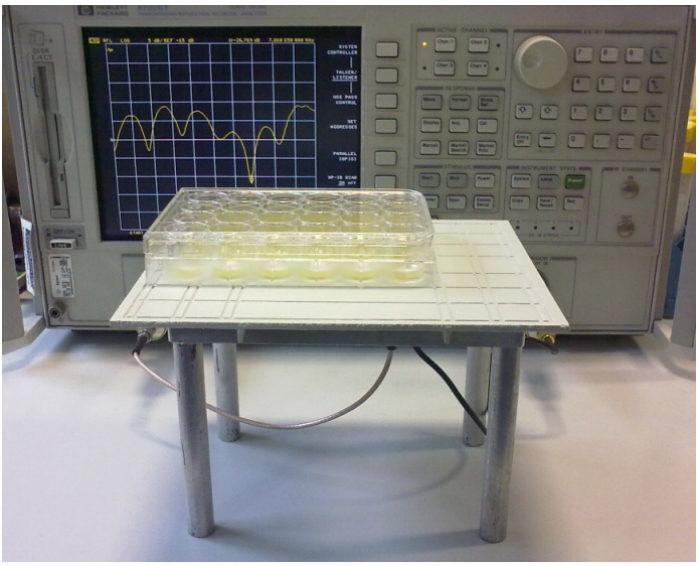

Fig. 7. On-going advancement of work to consider alternative format microwave sensors applicable for use with cell cultures presented in microtitre plates

References

[1] Ott, J.J., et al.: The importance of early symptom recognition in the context of early detection and cancer survival. European Journal of Cancer 45, 2743–2748 (2009)
[2] Schwarzer, R., et al.: Changes in finding benefit after cancer surgery and the prediction of well-being one year later. Social Science & Amp; Medicine 63, 1614–1624 (2006)
[3] Rustin, G.J.S., et al.: Early versus delayed treatment of relapsed ovarian cancer (MRC OV05/EORTC 55955): a randomised trial. The Lancet 376, 1155–1163 (2010)
[4] Mhaskar, A.R., et al.: Timing of first-line cancer treatments – Early versus late – A systematic review of phase III randomized trials. Cancer Treatment Reviews 36, 621–628 (2010)
[5] Lerique, B., et al.: Triacylglycerol in biomembranes. Life Sciences 54, 831–840 (1994)
[6] Balogh, G., et al.: Lipidomics reveals membrane lipid remodelling and release of potential lipid mediators during early stress responses in a murine melanoma cell line. Biochimica et Biophysica Acta (BBA) - Molecular and Cell Biology of Lipids 1801, 1036–1047 (2010)

[7] Abdou, A.A., et al.: A Review of Underwater EM Wave Propagation to Investigate the Development of a Through Water WSN. Presented at the Built Environment and Natural Environment (BEAN) 2011, Liverpool, UK (2011)
[8] Bozza, P.T., Viola, J.P.B.: Lipid droplets in inflammation and cancer. Prostaglandins, Leukotrienes and Essential Fatty Acids 82, 243–250 (2010)
[9] Warnick, G.R., Nakajima, K.: Fasting versus Nonfasting Triglycerides: Implications for Laboratory Measurements. Clinical Chemistry 54, 14–16 (2008)
[10] Hokanson, J.E., Austin, M.A.: Plasma triglyceride level is a risk factor for cardiovascular disease independent of high-density lipoprotein cholesterol level: a meta-analysis of population-based prospective studies. J. Cardiovasc. Risk 3, 213–219 (1996)
[11] Markx, G.H., Davey, C.L.: The dielectric properties of biological cells at radiofrequencies: applications in biotechnology. Enzyme and Microbial Technology 25, 161–171 (1999)
[12] Sun, T.-P., et al.: The use of bioimpedance in the detection/screening of tongue cancer. Cancer Epidemiology 34, 207–211 (2010)
[13] Kerhet, A., et al.: A SVM-based approach to microwave breast cancer detection. Engineering Applications of Artificial Intelligence 19, 807–818 (2006)
[14] Bellorofonte, C., et al.: Non-Invasive Detection of Prostate Cancer by Electromagnetic Interaction. European Urology 47, 29–37 (2005)
[15] Jerzy, K.: Frequency domain complex permittivity measurements at microwave frequencies. Measurement Science and Technology 17, R55 (2006)
[16] Grosse, C., Delgado, A.V.: Dielectric dispersion in aqueous colloidal systems. Current Opinion in Colloid & Interface Science 15, 145–159 (2010)
[17] Sheen, J.: Measurements of microwave dielectric properties by an amended cavity perturbation technique. Measurement 42, 57–61 (2009)
[18] Verma, A., Dube, D.C.: Measurement of dielectric parameters of small samples at X-band frequencies by cavity perturbation technique. IEEE Transactions on Instrumentation and Measurement 54, 2120–2123 (2005)
[19] Sheen, J.: Study of microwave dielectric properties measurements by various resonance techniques. Measurement 37, 123–130 (2005)
[20] Cataldo, A., et al.: Quality and anti-adulteration control of vegetable oils through microwave dielectric spectroscopy. Measurement 43, 1031–1039 (2010)
[21] Grant, E.H., et al.: Dielectric behavior of water in biological solutions: Studies on myoglobin, human low-density lipoprotein, and polyvinylpyrrolidone. Bioelectromagnetics 7, 151–162 (1986)

Dielectric Properties of Wood for Improved Internal Imaging

W.S. Holmes[1], S.C. Mukhopadhyay[2], and S.G. Riley[3]

[1] Dept of Electrotechnology
Unitec Institute of Technology,Auckland, New Zealand
wholmes@unitec.ac.nz
[2] School of Engineering and Advanced Technology
Massey University, Palmerston North, New Zealand
S.C.Mukhopadhyay@massey.ac.nz
[3] Wood and Biofibre Technologies
Scion,Rotorua, New Zealand
Steve.riley@scionresearch.com

Abstract. This paper describes the measurement of the dielectric properties of the typical log features of Heartwood, Sapwood and internal Branches. Measurements were made using the waveguide cell technique covering the frequency range of 2.3 to 6.5GHz. This has shown that for the desired contrast between heartwood and Sapwood to be achieved the imaging system must operate above 4GHz. Additional work was undertaken to establish a method to correct these measurements for variations in basic density and Earlywood\Latewood banding, giving rise to a potential moisture content estimation error of 0.63%. This will lead to improved spatial location of features of interest.

1 Introduction

The cost of any manufacturing process can be minimized by assessing the raw material quality at the earliest possible stage. In the case of the timber industry, assessment of log quality would be most ideally performed in the forest. At this early stage, logs could be graded and assigned to the most appropriate timber processor and so leading to optimized use of the timber resource.

When a tree is pruned at six years the branches and high-density timber remain within the tree at time of harvest. This defect core affects the strength and stability of the final lumber and it is desirable to process this defect core separately. Currently there is no means of detecting the defect core within the log at the time of breakdown and this result in an inferior product. This has been one of the prime motivators behind many forestry companies ceasing to prune its trees and move to re-engineered timber products. The second problem of compression wood has a similar effect but is caused primarily by the tree growing in a fashion where it is leaning, such as when planted on banks.

The development of internal imaging systems provide the saw-miller with information about the interior of the log which will have the effect of improving

S.C. Mukhopadhyay et al. (Eds.): Advancement in Sensing Technology, SSMI 1, pp. 93–104.
springerlink.com

lumber quality (both strength and stability) and maximise the economic return from the log to the processor by reducing wastage.

Timber quality is influenced by structural defects in the log as well as material properties such as basic density (density of dry matter) and moisture content (mc). Many inspection procedures exist to assess structural defects on logs using either visual techniques or measured at the time of felling. Current techniques to measure basic properties of logs are of limited accuracy and so of limited use to the timber processor.

1.1 Microwave Imaging

The development of electromagnetic and microwave systems for the interior imaging of logs has been ongoing for many years. Commercial Ground Penetrating Radar (GPR), Microwave Tomography and Synthetic Aperture Radar systems (SAR) have been employed in these studies. Whilst all of these have shown promise and can reveal features within the log, they all suffer from the same problems of poor image contrast and spacial resolution.

The use of existing commercial GPR system has become the most common tool used by researchers to investigate the possibilities of such imaging systems. Such systems operated around the 1000GHz region and are designed to be portable allowing ease of trialing in the field. One such study undertaken by Parker (2006) applied this technique to logs for the detection of internal branching with some success. In this trial a third of internal branches were detected and accurately positioned, a third were detected but not accurately located, and the remainder were unseen by the technique. An example of the resulting log images from this trial is shown below in figure1.

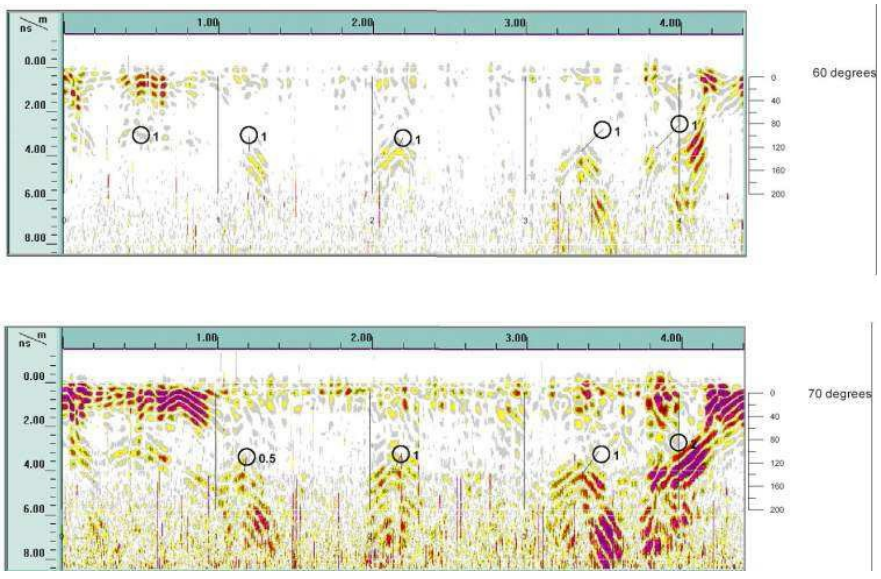

Fig. 1. GPR image of sample Log

In order to improve the performance of these systems and locate features such as Sapwood, Heartwood and internal branches, a more detailed study of the dielectric properties of these log components is needed. An additional obstacle for such systems is that from the time the tree is cut down up to the time of scanning, the logs moisture is being lost and hence the dielectric properties within the log are changing.

Considerable work has been performed in the application of microwave energy to sawn lumber for the determination of grain angle, defects and knot locations. Microwave sensing systems such as those developed by King (1985), Skaar (1972) and Holmes (2011) rely on the transmission and reflection characteristics of sawn timber, but little or no effort has been expended into examining how microwave sensing would perform on unprocessed timber.

Electromagnetic sensors essentially measure either the energy transmitted or reflected back from a material. The composition and structure of the material give rise to a measurable signature that then can be related to other physical properties such as moisture content or density. This defines the microwave signature of a material arises from a physical constant known as permittivity, (dielectric constant) which relates the electric flux density (**D**) illuminating the material to the electric field strength intensity (E), inside the material. Often the permittivity of a material is expressed as a multiplier of the permittivity of free space ($\boldsymbol{\varepsilon_0}$) and is then known as relative permittivity ($\boldsymbol{\varepsilon_r}$). **D** and **E** are both vector quantities and contain both phase and magnitude information.

$$\overline{D} = \varepsilon_o \cdot \varepsilon_r \cdot \overline{E}$$

The magnetic field component of the microwave energy similarly has a physical constant of permeability but only ferrous materials have a relative permeability of greater than one and in the context of the types of measurements undertaken in this work, it will always be assumed to be one.

As wood is an anisotropic media for the propagation of electromagnetic waves, the energy reflected and transmitted are highly dependent upon the grain angle, basic density and moisture content (which would attenuate the transmitted wave in the timber). Both the grain angle and moisture content of the internal branch stubs are considerably different from the surrounding sapwood; this suggests that the energy incident upon the branch stub would show as a significant feature within the image. As the timber in the sapwood region without knots has a grain angle which is orthogonal to the incident electric and magnetic fields, and higher moisture content, hence much of the microwave energy is reflected back towards the source.

1.2 Practical Considerations

Many factors affect how electromagnetic energy interacts with timber. Grain angle, the heterogeneous structure of wood, density and moisture content, all effect the measurements. If possible, variation due to the properties which are not of interest must be either eliminated or minimized.

Studies into the application of microwaves to the imaging and measurement of timber properties have been performed have primarily been confined to examination of timber that has been dried to below the fibre saturation point (FSP). Work performed by King (1985) showed that below the FSP, effects due to basic density are small compared to the dominant mc effects, but however are still measurable.

Extracting the density information requires that the anisotropic nature of the wood due to early wood / late wood (EW/LW) bands be minimized. As grain angle will introduce marked effects on the reflected microwave energy, it is desirable to select a measurement site at which the grain angle could be considered to be normal to the plane of incidence. In the case of logs, applying energy into the side of the log will fix the EW/LW boundaries as orthogonal to the plain of incidence.

To reduce the effects of the non-homogeneity of timber due to the EW/LW bands, a sensor structure is required which will interact with a large volume of wood to perform an averaging function. A suitable sensing structure to perform this averaging task is an open-ended waveguide. This is a radiating structure which, as well as interacting with a larger sample surface area, will also allow for microwave energy to penetrate significantly into the sample.

A second factor which will have a direct influence on the microwave measurement is moisture content. In the case of the freshly felled logs, we have assumed that the moisture content can be considered constant and hence basic density will become the dominant factor influencing the measurement. Details underlying this assumption can be found in a paper by Cown (1992).

To determine the characteristics of various structural features of logs, a series of experiments were conducted. A permittivity survey of Pinus radiata bark types using an open ended coaxial probe showed that the variation in permittivity between different bark types (eg. clumpy and slimy barks) was large. In addition, the survey showed that the electromagnetic loss factor of the bark material was extremely high which would suggest that much of the incident energy would be attenuated in the bark rather than the woody tissue itself. For these reasons, it was determined that for performing microwave measurements of logs it would be desirable for the bark to be removed.

1.3 Coupling Microwave Energy into the Log

If we consider the log to act as a dielectric rod then any incident electromagnetic energy tends to be contained within the tree and little energy radiates externally. In particular the incident wave is focused towards the centre of the tree. This focusing effect of the energy has been described by Keam (1994) for an infinite dielectric rod, and Neelakantaswamy (1973) in the construction of antennas with much reduced side lobes. In the case of the high moisture content living tree, the electromagnetic waves are focused within the tree and are quickly attenuated within the tree and little is re-radiated. This effect is desirable in this application as scatterers external to the log have little effect on the measured fields.

2 Permittivity Measurments

The following presents the methods and results of a series of microwave permittivity measurements performed on timber samples taken from freshly felled logs. From each of three logs, samples of heart, Sap and Branch wood were taken and dimensioned to fit into waveguide cells. This work is the first step in the development and understanding of the potential of microwave based systems in the imaging of freshly felled logs.

Waveguide cell measurements were selected as the best means to provide the bulk permittivity of the various types of wood, this was due to the fact that both transmission and reflection data is measured. As Wood is anisotropic in nature the waveguide cells were designed in a square cross-section allowing the samples to be cut as cubes. The cubic samples could then be rotated and measured to allow us to see this anisotropic effect in the measured results.

Waveguide cells were fabricated to cover the 2.3 to 4.2 GHz band, and other cells to cover the frequency range 4.5 to 9 GHz. As the waveguide cells are square in cross section, the possibility of more than one mode of wave propagation exists. Within our measured data this effect did occur once the cell length exceeded a half wavelength within the material, and hence the presented results show only the single moded region from 2.3 to 3 GHz for cell 1 and 4.5 to 6.5 GHz for cell 2.

The measurements were undertaken using an Agilent PNA vector network analyzer and each sample was weighed after measurement. The PNA is a two port device which allowed the measurement of microwave reflection and transmission coefficients. Using these measured microwave parameters the permittivity was calculated using the standard Nicholson-Ross-Wier (1968) algorithm.

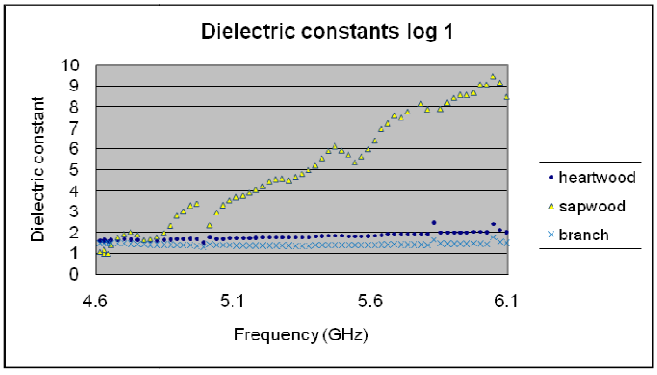

Fig. 2. Dielectric constant of wood types in sample log 1

The Dielectric constants (real part of permittivity) of both Branch and Heart wood at the frequencies measured are similar. The Loss Factor of both Branch and Heart wood whilst similar shows some small frequency dependence in the Branch wood which is not apparent in the Heart wood. As the reflection from the

boundary of two media comprises both dielectric constant and loss factor there should be a small but still measurable reflection between Branch and Heartwood

The Sapwood samples showed that at the lower band 2.3-3 GHz region, the measured dielectric constant and loss factor to be low, so as to make the sapwood almost transparent in a image. Both the dielectric constant and loss factor showed, as expected, a frequency dependence increasing rapidly as we approach 10GHz due to the large free water component within the sapwood structure.

3 Density Effects

This section looks at the effect of basic density on the accuracy of the wood measurements and examines potential methods to compensate for its impact.

3.1 Dielectric Models

The initial approach to accounting for density variations was to develop a model that describes the dielectric behavior of a material by using the permittivity of the individual constituents. The most commonly used model would be a volumetric one, which simply sums the permittivity of each part, multiplied by its fraction of the volume. Hence, a simple model would be the permittivity of dry wood plus water plus air. Then using the frequency dependence of the sum (usually the water component as the permittivity of air and solids change slowly with frequency) the individual volume fractions of each constituent can be determined.

$$\varepsilon = \varepsilon_{water} \cdot V + \varepsilon_{wood} \cdot (1 - V)$$

Where V is the volume fraction of water in the mixture. This simplistic model can then used to determine the moisture content from the measured

$$V = \frac{\varepsilon - \varepsilon_{wood}}{\varepsilon_{water} - \varepsilon_{wood}}$$

Hence the moisture content by percentage dry basis can be found as

$$mc = \frac{V}{1 - V} \cdot 100 \quad (\%)$$

In this work, both the published data and the experimental permittivity data were measured. Figure 3 shows that the permittivity of wood below 33% moisture content, the Fibre Saturation Point (FSP), is essentially constant over the 4 to 8 GHz range. In essence, the remaining water within the wood structure is so tightly bound that it no longer contributes significantly to the dielectric losses. This gives wood below FSP a very slow variation in dielectric properties with frequency.

Without any change in permittivity, the model approach cannot be considered a useful approach for removing the basic density effect.

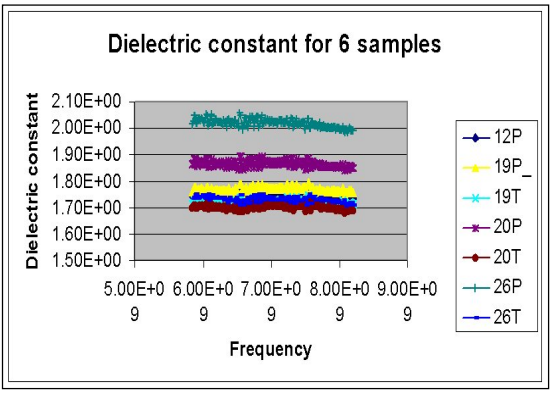

Fig. 3. Dielectric constant versus Frequency for 6 samples

3.2 Density Independent Function

An alternative approach is to use the density independent function developed at the USDA by Trabelsi and Nelson. This is a commonly used method for microwave sensors to remove the effect of density from their measurements. The universal permittivity based method for determining moisture content independent of density was reported by Trabelsi (2003)and has the form

$$\Psi = \sqrt{\frac{\varepsilon''}{\varepsilon'\cdot\left(a_f\varepsilon' - \varepsilon''\right)}}$$

Where a_f is a constant that is a function of frequency and the resulting function Ψ varies linearly with moisture content.

Figure 4 shows the density independent function versus moisture content for a range of wood densities spanning 300 to 700 KG/m3 using data from Torgovnikov(1993). It can be easily seen that as the moisture content drops below the FSP, the function no longer accounts for the density variation.

The explanation for the failing of the density independent function is in the nature of the water binding below the FSP. The water in this region is heavily bound in the structure of the wood and the dielectric properties of the water approach that of ice. This means that the remaining water no longer contributes significantly to the dielectric losses, and the loss factor (ε") becomes small.

However, what this figure does show is that above the FSP we can easily negate the effects of density and accurately extract the moisture content. This in turn would also let us accurately determine the density so that it can be used later as a correction in measurements below the FSP.

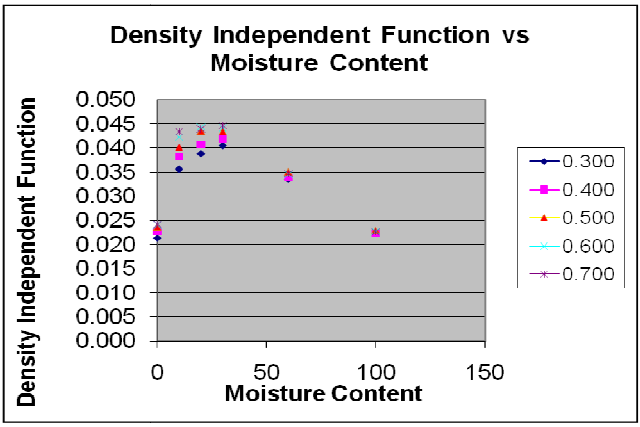

Fig. 4. Density independent function versus moisture content for published data

Using the fact that we can use the density independent function in the earlier phases of drying to determine the basic density, we can apply this as a correction to the measurements made below the FSP.

The plot in Figure 5 shows the experimental measurements made on 12 samples at 10% moisture content. The two solid lines represent published data for 400 and 300 kg/m3 respectively, the measurement data ranges from 340 to 440 Kg/.m3.

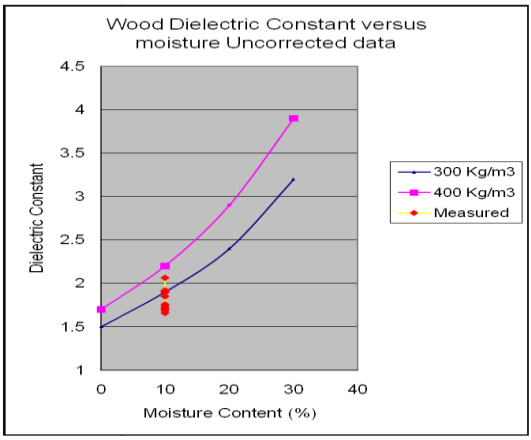

Fig. 5. Moisture content versus dielectric constant with no density correction

The degree in spread of the data, if density was not known, would yield an RMS error in moisture content estimation of 3.59% with a mean of 0.2%. If we now correct the data using the density previously determined, in this case normalize to 300KG/m3, the resulting Figure 6 is found. This yields an RMS error of 1.38% with a mean of 0.012%.

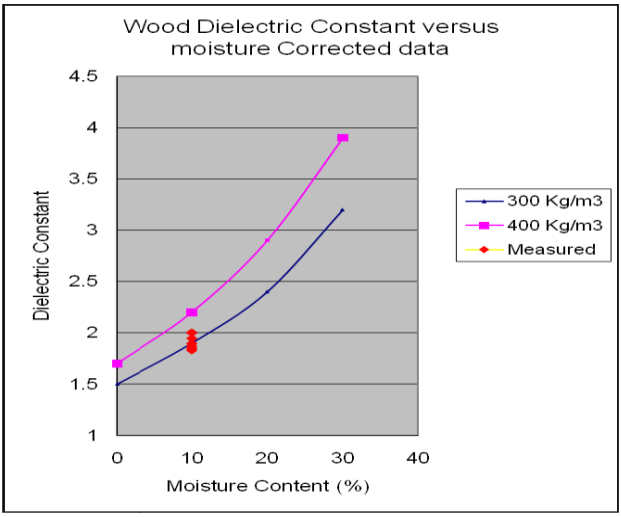

Fig. 6. Density corrected dielectric constant versus moisture content

This figure shows an improved result however, there still exists a significant error (> 1%).The normalization process is simple as the variation due to density is a simple linear function, as shown in Figure 7. In this Figure measured data is from all measurements made and the trend line comes from those published by Torgovnikov (1993) for moisture contents of 10%.

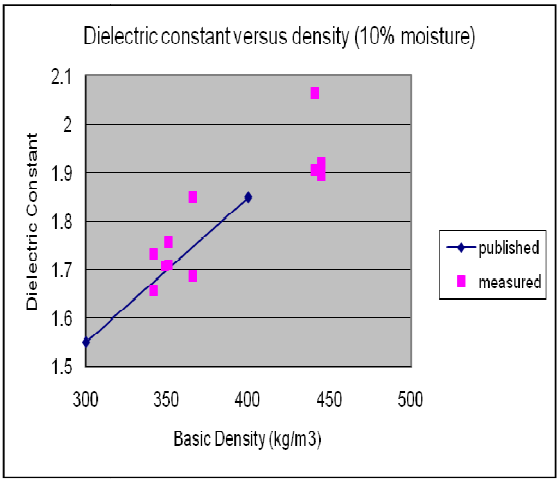

Fig. 7. Dielectric Constant versus Basic Desity

Although he does not directly mention the effect of the early wood late wood layer orientations, Torgovinikov (1993) does present measurements on polarization of the applied field and also the ratio of Early wood (EL) to Late wood (LW). The following section looks at the effect of this EW/LW layer orientation on the permittivity of wood.

4 EarlyWood/LateWood Layer Orientation

The following section looks at the effect of Earlywood /Latewood (EW/LW) layer orientation on inferring moisture content from permittivity measurements.

Wood has an anisotropic structure that arises from the cell pattern laid down in a defined direction by seasonal changes while the tree is growing. This EW/LW layering has the effect of ducting the microwave energy in a preferred direction

The change in polarization of the microwave fields due to EW/LW layering has given rise to many systems proposed for the measurement of grain angle. One such system was developed by King (1985), which involved a rotating antenna that used the angle of the antenna and a maximum in the received signal to determine the grain angle of lumber.

This EW/LW experiment (Figure 8) showed the cyclic variation in permittivity due to the EW/LW regions. The step change is due to the second sample having a significantly higher basic density. This graph does demonstrate the difference in permittivities of EW and LW. Holmes (2011) undertook coaxial probe permittivity measurements, which were made on a number of sawn lumber samples. The measurements where made every 5mm and the permittivity for two samples was plotted versus distance across the sample to produce figure 8.

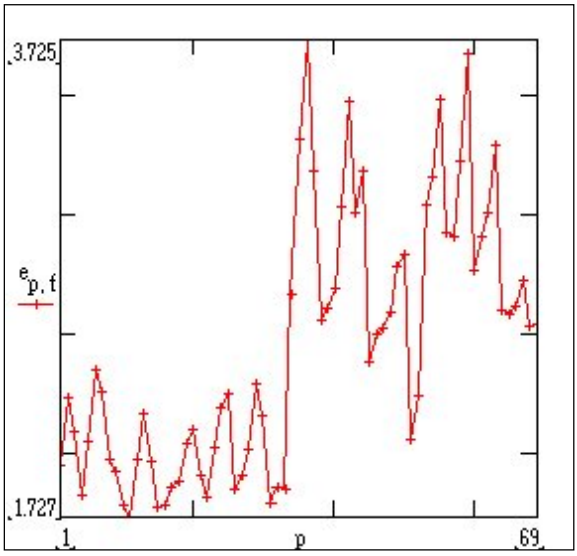

Fig. 8. EWLW variation across wood sample

The measurements undertaken in the previous sections purposefully covered the full range of EW/LW layer orientations so as to reflect flat, intermediate and quarter sawn lumber.

Hence to examine the effect of this, the data covering flat and intermediate sawn were chosen to repeat the error analysis. Figure 9 below using only this data shows that the RMS error in moisture content using density correction is now reduced to 0.63%.

Hence, we can see that much of the residual error in the previous section can be demonstrated to be due to the effect of EW/LW layer orientation.

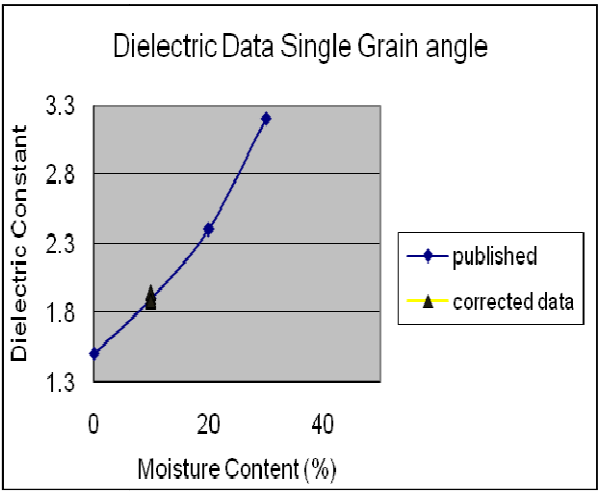

Fig. 9. Density corrected measurements for flat and quarter sawn samples

5 Conclusions

These experiments have provided us with the bulk permittivity data for various log samples and wood types, whilst averaging out the effects of smaller structural effects such as basic density and EW/LW bands.

In order to achieve a useful image with sufficient contrast we require that the differing structures have permittivity's which are sufficiently different. These differences will create a significant reflection at the media boundaries. From this work, we have shown that measurements at frequencies greater than 4GHz is required to clearly differentiate between Sapwood, branches and Heartwood

Resolution is also an issue in microwave images, which is usually handled by either increasing frequency and/or frequency bandwidth or by performing multiple measurements separated spatially as in Synthetic Aperture Radar.

The permittivity difference between early and late wood is large and if an imaging system has sufficient resolution then these structures will be clearly visible in the image.

Penetration into a media is also a commonly held concern as the moisture present in the material is seen to absorb the microwave energy. However, little attention is given to the manner in which the water molecule is bound within the material, and as this work has shown it gives rise to a lower attenuation than expected.

This work has also shown that there is the potential to accurately determine the moisture content of the log, whilst catering for the large variation in basic densities. This has the benefit of allowing for spatial corrections to be made to the image and hence the accurate positioning of features of interest, such as internal branches and the heart sapwood boundary.

Acknowledgment. The Authors would like to thank Scion and its staff for funding this work and their work on sample gathering and preparation.

References

1. King, R.J.: Microwave electromagnetic nondestructive testing of wood. In: Proceedings, Fourth Nondestructive Testing of Wood Symposium, Vancouver, August 28-30, pp. 121–134 (1978)
2. King, R.J., et al.: A Microwave Method for Measuring Moisture Content, Density, and Grain Angle of Wood. USDA Research Note FPL-0250 (March 1985)
3. Skaar, C. (ed.): Water in Wood. Syracuse Wood Science Series, vol. 4, pp. 171–204. Syracuse University Press (1972)
4. Holmes, W., Cown, D.: Microwave Density Measurement of Standing Trees. In: Proc. 9th Conf. on Electromagnetic Wave Interaction with Water and Moist Substances, ISEMA, pp. 39–41 (June 2011)
5. Parker, R., Roper, J., Watson, M.: Radar scanning on green pruned logs. In: Proc. SCANTECH 2006, pp. 51–58. FIEA, Australia (2006)
6. James, W.L.: A microwave method for measuring moisture content, density, and grain angle of wood. USDA Research Note FPL - 0250 (March 1985)
7. Trabelsi, S., Nelson, S.O.: Dielectric methods for multiparameter microwave sensor. In: Proc. 5th ISEMA Conf. 2003, pp. 56–62 (2003)
8. Torgovnikov: Dielectric Properties of wood and wood based materials. Springer (February 1993) ISBN-10: 0387553940
9. Holmes, W., Cown, D.: Microwave Density Measurement of Standing Trees. In: Proc. 9th Conf. on Electromagnetic Wave Interaction with Water and Moist Substances, ISEMA, pp. 39–41 (June 2011)
10. Nicolson, A.M., Ross, G.F.: Measurement of the intrinsic properties of materials by time domain techniques. IEEE Trans. I&M IM-17, 395–402 (1968)
11. Keam, R.B.: Plane Wave Excitation of an Infinite Dielectric Rod. IEEE Microwave and Guided Wave Letters 4(10), 326–328 (1994)
12. Neelakantaswamy, P.S., Banerjee, D.K.: Radiation Characteristics of Waveguide - Excited Dielectric Spheres with Matched Sphere-Air Boundary. Electronic Letters 9(2), 40–41 (1973)

Laser-Induced Breakdown Spectroscopy Measurements for Dielectric Materials and Metals

S. Ikezawa, M. Wakamatsu, and T. Ueda

Graduate School of Information Production and Systems
Waseda University, Kitakyushu, Fukuoka, Japan
ikezawa@y.fuji.waseda.jp

Abstract. This chapter describes an optical sensing system for elemental analysis using laser-induced electro-avalanche fluorescence on wide bandgap materials, and laser-induced plasma on metal objects. This method of measurement and analysis is called "laser-induced breakdown spectroscopy" (LIBS). In LIBS, the vaporizing and exciting plasma is produced by high-powered focused laser pulses. Pulses from a laser are focused on the sample using a lens, and plasma emission light is collected and collimated using a second lens. The light is transported to a wavelength selective device on the spectrograph, and recorded time-resolved, or gate setting, devices to improve the signal-to-noise and signal-to-background ratio. This provides discrimination against interference from an emission continuum, called "bremsstrahlung." Plasma light is initially dominated by a white light continuum, that has little intensity variation as a function of wavelength because of bremsstrahlung and radiation from the plasma as free electrons and ions recombine in the plasma cooling process. If the emission is recorded over the entire time, this light continuum seriously interferes with the detection of weaker emissions from atomic species. For this reason, temporal resolving measurement is carried out using LIBS. This chapter introduces a LIBS system applied to wide-bandgap materials like sodium, and metal objects containing small metal particles.

1 Introduction

A cardinal study of laser-induced breakdown spectroscopy (LIBS) is that of F. Brech and L. Cross, titled "Optical microemission stimulated by a ruby laser" and published in 1962 [1], only two years before experiments using ruby lasers were conducted by T. H. Maiman. The acronym "LIBS" has been used for approximately twenty years less than the acronym "LASER." In 1983, the pioneering spectroscopic investigation in which laser spark emissions were used for elemental analysis was conducted by D. A. Cremer and L. J. Radziemski at the Los Alamos National Laboratory. They coined the name "Laser-Induced Breakdown Spectroscopy" for this technique, in which the spectra of laser-produced plasma were used for spectrochemical analysis. Since the 1980s, LIBS has been extensively investigated for environmental monitoring [2-9], forensics [10],

S.C. Mukhopadhyay et al. (Eds.): Advancement in Sensing Technology, SSMI 1, pp. 105–120.
springerlink.com

biological identification [11], industrial applications [12, 13], works of art [14, 15], and planetary applications [16-31]. LIBS is a useful technology that can be used to determine the distinct spectral signatures of almost all chemical species in various environments. A high-energy laser pulse is focused on, or inside, the sample to create plasma. Emissions from the atoms and ions in the plasma are collected using lenses, guided toward a spectrograph capable of recording spectra over a wide range of wavelengths, and characterized using a time-resolved analysis. LIBS is considered to be in the same category as atomic emission spectroscopy (AES). Some of the well-known AES methods for vaporization and excitation include arc/spark spectrometry, direct-coupled plasma (DCP) spectrometry, inductively coupled plasma (ICP) spectrometry, microwave-induced plasma (MIP) spectrometry, and laser ablation inductively coupled plasma mass spectrometry (LA-ICP-MS). These methods typically require laboratory-scale analytical facilities. LIBS has the advantage of being a compact and simple system for determining the elemental composition of various materials, regardless of their physical state (solid, liquid, or gas), and it requires no pre-processing. By selecting the laser of the correct wavelength to permeate measured materials, LIBS is able to analyze the elemental component of the inside, separate it from the surface component as well as to obtain the depth profile. Despite the advantage of using a qualitative analysis, LIBS is often limited as an elemental analysis technique when compared to other AES methods because it displays instability with higher intensity signals, and provides insufficient recovery countermeasures to reproducible quantitative analysis errors.

2 Electron Orbit and Quantum Number

According to Bohr's theory of atomic structure, light with a frequency v should be considered as a photon with an energy hv. Planck's constant $h \approx 6.63\times10^{-34}$ J•s. The transition energy of an electron stationary state from E_n to $E_{n'}$ is determined by

$$\nu = \frac{E_n - E_{n'}}{h} = \frac{2\pi^2\kappa^2 me^4}{h^3}\left(\frac{1}{n'^2} - \frac{1}{n^2}\right)$$

where κ is Coulomb's constant ($\kappa = 1/4\pi\varepsilon_0 \approx 8.99$ N•m^2•C^2), m is electron mass ($m \approx 9.11\times10^{-31}$ kg), and e is the quantum of electricity ($e \approx 1.60\times10^{-19}$ C).

As presented above, the electron orbit is considered to be a circle. When the electron orbit is regarded as elliptical, a radial component r and an azimuthal component are required. Corresponding to these two components, two quantum conditions are required. One is the main quantum number n, which corresponds to the radial component in the elliptical orbit. The other is the azimuthal quantum number l, which corresponds to the azimuthal component. The relationship between n and l is described by

$$l = 0, 1, 2, \cdots, n-1$$

The quantum number n denotes the variety in orbital size, and the azimuthal quantum number l represents its ellipticity. Thus, n corresponds physically to the

kinetic energy of the electron and l corresponds to its angular momentum. The electron energy is given by

$$E_n = -\frac{2\pi^2 k_0^2 me^4}{h^2} \cdot \frac{1}{n^2} \qquad (n = 1, 2, \ldots)$$

To describe the electron orbit three-dimensionally, a third, magnetic quantum number m_l, must be introduced. The range of m_l is related to the azimuthal quantum number l, and shown by

$$-l \le m_l \le l$$

The existence of a third quantum condition implies that the direction of the electron orbital plane is quantum-restricted. The direction of the plane is defined between the direction of the magnetic field and a normal vector on the orbital plane. Thus, the quantum number m_l is called "magnetic quantum number." When the magnetic field exists, the variation of electron energy depends on the value of m_l.

Finally, there is a fourth quantum number. The spin quantum number m_s parameterizes the intrinsic angular momentum of an electron in a manner corresponding to its right-hand rotation or left-hand rotation in classical atomic theory. The spin quantum number m_s can have only two values,

$$m_s = \pm\frac{1}{2}$$

The electron configuration in multielectron atoms obeys the Pauli Exclusion Principle: no two identical fermions (particles with half-integer spin) may occupy the same quantum state simultaneously. The electron shell structure description is tabulated in Table 1.

Table 1. Electron shell structure

Major shell	Quantum number		Sub shell	Number of orbit (*ml*)	Number of electron (*ms*)
	n	*l*			
K	1	0	1s	1	2
L	2	0	2s	1	2
		1	2p	3	6
M	3	0	3s	1	2
		1	3p	3	6
		2	3d	5	10
N	4	0	4s	1	2
		1	4p	3	6
		2	4d	5	10
		3	4f	7	14

3 Laser-Induced Breakdown

The characteristics of early plasma generation processes induced by laser vary depending on the light absorption characteristics of the measured objects. In the case of light-absorbing objects like metals, laser light energy converts rapidly to heat energy on the surface, causing melting, then vaporizing, and finally generating plasma on the surface. Because the surface plasma absorbs laser energy, that energy does not then reach the object surface, making the detection of quantitative spectroscopic data from the metal materials difficult. In the case of dielectric materials with a wide bandgap structure, the difficulty in performing a quantitative analysis originates in certain types of dielectric breakdown mechanisms that occur during plasma generation.

4 Breakdown Process on Dielectric Materials

In the laser-induced breakdown process on wide bandgap materials, an electron raised from ground state to the conduction band behaves as a free electron. There are three ways to raise an electron to the conduction band. (1) Excitation by incident photon energy. (2) Excitation from defect energy levels. (3) Excitation by a multiphoton process. In case (1), the wavelength of the laser is required to correspond to the excitation energy level. For LIBS on materials with a wide bandgap structure, a laser with higher photon energy (i.e. shorter wavelength) is required. In case (2), materials typically contain a trace of impurities or have a slightly defective structure. Even slight defects are sufficient to generate laser-induced plasma. The defective structure not only contributes to the excitation of one electron from its defect-energy level to the conduction band, which corresponds to the laser wavelength, but it also produces an electron avalanche. An electron avalanche is a phenomenon in which a number of electrons raised to the conduction band are rapidly accelerated by the laser electric field, ionizing the atoms by collision, and thereby forming new electrons to undergo the same process in successive cycles. Through electron avalanche, electron density reaches the dielectric breakdown level. The rate of the dielectric breakdown on wide bandgap materials is related to the impurity concentration [32, 33]. In case (3), the interaction is based on elementary single photon absorption and emission events [34]. The perturbation theory approximates an elementary event involving the simultaneous participation of many photons. A photon transition may be considered as a transition that passes in upper stages through intermediate states of the system: first one photon is absorbed and the system passes from ground state to the first upper state, then, a second photon is absorbed and the system passes into its second upper state, and so on. Finally, as a result of elementary single photon events, the system passes into the final state. The concept of multiphoton processes was developed in quantum field theory to describe the interaction of

radiation with matter. However, observing multiphoton processes is difficult because of their extraordinarily lower probability than single photon processes. Before the appearance of lasers, only two photon processes, such as resonance fluorescence, Rayleigh scattering, Brillouin scattering, and Raman scattering, were observed in the optical range. Multiphoton processes have become increasingly important with the application of high-intensity lasers. On account of the laser-induced plasma produced by a short-pulsed laser with high peak intensity, the photon density is sufficient to produce a multiphoton process. Using laser sources with high radiation power density (10^{15} W/cm^2), the probability of multiphoton processes becomes comparable to the probability of single photon transitions.

5 Breakdown on Metal Objects

Since the 1980s, many liquid miniaturization analytical techniques for LIBS to carry out proper chemical analysis of specimens have been reported [35-37]. Our research group has investigated and improved the LIBS system since the 1990s for use in quantitative analysis [38-40]. From our investigations, important information has emerged about the relationship between the time profile of the plasma emission intensity and the measurement conditions, i.e., particle size, type of ambient gas, and atmospheric pressure [41, 42]. We used this knowledge in the present work to improve quantitative calibration techniques. By using the present LIBS system, it is possible to obtain information about the density of metal nanopaste ink. The nanoscale metal ink is attracting increased attention as a new material for use in interconnects for micro-devices, and for electrical circuit wiring with low temperature sintering. For example, the sintering time of silver nanoparticle ink is only 60 min at 200°C. The nanoscale silver particles are dissolved in an organic solvent (n-tetradecane) and formed by adding organic dispersant components. Rapid analysis is important for maintaining the dispersed state of the metal particles in the ink. The present work consumes only 1 mL of the sample for three measurements obtained from every 100 laser pulse shots, and allows instantaneous LIBS measurements for the nanoscale metal ink.

6 Experiments

Fig. 1 shows a schematic of the LIBS system. The optical layout consisted of four subsystems: a Nd:YAG laser, spectrograph, streak camera, and delay pulse generator. The Nd:YAG laser was operated at 1064 nm to generate a 52.8-mJ Q-switched pulse with a width of 8 ns (full width at half maximum, FWHM). The emissions from the target were guided into the spectrograph and dispersed by a grating with a groove density of 1200 lines/mm. The resulting electrical signal was recorded using a streak camera, and the data were stored in a PC.

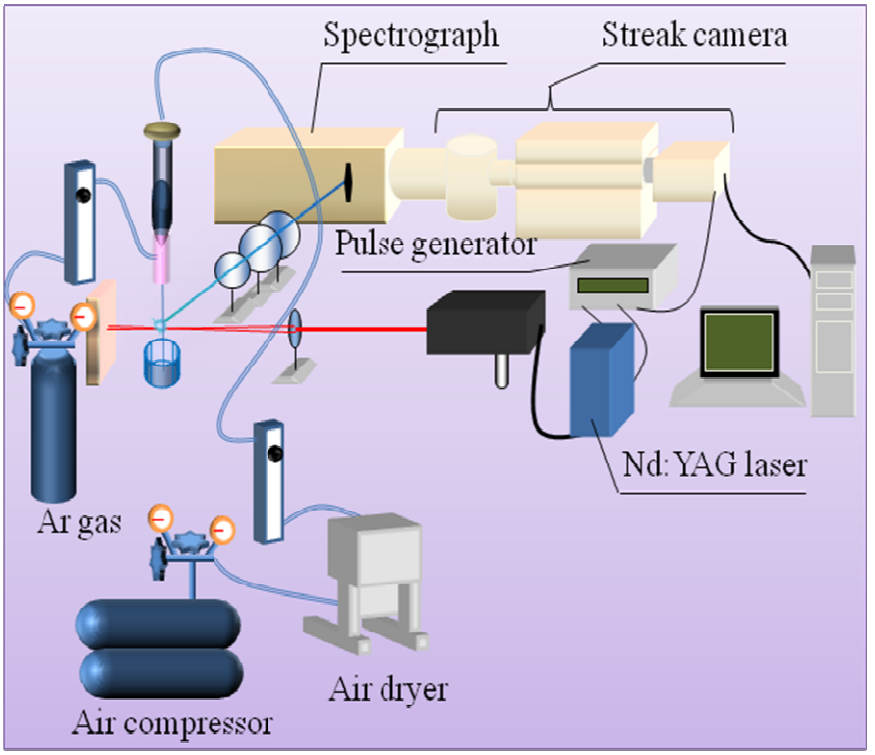

Fig. 1. Schematic of LIBS system

The sampling system for LIBS consisted of an ink-jet nozzle and a gas-flow assist system. The inner diameter of the nozzle was 30 μm. The liquid was ejected from the syringe under pressure from an air compressor, and the ink-jet hit the target area crossed by a laser beam spot. To prevent an oxygen reaction, argon gas was jetted out from a 10-mm orifice tube attached to the syringe. This ambient gas also facilitated the emission of liquid from the plasma. The gas flow rates were adjusted to 0.2 L/min. Extraction and relaxation of the spectrum of element formation, and the subsequent dissipation of the laser plasma occurred very rapidly. Within 4 μs of plasma initiation, intense continuum radiation was observed, along with ionic lines over a broad wavelength range; within 30 μs of atomic emission, the spectrum of the element was observed. The plasma emission within 4 μs was caused by bremsstrahlung spectra and recombination radiation from the plasma as free electrons and ions recombined in the cooling plasma. The intensity of the spectrum emission was optimized with respect to the plasma background. Spectral measurements were carried out after an appropriate time delay to allow for the decay of the radiation continuum. To accomplish rapid observation in under 1 μs, a streak camera was used in this LIBS system. The streak camera was operated by directing the light onto a photocathode. Photons

produced electrons via the photoelectric effect. The electrons were accelerated in a cathode ray tube and passed through an electric field produced by a pair of sweep electrode plates, which deflected the electrons sideways. By modulating the electric potential between the plates, the electric field was quickly changed to produce a time-varying deflection of the electrons, sweeping and amplifying the electrons by a micro-channel plate (MCP) across a phosphor screen at the end of the tube. Finally, a CCD array was used to measure the streak pattern on the screen, and thus provide the temporal profile of the light pulse.

7 Results

The spectra resulting from LIBS for ambient air and argon are shown in Fig. 2. Fig. 3 shows a time profile of the normalized intensity spectra of argon and air compared with the pulse laser profiles used to conduct this experiment.

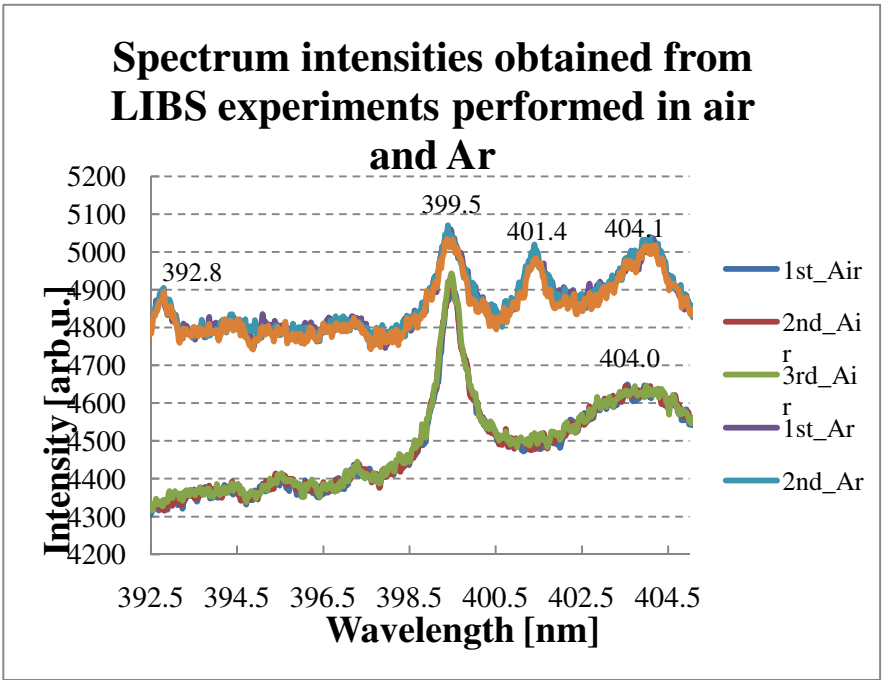

Fig. 2. Spectrum intensities obtained from LIBS experiments performed in air and argon

Figs. 4 to 6 show a part of the experimental data for the sodium liquid. The measurements were carried out using typical element-specific radiation emanating from sodium at wavelengths of 588.995 nm and 589.592 nm. The intensity of the signal was based on data obtained for 100 laser pulse shots.

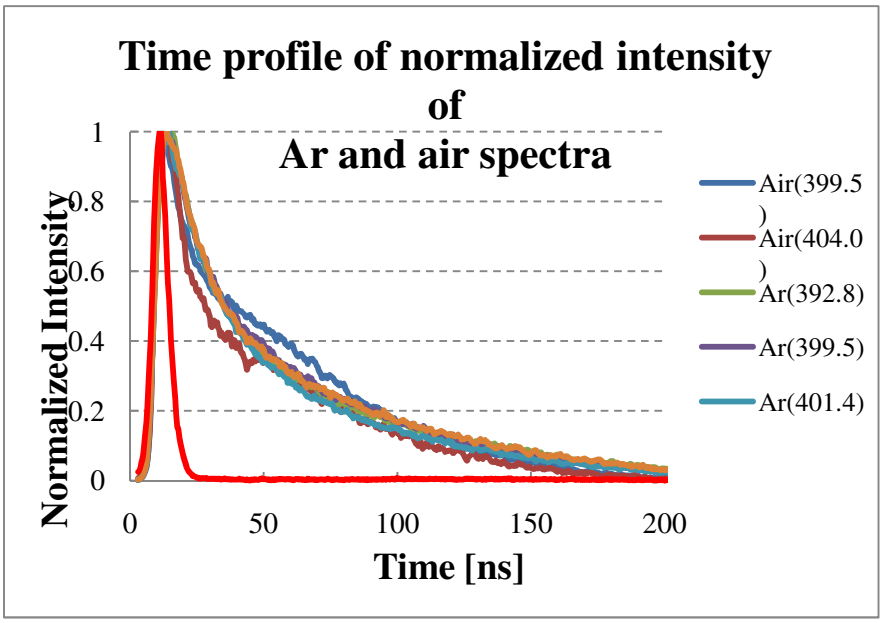

Fig. 3. Time profile of normalized intensity of argon and air spectrum compared with laser profile

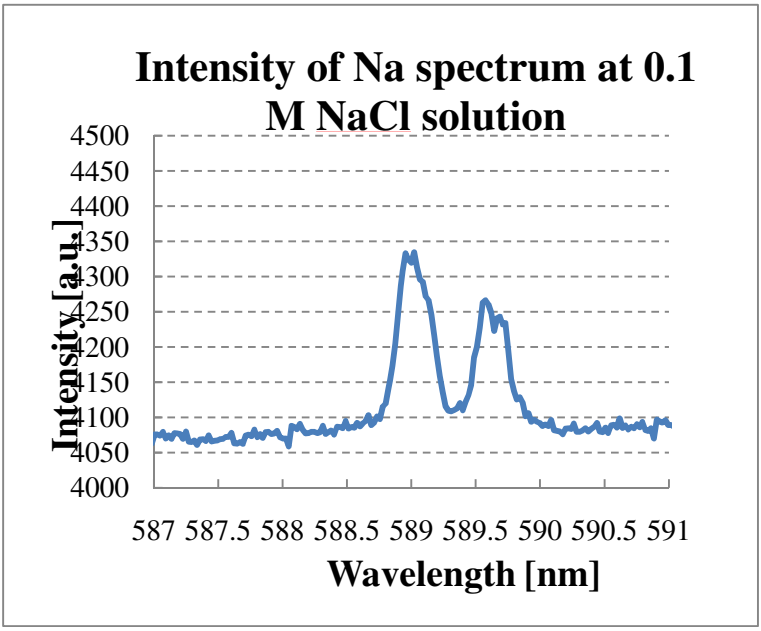

Fig. 4. Na emission intensity from the measurement of 0.1 M solution

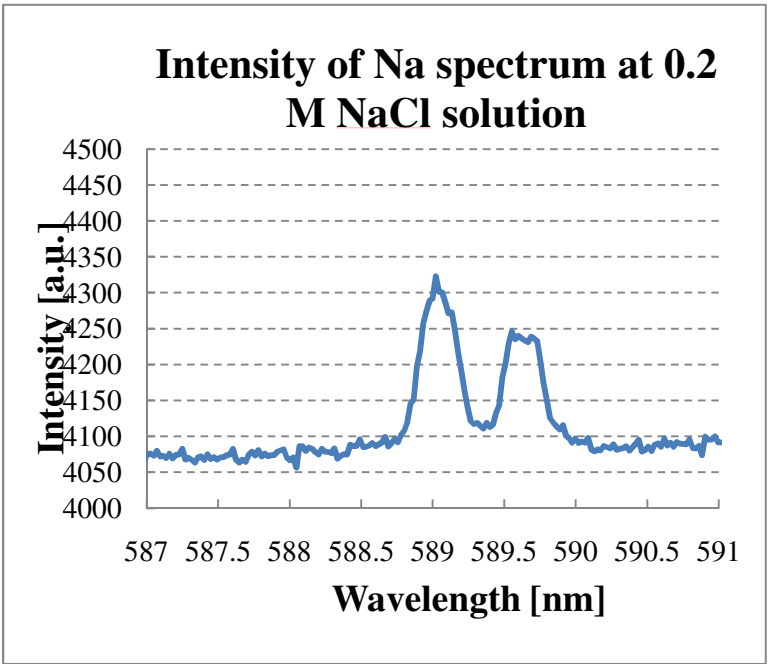

Fig. 5. Na emission intensity from the measurement of 0.2 M solution

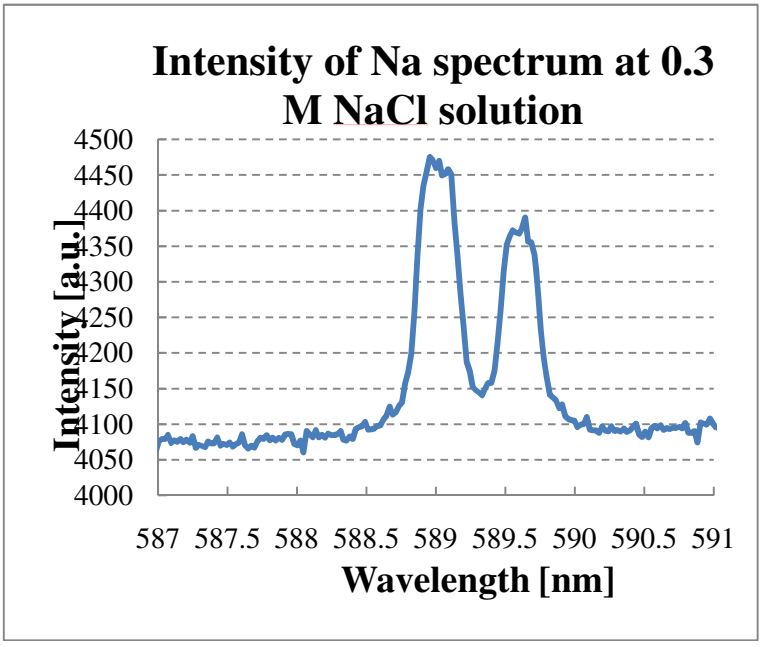

Fig. 6. Na emission intensity from the measurement of 0.3 M solution

Figs. 7 to 9 show a part of the experimental data for the silver nanoparticle ink. These measurements were carried out using typical element-specific radiation emanating from silver at wavelengths of 328.068 nm and 338.289 nm. The intensity of the signal was based on data obtained for 100 laser pulse shots from three measurements.

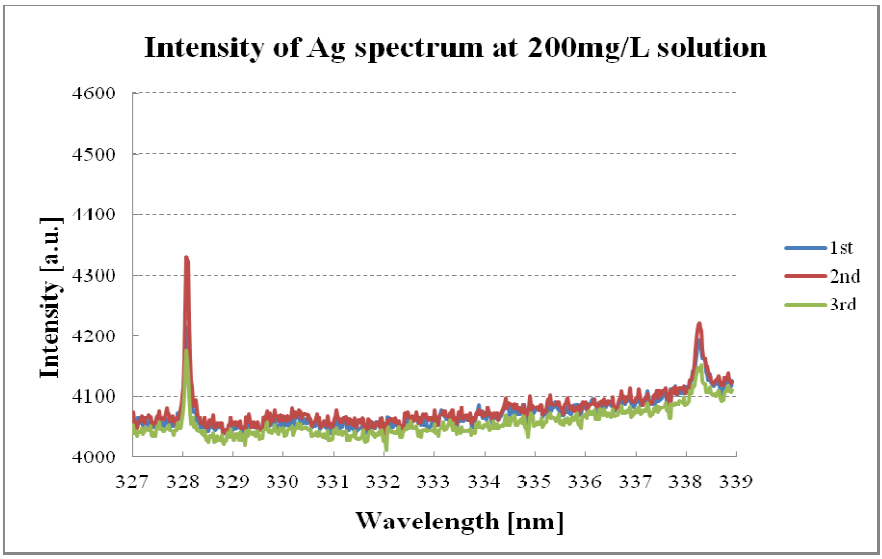

Fig. 7. Variation in the Ag emission intensity from three measurements of 200 mg/L solution

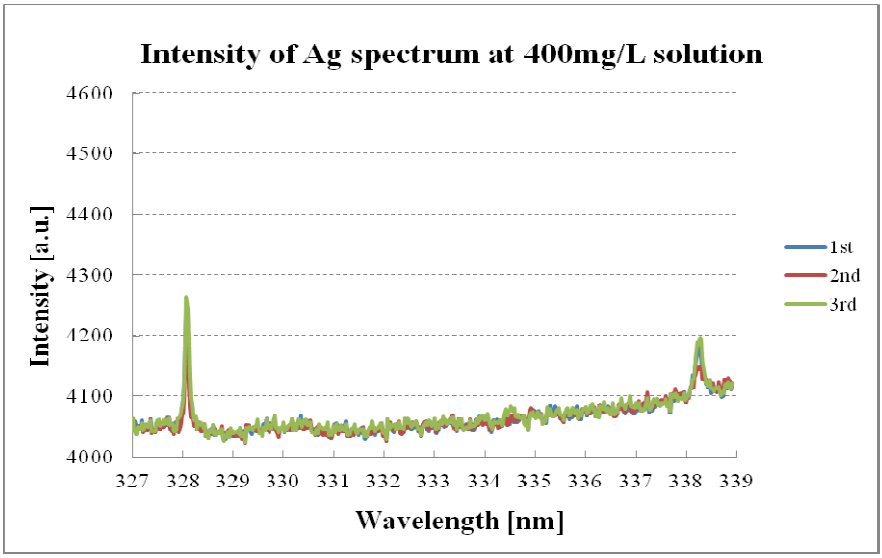

Fig. 8. Variation in the Ag emission intensity from three measurements of 400 mg/L solution

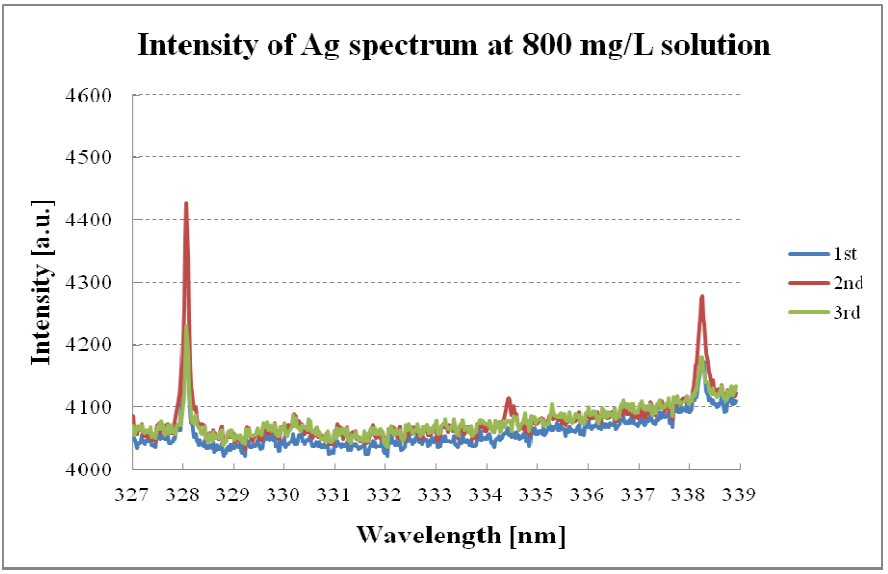

Fig. 9. Variation in the Ag emission intensity from three measurements of 800 mg/L solution

Figs. 10 to 12 show some of the experimental data for the copper nanoparticle ink. These measurements were carried out using typical element-specific radiation emanating from copper at wavelengths of 324.754 nm and 327.396 nm. The intensity of the signal was based on data obtained for 100 laser pulse shots from three measurements.

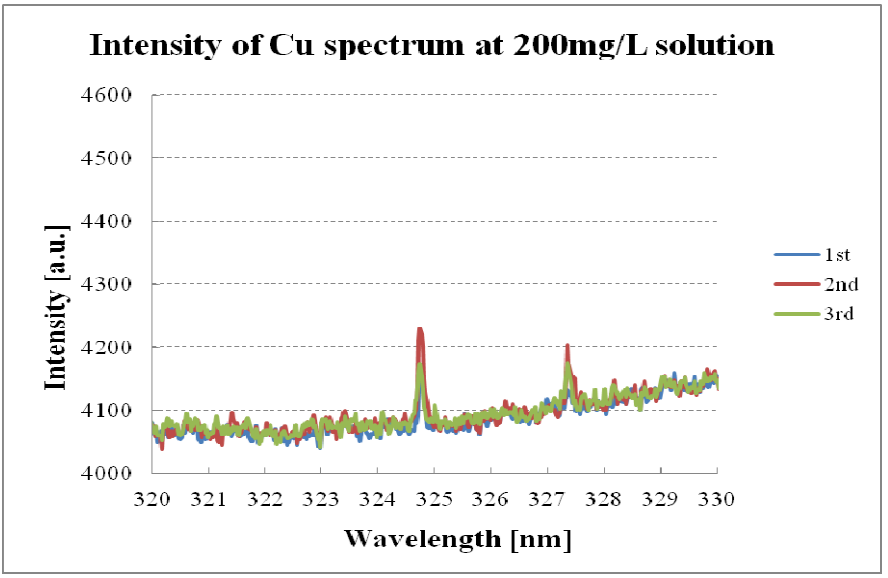

Fig. 10. Variation in the Cu emission intensity from three measurements of 200 mg/L solution

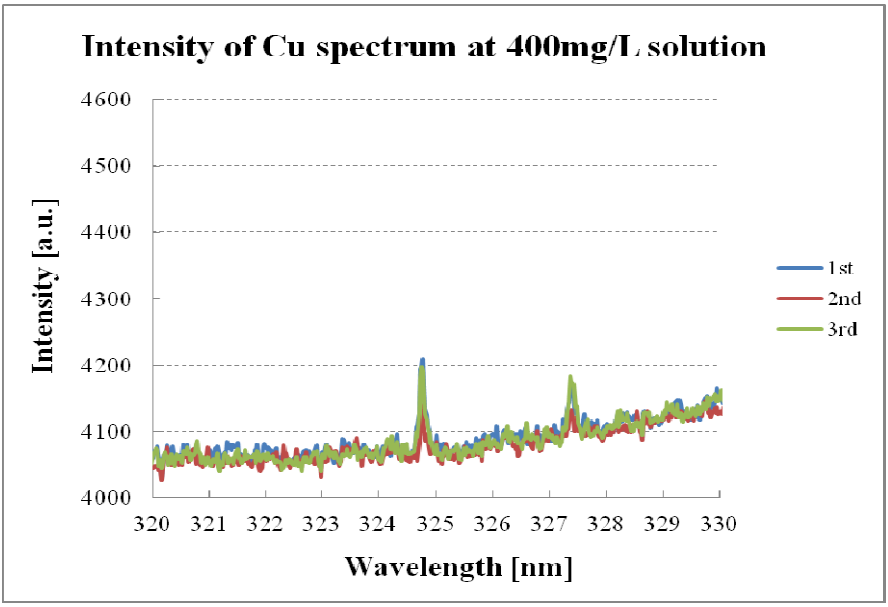

Fig. 11. Variation in the Cu emission intensity from three measurements of 400 mg/L solution

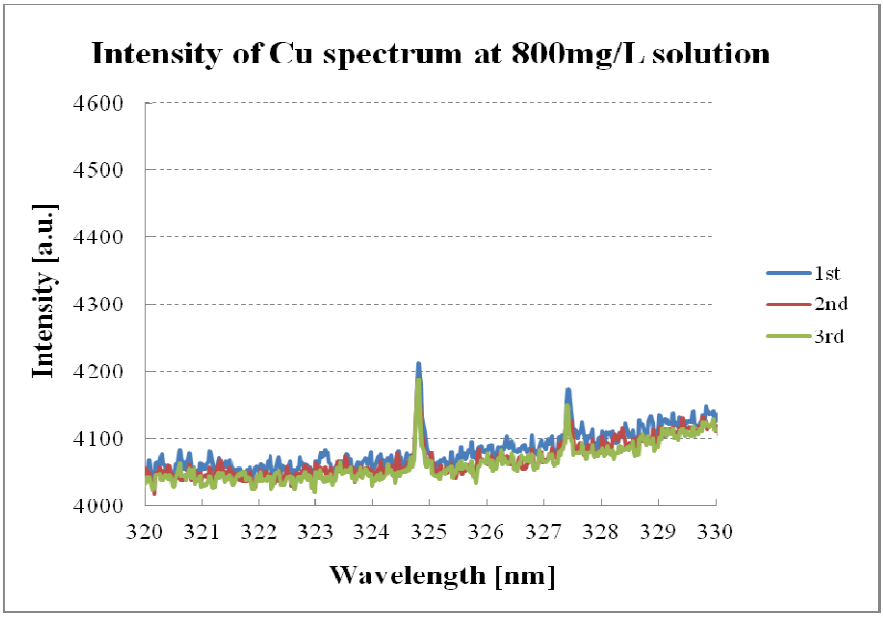

Fig. 12. Variation in the Cu emission intensity from three measurements of 800 mg/L solution

7 Conclusions

Elemental analysis on wide-bandgap materials (Na) and metal objects (Ag, Cu) using LIBS was successfully carried out. During metal material detection, good spectral peak resolutions were obtained when the spectra were recorded at wavelengths of 328.068 nm and 338.289 nm for silver, and 324.754 nm and 327.396 nm for copper. The use of nano particle ink allows density control, because it is amenable to quantitative calibration. The LIBS system, with ink-jets and an argon gas-assist system, was used for the quantitative detection of silver and copper nano particles in an oil-based ink. Argon, as an ambient gas, increased the sensitivity of the LIBS system and protected the equipment from the chemical reaction between the flammable solvent (n-tetradecane) and oxygen in the air. Quantitative analysis of the intensity of dispersion remains a problem. Measurement of metal nanoparticle ink using LIBS plays an important role in the environmental monitoring of metal particles in a clean room. Some of the contaminated matter consisted of carbonaceous particles that could have entered from outside; other contaminates were metal particles that could have originated in the clean room. The origin of metal particles is not well understood at present. It is speculated that they originate from the motor brushes in the clean room or are generated during the sputtering or reflow processes during the fabrication of MEMS devices. LIBS measurements are an effective way to clarify the origin of metal particles. Salt particles are also a severe problem in fabrication processes. Controlling nanoparticle contamination with the help of the chemical component information obtained by LIBS significantly enhances the production yield rate.

References

[1] Brech, F., Cross, L.: Optical microemission stimulated by a ruby laser. Appl. Spectrosc. 16(2) (1962)

[2] Gondal, M.A., Hussain, T., Yamani, Z.H., Baig, M.A.: On-line monitoring of remediation process of chromium-polluted soil using LIBS. J. Hazard. Mater. 163, 1265–1271 (2009)

[3] Hussain, T., Gondal, M.A.: Monitoring and assessment of toxic metals in Gulf war oil spill contaminated soil using laser-induced breakdown spectroscopy. Environ. Monit. Assess. 136, 391–399 (2008)

[4] Kim, T., Specht, Z.G., Vary, P.S., Lin, C.T.: Spectral fingerprints of bacterial strains by laser-induced breakdown spectroscopy. J. Phys. Chem. B 108, 5477–5482 (2004)

[5] Hotokezaka, H., Aoyagi, N., Kawahara, Y., Yamaguchi, N.U., Nagasaki, S., Sasaki, K., Tanaka, S.: Selective and in-situ determination of carbonate and oxide particles in aqueous solution using laser-induced breakdown spectroscopy (LIBS) for wearable information equipment. Microsystem Technologies 11(8-10), 974–979 (2005)

[6] Ajiro, T., Fujimori, H., Matsui, T., Izumi, S.: Particle size dependence of correlation between plasma emission delay time and plasma emission intensity of laser breakdown induced by particles. Jpn. J. Appl. Phys. 31(1, 9A), 2760–2761 (1992)

[7] Fujimori, H., Matsui, T., Ajiro, T., Yokose, K., Hsueh, Y.M., Izumi, S.: Detection of fine particles in liquids by laser breakdown method. Jpn. J. Appl. Phys. 31(1, 5A), 1514–1518 (1992)
[8] Hotokezaka, H., Tanaka, S., Suzuki, A., Nagasaki, S.: Speciation analysis on europium(III) using laser-induced breakdown spectroscopy. Radiochim. Acta 88, 645–648 (2000)
[9] Nakamura, S., Ito, Y., Sone, K., Hiraga, H., Kaneko, K.: Determination of an iron suspension in water by laser-induced breakdown spectroscopy with two sequential laser pulses. Anal. Chem. 68, 2981–2986 (1996)
[10] Rodriguez-Celis, E.M., Gornushkin, I.B., Heitmann, U.M., Almirall, J.R., Smith, B.W., Winefordner, J.D., Omenetto, N.: Laser induced breakdown spectroscopy as a tool for discrimination of glass for forensic applications. Anal. Bioanal. Chem. 391, 1961–1968 (2008)
[11] Baudelet, M., Guyon, L., Yu, J., Wolf, J.P., Amodeo, T., Frejafon, E., Laloi, P.: Femtosecond time-resolved laser-induced breakdown spectroscopy for detection and identification of bacteria: A comparison to the nanosecond regime. J. Appl. Phys. 99, 084701 (2006)
[12] Sturm, V., Vrenegor, J., Noll, R., Hemmerlin, M.: Bulk analysis of steel samples with surface scale layers by enhanced laser ablation and LIBS analysis of C, P, S, Al, Cr, Cu, Mn and Mo. J. Anal. At. Spectrom. 19, 451–456 (2004)
[13] Noll, R., Mönch, I., Klein, O., Lamott, A.: Concept and operating performance of inspection machines for industrial use based on laser-induced breakdown spectroscopy. Spectrochim. Acta B 60(7-8), 1070–1075 (2005)
[14] Osticioli, I., Wolf, M., Anglos, D.: An optimization of parameters for application of a laser-induced breakdown spectroscopy microprobe for the analysis of works of art. Appl. Spectrosc. 62, 1242–1249 (2008)
[15] Ciupiński, Ł., Fortuna-Zaleśna, E., Garbacz, H., Koss, A., Kurzydłowski, K.J., Marczak, J., Mróz, J., Onyszczuk, T., Rycyk, A., Sarzyński, A., Skrzeczanowski, W., Strzelec, M., Zatorska, A., Żukowska, G.Z.: Comparative laser spectroscopy diagnostics for ancient metallic artefacts exposed to environmental pollution. Sensors 10(5), 4926–4949 (2010)
[16] Radziemski, L., Cremers, D., Benelli, K., Khoo, C., Harris, R.D.: Use of the vacuum ultraviolet spectral region for LIBS-based Martian geology and exploration. Spectrochim. Acta B 60, 237–248 (2005)
[17] Sallé, B., Cremers, D.A., Maurice, S., Wiens, R.C.: Laser-induced breakdown spectroscopy for space exploration appications: Influence of ambient pressure on the calibration curves prepared from soil and clay samples. Spectrochim. Acta B 60, 479–490 (2005)
[18] Sallé, B., Cremers, D.A., Maurice, S., Wiens, R.C.: Evaluation of a compact spectrograph for in-situ and stand-off laser-induced breakdown spectroscopy analyses of geological samples in Martian missions. Spectrochim. Acta B 60, 805–815 (2005)
[19] Sallé, B., Lacour, J.-L., Vors, E., Fichet, P., Maurice, S., Cremers, D.A., Wiens, R.C.: Laser-induced breakdown spectroscopy for Mars surface analysis: Capabilities at stand-off distance and detection of chlorine and sulfur elements. Spectrochim. Acta B 59, 1413–1422 (2004)
[20] Arp, Z.A., Cremers, D.A., Harris, R.D., Oschwald, D.M., Parker, G.R., Wayne, D.M.: Feasibility of generating a useful laser-induced breakdown spectroscopy plasma on rocks at high pressure: preliminary study for a Venus mission. Spectrochim. Acta B 59, 987–999 (2004)

[21] Arp, Z.A., Cremers, D.A., Wiens, R.C., Wayne, D.M., Sallé, B., Maurice, S.: Analysis of water ice and water ice/soil mixtures using laser-induced breakdown spectroscopy: Application to Mars polar exploration. Appl. Spectrosc. 58, 897–909 (2004)
[22] Brennetot, R., Lacour, J.L., Vors, E., Rivoallan, A., Vailhen, D., Maurice, S.: Mars analysis by laser-induced breakdown spectroscopy (MALIS): Influence of Mars atmosphere on plasma emission and study of factors influencing plasma emission with the use of Doehlert designs. Appl. Spectrosc. 57, 744–752 (2003)
[23] Knight, A.K., Scherbarth, N.L., Cremers, D.A., Ferris, M.J.: Characterization of laser-induced breakdown spectroscopy (LIBS) for apprication to space exploration. Appl. Spectrosc. 54, 331–340 (2000)
[24] Sharma, S.K., Misra, A.K., Lucey, P.G., Clegg, S.M.: Combied remote LIBS and Raman spectroscopy of sulfur-containing minerals, and minerals coated with hematite and covered with basaltic dust at 8.6 m. Spectrochim. Acta A 68, 1036–1045 (2007)
[25] Wiens, R.C., Sharma, S.K., Thompson, J., Misra, A., Lucey, P.G.: Joint analyses by laser-induced breakdown spectroscopy (LIBS) and Raman spectroscopy at stand-off distances. Spectrochim. Acta A 61, 2324–2334 (2005)
[26] Fabre, C., Boiron, M.-C., Dubessy, J., Cathelineau, M., Banks, D.A.: Palaeofluid chemistry of a single fluid event: a bulk and in-situ multi-technique analysis (LIBS, Raman Spectroscopy) of an Alpine fluid (Mont-Blanc). Chem. Geol. 182, 249–264 (2002)
[27] Marquardt, B.J., Stratis, D.N., Cremers, D.A., Angel, S.M.: Novel probe for laser-induced breakdown spectroscopy and Raman measurements using an imaging optical fiber. Appl. Spectrosc. 52, 1148–1153 (1998)
[28] Castillejo, M., Martín, M., Silva, D., Stratoudaki, T., Anglos, D., Burgio, L., Clark, R.J.H.: Analysis of pigments in polychromes by use of laser induced breakdown spectroscopy and Raman microscopy. J. Mol. Struct. 550-551, 191–198 (2000)
[29] Effenberger Jr., A.J., Scott, J.R.: Effect of atmospheric conditions on LIBS spectra. Sensors 10, 4907–4925 (2010)
[30] Shu, R., Qi, H.X., Lu, G., Ma, D.M., He, Z.P., Xue, Y.Q.: Laser-induced breakdown spectroscopy based detection of lunar soil simulants for moon exploration. Chin. Opt. Lett. 5, 58–59 (2007)
[31] Wiens, R.C., Maurice, S.: Chemcam's cost a drop in the Mars bucket. Science 322, 1464–1464 (2008)
[32] Van Stryland, E.W., Soileau, M.J., Smirl, A.L., Williams, W.E.: Pulse-width and focal-volume dependence of laser-induced breakdown. Phys. Rev. B 23, 2144 (1981)
[33] Bandyopadhyay, P.K., Merkle, L.D.: Laser-induced damage in quartz: A study of the influence of impurities and defects. J. Appl. Phys. 63 (1988)
[34] Bonch-Bruevich, A.M., Khodovoi, V.A.: Multiphoton Process. Sov. Phys. Usp. No. 85, 3–64 (1965)
[35] Archontaki, H.A., Crouch, S.R.: Evaluation of an isolated droplet sample introduction system for laser-induced breakdown spectroscopy. Appl. Spectrosc. 42(5), 741–746 (1988)
[36] Janzen, C., et al.: Analysis of small droplets with a new detector for liquid chromatography based on laser-induced breakdown spectroscopy. Spectrochim. Acta Part B 60, 993–1001 (2005)
[37] Kumar, A., Yueh, F.Y., Miller, T., Singh, J.P.: Detection of trace elements in liquids by laser-induced breakdown spectroscopy with a Meinhard nebulizer. Appl. Optics 42(30), 6040–6046 (2003)

[38] Andreev, A., Ueda, T.: Simulation of laser plasma emission characteristics of small solid particles in different gas atmospheres at various pressures. Trans. IEE of Japan 121-E(11), 593–598 (2001)
[39] Hayashi, H., Ueda, T.: Measurement of particle size with laser induced breakdown. In: Proc. of SICE 1999, pp. 645–646 (1999)
[40] Ueda, T., Okamoto, Y.: "In-situ status measurement technology. In: The 2nd Symp. on Advanced Photon Processing and Measurement Technol., pp. 38–44 (1998)
[41] Wakamatsu, M., Ikezawa, S., Ueda, T.: Particle element and size simultaneous measurement using LIBS. IEEJ Trans. Sensors Micromach. 127(9), 397–402 (2007)
[42] Ikezawa, S., Wakamatsu, M., Pawlat, J., Ueda, T.: Sensing System for Multiple Measurements of Trace Elements Using Laser-induced Breakdown Spectroscopy. IEEJ Trans. Sensors Micromach. 129(4), 115–119 (2009)

Microdevice with Half-Ring Shaped GMR Sensors for Magnetic Bead Manipulation and Detection

C.P. Gooneratne[1], I. Giouroudi[2], and J. Kosel[1]

[1] King Abdullah University of Science and Technology, Thuwal, Saudi Arabia
[2] Vienna University of Technology, Vienna, Austria

Abstract. Micro and nanosized superparamagnetic beads (MBs) have been used in several biomedical applications due to their comparable size to biomolecules and their ability to respond to external magnetic fields. The stray fields of magnetized MBs can be detected by a magnetic sensor, which is utilized for quantification of target biomolecules present in immunoassays when MBs are used as biomolecular labels.

In this chapter, we describe the design, fabrication and testing of a microdevice for manipulating, trapping and detecting MBs. Manipulation and trapping is accomplished with a microstructure comprising conducting rings to produce magnetic field gradients, which exert a force on MBs. Controlling the movement of MBs paves the way for their rapid detection, since the beads can be attracted and transported towards a sensing site. In order to ensure that the majority of the MBs trapped at the sensing site are detected, we designed a spin valve type giant magnetoresistance (GMR) sensor with half-ring geometry. Analytical and numerical analysis leading towards the fabrication of the microstructure and the half-ring GMR sensor are presented. Full characterization of a single half-ring sensing element showed a DC magnetoresistance of 5.9 %, a small signal AC sensitivity of 0.53 mV/mT and a noise level of 6 nV/√Hz. An analytical model backed up by experimental results is presented to characterize the behavior of MBs in solution. Experimental results showed that the half-ring GMR sensor detected the presence of 2 μm MBs, thus indicating the feasibility of integrating an MB manipulation microstructure with half-ring GMR sensors to optimize the active sensing site.

1 Introduction

Superparamagnetic beads (MBs) can be used as biological entity tags to sort, separate and purify cells of interest in immunoassays [1, 2]. MBs are magnetized only in the presence of an external magnetic field. Therefore, the magnetization of the beads can easily be switched off by removing the external magnetic field, preventing them from agglomeration. Integration of magnetic detection with MB

S.C. Mukhopadhyay et al. (Eds.): Advancement in Sensing Technology, SSMI 1, pp. 121–138.
springerlink.com

manipulation seems very promising for sensitive, rapid and miniaturized bio-assays. Miniaturization results in lower sample and reagent consumption, faster reactions and enables accurate and efficient manipulation of target biological entities [3-7]. Moreover, such integrated microdevices are highly sensitive and compact offering the option of on-site analysis with handheld units. Employing standard microfabrication technologies, they also can be mass produced at low costs [8-10].

A controlled transport of MBs to a sensing site ensures a reliable, sensitive and rapid detection system. Hence, controlled, micro-sized magnetic field generators that produce strong magnetic field gradients are required. However, these magnetic field generators should be compatible with integrated magnetic sensors to detect and count MBs, which, e.g., might tag biological cells. The field can be produced by micro-sized permanent magnets or electromagnets [11-18]. Even though permanent magnets produce strong localized magnetic fields they are more difficult and expensive to fabricate. Electromagnets have been employed with complex patterns such as spiral, meander or loop, which do not allow precise control of a few MBs. Moreover, none of these patterns have been integrated with sensing functionality. In this chapter, we discuss a microdevice that is a combination of a magnetic microsensor and electromagnetic microstructures for concentrating, trapping and detecting MBs. A micro-ring trap as shown in Fig. 1 is used to attract, trap and transport MBs to a sensing zone. By sequentially applying current to the different micro-ring elements, MBs can be transported from the outermost ring to the innermost ring, where sensors can detect the MBs. The number of rings can easily be increased in order to cover a larger area if needed. A ring microstructure does not have any edges such as square loops; so, the magnetic field is uniform along the periphery of the ring. Hence, MBs can be precisely manipulated and homogeneously trapped all around the ring element. Moreover, the micro-ring trap is cheap and simple to fabricate.

In order for the MBs to be immobilized on the innermost ring, above the sensor element, they need to be under the influence of a magnetic force. The magnetic field providing this force also maintains the magnetization of the beads giving rise to stray fields, which can be detected by the sensor. Giant magnetoresistance (GMR) sensors are commonly employed for applications involving MB detection, since only small fields are needed to change the resistance, and they have advantages in size, power, cost and thermal stability with respect to search coils, fluxgates, SQUIDs and Hall sensors. Several microchips have been investigated for the manipulation and detection of MBs using GMR sensors [19-24]. However, these microchips lack the precise control required for transporting a high percentage of MBs to the sensing site and, for example, rely on a continuous liquid flow. Also, once at the sensing site, MB immobilization depends on the interaction with a functionalization layer (e.g., biological probes) on top of the surface of the GMR sensor. The micro-ring trap structure proposed in this chapter not only concentrates the MBs at the sensor site but also immobilizes them there without the need of a liquid flow or functionalization layer. With half-ring GMR

sensors underneath the micro-ring trap (Fig. 1), the immobilized beads can be efficiently detected. The purpose of a half-ring instead of a full-ring structure is for connecting the half-ring GMR sensors to a Wheatstone bridge circuit to reduce noise and increase sensitivity.

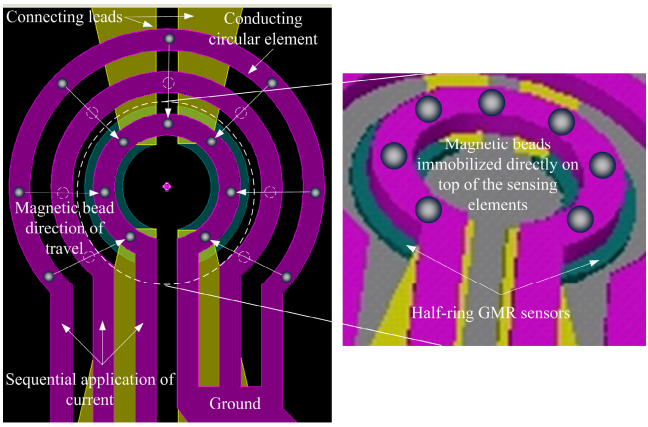

Fig. 1. Micro-ring trap to manipulate and transport magnetic beads to the sensing area

2 Principles of Manipulation and Detection of Magnetic Beads

2.1 Magnetic Bead Manipulation

MB manipulation is achieved by the application of a magnetic field. MBs have a positive magnetic susceptibility and are magnetized in the direction of the applied magnetic field. Since MBs have a single domain, each bead can be considered a magnetic dipole. The force F_b, acting on a magnetic dipole can be expressed as

$$\vec{F}_b = (\vec{m} \bullet \nabla)\vec{B}, \tag{2.1}$$

where $\vec{B}$ is the magnetic field. Since the magnetic moment of the dipole $\vec{m} = \vec{M}V$, where $\vec{M}$ and V are the magnetization and volume of the MB, respectively, equation (2.1) can be rewritten as

$$\vec{F}_b = \frac{V\chi}{\mu_0}(\vec{B} \bullet \nabla)\vec{B}, \tag{2.2}$$

where χ is the susceptibility of the MB and μ_0 is the permeability of free space.

From equation (2.2) it can be seen that the translational force acting on the MBs can be controlled through the gradient of the magnetic field. Generally, MBs have low susceptibilities and very small volumes. Therefore, a non-uniform magnetic field with a large gradient is required to efficiently manipulate the MBs.

The hydrodynamic drag force F_d acting on a magnetic bead, in a flowing solution with viscosity η, can be expressed as

$$\vec{F}_d = 6\pi a \eta \Delta v, \tag{2.3}$$

where a is the radius of the MB and Δv is the difference between the MB velocity and the flow velocity of the solution.

In addition to the drag force, moving MBs along the surface of the microchip has to overcome the dynamic frictional force F_f given by

$$F_f = C_f F_g \,, \tag{2.4}$$

where C_f is the coefficient of dynamic friction and F_g is the gravitational force of the MB. F_g can be expressed as

$$F_g = (p_m - p_s) g V \,, \tag{2.5}$$

where ρ_m and ρ_s are the densities of the MB and surrounding medium, respectively, and g is the acceleration due to gravity. A static frictional force can, typically, be neglected, since the MBs are constantly in Brownian motion.

In this device, a current-carrying micro-ring structure is used to apply magnetic forces to the MBs in order to concentrate MBs to a sensing site. The design of the ring structure has a strong influence on several parameters, e.g., the forces produced, the current values required, and thermal heating. Therefore, numerical analyses were performed using commercial finite element software (COMSOL) to simulate the influence of different design aspects. Here, we present the results for conducting rings made of aluminum 4 μm in width and a thickness of 0.5 μm. The innermost ring has a radius of 10 μm while the rest of the rings are 5 μm apart. A current of 100 mA is applied in a sequential pattern and the quasi-static solution is calculated. Figure 2(a) shows the distribution of the magnetic field when current is applied to the different rings. The magnetic field, which is highest at the edges of the conducting rings, is strongly localized and drops about 83 % at a distance of 10 μm from the edges. F_b acting on MBs of 2 μm diameter and 0.22 susceptibility (Micromod®) is shown in Fig. 2 (b). The peak forces produced are around 150 pN. The forces are larger at the inner sides of the rings than at the outer sides. This is due to the superposition of the magnetic fields produced at opposite sides of the rings, which is additive at the inside and subtractive at the outside. As the ring radius decreases, the mutual influence of the fields from opposite sides of the rings becomes stronger increasing this superposition effect. From these results it can be seen that an MB located at a ring experiences a magnetic force generated by the neighboring ring of $F_b = 0.26$ pN. Assuming a friction constant of 0.2 [25, 26], F_f is 0.0049 pN, which is considerably smaller than F_b; so the MB can readily be attracted to the neighboring ring, whereby the time required for this also depends on F_d.

The simulated micro-ring structure was fabricated on a Si/SiO_2 substrate, and a sample of MBs dispersed in water with a density of 10 mg/ml was applied to the surface of the chip. Figure 2 (c) shows the efficient attraction, of MBs to the rings

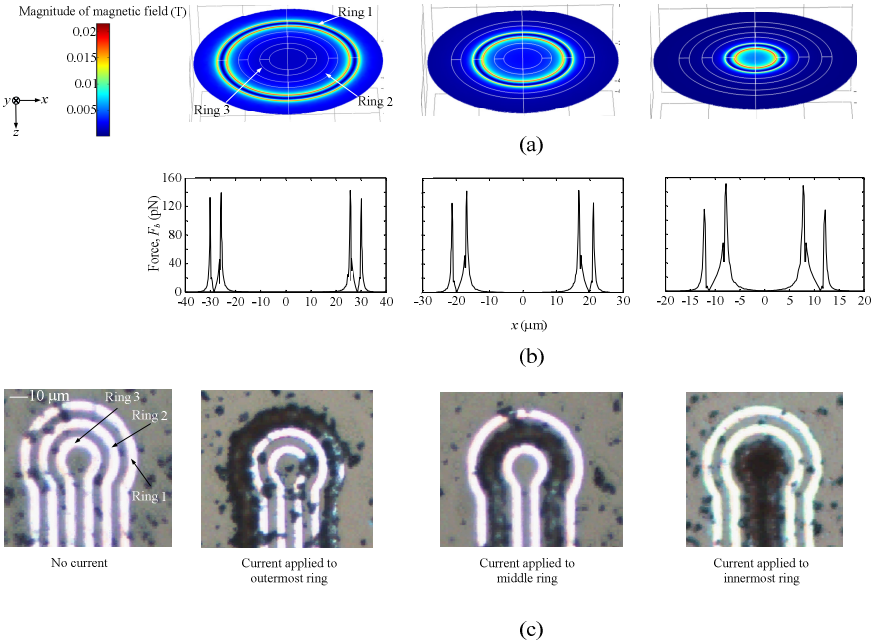

Fig. 2. (a) Numerical simulation results showing magnetic field distribution in conducting micro-rings. (b) Force applied on a 2 μm magnetic bead by micro-rings. (c) Experimental results showing magnetic beads being transported to a sensing zone.

and their controlled manipulation towards the center of the structure [27, 28]. At the start of the experiments, current is applied to ring 1, subsequently switched to ring 2 and, finally, to ring 3. This cycle can be repeated to increase the trapping rate.

2.2 Magnetic Bead Detection

Under the influence of a magnetic field MBs become magnetized and produce magnetic stray fields. When in close proximity, these stray fields can be detected by a magnetic sensor such as the proposed half-ring GMR sensor. Using the micro-ring structure described in section 2.1, MBs immobilized on the innermost ring element will be magnetized by the current through the ring in a parallel or perpendicular direction depending on their location with respect to the ring (Fig. 3). As shown in Fig. 2(b), the forces on magnetic beads are strongest at the edges of the rings. Therefore, in experiments with a single MB or samples with low MB-concentration, the MBs are attracted to the edge of the ring, and they will be magnetized in a perpendicular direction (Fig. 3 (a)). However, if the concentration of MBs is high, the MBs will be distributed along the surface of the ring, and some will be magnetized in a parallel direction, as shown in Fig. 3 (b) and some in perpendicular direction.

The distance that separates the GMR sensor from MBs is an important parameter to consider with respect to the detection of the magnetic stray fields and the sensitivity [7, 9]. The separation is due to a passivation layer 1, insulating the GMR sensor from the conducting ring structure, and a passivation layer 2, protecting the ring structure from corrosive and conducting sample solutions. From experimental results and taking into account the heating and electromigration limits of aluminum, a thickness of 500 nm is reasonable for the conducting ring element. Hence, flexibility to control the distance between the GMR sensor and MBs is available from the thickness of the passivation layers.

The magnetic stray field along the sensitive direction of the sensors (x-direction) produced by a single MB, magnetized in a perpendicular direction (Fig. 3 (a)) is given by,

$$B_x = \frac{\mu_0 3mzx}{4\pi\left(x^2 + y^2 + z^2\right)^{5/2}}. \tag{2.6}$$

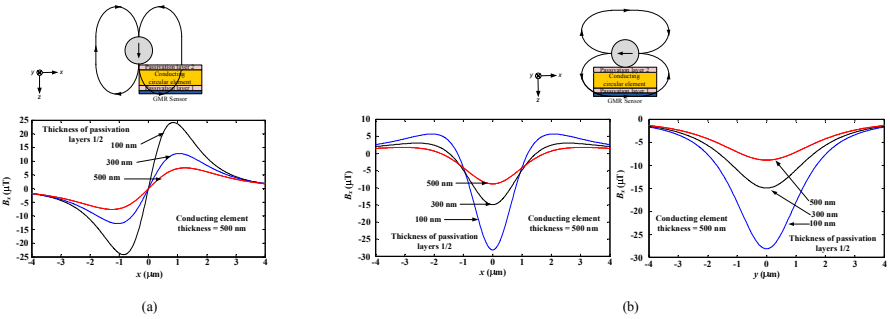

Fig. 3. The stray fields produced by a 2 μm magnetic bead magnetized at a field of 330 A/m in the a) perpendicular and, b) parallel direction. The origin (0,0,0) is located at the top surface of the GMR sensor (z = 0) at the intersection with a virtual line from the center point of the bead (x = 0, y = 0).

For a bead of radius a magnetized in a parallel direction, as shown in Fig. 3 (b), the magnetic stray field can be expressed as

$$B_x = \frac{\mu_0 m}{4\pi\left(x^2 + y^2 + z^2\right)^{3/2}}\left(\frac{3x^2}{\left(x^2 + y^2 + z^2\right)^{5/3}} - 1\right). \tag{2.7}$$

By substituting $z = (a+t)$ (where the thickness t is the separation distance between the GMR sensor and the MB), $d = \sqrt{x^2 + y^2}$ and $V = \frac{4}{3}\pi a^3$ into equations (2.6) and (2.7) the following equation can be obtained for the perpendicular (2.8) and parallel (2.9) magnetizations.

$$B_x = \mu_0 M \frac{a^3 (a+t) d}{\left((a+t)^2 + d^2\right)^{5/2}} . \qquad (y = 0) \tag{2.8}$$

and

$$B_x = \frac{\mu_0 M a^3}{3\left(d^2 + (a+t)^2\right)^{3/2}} . \qquad (x = 0)$$

$$B_x = \frac{\mu_0 M a^3}{3\left(d^2 + (a+t)^2\right)^{3/2}} \left(\frac{3d^2}{\left(d^2 + (a+t)^2\right)^{5/3}} - 1 \right). \qquad (y = 0) \tag{2.9}$$

In order to obtain the value of *M*, the magnetization curve for 2 µm MBs with a density of 50 mg/ml has been measured using vibrating sample magnetometry (Fig. 4). The magnetization at a magnetic field of 2 mT (magnetic field used for experiments in section 4.2) is approximately 330 A/m (0.3 emu/g). The magnitude of the magnetic stray fields originating from a single MB of diameter 2 µm is shown in Fig. 3 (a) and (b) for perpendicular and parallel magnetization directions, respectively.

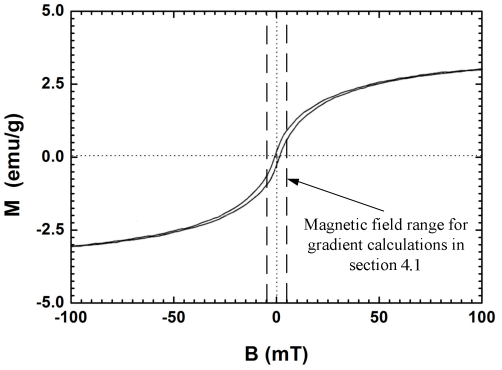

Fig. 4. Magnetization curve for 2 µm magnetic beads from Micromod® [www.micromod.de]

These figures can be used as guidelines to optimize the sensor design. In general, the sensor size should be as small as possible with respect to the amount of MBs that are supposed to be detected, to obtain a high sensitivity. Therefore, for single bead detection, the sensor size should be in the range of the bead size. However, sensors this small are difficult or impossible to fabricate (depending on the size of the MB) and limit the applicability of the device. Larger sensors are less sensitive since the stray field from the MB reduces quickly with the distance

from the MB. Depending on the sensor noise level, the maximum width of the sensor, for which it still produces a signal, can be found from Fig. 3 (a). For example, if a field of 2 μT can be resolved, a sensor width of 4 μm (in case of 100 nm thick passivation layers) is suitable. Accordingly, if MBs cover both edges of the conducting element, a sensor with 8 μm in width would be suitable. It can also be seen that the two stray field peaks with opposite polarity are approximately 1 μm away from the center of the MB. Hence, either a single sensor with a width of 2 μm, or two sensors with widths of 1 μm each located directly under each peak, could be used to detect the peak stray fields. If a larger number of MBs is supposed to be detected, they will occupy the surface above the sensor (Fig. 3(b)), where they are magnetized parallel to the sensor. For an MB trapped at the center of the conducting ring, the stray field reduces from a peak value of 28 μT to 2 μT at a distance 4 μm from the center of the bead. Thus, the sensor width should be selected according to the number of beads that are supposed to be detected. It can also be seen from Fig. 3 that B_x is inversely proportional to t, which is the thickness of the passivation layers and the conducting layer. The magnetic stray fields decrease by approximately 70 % when the passivation layer thickness is increased from 100 to 500 nm.

3 Half-Ring Shaped GMR Sensors

3.1 Design of Half-Ring GMR Sensors

In this device, half-ring GMR sensors are used for MB detection. In order to be flexible with the number of MBs to be detected, the sensor was designed with a width of 18 μm and a length of 120 μm. The conducting layer was made of gold with a thickness of 500 nm, while the passivation layers were made of Silicon Nitride (Si_3N_4) with a thickness of 100 nm. The sensor design is shown in Fig. 5. Two half-ring GMR sensing elements are located directly below and all around the micro-ring trap. The two active half-ring sensors are connected to two reference sensors in a Wheatstone bridge architecture to compensate for thermal and electrical drift and bias signals. In this way, GMRs 1 and 2 have the same lower resistance, and GMRs 2 and 4 have the same high resistance, when no MBs are present, resulting in a zero differential output (V_{out}-V_{ref}). When MBs are present, their stray magnetic fields affect only GMRs 1 and 2, changing their resistance values in opposite directions. This produces a measurable differential voltage output

$$V_{out} - V_{ref} = \left(\frac{V_{cc}}{2}\right) \times \left(\frac{\Delta r_{sc} - \Delta r_c}{R}\right). \tag{3.1}$$

where Δr_c is the resistance change due to the radial magnetic field from the conducting micro-rings, Δr_{sc} is the resistance change due to the magnetic stray fields of the MBs and the radial magnetic field from the conducting micro-rings.

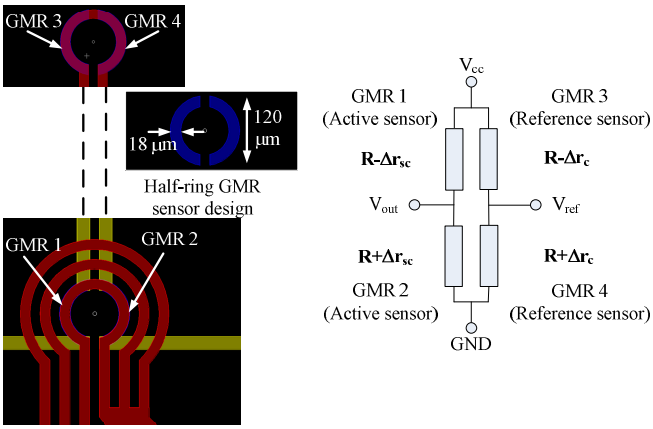

Fig. 5. Proposed design using half-ring GMR sensors and bridge circuit architecture

3.2 Fabrication Process

The spin valve type GMR sensing elements were fabricated at the Austrian Institute of Technology (AIT). The "bottom" spin valve structure of Si / SiO_2 (50 nm) / MgO (10 nm) / $Ni_{80}Fe_{20}$ (2.5 nm) / $Mn_{83}Ir_{17}$ (15 nm) / $Co_{70}Fe_{30}$ 4.5 / Ru 0.8 / $Co_{70}Fe_{30}$ 1.0 $Ni_{80}Fe_{20}$ (4 nm) / $Co_{70}Fe_{30}$ (1.5 nm) / Cu (3 nm) / $Co_{70}Fe_{30}$ (1.5 nm) / $Ni_{80}Fe_{20}$ (5 nm) / Ru (1 nm) was deposited using a Leybold Univex 450C magnetron sputtering system on an oxide-coated Silicon wafer. Argon gas was used at a pressure of 5 μbar for MgO and 2 μbar for all other materials. The deposition rates ranged from 0.03 to 0.24 nm/s. A synthetic antiferromagnet (SAF) consisting of $Co_{70}Fe_{30}$/Ru/$Co_{70}Fe_{30}$ was exchange coupled with an $Mn_{83}Ir_{17}$ layer. A 0.8 nm thick Ru layer provides strong antiparallel coupling between CoFe layers. The SAF shows superior pinning properties compared to a single ferromagnetic/antiferromagnetic (FM/AFM) pinned layer system due to the reduced net moment of $Co_{70}Fe_{30}$/Ru/$Co_{70}Fe_{30}$, which is because the magnetization of the two FM layers are aligned in an anti-parallel direction. The magnetic stability is also improved because the torque exerted by a magnetic field will be reduced for an SAF compared to a FM/AFM pinned layer. Furthermore, experimental results have shown that there is less hysteresis in spin-valves with SAFs than simple spin-valves. The principle of exchange biasing is implemented by pinning the magnetization of one NiFe layer with MnIr, while the magnetic moment of the CoFe layer is free to move in the presence of a magnetic field. A transverse magnetization direction is induced in the pinned layer during annealing at a temperature of 250 ºC under an applied magnetic field of 600 Oe. The layers were then cooled at room temperature in a magnetic field. It is also important to consider the thickness of the Cu spacer layer because, in order to obtain a GMR effect, the spacer layer must be thin compared to the mean free path of the electrons so that electrons spin polarized in one layer can pass into the other layers before their polarization is disturbed. The GMR effect is inversely proportional to

the non-magnetic spacer layer thickness. With increasing spacer thicknesses current shunting and scattering effects increase, leading to a decrease in the GMR effect. However, at very small spacer thicknesses the magnetic layers may become strongly coupled ferromagnetically due to the presence of pinholes in the nonmagnetic film, leading to a decreased GMR ratio [29].

After deposition, spin valve elements were patterned by electron beam lithography with an electron dose of 140 – 200 μC/cm². This was followed by ion beam milling with Ar gas, at an angle of 45º, beam current of 45 mA, beam and accelerator voltage of 500 V and process pressure 1×10^{-4} mbar. Au was sputtered as conducting leads to the GMR sensing element. The sense currents pass through the conducting leads to the spin valve GMR sensing element, to produce an electrical signal, the sensor output. Finally, the sensing elements were covered with a 100 nm Si_3N_4 passivation layer for covering the spin valve GMR elements and lead conductors, except parts of the connection/bonding pads. The fabricated GMR half-ring sensing elements are shown in Fig. 6.

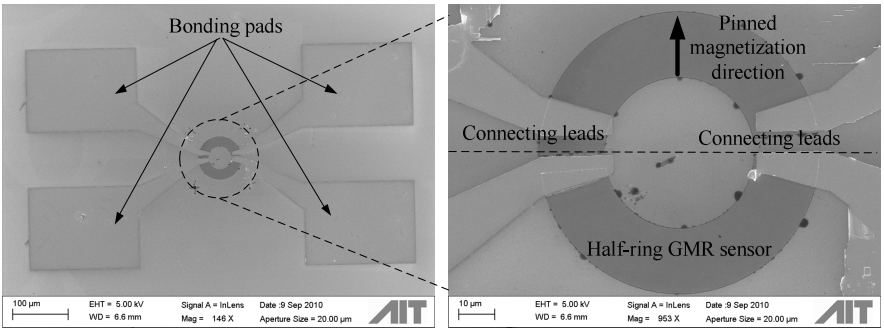

Fig. 6. Fabricated half-ring spin valve type GMR sensor

3.3 GMR Sensor Characterization

A four-probe measurement tool (Keithley 2400C Sourcemeter) was used to characterize the half-bridge GMR sensing element. A dc current of 5 mA was applied while the voltage was measured as a function of a DC magnetic field. The field was applied in the parallel and perpendicular directions to the pinned direction with a strength ranging from -10 to 10 mT. When the applied field is parallel to the pinned layer, the maximum magnetoresistance is approximately 5.9 % as shown in Fig. 7 (a). The gradient in the linear region between 1 and 3 mT is approximately 1.3 mV/mT. When the magnetic field is applied parallel to the pinned layer, the free layer magnetization follows the applied field faster than the pinned layer magnetization due to its smaller coercivity. Since the pinned layer magnetization is pinned only in one direction the magnetoresistance increases when the free layer magnetization and pinned layer magnetization are anti-parallel

and decreases when both the magnetizations are parallel as shown in Fig. 7 (a). Figure 7 (b) shows that the magnetoresistance curve is almost symmetrical when the applied magnetic field is perpendicular to the pinned direction. The characterization results verify the magnetic behavior expected from a spin valve type GMR sensor. The small signal AC sensitivity of the GMR sensing element was measured along its sensitive axis (parallel to the pinned direction) for a bias current of 5 mA. A Helmholtz coil (Schwarzbeck Mess-Elektronik HHS 5201-98) was used to produce a uniform magnetic field of 15 mT at a frequency of 140 Hz. The small signal AC sensitivity of the GMR sensing element is approximately 0.53 mV/mT as shown in Fig. 7 (c).

The performance of the MB detection system depends not only on the sensitivity of the sensor but also on many other factors like chemical or biological interferences and the noise of the sensor element or the electronic circuitry. We will discuss only the noise characteristics of the sensing element since a thorough analysis of the other factors is beyond the scope. Johnson-Nyquist or thermal noise is one of the main noise sources that have to be considered. Thermal noises are generated by the thermal agitation of electrons inside an electrical conductor and are independent of the applied voltage. The thermal noise spectral density can be expressed as

$$V_t = 4kTR\ . \tag{3.2}$$

where k is the Boltzmann constant (1.38×10^{-23} J/°K), T is the absolute temperature in Kelvin, and R is the GMR sensor's resistance in Ohms [30]. Due to its constant power spectral density throughout the frequency spectrum, except at very high frequencies, V_t can be approximated as white noise.

At low frequencies, another type of electronic noise that needs to be considered is the flicker noise or 1/f noise. 1/f noise occurs in almost all electronic devices at low frequencies and the spectral density can be expressed as

$$V_f = \frac{\alpha}{Nf}(IR)^2\ , \tag{3.3}$$

where α is the dimensionless (sometimes field dependent) Hooge constant, N is the total number of conduction electrons in the sensor (often taken as the number of atoms in the active area of the sensor), f is the frequency in Hz, I is the sense current in Amperes and R is the GMR sensor's resistance in Ohms [30]. The influence of the flicker noise decreases with increasing frequency and, from the corner frequency (f_c) on, the thermal noise dominates. A lock-in amplifier was utilized to measure the noise spectrum of the half-ring GMR sensing element at a frequency bandwidth of 0.26 Hz. Figure 7 (d) shows the noise spectrum of a single half-ring GMR element. f_c was found to be 30 Hz, which is the lowest frequency measurements should be performed at, if a high signal to noise ratio is supposed to be obtained. The noise value at f_c is approximately 6 nV/√Hz. These values were taken into consideration for experiments that were performed to detect MB weight densities in section 4.2.

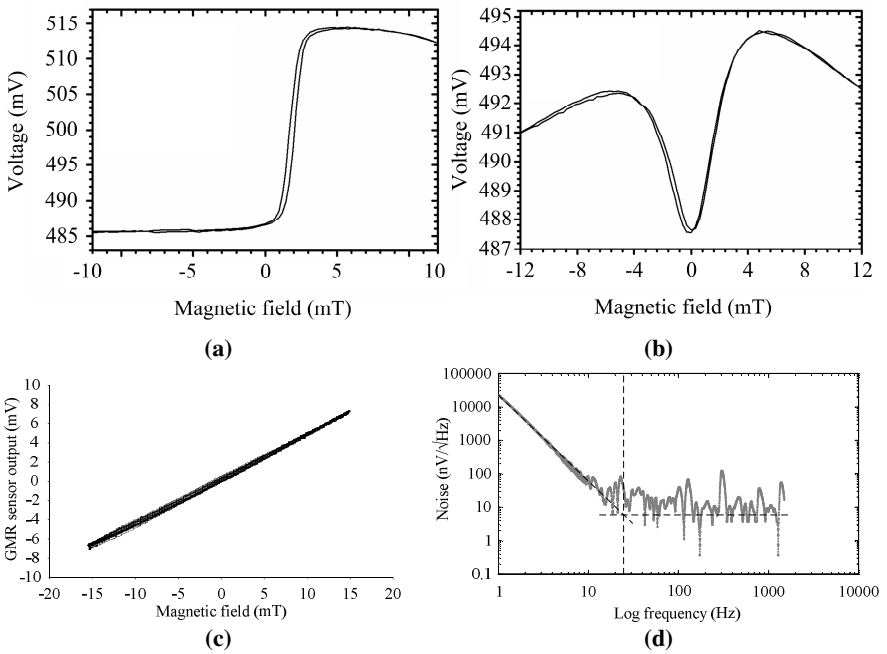

Fig. 7. (a) DC magnetic field characterization of a half-ring GMR sensor when applied field is a) parallel and, b) perpendicular to the pinned layer. (c) Small signal AC characteristics at 140 Hz. (d) Noise spectrum.

4 Experimental Results

4.1 Magnetic Bead Analysis

Superparamagnetism is a phenomenon, which occurs in ferromagnetic materials when their size is reduced below a particular value. This is the case for MBs making them easy to disperse in solution, because there is no remanent magnetization; hence, no residual force between the beads without an applied magnetic field. MBs have hydrophobic surfaces and when they interact with each other the beads agglomerate and form clusters, which increase the bead size. In order to prevent agglomeration, a stabilizer such as a surfactant or polymer is usually added during preparation. Micromod® MBs used for experiments have a core that consists of nano-sized magnetite crystals. The core is coated with a polystyrene copolymer (PEG-COOH) to prevent bead clustering. MBs of 2 μm in diameter (Micromod®) were analyzed with the aid of a vibrating sample magnetometer (VSM) to study the magnetic characteristics of MBs as a function of the bead weight density (W_d). W_d refers to the ratio of the weight of MBs to the total weight of a 1 ml solution of beads and water. Figure 8 shows the magnetic

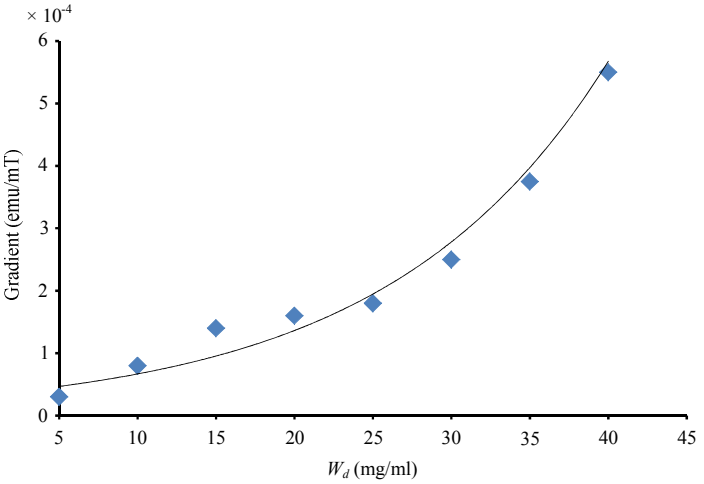

Fig. 8. Magnetic moment per magnetic field obtained from VSM analysis

moment per magnetic field (emu/mT), for applied fields from -5 mT to 5 mT and W_d ranging from 5 to 40 mg/ml. It can be seen that there is an exponential increase in emu/mT with increasing W_d. This can be explained by the distance between MBs in the sample. A high value of W_d leads to a reduced distance between MBs, causing a change of the permeance of the magnetic path through the liquid (water) and through the bead [31].

The permenace of the magnetic path through the MB can be found by

$$P_b = \frac{\mu\pi D^2}{r}\left(1+\frac{D}{r}\right), \tag{4.1}$$

where D is the diameter of a MB and r is the distance between two MBs.

The permeance of the magnetic path through water is

$$P_w = \frac{\mu_0\left(r^2-\pi D^2\right)}{r}. \tag{4.2}$$

Therefore, the permeance per unit volume is

$$P = \frac{\mu S}{l} = \frac{\mu_0\mu^* 1^2}{1} = \mu_0\mu^* = \left(P_b+P_w\right)\left(\frac{1/r^2}{1/r}\right) = \frac{P_b+P_w}{r}. \tag{4.3}$$

Expanding Eq. (4.3), we obtain

$$\mu^* = 1+\frac{\pi D^3}{r^3} \tag{4.4}$$

Since, $\vec{M} = \vec{m}/v = \chi H$, where χ is the magnetic susceptibility, and the relative permeability $\mu^* = \chi + 1$, the above equation can be written as

$$\frac{m}{H} = \frac{\pi D^3 v}{r^3}. \tag{4.5}$$

Equation (4.5) shows how the magnetic moment per magnetic field is inversely proportional to the cube of the distance between MBs. This relationship is reflected by the experimental results obtained by the VSM. Also, note that the diameter of the MBs plays a crucial part in the slope of the function.

4.2 Detection of Magnetic Bead Weight Density

In order to verify the concept proposed in this research, experiments were performed to obtain the response of a single half-ring GMR sensor for different values of W_d using 2 µm MBs (Micromod®). The experimental setup is shown in Fig. 9. The half-ring GMR sensor was placed at the center of a Helmholtz coil where the magnetic field is most uniform. A DC bias current of 5 mA was applied to the GMR sensor. The Helmholtz coil was used to generate a magnetic field of 2 mT at a sinusoidal frequency of 140 Hz. The direction of the magnetic field is in the sensitive axis of the GMR sensor. This is the same condition as in case of an integrated GMR sensor and micro-ring device, since the half-ring sensors are located directly below and all around the innermost conducting ring element. It is important to ensure that the applied magnetic field does not saturate the sensor and, consequently, its sensitivity to the smaller stray fields originating from the MBs.

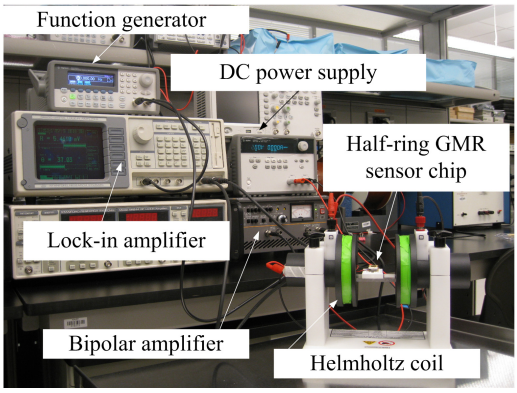

Fig. 9. Experimental setup

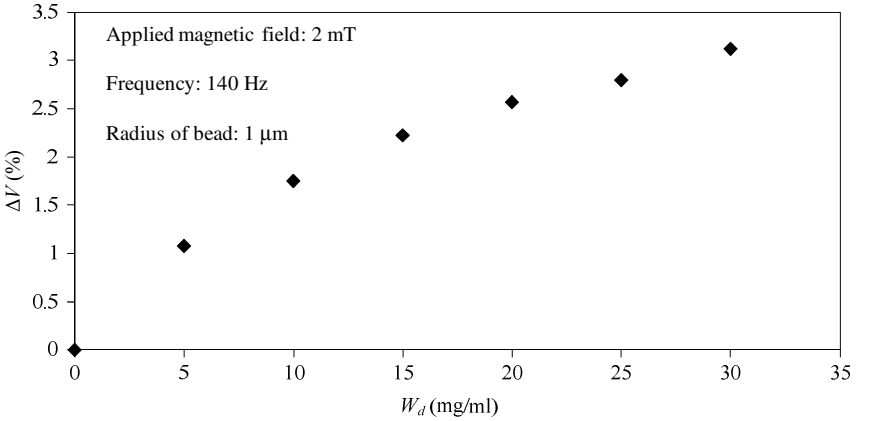

Fig. 10. Response of a single half-ring GMR sensing element to various magnetic fluid weight density values

The output signal was measured with a digital lock-in amplifier. An output signal was present even in the absence of MBs. In the integrated version of the device this signal is removed by the Wheatstone bridge circuit. However, in this experiment calibration was performed by taking the output signal in the absence of MBs as an offset, and the change in signal was calculated as

$$\Delta V\ (\%) = \frac{\left(V_{W_d} - V_{NoBeads}\right)}{V_{NoBeads}} \times 100\ . \tag{4.6}$$

MBs were applied directly on top of a single half-ring GMR sensor. A microscope glass coverslip was used to confine the MBs to the half-ring GMR sensor. Fig. 10 shows the output signal of the sensor is a function of W_d ranging from 5 to 30 mg/ml. While a linear relationship can be observed for lower W_d the signal starts saturating at higher W_d.

Even though the signal increases with increasing W_d, it is not the result expected from the discussion in section 4.1. The reason for this is that as the values of W_d become larger, the sensor signal saturates. As W_d increases the number of beads also increases. However, the number of beads that can cover the sensor and have an influence on the sensor signal is limited due to the size of the sensor. Therefore, the sensor response saturates for higher W_d. While the results show that the half-ring shaped GMR sensor is a feasible option to detect MBs trapped around the micro-ring trap the above considerations need to be taken into account for optimizing the half-ring GMR sensor for specific applications.

5 Conclusion

This research has shown the concept of an integrated device combining a conducting microstructure for concentrating and trapping MBs in order to detect them with a half-ring GMR sensor. The design, fabrication, characterization as

well as analytical, numerical and experimental analysis were carried out. Numerical analysis was performed to calculate the forces exerted on the MBs by the micro-rings. Experimental results were presented to show the manipulation of MBs to a sensing site using three rings. The number of rings can be increased to accommodate the requirements of specific applications. The GMR half-ring sensor was designed to maximize the coverage with MBs trapped by the micro-ring structure. An analytical study was carried out to optimize the sensor design with respect to the number of beads covering the sensor. By having two active half-ring sensing elements around the ring a high percentage of MBs can be detected. Furthermore, by connecting two reference sensing elements to the active elements a Wheatstone bridge circuit can be realized ensuring low noise and high sensitivity. An analytical model was presented to show the magnetic moment increases exponentially with the weight density W_d of the MBs. Experiments with a single half-ring GMR sensing element showed an increasing sensor signal with increasing values of W_d, and saturation at very high values of W_d.

Acknowledgement. The authors gratefully acknowledge Drs. Hoeink Volker and Hubert Brückl of the Austrian Institute of Technology for their help in GMR sensor fabrication. The authors thank Dr, Joachim Teller of Micromod® for providing magnetization curves for MBs used for experiments. The authors would also like to thank Drs. Ren Jian, Zhihong Wang and Messrs. Basil Chew, Xiang Yu, and Guodong Li for their help with microfabrication and material characterization.

References

[1] Berry, C.C., Curtis, A.S.G.: Functionalisation of magnetic nanoparticles for applications in biomedicine. Journal of Physics D: Applied Physics 36, R198–R206 (2003)

[2] Gupta, A.K., Gupta, M.: Synthesis and surface engineering of iron oxide nanoparticles for biomedical applications. Biomaterials 26, 3995–4021 (2005)

[3] Pankhurst, Q.A., Connoly, J., Jones, S.K., Dobson, J.: Applications of magnetic nanoparticles in biomedicine. Journal of Physics D: Applied Physics 36, R167–R181 (2003)

[4] Earhart, C.M., Nguyen, E.M., Wilson, R.J., Wang, A.Y., Wang, S.X.: Designs of a Microfabricated Magnetic Sifter. IEEE Transactions on Magnetics 45, 4884–4887 (2009)

[5] Haun, J.B., Yoon, T.J., Hakho, L., Weissleder, R.: Magnetic nanoparticle biosensors. WIREs Nanomedicine and Nanobiotechnology 2, 291–304 (2010)

[6] Heer, R., Eggeling, M., Schotter, J., Nohammer, C., Pichler, R., Mansfeld, M., Bruckl, H.: Acceleration of incubation processes in DNA bio chips by magnetic particles. Journal of Magnetism and Magnetic Materials 311, 244–248 (2007)

[7] Baier, T., Mohanty, S., Drese, K.S., Rampf, F., Kim, J., Schonfeld, F.: Modelling immunomagnetic cell capture in CFD. Microfluid Nanofluid 7, 205–216 (2009)

[8] Lim, Y.C., Kouzani, A.Z., Duan, W.: Lab-on-a-chip: a component view. Microsystems Technologies 16, 1995–2015 (2010)

[9] Yeo, L.Y., Chang, H.C., Chan, P.P.Y., Friend, J.R.: Microfluidic Devices for Bioapplications. Biomicrofluidics 7, 12–48 (2011)

[10] Gervais, L., de Rooji, N., Delamarche, E.: Microfluidic Chips for Point-of-Care Immunodiagnostics. Advanced Materials 23, H151–H176 (2011)
[11] Pamme, N.: Magnetism and Microfluidics. Lab Chip 6, 24–38 (2006)
[12] Liu, C., Stakenborg, T., Peeters, S., Lagae, L.: Cell manipulation with magnetic particles toward microfluidic cytometry. Journal of Applied Physics 105, 102014 (2009)
[13] Fulcrand, R., Jugieu, D., Escriba, C., Bancaud, A., Bourrier, D., Boukabache, A., Gue, A.M.: Development of a flexible microfluidic system integrating micro-actuators for trapping biological species. Journal of Micromechanics and Microengineering 19, 105019 (2009)
[14] Conroy, R.S., Zabow, G., Moreland, J., Koretsky, A.P.: Controlled transport of magnetic particles using soft magnetic patterns. Applied Physics Letters 93, 203901 (2008)
[15] Koschwanez, J.H., Carlson, R.H., Meldrum, D.R.: Easily fabricated magnetic traps for single-cell applications. Review of Scientific Instruments 78, 044301 (2007)
[16] Bu, M., Christensen, T.B., Smistrup, K., Wolff, A., Hansen, M.F.: Characterization of a microfluidic magnetic bead separator for high-throughput applications. Sensors and Actuators A 145-146, 430–436 (2008)
[17] Rida, A., Fernandez, V., Gijs, M.A.M.: Long-range transport of magnetic microbeads using simple planar coils placed in a uniform magnetostatic field. Applied Physics Letters 83, 2396–2398 (2003)
[18] Chitu, L., Luby, S., Majkova, E., Hrkut, P., Matay, L., Kostic, I., Satka, A.: Assembling of nanoparticle arrays using microelectromagnetic matrix. Superlattices and Microstructures 44, 528–532 (2008)
[19] Freitas, P.P., Ferreira, H.A., Graham, D.L., Clarke, L.A., Amaral, M.D., Martins, V., Fonseca, L., Cabral, J.M.S.: Magnetoresistive DNA Chips. In: Johnson, M. (ed.) Magnetoelectronics, pp. 331–396. Academic, New York (2004)
[20] Boer, B.M., Kahlman, J.A.H.M., Jansen, T.P.G.H., Duric, H., Veen, J.: An integrated and sensitive detection platform for magneto-resistive biosensors. Biosensors and Bioelectronics 22, 2366–2370 (2007)
[21] Tamanha, C.R., Mulvaney, S.P., Rife, J.C., Whitman, L.J.: Magnetic labeling, detection and system integration. Biosensors and Bioelectronics 24, 1–13 (2008)
[22] Graham, D.L., Ferreira, H.A., Feliciano, N., Freitas, P.P., Clarke, L.A., Amaral, M.D.: Magnetic field-assisted DNA hybridization and simultaneous detection using micro-sized spin-valve sensors and magnetic nanoparticles. Sensors and Actuators B 107, 936–944 (2005)
[23] Megens, M., Prins, M.: Magnetic biochips: a new option for sensitive diagnostics. Journal of Magnetism and Magnetic Materials 293, 702–708 (2005)
[24] Suh, J.D., Jung, S.D., Chung, M.A.: Spin valve ring sensors for superparamagnetic bead detections. IEEE Transactions on Magnetics 45, 2730–2732 (2009)
[25] Tao, R.: Super-strong magnetorheological fluids. Journal of Physics: Condensed Matter 13, R979–R999 (2001)
[26] Lee, C.H., Lee, D.W., Choi, J.Y., Choi, S.B., Cho, W.O., Yun, H.C.: Tribological Characteristics Modification of Magnetorheological Fluid. Journal of Tribology 133, 031801 (2011)
[27] Gooneratne, C.P., Liang, C., Giouroudi, I., Kosel, J.: A giant magnetoresistance ring-sensor based microsystem for magnetic bead manipulation and detection. Journal of Applied Physics 109, 07E517 (2011)

[28] Gooneratne, C.P., Liang, C., Useinov, A., Giouroudi, I., Kosel, J.: A half-ring GMR sensor for detection of magnetic beads immobilized on a circular micro-trap. In: Proceedings of the 5th International Conference on Sensing Technology 2011, vol. 9, pp. 106–111. IEEE (2011), doi:10.1109/ICSensT.2011.6136942, ISBN 978-1-4577-0168-9

[29] Tripathy, D., Adeyeye, A.O., Shannigrahi, S.: Effect of spacer layer thickness on the magnetic and magnetotransport properties of Fe_3O_4/Cu/Ni_80Fe_20 spin valve structures. Physical Review B 75, 012403 (2007)

[30] Wang, S.X., Li, G.: Advances in Giant Magnetoresistance Biosensors with Magnetic Nanoparticle Tags: Review and Outlook. IEEE Transactions on Magnetics 44, 1687–1702 (2008)

[31] Yamada, S., Gooneratne, C.P., Iwahara, M., Kakikawa, M.: Detection and Estimation of Low-Concentration Magnetic Fluid Inside Body by a Needle-Type GMR Sensor. IEEE Transactions on Magnetics 44, 4541–4544 (2008)

Design of Induction Gradiometer for MCG Measurement

Kunihisa Tashiro, Shin-ichiro Inoue, and Hiroyuki Wakiwaka

Department of Electrical and Electronic Engineering,
Shinshu University, Wakasato 4-17-1, Nagano, Japan
tashiro@shinshu-u.ac.jp

Abstract. This paper presents a design of an induction gradiometer for MCG measurement in our laboratory environment. The pickup coil consists of two air-core coil having a diameter of 12 cm, connected in a differential structure. With two simple equivalent circuit models, we emphasize the benefit of current detection model compared with voltage detection model. To address the problems in conventional current-to-voltage converter, we propose a differential structured current-to-voltage converter and a suitable grounding technique. For MCG measurement in our laboratory environment, we design a signal conditioning circuits for the electronics. The sensitivity is as high as 32.3 mV/pT when the frequency is higher than the cutoff frequency of 18 Hz. It is a challenge to detect MCG signal without magnetically shielded environment. To suppress environmental noise contained in the output voltage, we use digital filters and an averaging technique. Although the sensitivity is enough to detect MCG signal, the phase profile of the electronics distorts the original signal. With a modeled MCG signal generated by one-turn coil, the expected output signal is confirmed. Finally, we demonstrate the detection of magnetic field from a human heart in our laboratory environment.

1 Introduction

Recently, a lot of magnetic sensors are being presented by researchers [1]. Sensors which can detect a weak magnetic field are important for a variety of applications, such as magnetometers for space research, gradiometers for biomagnetism, current sensors for hybrid vehicles, etc. The objective of this study is the development of a portable magnetic sensor which can detect weak magnetic fields in the low frequency range. In order to detect magnetic fields of less than 1 pT, three kinds of detection methods are well known. The first detection method is the use of a superconducting quantum interference device (SQUID). Although a SQUID magnetometer is a standard tool for biomagnetic measurements, liquid nitrogen or helium and its maintenance are essential. The second detection method is the use of the Zeeman effect. While an optically pumped magnetometer is based on this method, the necessity of an alkali-metal vapor, a radio-frequency generator and a high power laser makes the system complicated. The third detection method is the use of Faraday's law, where an induction magnetometer detects the induced voltage of a pickup coil. Though most previous works mention magnetometers

S.C. Mukhopadhyay et al. (Eds.): Advancement in Sensing Technology, SSMI 1, pp. 139–164.
springerlink.com

through Faraday's law, an approach from the definition of self-inductance is important when the target of the magnetic field is weak and low-frequency. One reason for this is the necessity of an ideal analogue integrator which does not have 1/f noise, dc drift, and a limitation in gain [2].

We have been developing induction magnetometers based on the definition of inductance [3-8]. Our proposed design of the pickup coil is based on a Brooks coil [9]. This shape of the coil can achieve a maximum inductance for a given length of winding wire, and the estimation error of the inductance is less than 3 % [6]. Induction magnetometers have the ability to detect weak magnetic fields from extremely low frequencies to those in the audible range (0.01 Hz ~ 10 kHz). Although induction magnetometers were proposed in several papers [1-2, 10-15], the technical details were usually not described. Because the nature of the coil is a fundamental basis of electromagnetism, the principles of induction magnetometers are easy to understand. However, the optimization of their design with numerous parameters is not easy. In order to simplify the design for the general shape of a pickup coil, we pay attention to the important relationships between flux linkage, current and voltage. In our previous report [7], we had determined four operation modes of a magnetometer which can be categorised with two detection models and two frequency ranges. The equivalent circuits for operation modes are based on Faraday's law, the definition of inductance, and Ohm's law. Some experimental results also showed the validity of these models. Previous systems [3-7] used a conventional current-to-voltage converter in the electronics. We have already reported that our sensor is very sensitive to electrical interference, and a suitable grounding point for the electronics is definitely required for detecting a weak magnetic field [16]. Therefore, we could not use the real performance of the magnetometer.

The purpose of this study is to demonstrate magnetocardiography (MCG) measurements obtained from a human heart. Magnetic field signals from the human heart were first detected by Baule and MacFee in 1963 [17]. Cohen detected magnetic fields outside of the human scalp in a multilayer magnetically shielded room [18]. In recent years, biomagnetism measurements have received considerable attention for the early detection of heart diseases. SQUID sensors are mostly used in real-time MCG measurements. This sensor is highly-sensitive but requires liquid helium/nitrogen during measurements [19]. Although the magnetically shielded room can provide a suitable environment for MCG measurement [20], it is extremely expensive, heavy, and practical problems. It is a challenge to detect MCG signal with simple instrumentations. In order to detect MCG signal in our laboratory environment, we designed an induction gradiometer. The pickup coil consists of two Brooks coils having a diameter of 120 mm which is connected in a differential structure [16]. Because this structure of the coil cannot detect a uniform magnetic field, it can help to suppress magnetic environmental noise contained in the output voltage.

First of all, we explained the operation principle of the induction gradiometer with two simple equivalent circuit models. Assuming the mutual inductance of two Brooks coils to be zero, the models are similar as the induction magnetometer [7]. According to the simulated results with LTSpice, we proposed a differential structured current-to-voltage converter. Compared with the conventional converter, the influence of grounding perturbation on the output voltage was found to be

insignificant. By using a Faraday cage to provide an electrically shielded space, we investigated electrical interference to the gradiometer. As a result, it was found that the electrical interference to the new converter with a dummy load was negligible. We identified that the dominant electrical interference was caused by electrical field of 60 Hz, the power-line frequency, to the pickup coil. With a suitable grounding condition, there was no significant electrical interference. The noise floor level of the gradiometer and the typical magnetic field of 60 Hz which appeared in the output voltage were also confirmed. Based on the preliminary results, we redesigned the electronics in the gradiometer for MCG measurement. Simulated results by LTSpice were in good agreement with the design. Although the sensitivity was enough to detect MCG signal, it was expected that the phase profile of the electronics may distort the original signal. With a modeled MCG signal generated by one-turn coil, we confirmed the possibility to detect MCG signal. By employing method such as digital filters and averaging technique, we successfully observe the corresponding signal of 0.9 $V_{p\text{-}p}$ when the value of R-wave in the modeled signal was 100 $pT_{p\text{-}p}$. Finally, we demonstrated the detection of magnetic field near the chest of a human subject in our laboratory environment.

2 Equivalent Circuit Model

Fig. 1(a) shows a model based on Faraday's law. We assume that a homogeneous magnetic flux B [T] of frequency f [Hz] is crossed with a coil having mean radius a [m]. The induced voltage V [V] is expressed by the following equation.

$$V = -(\mathrm{d}\Phi / \mathrm{d}t) = -\mathrm{j}2\pi^2 f\, n\, a^2\, B \quad [\mathrm{V}] \tag{1}$$

Where j is an imaginary number and n is the number of coil windings. When we measure the voltage and integrate it with an ideal integrator, we can obtain the waveform of the magntic flux density. Fig. 1(b) shows a model based on the definition of inductance. The relationship between the current I [A] and flux linkage Φ is expressed by the following equation.

$$\Phi = L\, I \quad [\mathrm{Wb}] \tag{2}$$

$$I = (nSB)/L = (\pi n a^2 B) / L \ [\mathrm{Wb}] \tag{3}$$

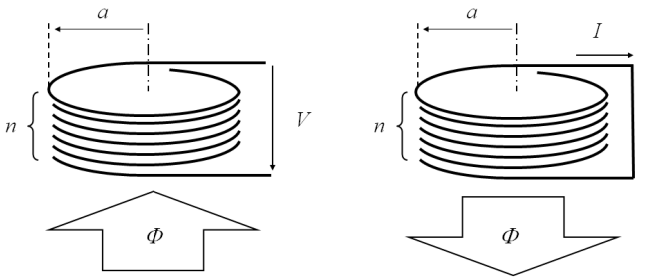

Fig. 1. Faraday's law and definition of inductance

Where L [H] is the inductance of the coil. When we measure the induced current, we can obtain the waveform of the magntic flux density. However, it should be disscussed with a finite resistance in the coil and instrumentation. Here, we consider that a pickup coil consists of two coils. The self-inductance and resistance of the coil are L_s and R_s, respectively. The coils are connected in differential structure. If the distance between two coils is relatively large, the mutual inductance is neglected. The total inductance and resistance of the pickup coil are $L = 2L_s$ and $R = 2R_s$, respectively. When a homogeneous magnetic flux is crossed with both coil, the same induced voltages appear in both coil. Because the coils are connected in differential structure, the voltages are cancelled. Therefore, a current is not induced in the pickup coil if the terminal of pickup coil is shorted. However, an induced current appears in the pickup coil if there is an imbalance of magnetic flux density in the pickup coil. We can also express the induced voltage of the pickup coil by eq(1).

Fig. 2 shows the voltage detection model. A homogeneous magnetic flux is crossed with one coil. The induced voltage is measured using instrumentation which has an input resistance of R_{in} [Ω]. Based on Thevenin's theorem, the pickup coil can be replaced with parameters of R, L, and V [7].

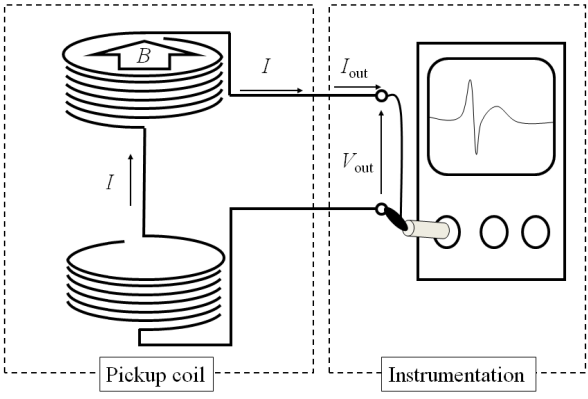

(a) Model

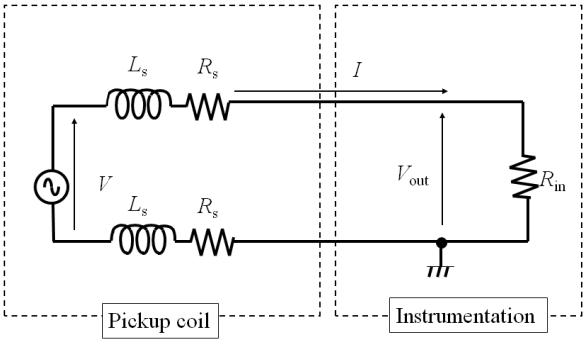

(b) Equivalent circuit

Fig. 2. Induced voltage detection model

Fig. 3 shows the current detection model with a current-to-voltage converter having a transimpedance gain, or a feedback resistance, R_f [Ω]. Because the plus pin of the opamp is connected to the ground, the input resistance is zero and the pickup coil is in a virtual short. The output voltage of the current-to-voltage converter is the product of R_f and I.

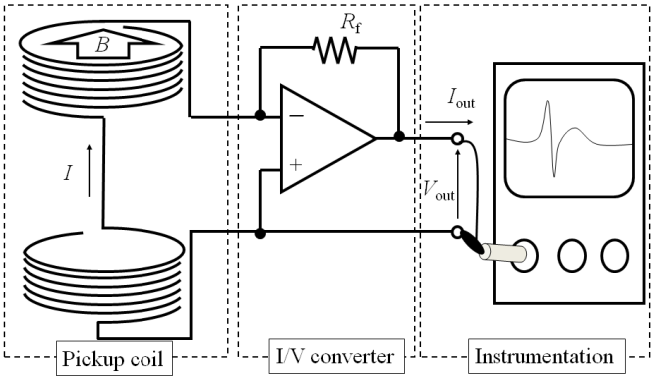

(a) Model

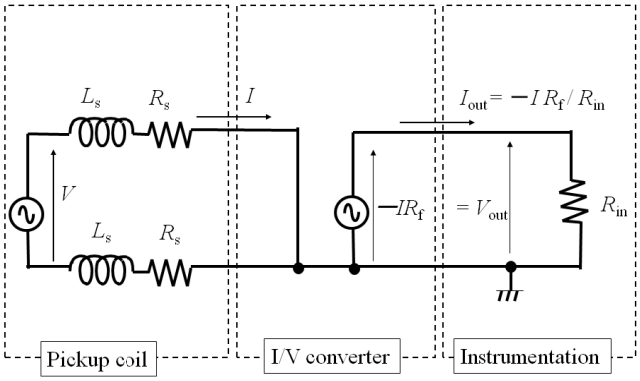

(b) Equivalent circuit

Fig. 3. Induced current detection model

The frequency response of the magnetometers can be considered by two frequency regions where the resistance or the inductance is dominant. Because the equivalent circuits of both detection types are regarded as a simple RL circuit, cutoff frequencies f_v and f_i can be defined.

$$f_v = R_{in} / (2\pi L) \quad \text{[Hz]} \quad \text{(For voltage detection model)} \tag{4}$$

$$f_i = R / (2\pi L) \quad \text{[Hz]} \quad \text{(For current detection model)} \tag{5}$$

When the frequency range is smaller than its own cutoff frequency, the output voltage is proportional to the frequency.

$$V_{out} = -j2\pi^2 f n a^2 B \quad [V] \qquad \text{(For voltage detection model)} \tag{6}$$
$$V_{out} = -(R_f/R) \times j2\pi^2 f n a^2 B \quad [V] \qquad \text{(For current detection model)} \tag{7}$$

When the frequency range is higher than its own cutoff frequency, the output voltage does not depend on the frequency.

$$V_{out} = -\pi n a^2 R_{in} B / L \quad [V] \text{ (For voltage detection model)} \tag{8}$$
$$V_{out} = -\pi n a^2 R_f B / L \quad [V] \text{ (For current detection model)} \tag{9}$$

Here, we define $|V / B|$ [V/T] as the sensitivity of the magnetometer. The sensitivity of both detection models is limited in the high frequency region. If we assumed that $R_f = R_{in}$, the sensitivities in the high frequency regions are the same. In order to simplify the equations of the sensitivity, we introduced two symbols.

$$F = 2\pi^2 f n a^2 \text{ [V/T]} \tag{10}$$
$$G = (R_f \pi n a^2) / L = (R_{in} \pi n a^2) / L \text{ [V/T]} \tag{11}$$

In this paper, we used a pickup coil which consists of two Brooks coils. This shape of the coil can achieve maximum inductance for a given length of winding wire, and the estimation error of the inductance is very low[9]. It is also known that the estimation method of mutual inductance between two Brooks coils. If the distance between the two coil is 10 times larger than the coil width, the mutual inductance is negligible. The value is 0.3 % compared with the self-inductance of one coil. Table 1 shows the specifications of our developed pickup coil for consideration in this paper.

Table 1. Specifications of the induction gradiometer

Property	Value
Brooks coil	
Mean diameter, a[m]	0.045
Coil width, c [m]	0.030
Inner diameter, $2c$ [m]	0.060
Outer diameter, $4c$ [m]	0.120
Number of windings, n [turn]	2827
Diameter of the wire, δ [m]	0.5×10^{-3}
Estimated resistivity of the wire, ρ [Ω m]	1.78×10^{-8}
Coil constant, P_0 [H/m]	1.6994×10^{-6}
Self inductance, $L_s = P_0 an^2$[H]	0.61
Resistance, $R_s = 2\pi an\rho / ((\delta/2)^2\pi)$ [Ω]	72
Induced voltage, $V = -j2\pi^2 fna^2 B$[V]	$-j113fB$
Pickup coil	
Distance between Brooks coils, l [m]	0.3
Inductance, $L = 2Ls$ [H]	1.22
Resistance, $R = 2R_s$ [Ω]	144
Cutoff frequency, $f_i = R / 2\pi L$ [Hz]	18.5
Sensitivity $(R_f/R)\times F = (R_f/R) \times 2\pi^2 fna^2$ [V/T]	$0.796 R_f f$
Sensitivity $G = R_f \pi n a^2 / L$ [V/T]	$14.7R_f$

The outer diameter is 120 mm, the inner diameter is 60 mm, the coil width is 30 mm, and the number of windings is 2827 with a copper wire of 0.2 mm in diameter. The distance between the two coils is 300 mm. Fig. 4 illustrates an example of the frequency response of the sensitivity for the two detection models. Both models require different methodologies for optimal pickup coil design. In the low frequency region, the sensitivity of the current detection model is (R_f /R) times than that of the voltage detection model. Although an increase in n makes the sensitivity large in the voltage detection model, the value of R becomes large. Because Johnson noise is proportional to $R^{1/2}$, the noise floor level of the magnetometer becomes worse. Although we can use a voltage amplifier in the voltage detection model, it should be noted that we can use a quite high the ratio of the transimpedance gain to the pickup coil resistance, R_f /R, in the current detection model. According to the considerations of the equivalent circuit model, an estimation of the resistance and inductance is very important for the design.

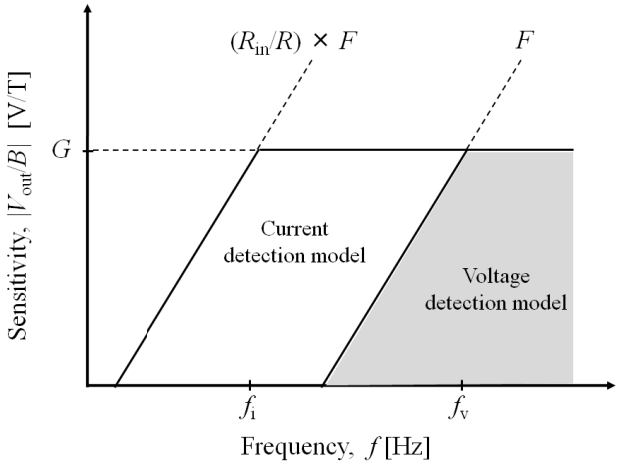

Fig. 4. Theoretical frequency response of the sensitivity for the two detection model

3 Current-to-Voltage Converter

Our proposed equivalent circuit model allows us to analyze the gradiometer with a circuit simulator, LTSpice(Linear technology Inc.). This simulator can reproduce the real properties of an op-amp made by Liner Technology faithfully. We have already reported two problems in current detection type induction magnetometers from previous experimental results. This kind of magnetometer is sensitive to power line noise and electrical interference, because the impedance of an equivalent circuit for the pickup coil is very low [16].

Fig. 5 shows the model with a conventional current-to-voltage converter for LTSpice. Because the feedback resistor R_f is 1 MΩ, the transimpedance gain is 1×10^6 V/A. In this model, practical conditions were also considered. In the power supply, a voltage source named “Perturbation” represents a disturbance in

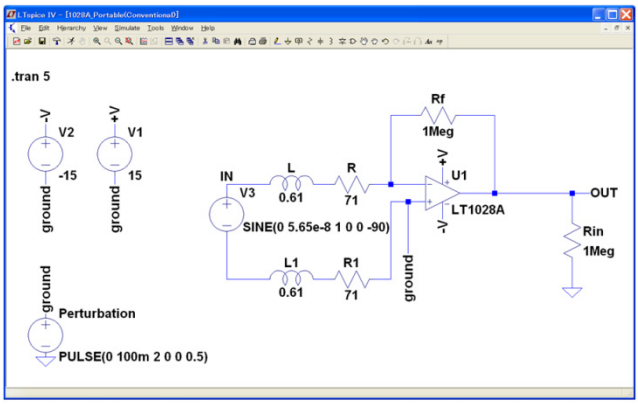

Fig. 5. A LTSpice model for a conventional current-to-voltage converter

grounding voltage. The voltage source in the pickup coil represents magnetic field crossing the pickup coil, which is expressed by eq. (1). A voltage source of 56.5 nV at 1 Hz corresponds to 1 $nT_{p\text{-}p}$.

Fig. 6 shows an example of a simulated output voltage waveform. The grounding voltage disturbance was not added. The output voltage for the magnetic field of 1 $nT_{p\text{-}p}$ at 1 Hz was 0.8 $mV_{p\text{-}p}$, which is same value as expected from eq (7). Fig. 7 shows the output voltage as a function of frequency for a magnetic field of 1 $nT_{p\text{-}p}$. The solid line represents the results simulated by LTSpice, and the dashed line represents our design with theoretical estimation. The simulated frequency response was similar as our expected. Fig. 8 shows an example of simulated output voltage waveform, which takes into account the unstable grounding.

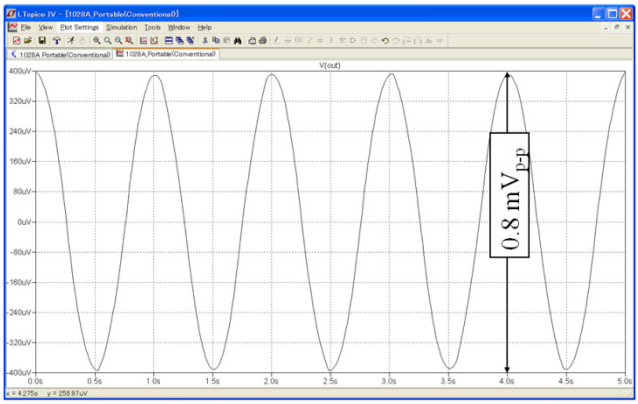

Fig. 6. Simulated output voltage waveform for a magnetic field of 1 $nT_{p\text{-}p}$ at 1 Hz. The grounding voltage disturbance was not added.

When a pulse voltage of 100 mV from 2 s to 2.5 s was added to the ground, the perturbation of the ground level appeared the output voltage, directly. Through an

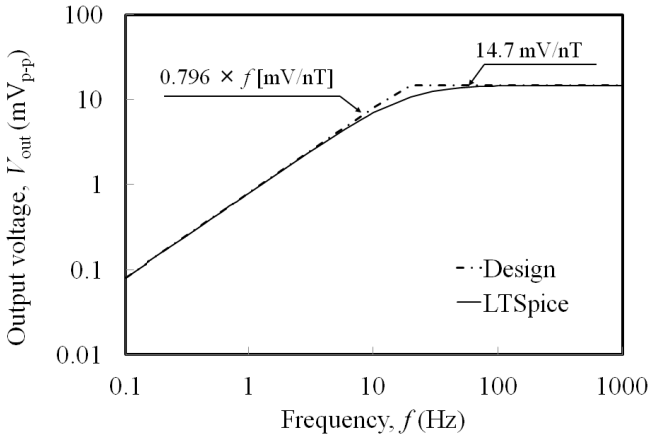

Fig. 7. Output voltage as a function of frequency for a magnetic field of 1 nT$_{p-p}$

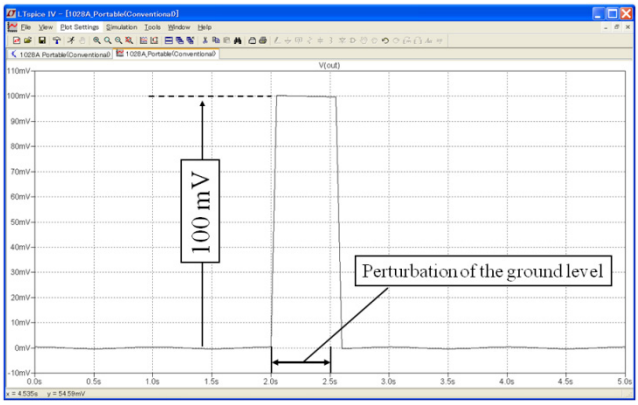

Fig. 8. Simulated output voltage waveform for a magnetic field of 1 nT$_{p-p}$ at 1 Hz. A pulse voltage of 100 mV from 2.0 s to 2.5 s was added to the ground.

experiment with a Faraday cage, we have already noticed the necessity for a suitable grounding point for electronics. However, some improvement of electronics should be considered to suppress the influence. If the sensor is based on a voltage detection model, an instrumentation amplifier is a suitable choice. It has good linearity gain even if it is under electrically noisy conditions. The most famous instrumentation amplifier consists of three op-amps. The input stage of the amplifier is a differential structure with two op-amps, which has the ability of common mode noise reduction. From these considerations, we propose a differential-input type current-to-voltage converter. To the best of the authors' knowledge, some structures of a differential input stage were proposed by other researchers [16-17]. However, we don't know this kind of a new structured circuit design for induction gradiometers.

Fig. 9 shows the model with a differential-input type current-to-voltage converter for LTSpice. The induced current in the pickup coil is converted into a

voltage with a differential-input type current-to-voltage converter. Because of the differential structure, the transimpedance gain is 2×10^6 V/A. Fig. 10 shows an example of a simulated output voltage waveform with the new converter. Although a pulse voltage of 100 mV from 2 s to 2.5 s was added to the ground, there was no significant disturbance in the waveform. The output voltage for a magnetic field of 1 n $pT_{p\text{-}p}$ at 1 Hz was 1.6 $mV_{p\text{-}p}$. It should be noted that the output voltage is twice compared with that of the conventional converter.

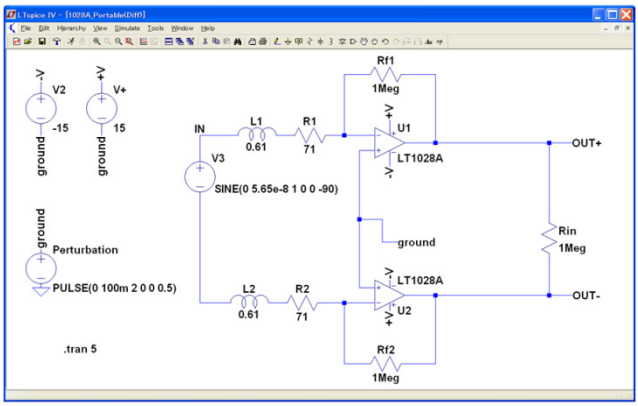

Fig. 9. A LTSpice model for differential-input type current-to-voltage converter

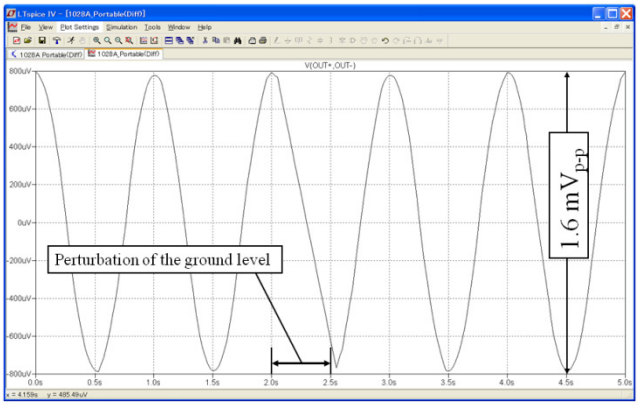

Fig. 10. Simulated output voltage waveform for a magnetic field of 1 $nT_{p\text{-}p}$ at 1 Hz. A pulse voltage of 100 mV from 2.0 s to 2.5 s was added to the ground.

4 Electrical Interference

According to the LTSpice simulation results, we confirmed that a grounding perturbation did not affect the output voltage of a differential-input type current-to-voltage converter. However, the source of the electrical interference is not unknown. In order to reveal the source, we conducted experiments with a Faraday cage.

Fig. 11 shows our constructed Faraday cage. It consists of copper mesh and wood, and is 2.0 m × 1.8 m × 1.8 m in size. The copper mesh size is 2 mm, and the diameter of the copper wire 0.45 mm. No magnetic materials are used for avoiding magnetic noise. We evaluated electric noise in our laboratory room environment using a battery powered oscilloscope (TPS2014, Textronics) and a typical voltage probe. Fig. 12 shows the evaluated laboratory rooms. (a) shows the typical laboratory room (Room 403), (b) shows a room (Room 408) where the Faraday cage is built. The measuring height is 1 m from the floor, and the measuring spacing is 0.2 m. The measured value of voltage is divided by probe distance (70 mm), and converted into units of electrical field.

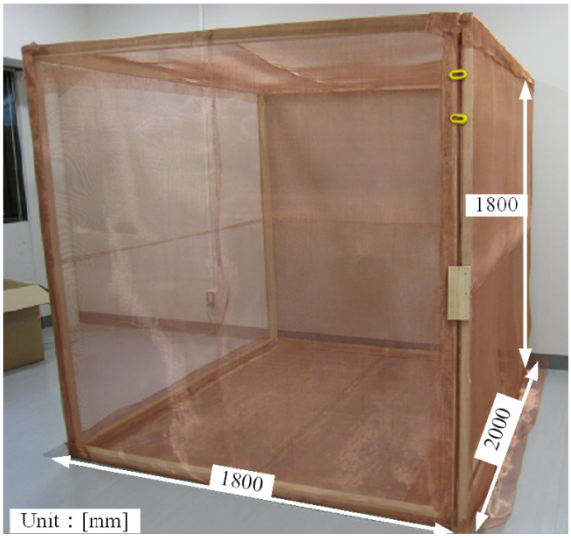

Fig. 11. Our constructed Faraday cage

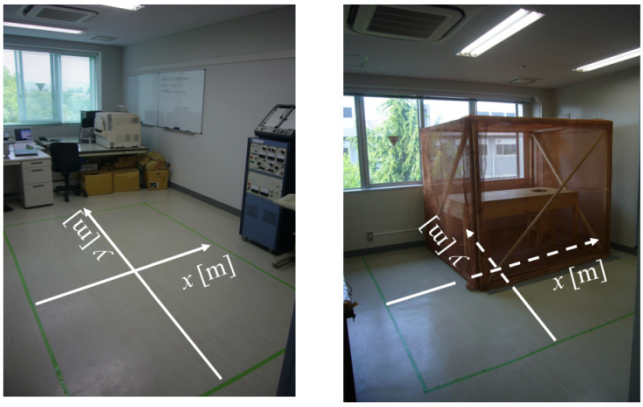

(a) Room 403 (b) Room 408

Fig. 12. Our laboratory's rooms

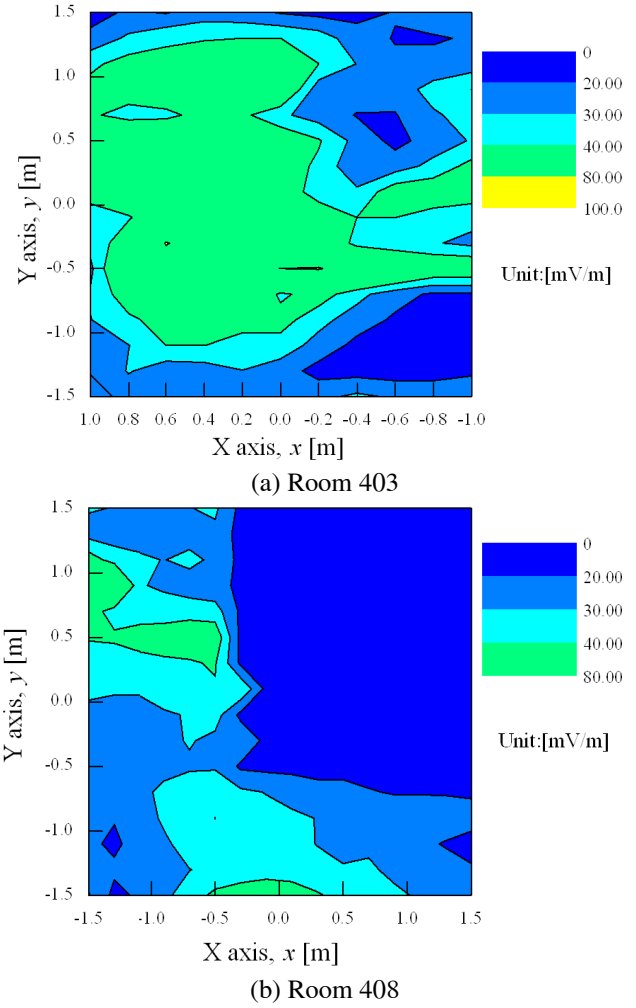

Fig. 13. Measured electrical field distributions

Fig. 13(a) shows the measured electrical field distribution in Room 403. The typical field was larger than 40 $mV_{p\text{-}p}/m$. After various traials, it was found that the primary source of noise was room light and the frequency component was 60 Hz. The measured field near the room light was larger than 200 $mV_{p\text{-}p}/m$. Fig. 13(b) shows the measured electrical field distribution in Room 403. We also confirmed that the field was large where the measuring point was under a light source. In contrast, the field inside the Faraday cage was less than 20 $mV_{p\text{-}p}/m$. In order to evaluate the magnetic shielding effect for low frequency fields of the cage, we measured magnetic noise using a fluxgate sensor (uMag-01, MEDA). The fluxgate sensor is placed on the wooden base. The measured value of geomagnetic field is

similar as 23 μT at both rooms. The measured amplitude of power line noise is also similar, as 10 to 100 nT, at the both Rooms. The differences in the amplitude were not larger than ten times between inside and outside of the cage. It means that the magnetic shielding effect of the cage was negligible.

Fig. 14 shows a schematic design of an induction gradiometer to investigate the electrical interference. The equivalent circuit is same as shown in Fig. 8 whose transimpedance gain is 2×10^6. We focused on the 60 Hz component of the output voltage, because it was the dominant frequency component of the electrical field. First of all, we used a dummy load instead of the pickup coil. The waveform of the output voltage was measured by the oscilloscope, and analyzed by FFT. The ideal output voltage is, needless to say, zero. However, an increase in the resistance produces an increase in thermal noise (Johnson noise) [6].

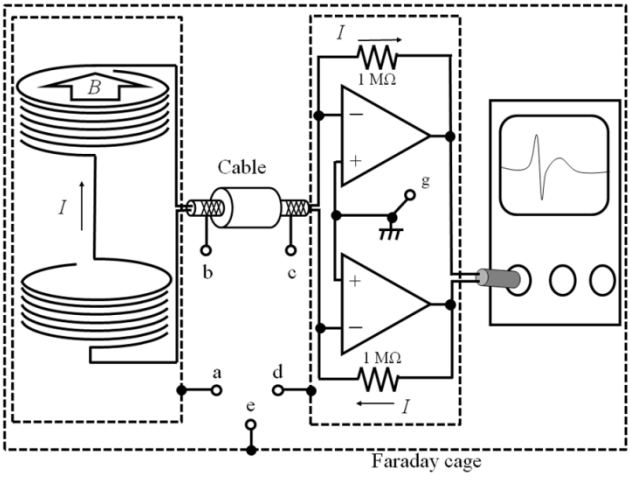

Fig. 14. Schematic design of an induction gradiometer to investigate the electrical interference

Fig. 15 shows an example of the FFT analysis result of the measured output voltage. The sensitivity of the sensor is 2.94×10^7 V/T where the frequency is higher than the cutoff frequency of 18 Hz. Because the noise floor level was about 0.1 mV, the corresponding noise floor level of the induction gradiometer was 3.4 pT. While this oscilloscope cannot analyze the output voltage of less than 0.1 mV, we confirmed that no electrical interference was observed which corresponded to the magnetic field of a few pT. It should be noted that there were no significant differences if the converter was placed outside of the Faraday cage.

Fig. 16 shows a photograph of the induction gradiometer. A battery is used for the DC power supply to the current-to-voltage converter. The point “a” and “d” represent the contacting points on the electrical shield for the pickup coil and the converter. The points “b” and “c” represent the contacting point on the cupper

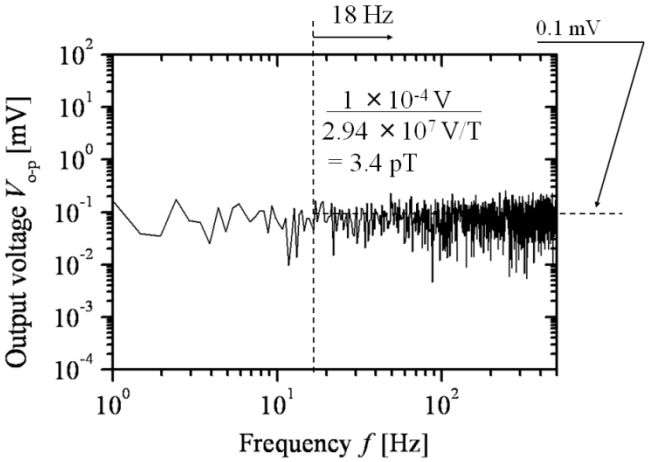

Fig. 15. An example of the FFT analysis result of the measured output voltage

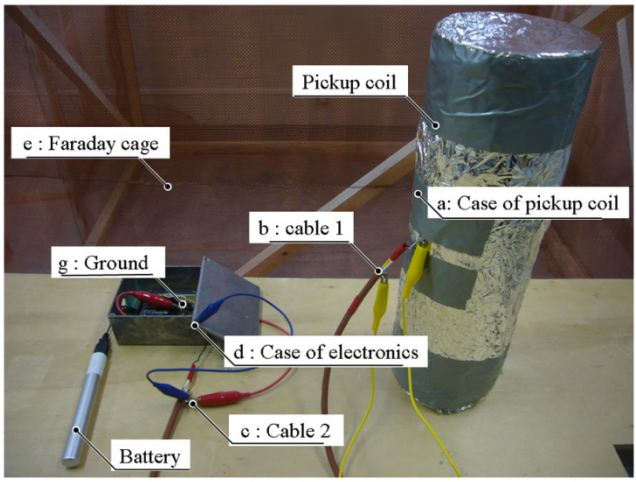

Fig. 16. Our developed induction gradiometer

mesh layer of the cable. The point "e" represents the contacting point on the Faraday cage. The point "g" represents the grounding point of the converter. The resistance values of the cables, used for the connecting points, are less than 0.2 Ω. In the previous presentation at ICST2011 [21], we investigated a suitable grounding point without the Faraday cage for practical use.

As a result, it was found that the output waveform was dramatically changed due to electrical interference to the pickup coil when the all connecting points were not connected. Fig. 17(a) shows an example of the observing output waveform outside the Faraday cage. All connecting points were not connected. The peak-to-peak voltage was about 400 mV, and the dominant frequency

component was power-line frequency of 60 Hz. In contrast, the peak-to-peak voltage was reduced about 1/20 when the gradiometer was placed inside the cage. It means that the difference in the output voltage was caused by electrical interference to the pickup coil. In contrast, there was no difference when all the connecting points were connected. Fig. 17(b) shows an example of the observing output waveform outside the cage. No significant difference was observed when the gradiometer was placed inside the cage. The peak-to-peak voltage was about 20 mV, and the corresponding magnetic flux density was 0.68 $nT_{p\text{-}p}$.

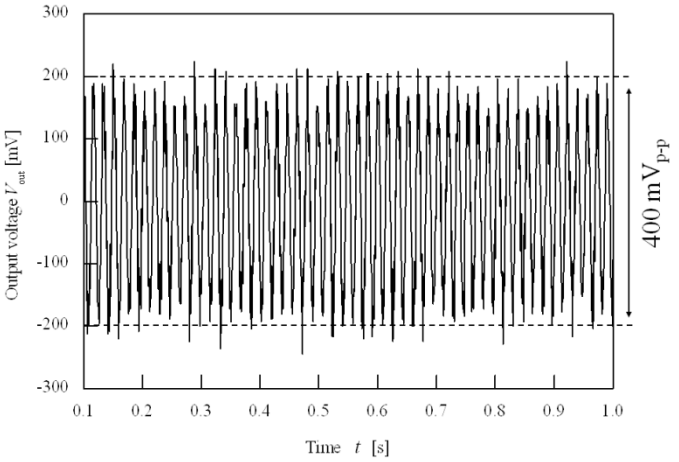

Fig. 17. (a) An example of the observing output waveform outside the Faraday cage. All connecting points were not connected.

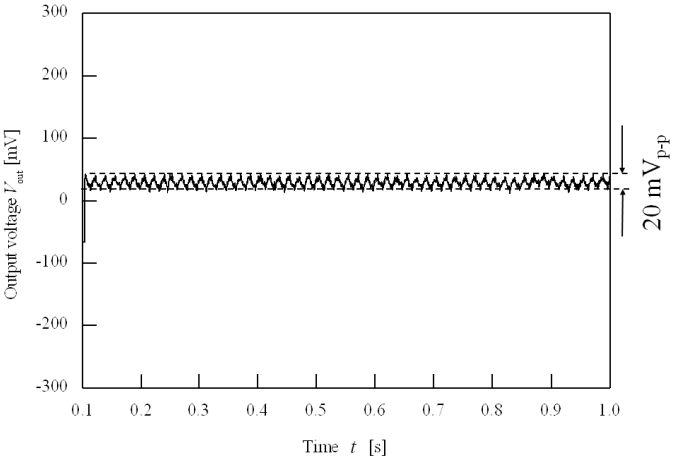

Fig. 17. (b) An example of the observing output waveform outside the Faraday cage. All connecting points were connected.

5 Electronics Design

For the observation of MCG signal from a human heart as low as 100 $pT_{p\text{-}p}$, we designed the electronics for the induction gradiometer. Fig. 18 shows a model of the electronics for LTSpice. The transimpedance gain of the current-to-voltage converter is 2×10^7 V/A which is ten times larger than before. A differential-input type HPF is also inserted to reject a finite offset voltage, and the cutoff frequency of both filters was set to 0.3 Hz. The gain of the final amplifier is 110.

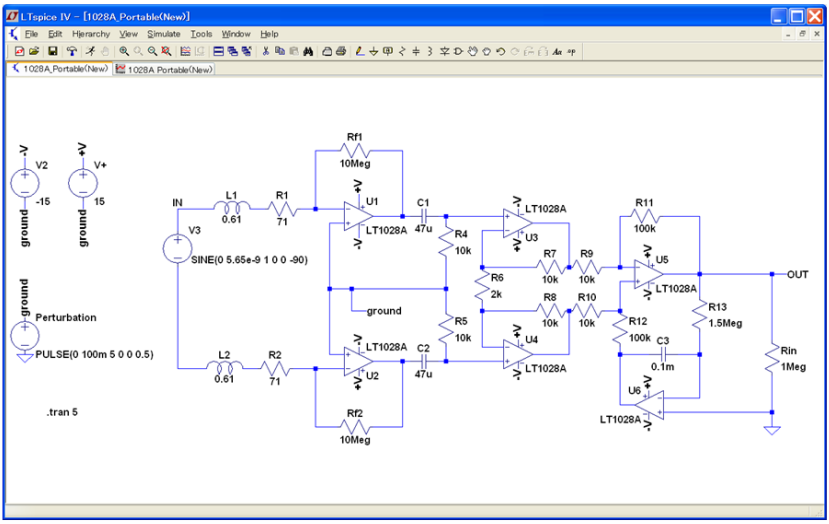

Fig. 18. A model of the electronics for the induction gradiomter

Fig. 19 shows an example of a simulated output voltage waveform with the new electronics. A voltage source of 5.65 nV at 1 Hz corresponds to 100 $pT_{p\text{-}p}$. For the demonstration of the grounding disturbance, a pulse voltage of 100 mV from 2 s to 2.5 s was added to the ground. There was no significant disturbance due to the grounding perturbation, and the output voltage for a magnetic field of 100 $pT_{p\text{-}p}$ at 1 Hz was 164 $mV_{p\text{-}p}$. We can see that a transient response due to the filters was observed rapidly. Fig. 20 shows the output voltage as a function of frequency for a magnetic field of 100 $pT_{p\text{-}p}$. Line represents the results simulated by LTSpice, and the dashed line represents our design with theoretical estimation. Although the simulated frequency response was as similar as our expected, the phase profile was changed due to the filters. Fig. 21 shows the phase profile as a function of frequency. The solid line represents the results with the new electronics, and the dashed line represents the current-to-voltage converter. It means that the detected signal would be distorted compared with the original MCG signal.

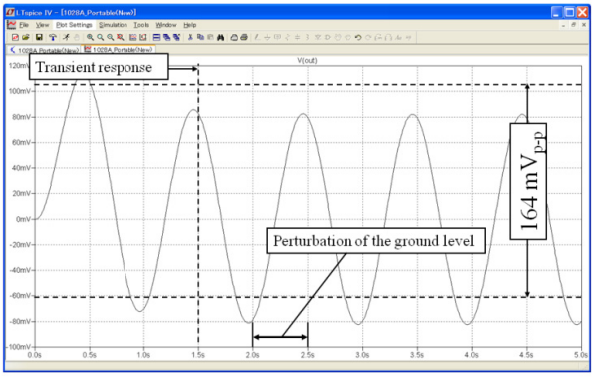

Fig. 19. Simulated output voltage waveform for a magnetic field of 100 pT_{p-p} at 1 Hz

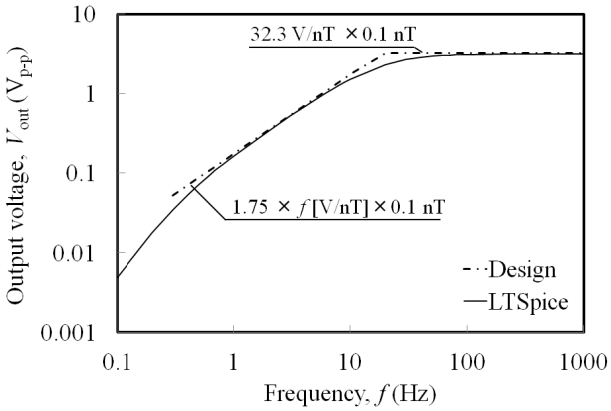

Fig. 20. Output voltage as a function of frequency for a magnetic field of 100 pT_{p-p}

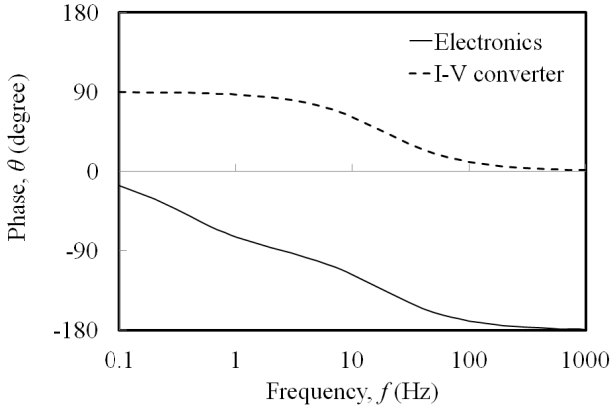

Fig. 21. Phase profile as a function of frequency

In order to check the expected output voltage waveform for the MCG signal, we demonstrated MCG measurement with a modelled MCG signal. One-turn coil of 14 cm diameter was used for generating a modelled MCG signal. A fluxgate sensor was set 2 cm away from the one-turn coil. We confirmed the relationship in the one-turn coil between generated magnetic field and applied current. From an experimental result, 120 mA_{p-p} generated magnetic field of 100 nT_{p-p}. We applied the modelled MCG signal to the one-turn coil using LabVIEW. In order to generate the signal whose R-wave peak amplitude became 1 nT_{p-p} and 100 pT_{p-p}, we set the current value of 1.2 mA and 0.12 mA. Fig. 22 and 23 show the experimental setup and schematic diagram of the measurement, respectively.

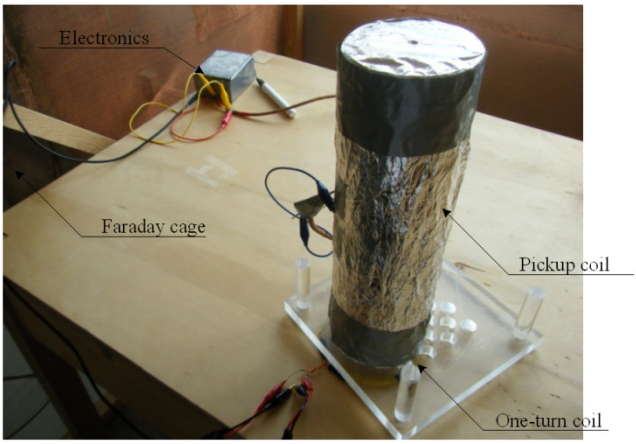

Fig. 22. Experimental setup for measurement of modelled MCG signal

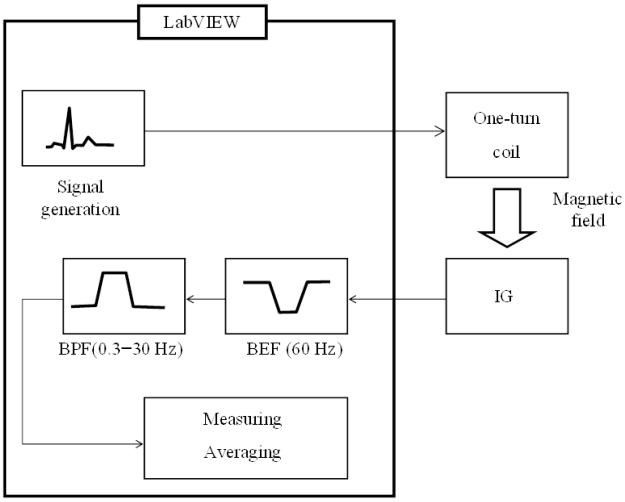

Fig. 23. Schematic design for measurement of modelled MCG signal

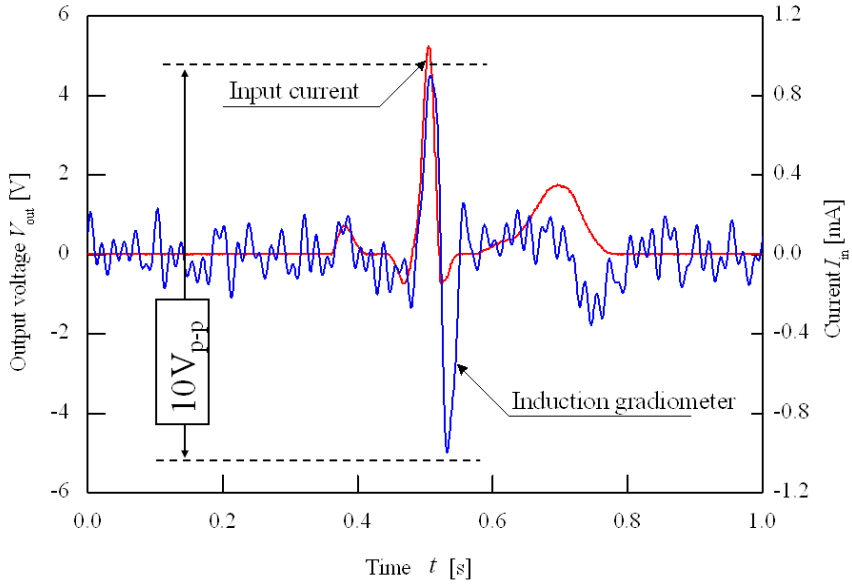

(a) R-wave of 1 nT_{p-p}

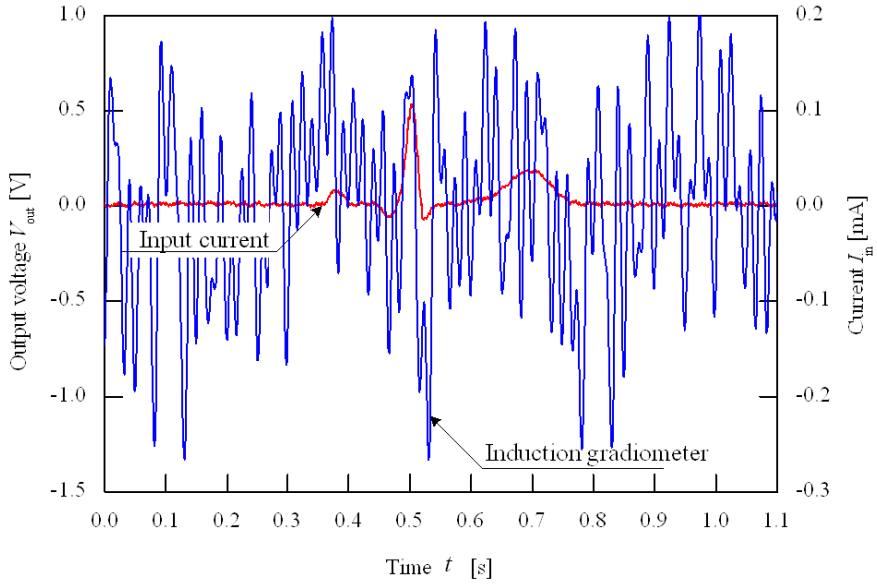

(b) R-wave of 100 pT_{p-p}

Fig. 24. Measured examples of the waveform for modelled MCG signal

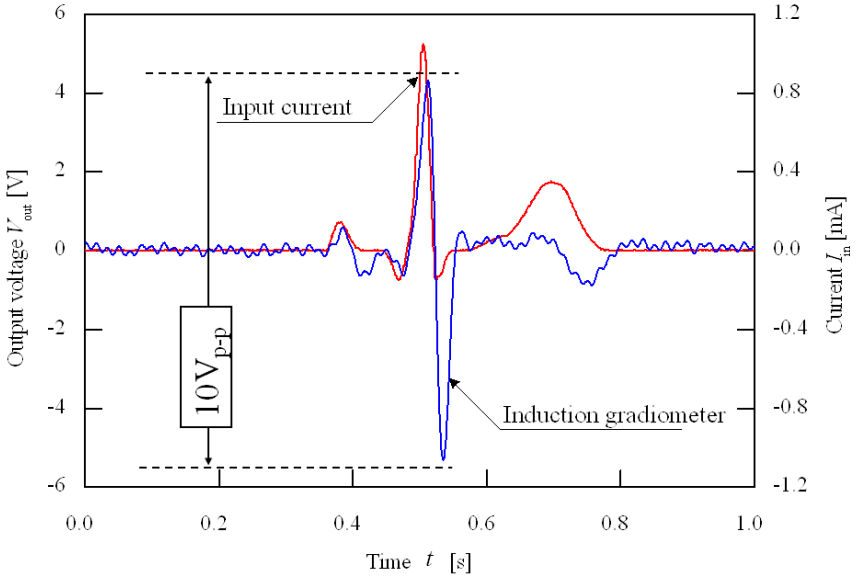

(a) R-wave of 1 nT_{p-p}

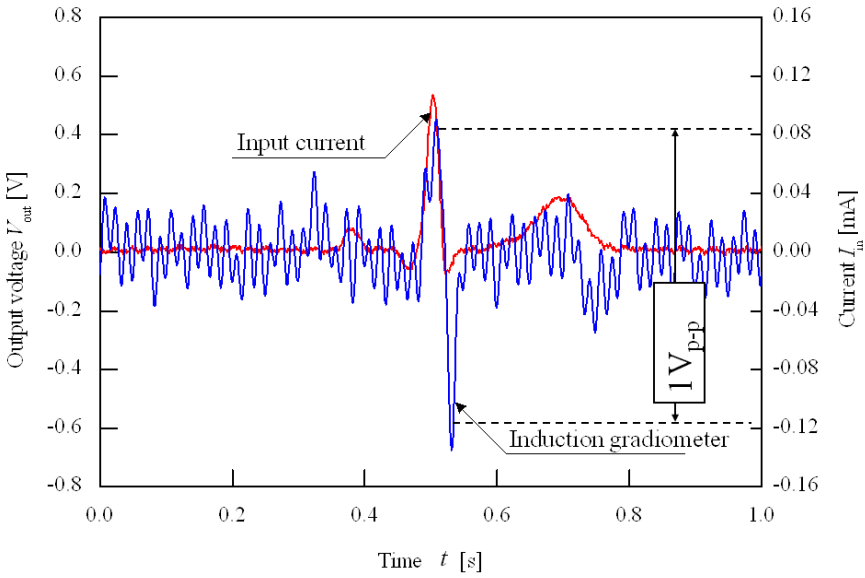

(b) R-wave of 100 pT_{p-p}

Fig. 25. Measured examples of the waveform for modelled MCG signal averaged 20 times

While the design of electronics for the induction magnetometer was as same as design mentioned before, we chose OP27 (Analog devices) for the op-amps in current-to-voltage converter. From our several considerations, the offset voltage in the output voltage with this op-amp was 10 times lower than that with LT1028A. The output signal of the gradiometer was processed by digital filter after the voltage was recorded by LabVIEW. Digital filters are band-pass filter (BPF) and band-eliminate filter (BEF). The cutoff frequency of this BEF corresponds to the power-line frequency of 60 Hz. This BPF allows passage of 0.3 ~ 30 Hz which corresponds to the frequency range of MCG signal.

Fig. 24 shows measured examples of the waveform for the modelled MCG signal. Although the output signal was distorted, we successfully observed the corresponding signal of 10 V_{p-p} when the value of the R-wave was 1 nT_{p-p}. However, we could not clearly observe the corresponding signal when the value of the R-wave was 100 pT_{p-p}. In order to suppress the noise component whose voltage was about 1 V_{p-p}, we decided to use an averaging technique. Fig. 25 shows examples of the waveform averaged 20 times. In this averaging, the applied current of MCG signal was used as a trigger signal. Even if the value of R-wave was 100 pT_{p-p}, we can find the corresponding signal of 1 V_{p-p}. From these results, we confirmed that the possibility to detect a MCG signal with this induction gradiometer.

6 MCG Measurement

It is a challenge to detect MCG signal without magnetically shielded environment. It is known that the typical value of magnetic field from human heart is a few hundred pT order. According to the electronics design, our developed induction gradiometer has sufficient sensitivity to detect the MCG signal. Although the measured signal was distorted, the output voltage was 1 V_{p-p} which corresponds to the value of the R-wave. The induction gradiometer allows us to detect an imbalance of magnetic flux in the pickup coil, and it has constant sensitivity when the frequency is larger than 18 Hz. However the corresponding magnetic noise of 60 Hz in our laboratory environment was about 0.68 nT_{p-p}. It was already confirmed that the digital filter is not enough to observe the MCG signal. In order to demonstrate real MCG measurement in our laboratory environment, we used averaging technique with ECG signal from a human heart as a trigger. We made instrumentation amplifiers for ECG measurement. The gain of the amplifiers was 100. For this measurement, a conventional bipolar lead (CM5) method with surface electrodes (Vitrode, Nihon koden) was used. The output signal was processed by digital filter after the voltage was recorded by LabVIEW. Digital filters are the same as those for the MCG measurement. Fig. 26 shows an example of the ECG measurement.

Fig. 27 shows a photograph of our experiment. A human subject lied on a wooden bed having a hole to hold the pickup coil of the induction gradiometer. The pickup coil was touched to the chest of the human subject. In order to suppress electrical interference to the pickup coil, the measurement was conducted inside the Faraday cage.

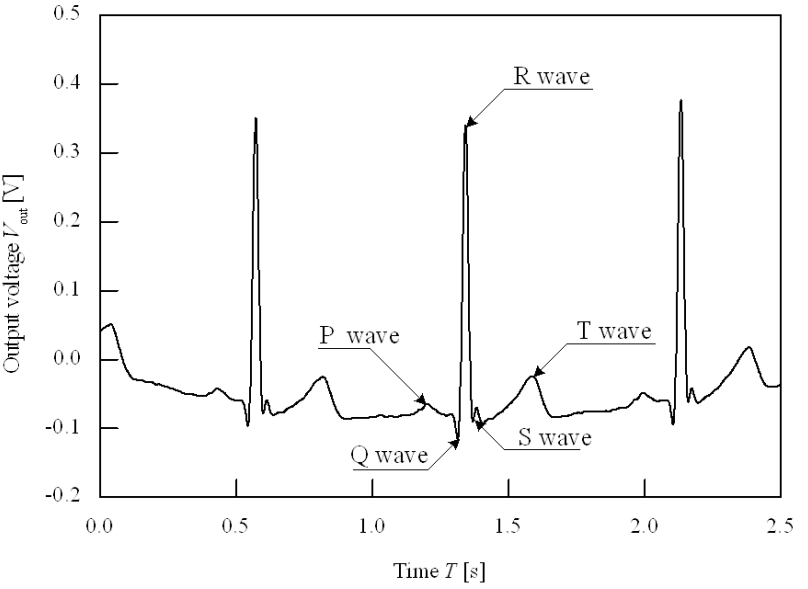

Fig. 26. An example of measured ECG signal from a human heart

Fig. 27. Experimental setup for ECG and MCG measurements from human heart

Fig. 28 shows an example of the measured waveforms of the MCG and ECG signals. As we expected, the noise component was about 1 $V_{p\text{-}p}$. In contrast, the red mark points were every time observed which corresponded to the ECG signal. Fig. 29 shows the waveforms averaged 100 times. We can find that the output voltage of 1.5 $V_{p\text{-}p}$ which corresponds to the ECG signal. According to the results with modelled MCG signal, it was an acceptable value because the corresponding R-wave peak was 150 $pT_{p\text{-}p}$.

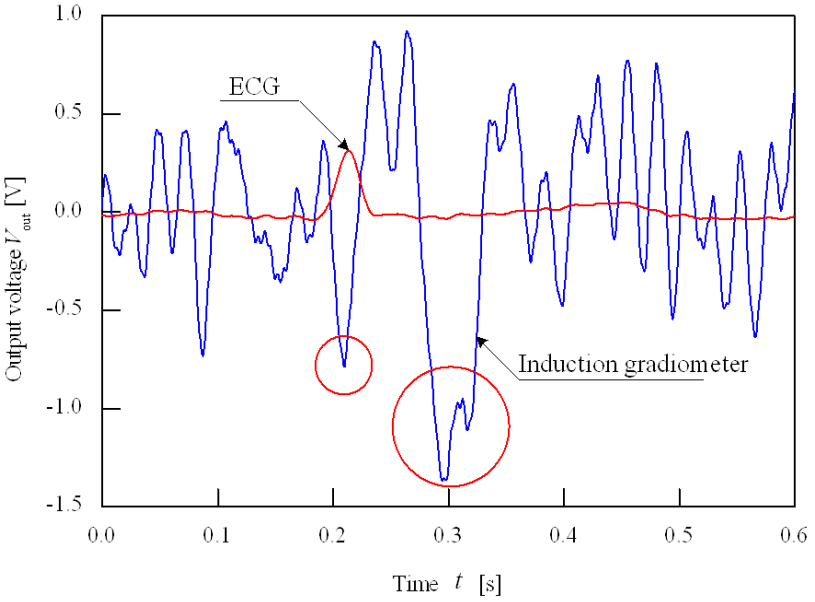

Fig. 28. An example of measured waveforms of MCG and ECG signal

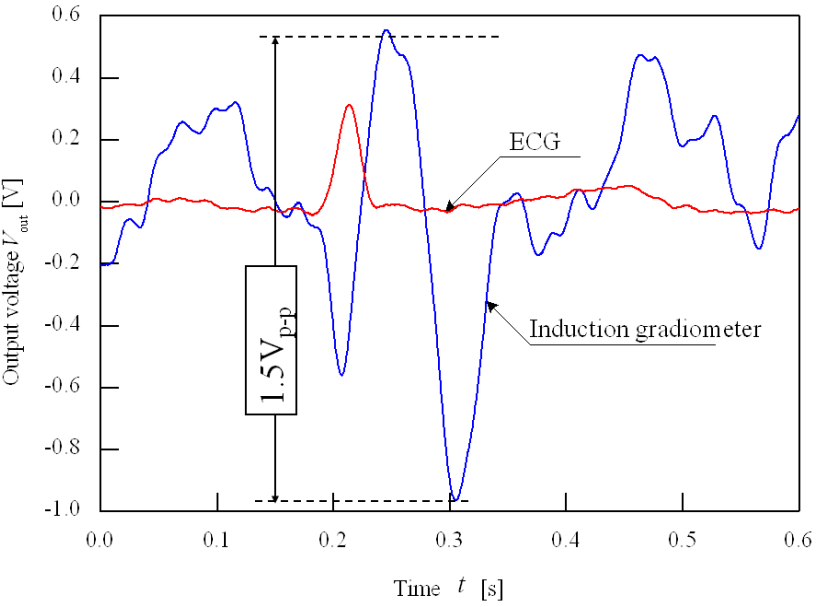

Fig. 29. An example of measured waveforms of MCG and ECG signal averaged 100 times

Fig. 30 shows an example of measured waveforms averaged 100 times without touching the pickup coil to the chest of the human subject. Because MCG signal can be observed near the surface of the human chest, it should not be observed a waveform which corresponds to ECG signal. At that time, the noise component in the output voltage was also about 1 $V_{p\text{-}p}$. It means that the noise environment was similar, and no electrical interference due to contact between human and pickup coil was found. In contrast, no typical profile was observed which corresponded to the ECG signal. From these results, we concluded that our developed induction gradiometer can detect magnetic fields from human heart.

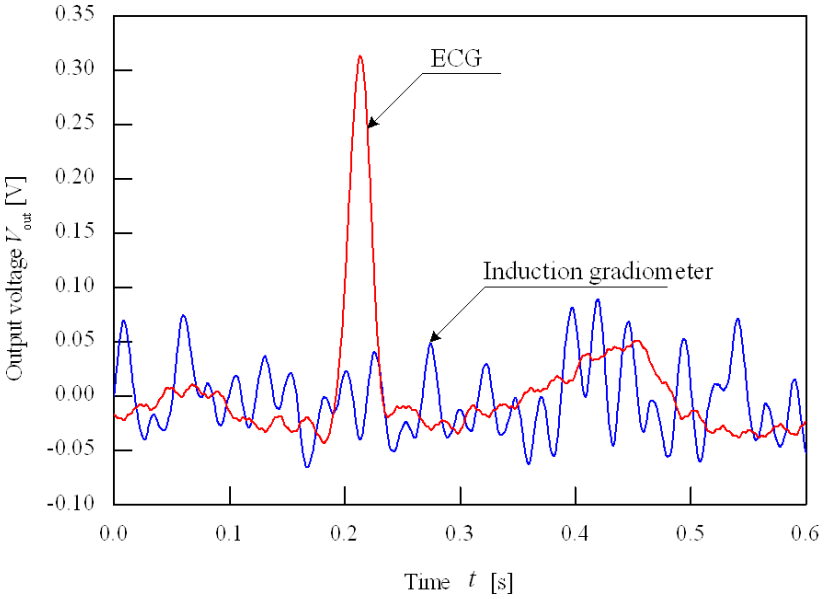

Fig. 30. An example of measured waveforms averaged 100 times. The chest of the human subject did not touch to the pickup coil of the induction gradiometer.

7 Conclusions

This paper has presented a design of an induction gradiometer for MCG measurement in a laboratory environment. It is a challenge to detect MCG signal with simple instrumentations. To detect MCG signal with an induction magnetometer in our laboratory environment, we have to reject both electrical interference and magnetic noise. Our proposed both current-to-voltage converter and grounding method effectively worked to suppress the electrical interference to the gradiometer. The differential structured pickup coil in the gradiometer allows us to suppress the magnetic noise component in the output voltage. It was less than 1 $nT_{p\text{-}p}$ in our laboratory environment. If we can use magnetically shielded

environment, the averaging technique is not required. It means that there is the possibility of simultaneous MCG measurement which is desired in clinical use. Although the detected signal was distorted by the phase profile in the electronics, an inverse filter could help to reconstruct the original MCG signal.

References

[1] Lenz, J., Edelstein, A.S.: Magnetic sensors and their applications. IEEE Sensors Journal 6, 631–649 (2006)

[2] Prance, R.J., Clark, T.D., Prance, H.: Compact broadband gradiometric induction magnetometer system. Sensors and Actuators a-Physical 76, 117–121 (1999)

[3] Tashiro, K.: Optimal design of an air-core induction magnetometer for detecting low-frequency fields of less than 1 pT. J. Magn. Soc. Jpn. 30, 439–442 (2006)

[4] Tashiro, K.: Broadband air-core Brooks-coil induction magnetometer. In: Proc. of SICE-ICASE International Joint Conference 2006, TA07-2 (2006)

[5] Tashiro, K.: Proposal of coil structure for air-core induction magnetometer. Proc. IEEE Sensor, 939–942 (2006)

[6] Tashiro, K., Wakiwaka, H., Kakiuchi, A., Matsuoka, A.: Comparative study of air-core coil design for induction magnetometer with current-to-voltage converter. In: Proc. of Second International Conference on Sensing Technology (ICST 2007), pp. 590–594 (2007)

[7] Tashiro, K., Inoue, S., Wakiwaka, H.: Sensitivity limits of a magnetometer with an air-core pickup coil. Sensors & Transducers Journal 9, 171–181 (2010)

[8] Inoue, S., Uchiyama, Y., Tashiro, K., Wakiwaka, H.: Observation of weak magnetic field in low-frequency range with portable induction magnetometer. Journal of the Japan Society of Applied Electromagnetics and Mechanics 19(supp.), 197–202 (2011)

[9] Grover, F.W.: Inductance Calculations. Dover Phoenix editions, pp. 94–113 (2004)

[10] Macintyre, S.A.: A portable low noise low frequency three-axis search coil magnetometer. IEEE Trans. Magn. 16, 761–763 (1980)

[11] Prance, R.J., Clark, T.D., Prance, H.: Compact room-temperature induction magnetometer with superconducting quantum interference device level field sensitivity. Rev. Sci. Instrum. 74, 3735–3739 (2003)

[12] Estola, K.P., Malmivuo, J.: Air-core induction-coil magnetometer design. J. Phys. E: Sci. Instrum. 15, 1110–1113 (1982)

[13] Korepanov, V., Berkman, R., Rakhlin, L., Klymovych, Y., Prystai, A., Marussenokov, A., Afanassenko, M.: Advanced field magnetometers comparative study. Measurement 29, 137–146 (2001)

[14] Sklyar, R.: Superconducting induction magnetometer. IEEE Sensors J. 6(2), 357–364 (2006)

[15] Tumanski, S.: Induction coil sensors - a review. Measurement Science & Technology 18, R31–R46 (2007)

[16] Tashiro, K., Kakiuchi, A., Moriizumi, K., Wakiwaka, H.: An Experimental Study of Stable Operating Conditions for a High-Sensitivity Induction Gradiometer. IEEE Trans. Magn. 45, 2784–2787 (2009)

[17] Baule, G., Mcfee, R.: Detection of Magnetic Field of Heart. American Heart Journal 66, 95–96 (1963)

[18] Cohen, D.: Magnetoencephalography: evidence of magnetic fields produced by alpha-rhythm currents. Science 161, 784–786 (1968)
[19] Sternickel, K., Braginski, A.I.: Biomagnetism using SQUIDs: status and perspectives. Superconductor Science & Technology 19, S160–S171 (2006)
[20] Koch, H.: SQUID Magnetocardiography: Status and Perspectives. IEEE Trans. Appl. Super. 11, 49–59 (2001)
[21] Tashiro, K., Wakiwaka, H., Inoue, S.: Electrical Interference with Pickup Coil in Induction Magnetometer. In: Proc. of the 2011 Fifth International Conference on Sensing Technology (ICST 2011), pp. 90–93 (2011)

Electroacoustic Model Based Pneumatic Fill-Level Measurement for Fluids and Bulk Solids

R. Brunnader and G. Holler

Graz University of Technology,
Graz, Austria

Abstract. Fill-level sensing remains an important issue in multiple fields of applications, ranging from industrial process control to applications in food storage, construction industry, and public and individual mobility. A main part of the established measurement methods provides satisfactory results only under consideration of a set of preconditions, and – especially in the automotive field – is competitive to modern methods only due to the low sensor cost.

Pneumatic level sensing methods have been proposed for fill-level measurement since many years, but usually have the disadvantage of providing accurate results only for perfectly sealed vessels. Hence, these methods cannot be applied to most automotive tank systems as well as to ventilated industrial tank systems. In order to make available the various benefits of pneumatic methods (independence on tank shape, tank orientation, bubble and foam formation, surface structure, …) for these application fields, we propose a pneumatic gauging method based on an electroacoustic equivalent model approach that is capable of measuring both fill level and leakage extent of a ventilated tank system in one single step.

The following sections provide a background about fill-level estimation, an overview of pneumatic fill-level measurement and the results of initial evaluation measurements of the proposed method demonstrating the applicability of the novel method.

1 Introduction

The vast majority of industrial production processes requires storage tanks for liquid and/or powdered materials in which raw materials or the actual product is stored. Monitoring the effective amount of material inside those tanks is an essential key for the automation of the process and must be performed over a wide measurement range with sufficient accuracy. In many cases it is also important to monitor the quality of the fill material (e.g. the moisture level). This quality monitoring also often requires the fill-level of the stored material.

A wide range of different fill-level measurement methods is applied in industrial applications today. Sensors based on the following gauging principles are well approved and can be obtained from various suppliers [1]:

- **Float gauges:** Especially in automotive applications, the traditional float gauge is the most widespread fill-level sensor device. The principle is based on a floating body that is used to detect the upper level of the liquid inside the tank.

S.C. Mukhopadhyay et al. (Eds.): Advancement in Sensing Technology, SSMI 1, pp. 165–180.
springerlink.com

- **Hydrostatic methods:** The hydrostatic pressure at the bottom of the tank system depends on the liquid density and the fill level. Hence, the fill-level can be derived for materials with known density. The density is usually assumed to be constant, leading to measurement uncertainties in the case of unexpected density or temperature variations.
- **Capacitive methods:** Capacitive level detection is a well proven method to measure the fill level inside tanks. The sensors are used in many applications and monitor the fill level by measuring the capacity between an electrode and the wall of the vessel or a second electrode [2]. Some systems measure the total impedance rather than just the capacitance. Capacitive methods can be implemented in contacting (electrodes in contact with media to be measured, [3], [4]) or non-contacting sensors (electrodes typically attached to the outer surface of a non-conducting vessel, [2], [5]).
- **Ultrasonic methods:** Several sensors to determine the fill level of tanks exploit ultrasonic wave propagation and reflection [6]. The basic approach is based on the time-of-flight measurement of an ultrasonic pulse between the transducer mounted on top of the tank and the surface of the stored material. The sound waves are emitted by the transducer and received back as echoes. The system determines the time between radiation and reception that is proportional to the distance between the surface of the material and the sensor head [7]. Acoustic methods are also proposed for non-contacting threshold detection in tanks containing solid media [8].
- **Radar and microwave-based methods:** Radar level measurement methods are similar to ultrasonic systems but exploit the propagation of electromagnetic waves instead of sound waves. As for ultrasonic systems, either the runtime or the phase shift between emitted and received wave packets can be used to determine the distance between the sensor head and the liquid level. The systems are mainly used for continuous level measurements. For further details refer to [9] or [10].

Several alternative approaches exist that are of minor importance in the fields of industrial process control and automotive applications:

- **Conductance measurement:** The level of conductive liquids can be measured by applying a low voltage to the liquid that drives a small current through the material to be measured. The change in the measured resistance depends on the fill level of the vessel. This is a simple and low cost method, but is restricted to conducting liquids [1].
- **Fibre-optical methods:** Optical fibre sensors can be used to detect the gas/liquid boundary in special applications [17], [18].
- **Multi-sensor methods:** In order to eliminate the sensitivity to surface orientation, multi-sensor methods can be applied to detect the fill level in solid media tanks [19]. However, multi-sensor approaches are not widely used since the cost of the system is usually higher compared to other sensors.

Even though many different solutions already exist for the measurement demands explained in the introduction, there are still some open issues left, including the precise detection of the fill level inside complex-shaped (and mainly geometrically unknown) tanks. The majority of sensor systems detects the gas/material boundary and therefore requires the knowledge of the exact geometry of the tank system to compute the actual tank fill level. Moreover, problems arise due to the fact that the material surface is usually measured only at one distinct position. This results in measurement errors for a non-uniform or twisted surface boundary of the material stored inside the tank (e.g. angle of repose of solid or powdered material, tilt or acceleration of the tank system). Finally dust and froth layers can cause tremendous measurement uncertainties.

Many of the above-mentioned problems can be avoided by using techniques detecting the free volume inside the tank as in the case of pneumatic gauging methods. These methods determine the tank fill level by observing the acoustic behaviour of the gas inside the tank. The fill level is computed by subtracting the measured free gas volume from the known (or initially measured) free volume of the empty tank. For applications where only fill level changes are considered (e.g. mixing of media at a specified mixing ratio), the knowledge of the free tank volume is not required at all.

2 Pneumatic Gauging Methods

Pneumatic gauging methods target on measuring the volume of gas remaining inside the vessel instead of determining the filling height of the stored medium. The methods are based on the acoustical behaviour of gas inside the tank. Two basic approaches are proposed in literature:

- Boyle´s Law based methods
- Helmholtz Resonator principle

2.1 Boyle´s Law Based Methods

Boyle´s Law based methods covers a range of principles that monitor state changes of the free gas inside a vessel due to an artificially introduced perturbation. The perturbation of the equilibrium can be a sudden volume change, a pressure change or even a temperature change. This results in a transient behaviour of the pressure and/or temperature of the gas inside the vessel that complies with the ideal gas law

$$p \cdot V = n \cdot R \cdot T \tag{1}$$

The method can be applied to liquid, powdered and solid media and was proposed in the late 1980s [11-13]. Experimental evaluations of the measurement method for closed tank systems exploit the modified “Boyle gas law” [20], [21]

$$p_0 \cdot V_0^{\kappa} = \left(p \pm \Delta p \right) \cdot \left(V_0 \mp \Delta V \right)^{\kappa} \tag{2}$$

with the isentropic exponent κ = 1.4, that assumes adiabatic behavior of the gas during compression and decompression. Solving (2) for V_0 yields,

$$V_0 = \Delta V \cdot \frac{1}{1 - \sqrt[\kappa]{\frac{1}{1 + \Delta p / p_0}}} \tag{3}$$

The simple model based on equation (2) is applicable only to ideally sealed tanks and an adiabatic change of state. If the behavior of the system is non-adiabatic (e.g. for media with a large surface compared to the volume), the value of the exponent will change from the isentropic value κ (known for type of gas and temperature) to the so-called polytropic value *n* (has to be determined).

Figure 1 shows measurement results for the Boyle´s Law based method for a closed and a vented vessel, respectively.

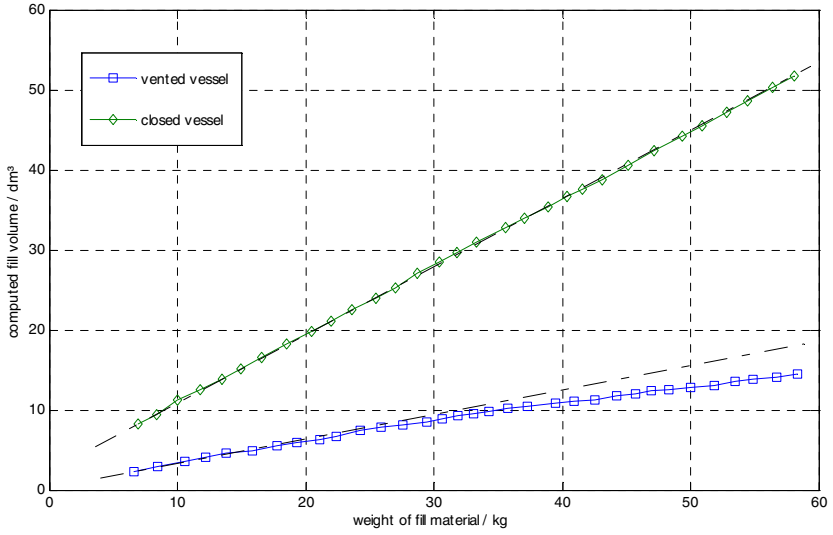

Fig. 1. Measurement results for closed (diamonds) and vented vessel (squares) neglecting the influence of tank leakage in the case of the vented vessel [25]

As observable in Figure 1, the fill level estimation leads to erroneous measurements results in the case of a vented vessel. For tanks with known leakage, the model can be calibrated at a certain known fill level to provide a better estimate of the actual fill level. However, this approach reduces the sensitivity of the method and introduces a nonlinear systematic error since the model itself can only describe the behavior of a closed tank (compare Figure 2). This is also reported by Watanabe and Takebayashi who have shown that a huge measurement error can occur when the influence of leakage is neglected [11].

Nevertheless, the approach eliminates many of the disadvantages of commonly-used measurement methods. In particular, the applied pneumatic gauging method is not sensitive to the orientation of the liquid/gas boundary (i.e. the tilt of the tank system), is not affected by tank geometry, and is not sensitive to the shape of the material/gas boundary. Using common measurement methods, the latter could only be considered by multi-sensor approaches requiring a strongly increased complexity of the sensor system [9]. However, the method was never broadly applied since the basic method works properly only for leak-proof tank systems.

2.2 Helmholtz-Resonator Principle

The Helmholtz-Resonator principle measures the free volume inside a vessel by determining the acoustic resonance frequency of the system [14-16]. The gas volume is therefor considered as the acoustic equivalent of a simple mass and spring system whose parameters are defined by the geometry of the closed chamber and the attached tube (compare Figure 2). The volume inside the tube corresponds to the oscillating mass, while the gas inside the chamber can be considered as the spring. Due to the inertia of the oscillating mass inside the tube a length correction factor l_c must be considered. Hence, changing the gaseous volume inside the chamber will change the resonance frequency of the system, according to

$$f = \frac{c}{2\pi}\sqrt{\frac{S}{(W-V)\cdot(l-l_c)}} \tag{4}$$

Therefore, the free volume inside the chamber can be derived from the natural frequency of the system by solving equation (4) for the free volume *(W-V)*. The relationship between the free volume and the resonance frequency for a nominal Helmholtz resonator is depicted in Figure 3. It can be seen, that there is a nonlinear relationship between the resonance frequency and the free volume. Also the lower sensitivity for higher free volumes (i.e. for lower fill levels) is a disadvantage of this principle, since this fill level range is of particular interest (e.g. in automotive applications).

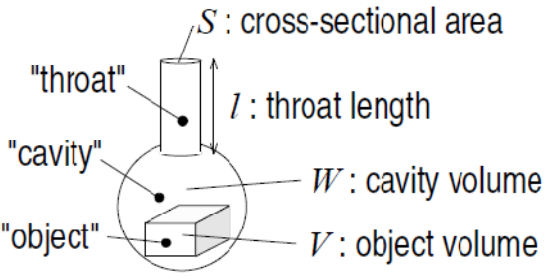

Fig. 2. Helmholtz-Resonator [14]

An exemplarily application of the principle is the measurement of the volume of an object inside the cavity if the "throat" (ventilation) is known [14]. Unfortunately additional leakages or other changes of the "throat" will cause measurement errors. Hence, this principle is only applicable for tank systems with known leakage condition. However, the key issue to be solved in order to apply the method in a broader field is its applicability to arbitrary non-sealed (vented) tank systems. Unfortunately actual Helmholtz-Resonator based sensors cannot handle arbitrary ventilated tank systems as required in many applications.

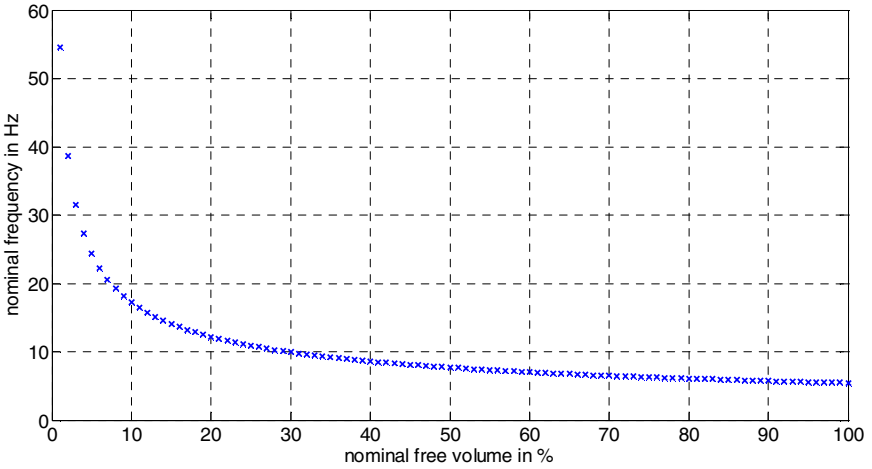

Fig. 3. Resonance frequency of Helmholtz-Resonator vs. free volume

3 Electroacoustic Model Approach

In order to compensate for the limitations of current pneumatic gauging methods, we propose the implementation of an extended pneumatic gauging method capable of distinguishing between sensor readings resulting from fill level changes and sensor readings induced by tank leakages and ventilation [21, 22, 23, 25, 26].

The electroacoustic model approach takes advantage of the effect that the vented tank can be modelled as a damped resonant circuit. For low frequencies this can be done with lumped elements, since wave propagation effects can be neglected in this case. Figure 4 shows the electroacoustic equivalent circuit of a ventilated tank in pI-analogy [24]. In this analogy the acoustic stiffness of the free volume is represented by an inductance, the acoustic mass is represented by a capacitance and the acoustic losses are modelled by resistances (exactly they are acoustic conductances).

Given that both volume velocity and pressure variation are harmonic quantities, the complex acoustic admittance can be defined as

$$\underline{Y}_a = \frac{\underline{q}}{\underline{p}} \tag{5}$$

with volume velocity q and pressure variation p.

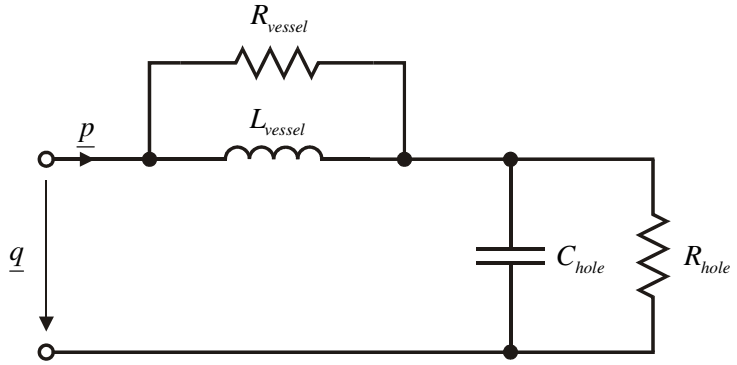

Fig. 4. Electroacoustic equivalent model [22]

Therefore, in the frequency domain the acoustic admittance can be written as

$$\underline{Y}_a = \left. \frac{\frac{R_{vessel}}{L_{vessel} \cdot C_{hole}} + \frac{R_{vessel} + \cdot R_{hole}}{R_{hole} \cdot C_{hole}} \cdot s + R_{vessel} \cdot s^2}{\frac{R_{vessel}}{R_{hole} \cdot L_{vessel} \cdot C_{hole}} + \left(\frac{R_{vessel}}{L_{vessel}} + \frac{1}{R_{hole} \cdot C_{hole}} \right) \cdot s + s^2} \right|_{s=j\omega} \tag{6}$$

To get the free volume of the tank, the static pressure p_0 is needed. With this information the free volume can be related to the inductance as follows:

$$L_{vessel} \sim \frac{V_0}{\kappa \cdot p_0} \tag{7}$$

Hence, if the inductance value is determined, the free volume inside the tank can be calculated from the static pressure p_0 when the behaviour of the gas (represented by the isentropic exponent κ) is known.

An indicator for the leakage of the tank is the capacitance value, which is – given the pI-analogy – represented by the so-called acoustic mass m_{hole}/A^2_{hole} of the tank-vents. This quantity is a factor that describes the mass of the gas in relation to the acoustic active surface of the vent(s). Therefore it defines a quality factor for the leakage rather than a physical value. Nevertheless, it is a good parameter to quantify tank leakage. The relationship between the capacitance value and the gas mass and surface, respectively, of the vents is as follows

$$C_{hole} \sim \frac{m_{hole}}{A^2_{hole}} \tag{8}$$

The acoustic conductances represent the active losses (friction, radiation) of the system.

4 Experimental Setup

The experimental setup is shown in Figure 5. Figure 6 depicts a schematic block diagram of the measurement principle for the electroacoustic model approach. As visible in the figures, an actuator and several sensors are necessary.

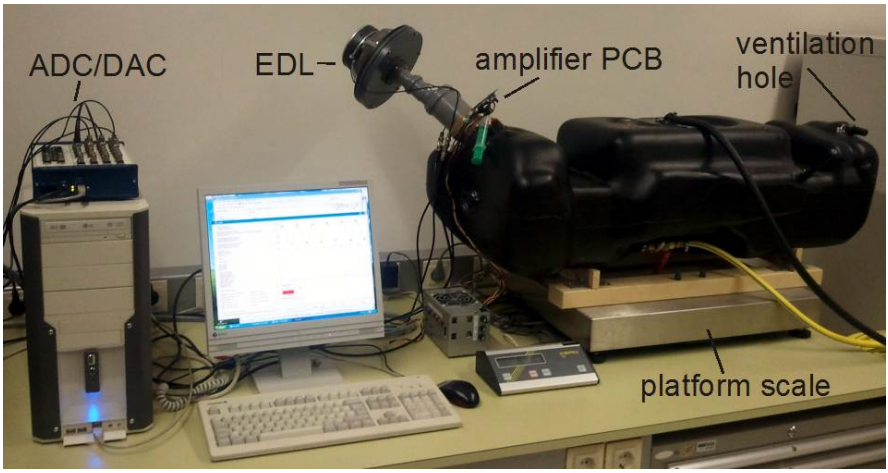

Fig. 5. Overview of the measurement setup [25]

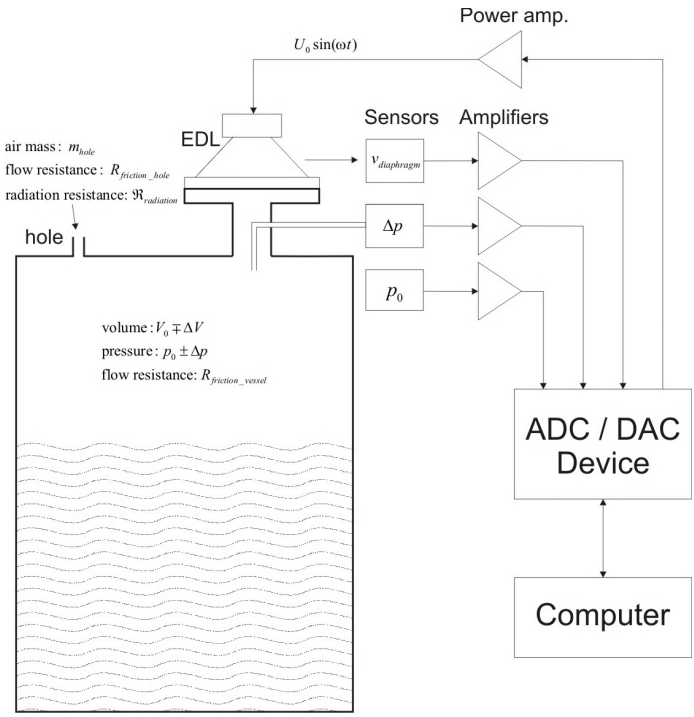

Fig. 6. Schematic block diagram [25]

4.1 Actuator

To excite the gas inside the tank system an actuator is necessary. Therefore an electrodynamic loudspeaker (EDL) is used, which enables introducing defined perturbations (i.e. curve shape, amplitude, frequency range).

4.2 Sensors

To achieve the acoustic parameters of the electroacoustic model, three measurement values (pressure variation, static pressure and volume velocity) are collected. To obtain these quantities a set of sensors exploiting different physical effects is used.

- **Pressure sensors:** Since the ranges of the measurement values highly diverge for the pressure variations (well below 1 kPa) and the static pressure (around 100 kPa), a setup with two separate sensors with appropriate measurement ranges and different sensor principles (e.g. electrostatic microphone, piezoelectric sensor) is used.
- **Volume velocity measurement:** To obtain the actual volume change, the membrane displacement is detected. This is done with a second coil on the electrodynamic loudspeaker, in which a membrane-velocity dependent voltage is induced. With this information on the actual membrane velocity and the known membrane surface the volume velocity can be calculated.

5 Experimental Results

5.1 Measurement Procedure

To demonstrate the applicability of pneumatic methods to vented tanks, we use the described electro-acoustic equivalent circuit model [24] that maps acoustic parameters of the sensor/tank system to idealized components in an electrical equivalent circuit [22], [25]. Figure 7 shows received acoustic admittances for different fill levels of a vented automotive fuel tank. Since we expect a nonlinear dependency between friction losses and pressure level, all measurements were done at the same pressure level.

To obtain the values of the lumped element parameters (R_{tank}, R_{hole}, L_{tank}, C_{hole}), a parameter fitting is done. For the optimization the MATLAB® optimization

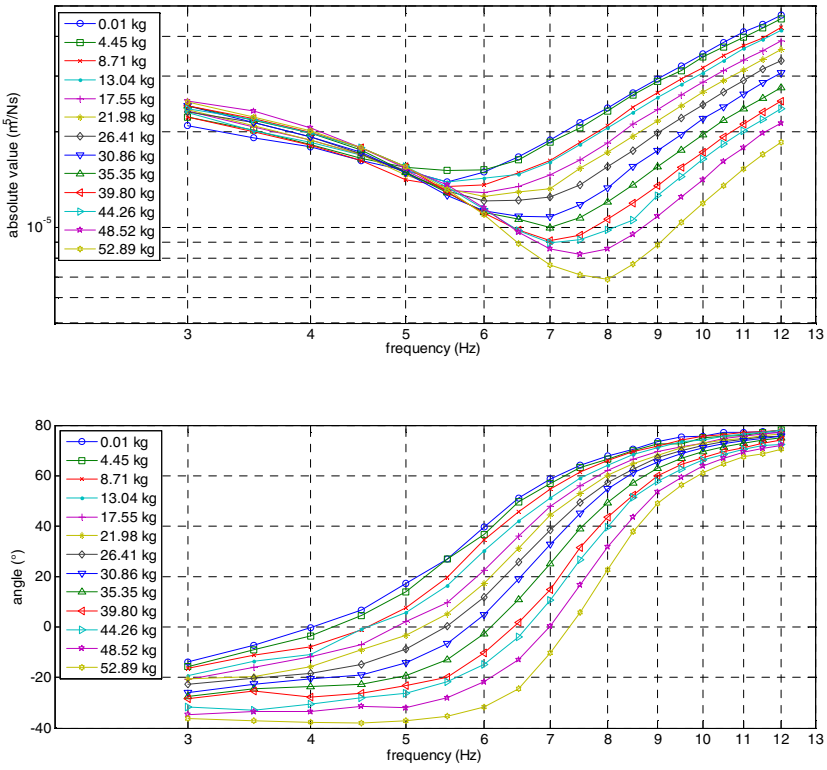

Fig. 7. Acoustic admittance of automotive fuel tank [25]

toolbox function "lsqnonlin" is used. This function minimizes a least square problem of the form

$$\min_x \left\| f(x) \right\|_2^2 = \min_x (f_1(x)^2 + f_2(x)^2 + \ldots + f_n(x)^2) \tag{9}$$

where $f_x(x)$ represents the error between measured and simulated acoustic admittance for the given excitation frequency x.

Figure 8 shows the result of one optimization process. The green crosses represent the measured acoustic admittance values. The blue line depicts the simulated acoustic admittance. The simulated acoustic admittance is calculated with the parameter values, received from the optimization function, according (6).

As result from the optimization process, the model parameters are obtained for each fill level of the tank. Therefore, the free volume can be calculated from (7). As there is no additional information provided in the last computation step (calculation of the free volume out of the inductance), the subsequent diagrams show the estimated values of the electroacoustic equivalent model elements instead of the free volume.

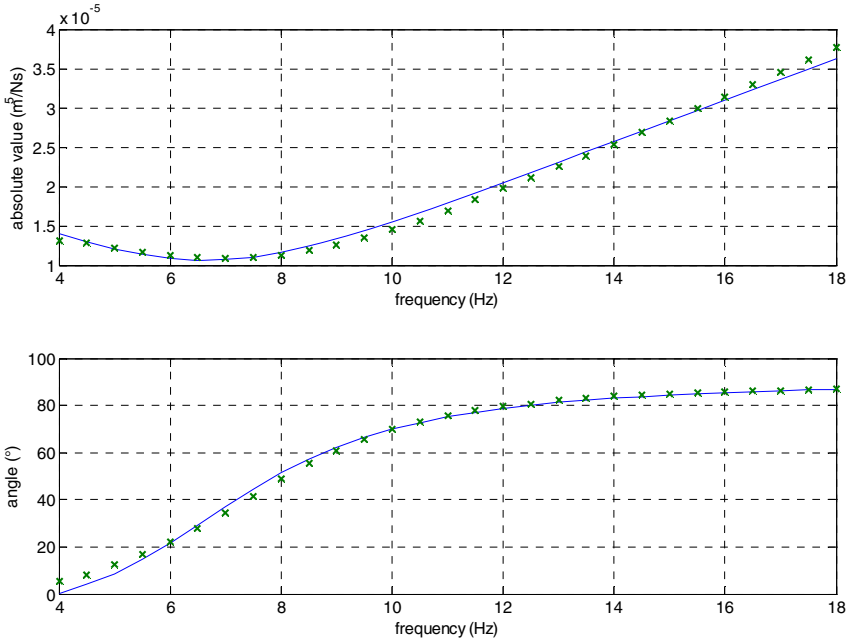

Fig. 8. Result of the parameter fitting demonstrated for the tank filled with 58.39 kg of water and one opened ventilation hole [22]

5.2 Measurement Results for Automotive Fuel Tanks

We carried out evaluation measurements using different automotive tank systems to assess the possibility of applying the pneumatic method to vented tanks by using a generalized model that considers the effect of small ventilation holes [22]. Figure 9 shows the automotive fuel tanks used for the measurements.

Fig. 9. Automotive fuel tanks used for measurements (from left to right: Tank A, Tank B, Tank C) [27]

5.2.1 Fill Level Estimation

To achieve the "in-vehicle" setup the fuel tanks were built-up including all auxiliary devices used in automotive applications (i.e. pressure equalization line, activated coal filter if applicable, fuel filler neck and filling pipe). Only the fuel

pump and fuel withdrawal line were dismounted for the measurements. According to Figure 5 the measurement devices (actuator and sensors) were fitted onto the top of the fuel tanks and the total setup was placed on a platform scale. The platform scale is used to get the reference fill level (i.e. net-weight) for the measurements. To simplify the handling, water is used as fill material instead of gasoline or diesel. This simplification does not influence the behavior of the system basically. Mainly the isentropic exponent changes due to the gaseous hydrocarbon inside the fuel tank.

A series of measurements is done for each automotive fuel tank at different fill levels. Due to the fact that the ventilation condition is not varied during the measurements, the results of the measurements should show a constant value of the capacitance for each series of measurements and a linear decreasing value of the inductance, respectively. The absolute value of the capacitance varies due to the different ventilation conditions of the fuel tank systems. Also the starting value of the inductance varies between the fuel tank systems due to the different empty volumes of the three tanks. Figure 10, Figure 11 and Figure 12 show the results for these series of measurements.

As shown in Figure 10 the estimated capacitance for tank A varies a little bit. The inductance obviously shows a decreasing behavior. Therefore, both results are in accordance to the theoretical considerations. Tank B and tank C show similar behavior, although the deviations from the expected values increase slightly.

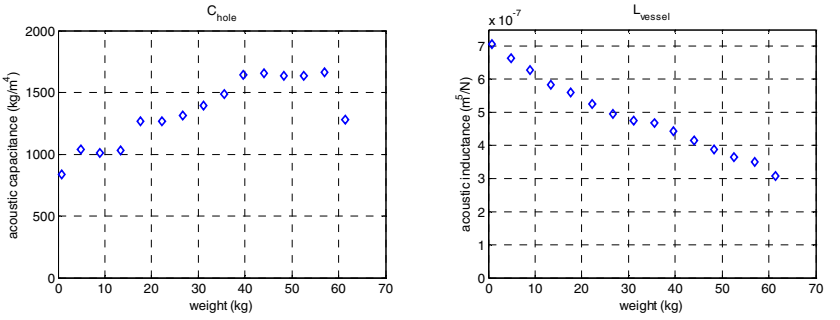

Fig. 10. Estimated values of the equivalent circuit model for tank A [27]

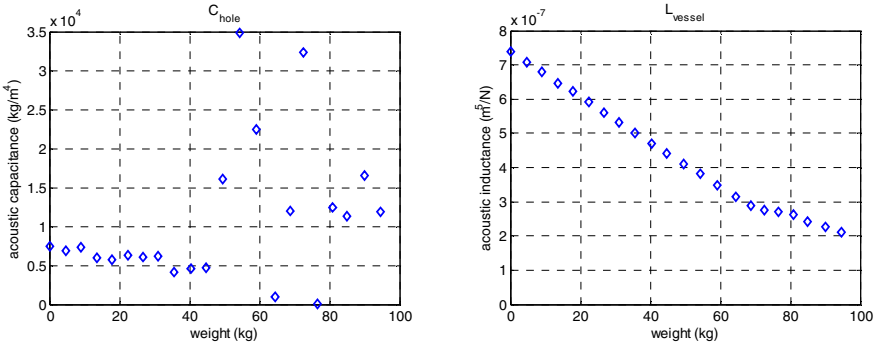

Fig. 11. Estimated values of the equivalent circuit model for tank B [27]

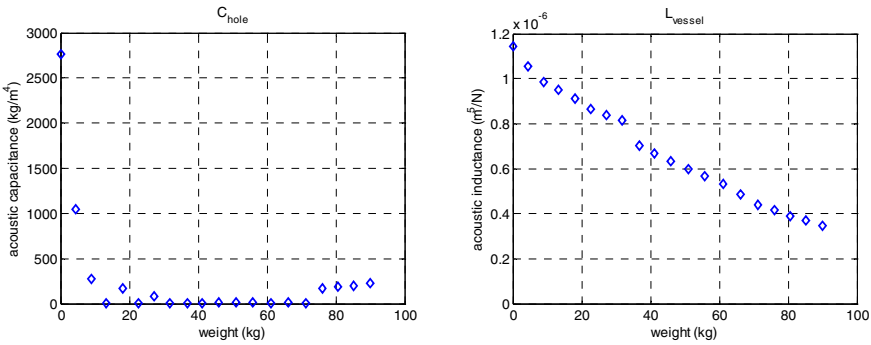

Fig. 12. Estimated values of the equivalent circuit model for tank C [27]

5.2.2 Leakage Estimation

Additional investigations were done regarding the sensitivity to changes of the ventilation condition. For this purpose tank B was modified. Instead of the original ventilation condition the openings for the pressure equalization line are used as separate holes. Therefore, they can be used to generate a set of predefined ventilation conditions. With this modification three ventilation holes are available, which can be opened or closed depending on the desired configuration:

- Two holes are located near the loudspeaker (EDL-hole) and on the opposite side of the tank (OEDL-hole),
- One hole is positioned in the middle of the tank (FLEX-hole). It is connected to roughly 1 m of flexible tube to simulate a hole with increased losses (i.e. higher resistance against airflow).

For each fill level, a set of six different ventilation-hole-configurations is used to evaluate the value of the capacitance and the inductance, respectively. An overview of the configurations is given in table 1 below.

Table 1. Ventilation Hole Configurations

config. #	Description
1	All ventilation holes closed
2	OEDL-hole opened
3	EDL-hole and OEDL-hole opened
4	All ventilation holes opened (EDL-, OEDL- and FLEX-hole)
5	FLEX-hole opened
6	EDL-hole opened

Fig. 13 and Fig. 14 show the estimated values of the acoustic inductance and the acoustic capacitance, respectively. As depicted in Fig. 13, the acoustic inductance (representing the fill level of the fuel tank) is hardly influenced by the ventilation configuration, but depends on the fill level. In contrast, the acoustic capacitance value (Fig. 14) reveals a clear influence on the ventilation configuration, whereas the value is marginally affected by the fill level. Therefore, the results of the measurements indicate the capability of the principle to separate the effects of fill-level and tank leakage.

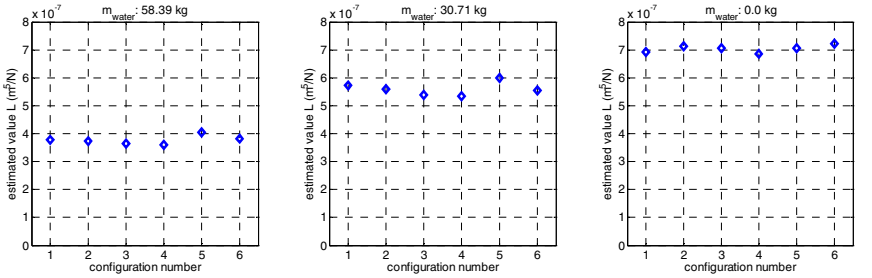

Fig. 13. Estimation of the vessel inductance parameter for different fill levels of the tank (subplots 1-3) and ventilation hole configurations (horizontal axis of the diagrams; compare table I). The inductance clearly depends on the fill level while the influence of ventilation holes is small [22].

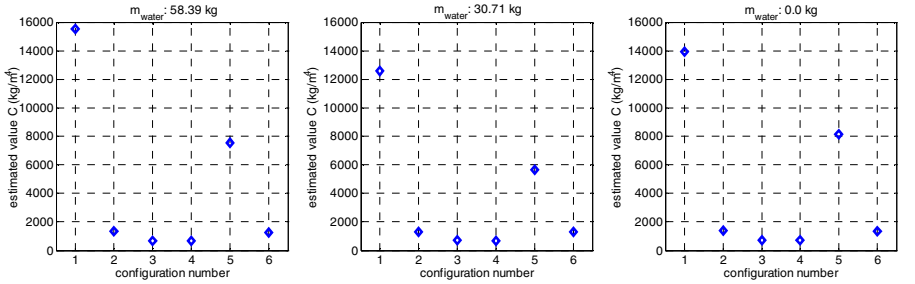

Fig. 14. Estimation of the capacitance parameter for different tank fill levels (subplots 1-3) and ventilation hole configurations (horizontal axis of the diagrams; compare table I). The subplots are quite similar indicating a negligible influence of the fill level, while the variations due to the ventilation hole configuration are in good accordance with the expected results (smallest values for “open” configurations 2, 3, 4, and 6, higher values for closed tank (configuration 1) and high-loss ventilation hole (configuration 5)) [22].

6 Conclusion

Evaluation measurements for the proposed pneumatic fill-level gauging method based on an electroacoustic equivalent-circuit model [22, 25, 27] demonstrate the applicability of the method for vented storage tanks in principle. The measurement results presented indicate the possibility of introducing pneumatic methods in multiple areas.

An extension of the method in order to reach uncertainties of some percent of the tank volume should enable a broad application in automotive industries due to the independence of the measurement results on tank orientation, acceleration, and foam layers combined with the simplicity of the basic measurement principle. Hence, future work will focus on optimizing the measurement setup to improve the measurement uncertainty. This improvement comprises an extension of the structure of the electroacoustic model (additional components representing important effects that were neglected in [22]) and the introduction of non-constant and/or nonlinear components that are used to describe nonlinear behavior of losses.

References

[1] Vass, G.: The Principle of Level Measurement. Sensors Magazine (17) (2000)
[2] Reverter, F., Li, X., Meijer, G.C.: Liquid-level measurement system based on a remote grounded capacitive sensor. Sensors and Actuators A 138, 1–8 (2007)
[3] Canbolat, H.: A Novel Level Measurement Technique Using Three Capacitve Sensors for Liquids. IEEE Transactions on Instrumentation and Measurement 58(10), 3762–3768 (2009)
[4] Shiratsuchi, T., Imaizumi, M., Naito, M.: High Accuracy Capacitance Type Fuel Sensing System. SAE Transactions 930359 (1993)
[5] Khan, S.: A Non-Contact Capacitance Type Level Transducer for Liquid Characterization. In: Proceedings of the International Conference on Computer and Communication Engineering, Kuala Lumpur, Malaysia (2008)
[6] Chen, L., Dong, X., Han, J., Ye, P.: Development of an Ultrasonic Instrument for the Sealed Container's Liquid Level Measuremen. In: Proceedings of the 6th World Congress on Intelligent Control, Dalian, China (2006)
[7] Dalci, K.B., Gulez, K., Mumcu, T.V.: The Design of the Measurement Circuit using Ultrasonic Sound Waves for Fuel Level of Automobile Tanks and the Detection of Bad Sectors of Tank by Neural Networks. In: SICE, Sapporo, Japan (2004)
[8] Ooshima, A., Kobayashi, K., Watanabe, K.: Development of a noninvasive powder level switch by acoustic method. In: Proceedings SICE Annual Conference, Sapporo, Japan (2004)
[9] Sai, B., Kastelein, B.: Highly Reliable and Accurate Level Radar for Automated Legal Custody Transfer and Inventory Management. In: Proceeding of the 2006 IEEE International Conference on Automation Science and Engineering, Shanghai (2006)
[10] Weiß, M., Knöchel, R.: A Sub-Millimeter Accurate Microwave Multilevel Gauging System for Liquids in Tanks. IEEE Transactions on Microwave Theory and Techniques 49(2), 381–384 (2001)
[11] Watanabe, K., Takebayashi, Y.: Volume Measurement of Liquid in a Deformed Tank - Application to the Fuel Meter of Automobiles. SAE Transactions 871964 (October 1987)
[12] Kobayashi, H., Watanabe, K., Kawa, E., Chen, Y.S., Ishizuka, H.: Gauging Fuel in Deformed Tanks by Pneumatic Methods – Application to Automobile Fuel Gauges. SAE Transactions 900467 900467 (February 1990)
[13] Watanabe, K., Takebayashi, Y., Himmelblau, D.M.: Volume Measurement of Deformed Materials in Tanks. ISA Transactions 27(4), 9–19 (1988)

[14] Nishizu, T., Ikeda, Y., Torikata, Y., Manmoto, S., Umehara, T., Mizukami, T.: Automatic, Continuous Food Volume Measurement with a Helmholtz Resonator. CIGR Journal of Scientific Research and Development III(Manuscript FP 01 004) (2001)

[15] Imanishi, M., Nagashima, A., Moriyama, A., Ishii, Y.: Measurement of Combustion-Chamber Volume Using an Acoustic Resonance Technique. In: IMTC, Hamanatsu (1994)

[16] Nakano, A., Torikata, Y., Yamashita, T., Sakamoto, T., Futaya, Y., Tateno, A., Nishizu, T.: Liquid volume measurement with a closed Helmholtz resonator under micro-gravity conditions. In: Cryogenics, vol. 46 (2006)

[17] Betta, G., Pietrosanto, A., Scaglione, A.: A Gray-Code-Based Fiber Optic Liquid Level Transducer. IEEE Transactions on Instrumentation and Measurement 47(1), 174–178 (1998)

[18] Vázqzez, C., Gonzalo, A., Vargas, S., Montalvo, J.: Multi-sensor system using plastic optical fibers for intrinsically safe level measurements. Sensors and Actuators 116, 22–32 (2004)

[19] Longbottom, F., Eren, H.: Ultrasonic multiple-sensor solid level measurements. In: Proceedings IEEE Instrumentation and Measurement Technology Conference (IMTC), vol. 2, pp. 749–752 (1994)

[20] Holler, G., Fuchs, A., Brasseur, G.: Fill level measurement in a closed vessel by monitoring pressure variations due to thermodynamic equilibrium perturbation. In: Proc. IEEE International Instrumentation and Measurement Technology Conference, Victoria, Canada, pp. 641–646 (2008)

[21] Holler, G., Brunnader, R., Schweighofer, B., Wegleiter, H.: Pneumatic level-sensing for liquid, powdered and solid media storage tanks. In: Proc. Fourth International Conference on Sensing Technology, Lecce, Italy, pp. 488–491 (2010)

[22] Brunnader, R., Holler, G.: Experimental Validation of a Leakage and Fill-level Estimation Method for Vented Tanks. In: Proceedings 5th International Conference on Sensing Technology, Palmerston North, New Zealand, pp. 395–398 (2011)

[23] Brunnader, R., Holler, G.: A Novel Measurement Method for Quality Parameters of Wood Pellets. In: 37th Annual Conference of the IEEE Industrial Electronics Society, Melbourne, pp. 4643–4647 (2011)

[24] Lerch, R., Sessler, G.M., Wolf, D.: Elektromechanische Ana-logien. In: Technische Akustik. Springer, Berlin (2009)

[25] Brunnader, R., Holler, G., Brasseur, G.: Model Verification and Parameter Evaluation for a Pneumatic Gauging Method for Vented Tanks. In: Instrumentation and Measurement Technology Conference (I2MTC), Hangzhou, pp. 1–6 (2011)

[26] Holler, G., Brunnader, R., Schweighofer, B., Wegleiter, H.: Experimental Assessment of a Pneumatic Level-sensing Method for Closed Tanks Applied to Water and Wooden Pellets. Sensors & Transducers Journal 9(12/10), 151–160 (2010)

[27] Brunnader, R., Holler, G.: Applicability evaluation of the pneumatic gauging method for automotive fuel tanks. In: Proc. IEEE International Instrumentation and Measurement Technology Conference (I2MTC 2012), Graz, Austria (2012)

New Developments in Electrode Materials for Electrochemical Sensors

U. Guth[1], J. Zosel[2], J. Riedel[1], T.N. Tran[1], M. Berthold[2], C. Vonau[2], U. Sasum[3], P. Shuk[4], M. Paramasivam[5], and V. Vashook[1]

[1] Dresden University of Technology,
Department of Chemistry and Food Chemistry, D-01062 Dresden, Germany
[2] Kurt-Schwabe Research Institute Meinsberg,
Kurt-Schwabe-Strasse 4, D-04720 Ziegra-Knobelsdorf, Germany
[3] Research Sensor Center D-17489 Greifswald, Germany
[4] Emerson Process Management, 6565P Davis Industrial Parkway Solon, OH 44139, USA
[5] Central Electrochemical Research Institute (CECRI), Karaikudi-630 006, Tamilnadu, India
guth@ksi-meinsberg.de

Abstract. Electrode materials are the key components for electrochemical sensors which can be used for determination of gaseous and dissolved species. The sensitivity as well as the selectivity are mainly influenced by the kind and the structure of sensitive electrode material. In this paper two kinds of materials are described. Screen-printed carbon electrodes (SPCE) can be modified by thin layers of conducting polymers like Poly(3,4-ethylendioxythiophene) (PEDOT) and gold nanoparticles. By means of differential pulse (DPV) and square wave voltammetry (SWV) it is possible to determine biogene amine like dopamine in liquids of human bodies and explosives in ground water in the nM und ppb level, respectively. Polyaniline (PANI) can be used not only in normal temperature sensors but also in high temperature sensors. For the first time we could show that zirconia based sensors with PANI electrodes in which Nb_2O_5 or $FeCl_3$ and $Co(NO_3)_2$ are embedded are suitable to measure hydrogen and hydrocarbons in oxygen containing gases at 450 °C. The sensitivities of such electrodes are much higher than those of the usual applied oxide systems like Nb_2O_5 or $La_{0.75}Ca_{0.25}Mn_{0.5}Ni_{0.5}O_{3-\delta}$. Due to the availability and compactness of electronic devices electrochemical sensors with modified electrodes can be applied in stationary (potentiometric) and non-stationary (SWV or DPV) mode in field application.

Keywords: screen-printed carbon electrodes, conducting polymers, gold nano-particles, mixed potential sensor based on zirconia solid electrolyte, hydrogen, hydrocarbons, dopamine, explosives, square wave volammetry, differential pulse volammetry.

1 Introduction

Electrochemical solid electrolyte sensors based on yttria stabilized zirconia are suited for the in situ measurement of hydrocarbons, hydrogen and NO in oxygen

S.C. Mukhopadhyay et al. (Eds.): Advancement in Sensing Technology, SSMI 1, pp. 181–189.
springerlink.com

containing gases e.g. in exhaust [1, 2] of automotive and industrial combustion processes. Mixed potential gas sensors in which a sensitive electrode for combustibles or NO and a non-sensitive electrode are combined can be used in the same gas atmosphere [3]. The simple construction as compared with amperometric sensors, however, requires electrodes with high sensitivity and selectivity.

During the past 10 years, many metal oxides have been tested on their sensing qualities in sensing cells. Miura et al. described experiments with spinel and perovskite type oxides AB_2O_4 (A = Zn, Ni, Cd and B = Mn, Fe, Cr) [4, 5] and ABO_3 (A = Ln, Ni, Y; B = Cr, Mn, Fe, Co, Ni) [5, 6]. We investigated the $La_{0.6}Ca_{0.4}Mn_{1-x}Me_xO_{3-\delta}$ (Me = Ni, Co, Fe) and have been found that the electrode material $La_{0.6}Ca_{0.4}Mn_{0.8}Ni_{0.2}O_{3-\delta}$ has the highest potentiometric response to NO at 500 °C [7].

Modified carbon electrodes were reported to measure bioactive compounds in liquids of human body [8]. There are a lot of efforts to improve the sensitivity by modifying conducting polymers in which gold nano-particles are embedded. But such electrodes are mainly hand made. Therefore their performances are statistically highly spread. Screen-printed (thick-film) technology has made it possible to establish a mass-production of inexpensive electrodes with controlled thickness, diameter and uniform quality.

Up to now, there is no information about conducting polymers as electrode material for high temperature sensors. It seemed to be impossible to use such materials at temperatures > 250 °C. In this paper we will show for the first time that polymers like PANI can be used up to 450 °C. Additionally, as a new oxide system for YSZ based sensors we investigate the system the series $Ca_{1-x}La_xTiO_3$ (x = 0.001 - 0.2).

In the second part we present results obtained with modified conducting polymers as an electrode for determination of dopamine and explosives like trinitrotoluene (TNT) prepared in industrial like screen printing technology.

2 Experimental

The conducting polymers were prepared as follows: Polyaniline (PANI) was chemically synthesized from aniline by oxidative polymerization using ammonium peroxydisulphate in an acidic media. 0.05 M of aqueous solution of aniline (different concentrations) in 1 M H_2SO_4/HCl (different concentrations) acid were mixed together in a 200 ml beaker containing 150 ml solution 0.1 M of aqueous solution of ammonium peroxy disulfate is added drop-wise into a stirring solution and then a solution of $FeCl_3$ and $Co(NO_3)_2$ in the ratio 0.75 : 0.25 was added during stirring condition. The stirring of the reaction mixture was continued 5 - 6 hours to ensure the completion of the reaction. Finally, the precipitate was filtered and washed repeatedly with distilled water until the filtrate was colourless and then it was dried under vacuum condition.

PEDOT, Poly(3,4-ethylendioxythiophene), was prepared electrochemically using an aqueous solution of monomers.

Following materials were prepared by using the oxide route: $Ca_{1-x}La_xTiO_3$ with x = 0.0015 - 0.2 by tempering the ground oxides at 1200 °C for 17 h. The sintered

materials were ground in ethanol over 8 h, characterized as powders and mixed with an organic binder for manufacturing of pastes for screen printing. After printing of electrode materials on slices of yttria stabilized zirconia (YSZ) of 0.5 mm thickness and 12 mm diameter the pastes were fired at 1000 °C for 1 h.

All powder materials were characterized with respect to their specific surface (BET, COULTER SA 3100), grain size (Laser particle sizer, COULTER SA 230), crystal structure (XRD, D8Advance, Bruker AXS) and catalytic activity (setup, described in [9]). Addionally thermo gravimetric investigation (TG, DTA Seteram) of pure and mixed polymers were performed.

The powders were mixed with an organic binder to get a printable paste. The printed layers were used without an additional firing process for high temperature sensors as well as for normal temperature sensors.

The screen-printed electrodes were tested with respect to their potentiometric sensitivity in different gas mixtures, containing O_2 and H_2 or hydrocarbons (C_3H_6, C_2H_4) respectively by using the experimental setups, described in Figure 1. The setup and procedure for mixed potential and conductivity measurements are given elsewhere [6, 9]. The YSZ disk with the freshly prepared polymer electrode was heated up to the operating temperature.

The normal temperature sensors shown in Figure 2 were applied in aqueous solution with increasing amount of TNT and dopamine, respectively.

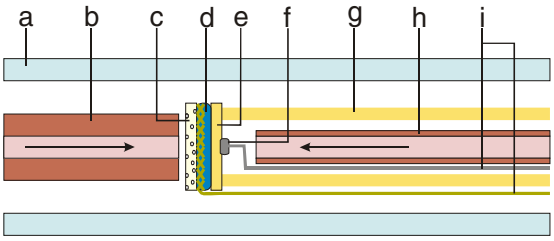

Fig. 1. Setup of YSZ cell with conducting polymer electrodes for potentiometric measurements a: Quartz tube, b: measuring gas, c: porose alumina disk, d: polymer electrode with gold net, e: YSZ-disk, f: Pt/air reference electrode, g: YSZ-tube, h: air supply, i: connecting leads

Fig. 2. Modifiable screen-printed carbon electrode for determination of dopamine and explosives in aqueous solutions

For the determination of the organic substances the well known electrochemical methods square wave voltammetry and differential pulse voltammetry were used. The case of dopamine determination 0.5 M ascorbic acid and 0.5 M uric acid were added in order to check the cross sensitiviy against other substances which are usually present in liquids of human body.

3 Results

3.1 A Structure and Morphology

An example of the morphology of modified screen-printed carbon electrodes is given in Figure 3. The picture shows that the surface of the polymer film is covered with gold nano-particles.

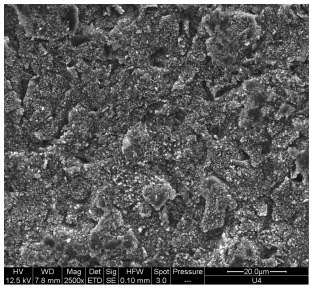

Fig. 3. SEM image of the screen-printed carbon electrode modified with PEDOT and gold nano-particles (Au-PEDOT-SPCE)

3.2 B Potentiometric Investigation

The potentiometric investigations in hydrogen and propen containing gases show pronounced sensitivtity of the conducting polymer containing electrode to low concentrations of gases as illustrated in Figure 4 and Figure 5. At higher concentrations a second process leads to a smalles increase of the signal.

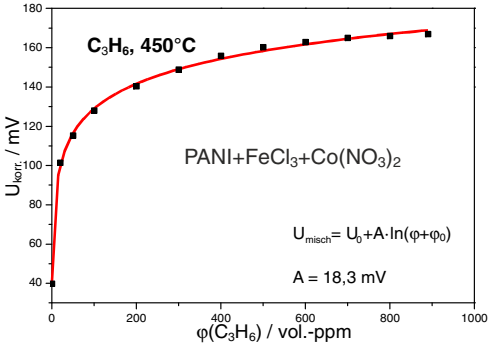

Fig. 4. Dependency of the potential on the C_3H_6-concentration of the YSZ cell with PANI electrode at 450 °C vs. Pt/air reference, oxygen concentration 1.5 vol-%

The voltage response after a jump in concentration is very fast (few seconds). Amazingly, the data obtained are very stable and reproducible over several days. For low concentrations of combustibles the sensitivity was found to be 3 mV/ppm C_3H_6. This is much higher than those obtained for mixed oxides electrodes. We found by means of TG/DTA investigations that a higher part of conducting polymer is decomposed and evaporated due to the thermal treatment at 450 °C. But the mass of the polymer is stable at this temperature for several days. Although the composition of the remaining part is not clear at the moment it seems to be that a net of organic structures was formed in which the inorganic species are embedded. Similar results were obtained for hydrogen as shown in Figure 6. The sensitivity for hydrogen was found to be 1.6 mV/ppm. The advantage of such polymer electrodes consists in the simple preparation without high temperature processes (up to 1200 °C) which are necessary in the case of oxide or mixed oxide electrodes.

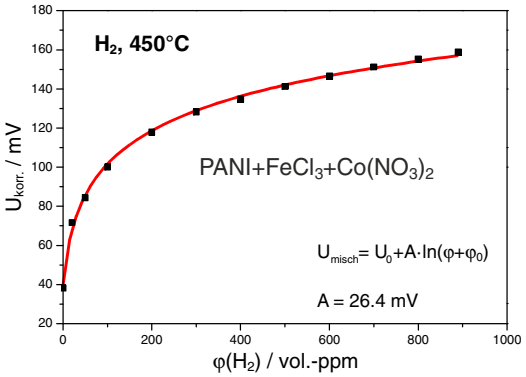

Fig. 5. Hydrogen concentration dependence of the mixed potential cell with electrode materials PANI- elctrode ϑ = 450 °C, flow rate 50 ml/min, vs. Pt/air reference, oxygen concentration 1.5 vol-%

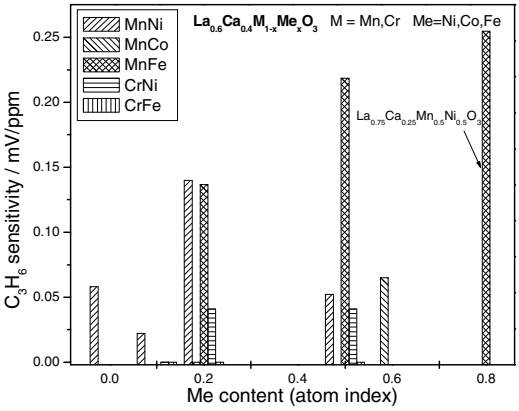

Fig. 6. Propen sensitivity for different perovskite electrodes at 550 °C, flow rate 50 ml/min, vs. Pt/air reference, oxygen concentration 1.5 vol-%

For comparison the results of the potentiometric measurements on $La_{0.6}Ca_{0.4}M_{1-x}Me_xO_{3-\delta}$ (M = Mn, Cr; Me = Ni, Co, Fe) electrodes, using C_3H_6-O_2-N_2 containing atmosphere are given in Figure 6. The Ni and Fe containing manganites in all compositions show a much lower sensitivity to C_3H_6 (up to 0.25 mV/ppm). The sensitivity values of the Fe manganites are higher than those of the Ni manganites [7].

In the investigated system $Ca_{1-x}La_xTiO_3$ a series of compound with high concuctivity could be prepared. Figure 7 shows the temperature dependence of the conductivity in Arrhenius like plots. Used as an electrode material they behave as equilibrium electrodes. That means combustibles react with oxygen in non equilibrated gases. Therefore those compounds are non siutable for mixed potential sensors.

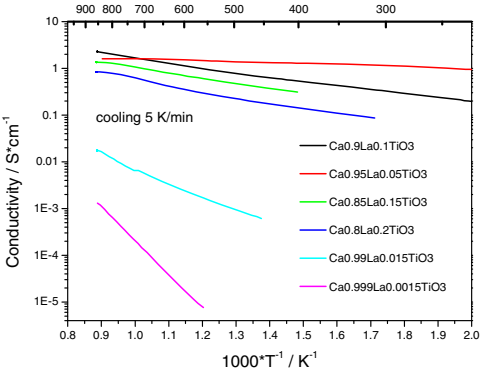

Fig. 7. Arrhenius plots of conductivity in the system $Ca_{1-x}La_xTiO_3$

3.3 C Voltammetric Results

Modified conducting polymers can be successfully applied to improve the sensitivity of carbon electrodes for dissolved bioactive species like dopamine and to reduce the cross sensitivity against other substances found in liquids of human body like ascorbic and uric acid. These modifications can be performed in one step easily from aqueous solutions under definite electrochemical conditions with high reproducibility.

The Figure 8 shows the square wave voltammograms of solutions containing 0.5 mM AA + 0.5 mM UA and various concentrations of DA in 0.1 M PBS (pH 7.4) at Au-PEDOT-SPCE. The Figure 9 shows the calibration curve between the peak current and concentration of dopamine. Due to the modifying of PEDOT modified screen-printed carbon electrodes (PEDOT-SPCE) by means of gold nano-particles, the sensitivity for dopamine was increased significantly to 19.9 $\mu A \mu M^{-1}$ on Au-PEDOT-SPCE in comparison to 0.311 $\mu A \mu M^{-1}$ on PEDOT-SPCE.

In the clinical relevant range from 10 nM to 2 µM dopamine the sensitivity was found to be 19.9 µA/µM. The sensitivity of the modified SPCEs for the determination of dopamine did not change after storage in air or in 0.1 M PBS (pH 7.4) for at least 2 months. This offers the possibility to produce such sensors in a large scale and makes attractive for their application in doctor's practice.

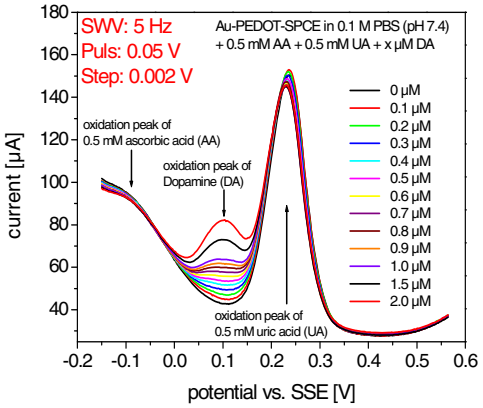

Fig. 8. Determination of dopamine (for concentrations 0.1 - 1.0 in steps of 0.1 and 1.5 and 2 µM, left peaks) in the presence of 0.5 mM ascorbic acid + 0.5 mM uric acid (right peak) at gold and PEDOT modified screen-printed carbon electrodes (Au-PEDOT-SPCE) by SWV

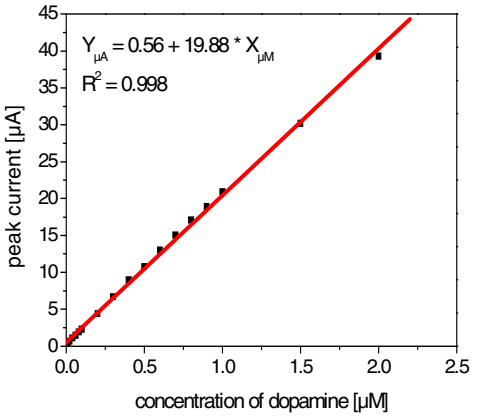

Fig. 9. Plot of the peak current vs. concentration of dopamine (calibration curve)

The determination of explosives like trinitrotoluene (TNT) in soil of abandoned military training areas is an important task. We could show in Figure 10 that such compounds are electrochemical active species which can be reduced elcectrochemically in two steps on unmodified screen-printed carbon electrodes.

Nowadays, well known quasi-stationary electrochemical methods like differential pulse and square wave voltammetry can be performed using small and inexpensive devices in field application. That makes the use of printed electrodes very attractive.

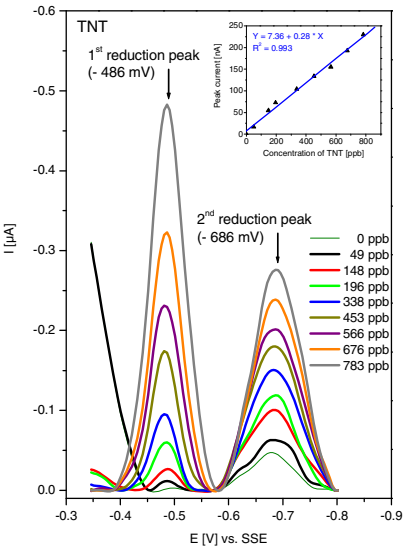

Fig. 10. Determination of TNT on screen-printed carbon electrode (SPCE) by DPV in 0.1M KNO_3/0.1M KCl solution (counter electrode Pt)

4 Conclusions

For the first time new electrode materials from the group of conducting polymers were successfully tested in solid electrolyte sensors based on YSZ. Surprisingly, it was possible to measure reproducibly mixed potential in dependence on concentration of combustibles at 450 °C over several days. We found as compared to electrodes made of mixed oxides a markedly enhanced sensitivity to C_3H_6 and H_2. For Fe^{3+} and Co^{2+} modified PANI the maximum sensitivity was found of about 3mV/ppm C_3H_6 at 450 °C. Further investigations of electrode materials and their structure and composition should give more information necessary for the development of taylored electrode materials. Carbon electrodes modified by PEDOT and PEDOT/Au can be succesfully applied using differential voltammetric methods to measure dopamine in presence of ascorbic and uric acid up to 0.1 µM with a sensitivity of 19.9 $\mu A \mu M^{-1}$. Such electrodes can also used for determination of dissolved explosives like TNT in ppb-level.

References

[1] Göpel, W., Reinhardt, G., Rösch, M.: "Trends in the development of solid state amperometric and potentiometric high temperature sensors'. Solid State Ionics 136-137, 519–531 (2000)

[2] Somov, S.I., Reinhardt, G., Guth, U., Göpel, W.: Tubular amperometric high-temperature sensors: simultaneous determination of oxygen, nitrogen oxides and combustible components. Sens. Actuators, B 65, 68–69 (2000)
[3] Schmidt-Zhang, P., Sandow, K.-P., Adolf, F., Göpel, W., Guth, U.: A novel thick film sensor for simultaneous O2 and NO monitoring in exhaust gases. Sens. Actuators, B 70, 25–29 (2000)
[4] Miura, N., Lu, G., Yamazoe, N.: High-temperature potentiometric/amperometric NOx sensors combining stabilized zirconia with mixed-metal oxide electrode. Sens Actuators, B 52, 169–178 (1998)
[5] Guth, U., Zosel, J., Vonau, W.: Recent development in electrochemical sensor application and technology – a review. Meas. Sci. Technol. 20 042002, 14 (2009), doi:10.1088/0957-0233/20/4/042002
[6] Zosel, J., Müller, R., Vashook, V., Guth, U.: Response behavior of perovskites and Au/oxide composites as HC-electrodes in different combustibles. Solid State Ionics 175, 531–533 (2004)
[7] Guth, U., Zosel, J., Franke, D., Vashook, V.: NO mixed potential sensor based on yttria stabilized zirconia. In: 2nd Int. Conference on Sensing Technology (extended abstracts), Palmerstone North, New Zealand, pp. 222–229 (2005)
[8] Mathiyarasu, J., Senthil Kumar, S., Phani, K.L.N., Yegnaraman, V.: PEDOT-Au nanocomposite film for electrochemical sensing. Materials Letters 62, 571–575 (2008)
[9] Vashook, V., Vasylechko, L., Zosel, J., Müller, R., Ahlborn, E., Guth, U.: Lanthanum–calcium chromites–titanates as possible anode materials for SOFC. Solid State Ionics 175, 151–155 (2004)

Optical Fiber Sensors Based on Lossy Mode Resonances

Miguel Hernáez, Carlos R. Zamarreño, Ignacio Del Villar, Francisco J. Arregui, and Ignacio R. Matias

Public University of Navarre, 31006 Pamplona, Spain

1 Introduction

In the last decades, optical fiber sensors have played an important role in niche applications because of their advantages over electronic sensors. First of all, optical fiber makes possible the multiplexing of a large amount of sensor data over long distances. This feature allows placing the sensing devices at kilometers from the electronic systems used to process the information. In addition, optical fiber is made of dielectric materials. Consequently, optical fiber sensors are not affected by electromagnetic fields, what makes them suitable to be used in situations under high electromagnetic fields or radiation doses [1]. Furthermore, this technology can be also used in medical applications due to its biocompatibility and has acquired a great importance in the development of biomedical instrumentation. Other interesting advantages of optical fiber sensors are their small size or their wide temperature working range [2-5].

Due to these interesting features, several optical fiber sensing architectures have been developed in the last decades. Just to mention some examples, there are optical fiber sensors based on fiber Bragg gratings (FBGs) [6], long period gratings (LPGs) [7], photonic crystal fibers (PCB) [8], tapered fibers [9], interferometers [10], electromagnetic resonances [11-15], etc…

In addition, the development of novel materials and deposition methods on the nanometric scale has meant an important breakthrough in different fields [16, 17]. More specifically, in the field of optical fiber sensors, nanostructured coatings allow the generation of optical effects that are not appreciable with the utilization of thick films. Electromagnetic resonances, such as surface plasmon resonances (SPR) or lossy mode resonances (LMR), that make possible the development of optical fiber sensors with tunable spectral response, are a good example of these new phenomena [18].

Among this variety of optical fiber techniques, SPR is one of the most widely studied. Since the first sensing application of SPR was reported in 1983 [19], a lot of structures based on this phenomenon have been developed, becoming a standard in the design and fabrication of sensors and biosensors.

This phenomenon consists of the excitation of a surface plasmon wave at the metal-dielectric interface. When some particular conditions of the incident and the surface plasmon wave match, a resonance is generated and a sharp absorption peak can be observed in the transmitted light. The resonance wavelength depends

S.C. Mukhopadhyay et al. (Eds.): Advancement in Sensing Technology, SSMI 1, pp. 191–210.
springerlink.com

on the refractive index of the material in contact with the metal. In other words, a change in this refractive index will produce a wavelength shift of the resonance peak [14]. This fact has been applied in the design and fabrication of sensors for different applications [20-27].

First studies about SPR used a complex optical setup (known as the Kretschmann configuration), including a prism, to excite the surface plasmon wave. This setup presents some important drawbacks, such as its big size and the presence of fragile mechanical parts. The optical fiber configuration, developed by Jorgenson and Yee [28], overcomes these disadvantages and allows the miniaturization of these devices, adding these features to the typical advantages of optical fiber sensors [29-32]. As a result, numerous optical fiber sensors based on SPR have been developed in the last years [11-13,33-39].

However, SPR-based devices have some limitations. Firstly, there are just a few stable metals that allow the generation of SPR in the visible and near-infrared spectral regions, such as gold or silver, and they are expensive. In addition, SPR is only visible with TM polarization of light, what makes necessary the use of a polarizer and an optical fiber that maintains the polarization to obtain a sharp absorption peak. Moreover, the conditions for SPR generation are very specific and for this reason, SPR is produced in a limited spectral region that depends on the deposited metal.

Recently, the use of metallic oxides to generate optical devices based on the Kretschmann configuration, have allowed the opening of this technology to new materials, such as Indium Tin Oxide (ITO) [40-43]. This fact allows overcoming the drawback of using only metals to obtain SPRs. The initial objective of this study was to generate electromagnetic resonances by depositing ITO coatings onto optical fiber. When this aim was achieved, a deeper study of the bibliography revealed that the obtained resonances were not SPRs, but Lossy Mode Resonances (LMR). These LMRs are a type of resonances that overcomes some of the limitations of SPRs and never had been observed before in an optical fiber configuration. In fact, more than twenty-two publications have been devoted to this topic in the last two years.

The phenomenon of LMR will be presented and analyzed in this chapter. Theoretical basis of LMR will be explained and the differences between this novel resonances and SPR will be demonstrated, emphasizing the advantages of LMR over SPR.

2 Lossy Mode Resonances (LMR)

When an optical waveguide is coated by a thin-film (see Fig. 1), the propagation of light is affected. If the refractive index of the coating has an imaginary part different to zero, it introduces losses that can produce electromagnetic resonances. Depending on the properties of the different materials involved in the system (the waveguide, the coating and the external medium), three different cases of electromagnetic resonances can be distinguished [44].

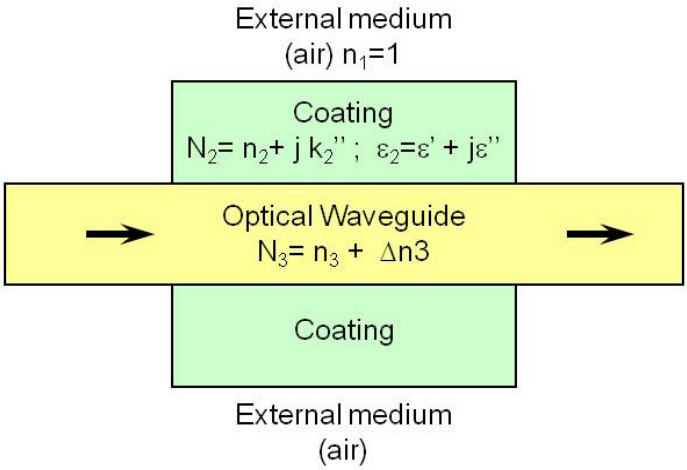

Fig. 1. Schematic representation of the optical system used to obtain electromagnetic resonances

The first case occurs when the real part of the thin-film permittivity is negative and higher in magnitude than both its own imaginary part and the permittivity of the material surrounding the thin film (i.e. the optical waveguide and the surrounding medium in contact with the thin film). In this case, coupling occurs between light propagating through the waveguide and a surface plasmon, which is called Surface Plasmon Polariton (SPP). This phenomenon produces a resonance called Surface Plasmon Resonance (SPR).

The second case occurs when the real part of the thin-film permittivity is positive and higher in magnitude than both its own imaginary part and the permittivity of the material surrounding the thin film. Some authors consider these modes as long-range guided modes [44], whereas others call them lossy modes [45, 46]. In this work, they will be called lossy modes to make a difference between them and the rest of guided modes. These lossy modes will produce the second type of resonances: the Lossy Mode Resonance (LMR).

Finally, the third case occurs when the real part of the thin-film permittivity is close to zero, while the magnitude of its imaginary part is large [44]. This case, known as long-range surface exciton polariton (LRSEP), falls beyond the scope of this study and will no longer be studied.

The permittivity of a material can be expressed in terms of its complex refractive index (N=n+jk) according to Eq. 1.

$$\varepsilon = \varepsilon' + j\varepsilon'' = N^2 = (n + jk)^2 = n^2 - k^2 + j2nk \tag{1}$$

And, finally,

$$\begin{aligned} \varepsilon' &= n^2 - k^2 \\ \varepsilon'' &= 2nk \end{aligned} \tag{2}$$

Thus, having the device schematically represented in Fig. 1 and the relations from Eq. 2, the conditions needed to obtain the different types of electromagnetic resonance (SPR, LMR and LRSEP) can be expressed in terms of the refractive index of the different materials involved in the system.

In Table 1 a summary of these conditions is presented, considering the case in which $n_2>0$ and $k_2<0$.

Table 1. Summary of the conditions needed to obtain the different types of electromagnetic resonances with the system represented in Fig.1.

Resonance	Permittivity	Refractive Index
Surface Plasmon Resonance **SPR**	$\varepsilon_2' < 0$ $\varepsilon_2' > \varepsilon_2''$ $\varepsilon_2' > \varepsilon_3'$	$\lvert n_2\rvert < \lvert k_2\rvert$ $n_2 > (1-\sqrt{2})k_2$
Lossy Mode Resonance **LMR**	$\varepsilon_2' > 0$ $\varepsilon_2' > \varepsilon_2''$ $\varepsilon_2' > \varepsilon_3'$	$\lvert n_2\rvert > \lvert k_2\rvert$
Long-Range Surface Exciton Polariton **LRSEP**	$\varepsilon_2' \approx 0$ $\varepsilon_2'' \uparrow\uparrow$	$\lvert n_2\rvert \approx \lvert k_2\rvert$ $2nk \uparrow\uparrow$

Although not too many studies have been published about LMR, there are some theoretical studies devoted to light propagation through semiconductor-cladded waveguides [47, 48]. The characteristics of these materials are adequate for generation of lossy modes. Moreover, attenuation maxima of the light propagating through the waveguide are obtained for specific thickness values [47]. This effect is produced as a consequence of a coupling between a waveguide mode and a particular lossy mode of the semiconductor thin film.

This coupling depends on two conditions: a considerable overlap between the mode fields and the phase-matching condition is sufficiently satisfied (i.e., the real parts of propagation constants are equal) [45]. Both conditions occur when modes propagating through the waveguide are near the cutoff condition. This cutoff condition sets the point in which a mode starts to be guided through the coating, and it is conditioned by two parameters: the wavelength and the coating thickness. Since the phenomenon occurs when the lossy mode is near cutoff, there are cutoff thickness values that lead to attenuation maxima [47]. For a fixed wavelength, as the thickness of the thin film on the waveguide is increased, some modes guided in the optical waveguide become guided in the film, which causes a modal redistribution or modal conversion [48, 49].

Previous studies have been focused on the variation of thickness. However, if the thin-film thickness is fixed, a resonance will be visible in the electromagnetic spectrum for those incident wavelength values where there is a mode near cut-off in the overlay. This is of great interest because one of the basic ways of using waveguides as sensors is by analysis of resonance wavelength shift. Hence, the

phenomenon studied here is the generation of resonances in the electromagnetic spectrum based on near cut-off lossy modes. The right term should be Near Cutoff Lossy Mode Resonance (NCLMR). However, for the sake of simplicity the term Lossy Mode Resonance (LMR) will be used, which indeed is similar to that mentioned in [46].

Finally, it is worthy to note the differences between these two types of resonances, LMR and SPR. The first difference is that they are generated under different optical conditions (see Table 1). Some materials present a complex refractive index which divides the spectrum in two regions, as it is the case of ITO which will be explained later. Hence, these materials are able to generate both LMR and SPR depending on the spectral region. However, other materials just present one of the spectral regions, and for this reason, they generate either SPR or LMR. Other remarkable question is that LMR allows the generation of multiple resonances as the thickness of the coating is increased. However, SPR presents only one resonance, and it disappears when the coating thickness reaches a certain value. This property makes LMR appropriate for fabricating multi-peak sensors with a better sensitivity and multiple- wavelength optical filters. In Table 2, a summary of the differences between LMR and SPR is shown.

Table 2. Main differences between lossy mode resonances and surface plasmon resonances

	SPR	LMR
Region of the spectrum	High-reflectance region	Low-reflectance region
Supporting coating	Metallic	Metallic or dielectric
Resonance Peaks	Single	Multiple

2.1 Optical Fiber Configuration

To perform this study, a new optical fiber transmission configuration was developed in order to characterize the novel LMR-based devices. This setup is based in an idea previously reported by Jorgenson and Yee [28] used to work with SPR-based optical fiber sensors. This Jorgenson's configuration is an adaptation to optical fiber of the well known Kretschmann configuration [13, 41, 43, 50]. This adaptation overcomes some of the inconveniences of Kretschmann model, such as the complexity of the setup and the need of an optical prism. Moreover,

the new setup presents the general advantages related to optical fiber sensors (immunity to electromagnetic interferences, biocompatibility, low weight, small size, high sensitivity…).

As it can be seen in Fig. 2, light is launched into the optical fiber and it is collected at the other end of the fiber by a spectrometer.

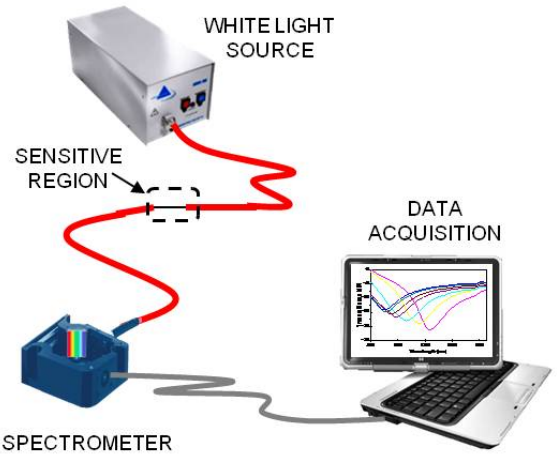

Fig. 2. Optical fiber configuration used to obtain and characterize the different resonances

In the middle of the optical path, there is a region where the optical fiber core is coated with the LMR supporting material. Cross section and longitudinal section of this region are shown in Fig. 3.

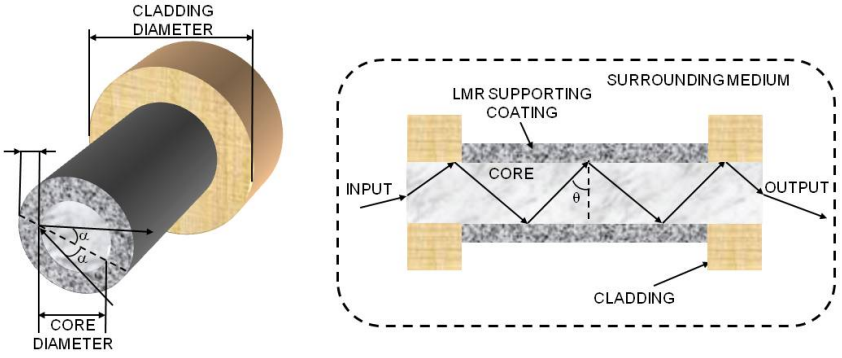

Fig. 3. Detail of the LMR supporting region. The cladding is chemically removed and the LMR supporting material is directly deposited onto the optical fiber core.

3 Optical Fiber Sensors Based on LMR

3.1 Devices Based on a Single Coating

Different devices can be designed and fabricated by following the scheme shown in Fig. 3, where a single coating of a LMR supporting material has been deposited directly onto the optical fiber core.

3.1.1 Optical Fiber Refractometers Based on ITO Coatings

ITO (Indium Tin Oxide) belongs to transparent conductive oxides (TCOs), which have been widely used in many scientific areas during the last decades: fabrication of heat shields, liquid crystal displays, flat panel displays, plasma displays, touch panels, electronic ink, organic light-emitting diodes, solar cells, antistatic coatings or even electromagnetic interference shields [51, 52]. This success is due to the good qualities that these materials present (electrochemical stability and high transmittance in the visible spectral range), if compared with other well-known conductive materials such as gold or silver. More specifically, ITO has been also used in many different sensing applications such as the fabrication of conductimetric or optical sensors [53-57], by exploiting the combination of conductive and transparency/reflectivity properties in the visible/infrared region respectively.

In fact, it is this dual behavior what makes ITO an adequate candidate for the simultaneous generation of SPR and LMR as well [18]. In Fig. 4, the optical properties of the ITO used in this work are shown. In the spectral region between 3-4.5 μm, the imaginary part of the ITO refractive index is of the order of metals. Consequently, this region is adequate for SPR generation. However, for the spectral region from 0.5-2 μm, the imaginary part is lower and permits the LMR generation, according to the conditions cited in Table 1.

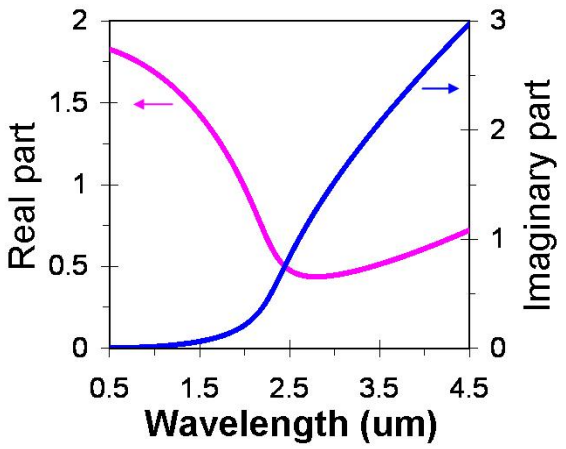

Fig. 4. Complex refractive index of ITO. Real part n (pink) and imaginary part k (blue) [18].

Moreover, the ITO coating features can be modified by introducing simple variations in the fabrication process. This fact allows tuning the resonance region. In other words, the resonance can be placed in the visible or in the infrared region, depending on the ITO characteristics.

The performance of the device as a refractometer was tested by obtaining the transmission response of the system for several surrounding media refractive indices: 1.321, 1.339, 1.358, 1.378, 1.400, 1.422 and 1.436, which were obtained from different water/glycerin concentration solutions from 0% to 85% respectively [58, 59].

Single LMR Generation

The transmission spectra obtained are represented in Fig. 5a and 5b for ITO thickness values of 115 nm and 220 nm, respectively [18]. The plots presented in each figure correspond to different refractive index values of the outer medium, as indicated previously. A resonance is observed in all spectra.

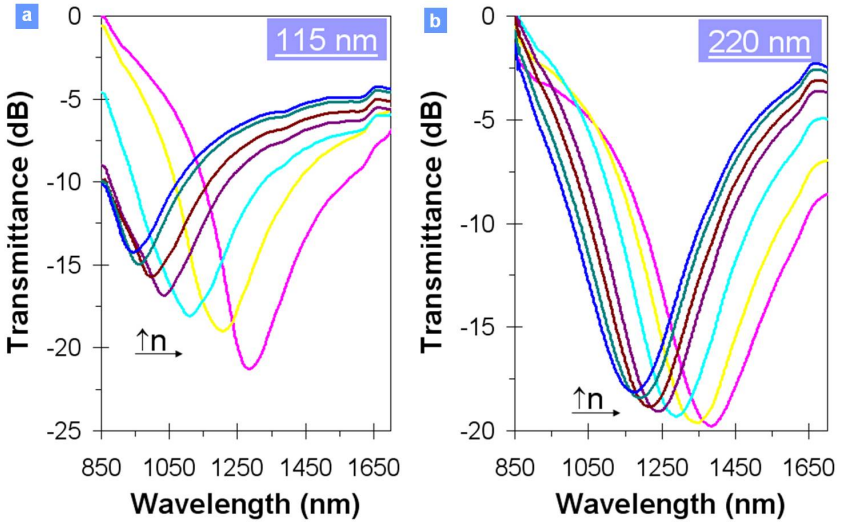

Fig. 5. Experimental results of LMR sensitivity versus surrounding medium refractive index: transmission spectra obtained when the ITO-coated region is immersed in different refractive index solutions for different ITO layer thickness values: a) 115 nm b) 220 nm [18]

Here, it is important to note that as the refractive index increases there is an optical redshift of the resonance. In addition to this, as the coating thickness increases, the sensitivity (i.e. the resonance shift depending on the surrounding refractive index) is reduced. In other words, the thickness can be used for controlling the sensitivity of the device, which is 2956 nm per refractive index unit (RIU) for the sensor coated with a 115 nm film and 1826 nm per RIU for the sensor coated with a 220 nm coatings. These values are in the range of the state of

art SPR sensors [60]. This effect can be clearly observed in Fig. 6, where the resonance wavelengths are shown as a function of the refractive index of the surrounding medium.

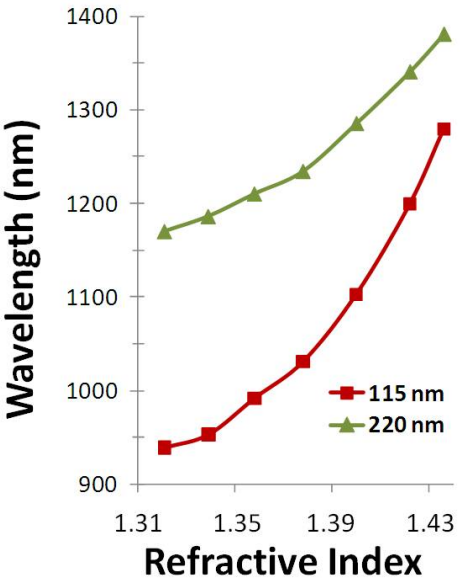

Fig. 6. Evolution of the theoretical (a) and experimental (b) LMR absorption peaks observed in Fig. 9 and 10 when the refractive index of the external medium changes

Multiple LMR Generation

It was observed in Fig. 5 and 6 that when the ITO thickness is increased, the sensitivity of an LMR to the surrounding refractive index decreases. In this section, a second effect of the variation of the ITO thickness will be presented. According to [47] and [49], there are attenuation maxima in the light transmitted through a coated optical fiber as a function of the coating thickness. These maxima coincide with a near cut-off mode in the coating. The same conclusion should be valid for the generation of LMR in the transmission spectrum. For specific wavelength values there are near cutoff modes in the coating. So far a single LMR has been visualized. However, if the ITO thickness is increased there should be more modes guided in this region. The consequence would be the generation of multiple LMR resonances. To prove this hypothesis, in Fig. 7 the response when the ITO thickness is 440 nm are presented.

Three different LMR can be distinguished in the transmission spectra when the surrounding refractive index is 1.321. These results prove the multiple LMR generation. The phenomenon can be exploited for the generation of multiple wavelength filters and sensors with multiple points of reference.

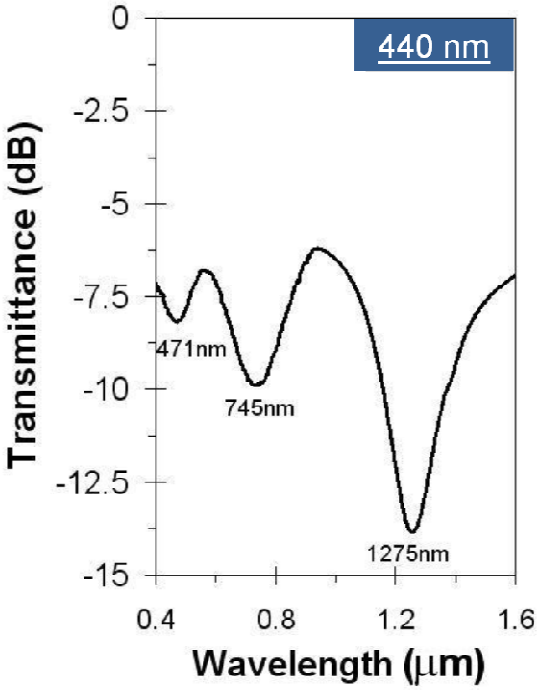

Fig. 7. Multiple LMR: Transmission spectrum obtained for an ITO layer thickness of 440 nm [18]

3.1.2 Optical Fiber pH Sensor Based on a PAH/PAA Thin-Film Deposited onto the Optical Fiber Core

As it was advanced before, LMR can be generated by very different materials. In this section, the capability of PAH/PAA (poly(allylamine hydrochloride) / poly(acrylic acid)) polymeric films to support LMR is presented. With this aim, 100 bilayers of these materials were deposited directly onto the optical fiber core. The LbL method was used to complete this process [61]. The evolution of the transmission spectra obtained during the deposition is shown in Fig. 8, where the generation of 3 different absorption peaks can be observed.

This way, the generation of LMR with polymeric coatings had been demonstrated. But the PAH/PAA structure is not only able to generate LMRs. In addition, if the coating is dipped into liquid solutions, its thickness can be modified as a function of the external medium pH. This effect has been named in previous works as *swelling/deswelling* phenomenon [62, 63]. Taking into account this feature, the behavior of these devices as pH sensors was tested. With this purpose, a device consisting of 25 bilayers of PAH/PAA was fabricated. The first LMR of this device was centered in the 400-1000 nm region.

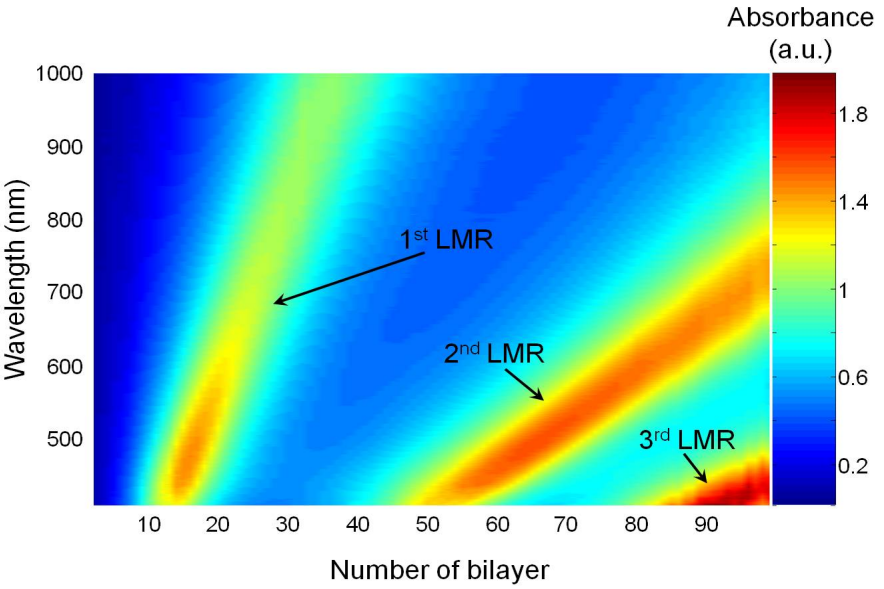

Fig. 8. Evolution of the transmitted spectra during the deposition of the PAH/PAA coating [61]

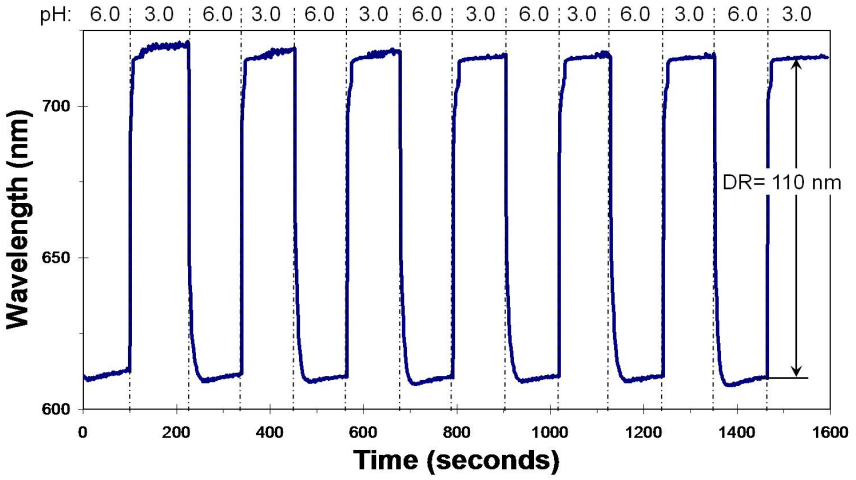

Fig. 9. Dynamical response of the sensing device when it is alternately immersed into solutions at pH 3 and 6 [61]

In Fig. 9 the shift of the LMR absorption peak is shown when the sensitive coating is alternately immersed into solutions at pH 3 and 6. The response is highly stable and repetitive. The absorption peak shows a shift of 110 nm in the tested pH range, what is equivalent to a sensitivity of 36.6 nm/pH unit. In addition, this device presents rise and fall times of 24 and 33 seconds, respectively [61].

Additionally, in order to observe the resonance wavelength shift for intermediate pH values, the device was exposed to repeated cycles of pH 6, 5, 4 and 3. In Fig. 10 it is represented the resonance wavelength shift as a function of time showing a durable and repetitive response for several pH change cycles between pH 6 and pH 3 [61].

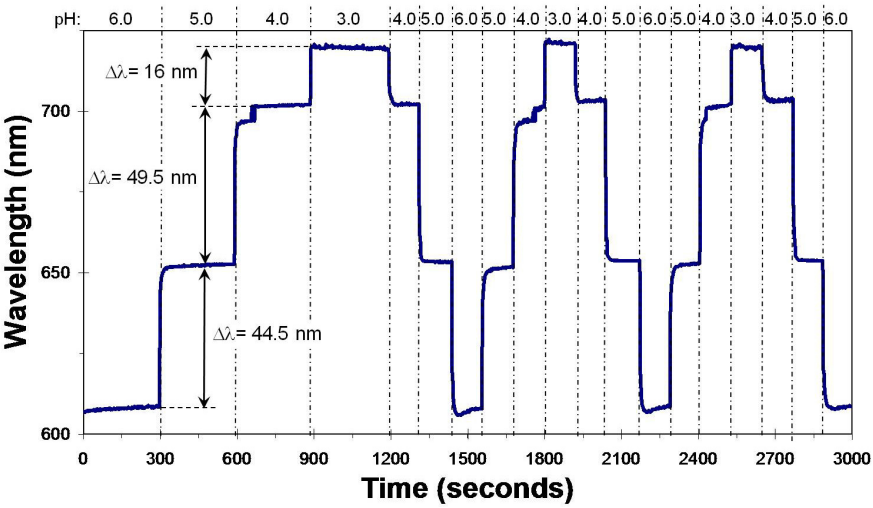

Fig. 10. Dynamical response of the sensor to cycles of pH 6, 5, 4 and 3 of different duration [61]

Here, it is observed that the sensitivity between pH 6 and pH 5 (45.45 nm/pH unit) is of the same order than that between pH 5 and pH 4 (50 nm/pH unit). However, the sensitivity between pH 4 and pH 3 (16.12 nm/pH unit) is about three times lower than that of the rest, which indicated smaller coating thickness variations.

3.2 Devices Based on Two Coatings: A LMR Supporting Coating and a Sensitive Coating

It has been observed in section 3.1.1 that the LMR peaks shift to the red when the refractive index of the external medium varies. If the LMR supporting layer (the ITO layer in our case) is coated with any material whose effective refractive index is sensitive to a certain magnitude, the LMR absorption peaks generated by the ITO coating will shift when this external magnitude varies. This way, different optical fiber sensors can be fabricated by just adding a coating of a sensitive material onto the LMR supporting layer. Some examples of this procedure are shown in the following sections.

3.2.1 Optical Fiber Humidity Sensor Based on an Agarose Sensitive Layer Deposited onto an ITO LMR-Supporting Layer

Agarose is the substance used to fabricate the sensitive layer of this first sensor based on LMR. The thickness of this gel varies with the external relative humidity (RH) [64]. In fact, the agarose layer becomes thicker when the RH rises because the structure receives water molecules that take up the place where there was air before. As the water refractive index (n = 1.33) is higher than the air (n = 1), the effective refractive index of the agarose will be higher when the RH rises. [65]. A schematic detail of the device is shown in Fig. 11.

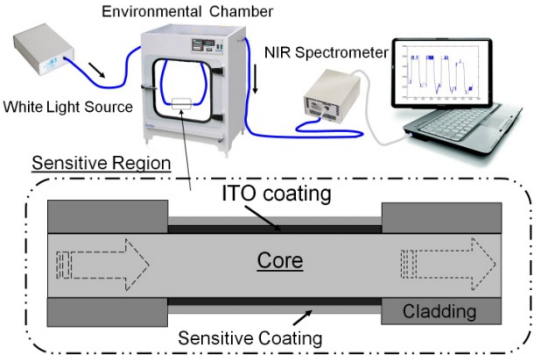

Fig. 11. Experimental setup utilized to characterize the sensor response and schematic detail of the sensitive region [66]

The experimental transmission setup used to characterize the sensor is also shown in Fig. 11. In order to subject the sensor to RH changes, the sensitive section was introduced into a climatic chamber.

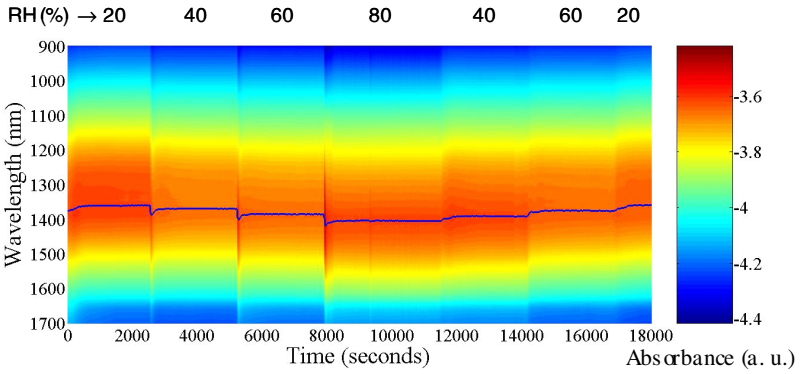

Fig. 12. Spectral response and maxima absorption wavelength variations (line) at different RH values [67]

The final device, that includes the agarose layer onto the ITO coating, shows a good sensitivity to changes in the external RH. This fact was tested by subjecting the sensor to a complete cycle of RH variation between 20 and 80%, with steps of 20% each 30 minutes [67].

In Fig. 12 the shift of the LMR absorption peak to higher wavelengths when the RH increases is shown. This figure represents the spectra collected during the experiment. The relative humidity is shown at the top of the graph and the time in seconds at the bottom, in the horizontal axis. The vertical axis represents the wavelength of the spectra. The colours chosen to represent the spectra are shown in the plot on the right. According to this palette, the red zones of the graph correspond to the LMR absorption peak. In order to show with higher clarity the evolution of the LMR, the maxima of these spectra have been remarked by a blue line. These experimental results corroborate the previous hypothesis about the variation of the agarose refractive index.

The dynamical response of the LMR maxima is shown with higher detail in figure 13. It can be observed here the shift of the LMR (blue line) with the changes in the RH (pink line). The sensor shows a dynamical range of 45 nm when the RH varies between 20 and 80%, what corresponds to a sensitivity of 0.75 nm/RH%.

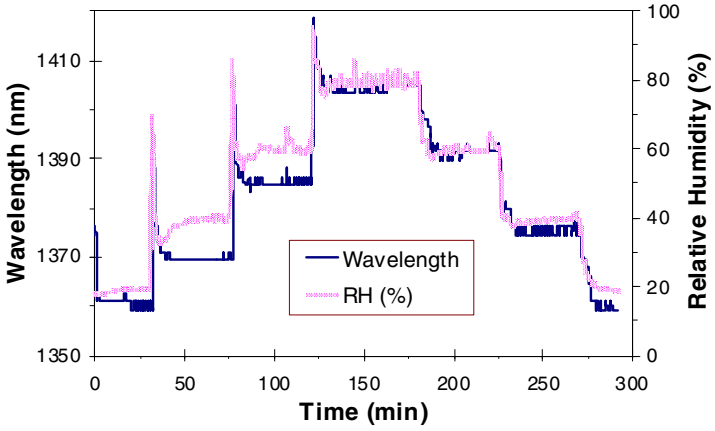

Fig. 13. Wavelength resonance when the sensor is subjected to RH changes [67]

3.2.2 Optical Fiber Humidity Sensor Based on a PAH/PAA Thin Film Deposited onto an ITO LMR-Supporting Coating

The agarose sensor presented in the previous paragraph shows a good response to humidity changes. However, the method applied to deposit the agarose onto the ITO layer makes difficult to control the thickness of the film. For this reason, it is only possible to select the sensor sensitivity and operation wavelength by changing the parameters of the ITO coating.

Another possibility is to find a different material to create the sensitive layer onto the ITO coating. The structure PAH/PAA presented in section 3.1.2 shows hydrophilic features and is sensitive to changes in the relative humidity. [6, 10, 68]. As the agarose gel, the PAH/PAA structure changes air by water when the RI rises, making higher its effective refractive index. But maybe the most important advantage of this structure is that the thickness of the deposited coating can be controlled with high accuracy.

To fabricate this humidity sensor, the refractometer based on an ITO coating with a thickness of 115 nm was used again. Two different sensors were fabricated by depositing onto the ITO coating two PAH/PAA coatings with different thickness values (sensor A with 20 bilayers of PAH/PAA and sensor B with 100 bilayers) [66].

Both sensors were tested for RH changes between 20% and 90% for several cycles using the experimental setup of Fig. 11. In both cases the resonance wavelength shift as a function of the RH follows perfectly the RH measurements obtained from the electronic sensor located in the climatic chamber. In addition to this, the sensor exhibits a fast response to changes in RH as it is shown in Fig. 14. Sensor A shows a variation of the resonance wavelength in the range studied of 13 nm, which corresponds to a sensitivity of 0.185 nm/RH%.

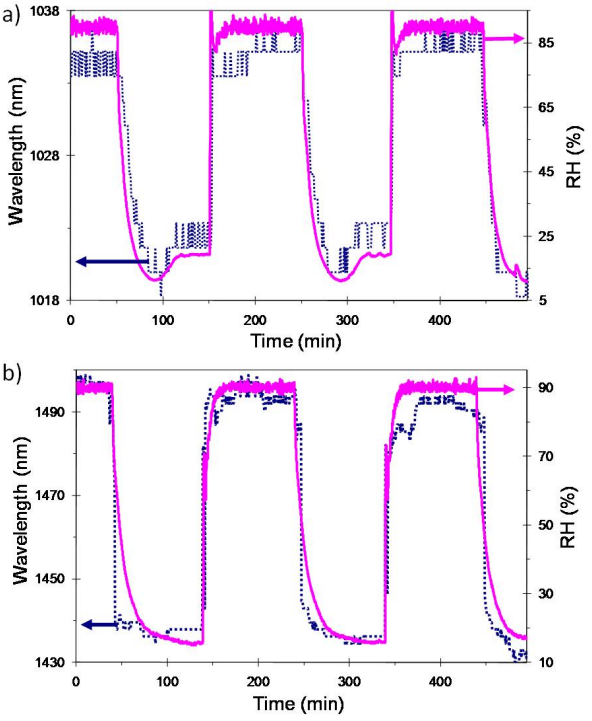

Fig. 14. Dynamical response of the sensors to changes in the RH of the external medium: a) sensor A (20 PAH/PAA bilayers) and b) sensor B (100 PAH/PAA bilayers) [66]

Similarly, in Fig. 14b, the dynamic response of sensor B to changes in RH from 20% to 90% is shown. As it can be seen, the dynamic range of this sensor in the studied range is 58 nm, which corresponds to a sensitivity of 0.83 nm/RH%.

This way, sensor B improves the characteristics of sensor A more than four times enabling the fabrication of OFHS suitable to be used in practical RH monitoring applications.

4 Conclusions

In this chapter, the theoretical basis of electromagnetic resonances produced when an optical waveguide is coated by a thin-film has been explained and the conditions needed to obtain the different types of resonance have been described. In particular, the phenomenon of Lossy Mode Resonance using an optical fiber configuration has been presented for the first time in the literature.

In order to distinguish this effect from the Surface Plasmon Resonance, their properties have been demonstrated.

In addition, the behavior of the different devices based on LMR as refractometers has been experimentally tested. It was observed that the wavelength of the LMR is sensitive to the refractive index of the external medium. In other words, the LMR peaks shift to higher wavelengths when the refractive index is increased. In addition, the sensitivity of this shift is higher when the thickness of the coating is lower.

This sensitivity to the refractive index of the external medium opens the door to a wide range of applications in the optical fiber sensors field. Any of these refractometers can be coated with a material whose refractive index is sensitive to a certain magnitude or substance. This way, a variation of this magnitude will produce a change in the refractive index of the sensitive material and, as a consequence, a shift in the LMR obtained. Some examples of sensors based on this technique have been presented and analyzed here in order to demonstrate this fact. In particular, different optical fiber humidity and pH sensors based on LMR have been characterized.

To summarize, a new kind of optical fiber sensors have been presented in this work. Taking into account the success of optical fiber sensors based on SPR, and due to the fact that some of their limitations are overcome by LMR sensors, this new phenomenon could be applied in a wide range of applications in the next years.

Acknowledgements. This work was supported by the Spanish Economy and Competitivity Ministry TEC2010-17805 and AIB2010NZ-00328 Research Grants.

References

[1] Gusarov, A., Fernandez Fernandez, A., Vasiliev, S., Medvedkov, O., Blondel, M., Berghmans, F.: Effect of gamma-neutron nuclear reactor radiation on the properties of Bragg gratings written in photosensitive Ge-doped optical fiber. Nuclear Instruments and Methods in Physics Research, Section B: Beam Interactions with Materials and Atoms 187, 79–86 (2002)

[2] Wolfbeis, O.S.: Fibre-optic sensors in biomedical sciences. Pure and Applied Chemistry 59, 663–672 (1987)
[3] Arregui, F.J.: Sensors Based on Nanostructured Materials. Springer, New York (2009)
[4] Dakin, J., Culshaw, B.: Optical Fiber Sensors, vol. I, II, III and IV. Artech House Publishers, Massachusetts (1988, 1989, 1996, 1997)
[5] Matias, I.R., Arregui, F.J., Claus, R.O.: Optical Fiber Sensors. American Scientific Publishers, New York (2006)
[6] Arregui, F.J., Matías, I.R., Cooper, K.L., Claus, R.O.: Simultaneous measurement of humidity and temperature by combining a reflective intensity-based optical fiber sensor and a fiber bragg grating. IEEE Sensors Journal 2, 482–487 (2002)
[7] Corres, J.M., Del Villar, I., Matias, I.R., Arregui, F.J.: Two-layer nanocoatings in long-period fiber gratings for improved sensitivity of humidity sensors. IEEE Transactions on Nanotechnology 7, 394–400 (2008)
[8] Larrión, B., Hernáez, M., Arregui, F.J., Goicoechea, J., Bravo, J., Matías, I.R.: Photonic Crystal Fiber Temperature Sensor Based on Quantum Dot Nanocoatings. Journal of Sensors (2009)
[9] Corres, J.M., Arregui, F.J., Matías, I.R.: Sensitivity optimization of tapered optical fiber humidity sensors by means of tuning the thickness of nanostructured sensitive coatings. Sensors and Actuators, B: Chemical 122, 442–449 (2007)
[10] Arregui, F.J., Liu, Y., Matias, I.R., Claus, R.O.: Optical fiber humidity sensor using a nano Fabry-Perot cavity formed by the ionic self-assembly method. Sensors and Actuators, B: Chemical 59, 54–59 (1999)
[11] Homola, J.: Surface plasmon resonance biosensing. In: CLEO/Europe - EQEC 2009 - European Conference on Lasers and Electro-Optics and the European Quantum Electronics Conference (2009)
[12] Homola, J.: Surface plasmon resonance biosensors: Advances and applications. In: Proceedings of SPIE - the International Society for Optical Engineering (2009)
[13] Homola, J.: Surface Plasmon Resonance Based Sensors. Springer, New York (2006)
[14] Gupta, B.D., Verma, R.K.: Surface plasmon resonance-based fiber optic sensors: Principle, probe designs, and some applications. Journal of Sensors (2009)
[15] Gupta, B.D., Sharma, A.K.: Sensitivity evaluation of a multi-layered surface plasmon resonance-based fiber optic sensor: A theoretical study. Sensors and Actuators, B: Chemical 107, 40–46 (2005)
[16] NTSC of the USA Government, "The national nanotechnology initiative. strategic plan (2004)
[17] Fundación OPTI, "Aplicaciones industriales de las nanotecnologías en españa en el horizonte 2020" (2008)
[18] Del Villar, I., Zamarreno, C.R., Hernaez, M., Arregui, F.J., Matias, I.R.: Lossy Mode Resonance Generation With Indium-Tin-Oxide-Coated Optical Fibers for Sensing Applications. Journal of Lightwave Technology 28, 111–117 (2010)
[19] Liedberg, B., Nylander, C., Lunström, I.: Surface plasmon resonance for gas detection and biosensing. Sensors and Actuators 4, 299–304 (1983)
[20] van Gent, J., Lambeck, P.V., Bakker, R.J., Popma, T.H.J.A., Sudhölter, E.J.R., Reinhoudt, D.N.: Design and realization of a surface plasmon resonance-based chemo-optical sensor. Sensors and Actuators: A.Physical 26, 449–452 (1991)
[21] Stenberg, E., Persson, B., Roos, H., Urbaniczky, C.: Quantitative determination of surface concentration of protein with surface plasmon resonance using radiolabeled proteins. J. Colloid Interface Sci. 143, 513–526 (1991)
[22] Dougherty, G.: Compact optoelectronic instrument with a disposable sensor based on surface plasmon resonance. Measurement Science and Technology 4, 697–699 (1993)

[23] Ekgasit, S., Tangcharoenbumrungsuk, A., Yu, F., Baba, A., Knoll, W.: Resonance shifts in SPR curves of nonabsorbing, weakly absorbing, and strongly absorbing dielectrics. Sensors and Actuators, B: Chemical 105, 532–541 (2005)
[24] Chyou, J., Chu, C., Chien, F., Lin, C., Yeh, T., Hsu, R.C., Chen, S.: Precise determination of the dielectric constant and thickness of a nanolayer by use of surface plasmon resonance sensing and multiexperiment linear data analysis. Appl. Opt. 45, 6038–6044 (2006)
[25] Chiang, H.P., Chen, C., Wu, J.J., Li, H.L., Lin, T.Y., Sánchez, E.J., Leung, P.T.: Effects of temperature on the surface plasmon resonance at a metal-semiconductor interface. Thin Solid Films 515, 6953–6961 (2007)
[26] Le Person, J., Colas, F., Compère, C., Lehaitre, M., Anne, M., Boussard-Plédel, C., Bureau, B., Adam, J., Deputier, S., Guilloux-Viry, M.: Surface plasmon resonance in chalcogenide glass-based optical system. Sensors and Actuators, B: Chemical 130, 771–776 (2008)
[27] Feng, W., Shenye, L., Xiaoshi, P., Zhuangqi, C., Yongkun, D.: Reflective-type configuration for monitoring the photobleaching procedure based on surface plasmon resonance. Journal of Optics A: Pure and Applied Optics 10 (2008)
[28] Jorgenson, R.C., Yee, S.S.: A fiber-optic chemical sensor based on surface plasmon resonance. Sensors and Actuators: B. Chemical 12, 213–220 (1993)
[29] Culshaw, B., Kersey, A.: Fiber-optic sensing: A historical perspective. J. Lightwave Technol. 26, 1064–1078 (2008)
[30] Cusano, A., López-Higuera, J.M., Matias, I.R., Culshaw, B.: Editorial optical fiber sensor technology and applications. IEEE Sensors Journal 8, 1052–1054 (2008)
[31] Lee, B.: Review of the present status of optical fiber sensors. Optical Fiber Technology 9, 57–79 (2003)
[32] Wolfbeis, O.S.: Fiber-optic chemical sensors and biosensors. Anal. Chem. 76, 3269–3284 (2004)
[33] Piliarik, M., Homola, J., Maníková, Z., Čtyroký, J.: Surface plasmon resonance sensor based on a single-mode polarization-maintaining optical fiber. Sensors and Actuators, B: Chemical 90, 236–242 (2003)
[34] Gentleman, D.J., Obando, L.A., Masson, J., Holloway, J.R., Booksh, K.S.: Calibration of fiber optic based surface plasmon resonance sensors in aqueous systems. Anal. Chim. Acta 515, 291–302 (2004)
[35] Mitsushio, M., Higashi, S., Higo, M.: Construction and evaluation of a gold-deposited optical fiber sensor system for measurements of refractive indices of alcohols. Sens. Actuators A Phys. 111, 252–259 (2004)
[36] Kim, Y., Peng, W., Banerji, S., Booksh, K.S.: Tapered fiber optic surface plasmon resonance sensor for analyses of vapor and liquid phases. Opt. Lett. 30, 2218–2220 (2005)
[37] Sharma, A.K., Jha, R., Gupta, B.D.: Fiber-Optic Sensors Based on Surface Plasmon Resonance: A Comprehensive Review. IEEE Sensors Journal 7, 1118–1129 (2007)
[38] Slavík, R., Homola, J., Tyroký, J., Brynda, E.: Novel spectral fiber optic sensor based on surface plasmon resonance. Sensors and Actuators, B: Chemical 74, 106–111 (2001)
[39] Rajan, Chand, S., Gupta, B.D.: Fabrication and characterization of a surface plasmon resonance based fiber-optic sensor for bittering component-Naringin. Sensors and Actuators, B: Chemical 115, 344–348 (2006)
[40] Rhodes, C., Cerruti, M., Efremenko, A., Losego, M., Aspnes, D.E., Maria, J., Franzen, S.: Dependence of plasmon polaritons on the thickness of indium tin oxide thin films. J. Appl. Phys. 103 (2008)

[41] Robusto, P.F., Braunstein, R.: Optical measurements of the surface plasmon of indium-tin oxide. Physica Status Solidi (A) Applied Research 119, 155–168 (1990)
[42] Brewer, S.H., Franzen, S.: Optical properties of indium tin oxide and fluorine-doped tin oxide surfaces: Correlation of reflectivity, skin depth, and plasmon frequency with conductivity. J. Alloys Compounds 338, 73–79 (2002)
[43] Brewer, S.H., Franzen, S.: Indium tin oxide plasma frequency dependence on sheet resistance and surface adlayers determined by reflectance FTIR spectroscopy. J. Phys. Chem. B 106, 12986–12992 (2002)
[44] Yang, F., Sambles, J.R.: Determination of the optical permittivity and thickness of absorbing films using long range modes. Journal of Modern Optics 44, 1155–1163 (1997)
[45] Marciniak, M., Grzegorzewski, J., Szustakowski, M.: Analysis of lossy mode cut-off conditions in planar waveguides with semiconductor guiding layer. IEE Proc. Part J Optoelectron 140, 247–252 (1993)
[46] Razansky, D., Einziger, P.D., Adam, D.R.: Broadband absorption spectroscopy via excitation of lossy resonance modes in thin films. Phys. Rev. Lett. 95, 1–4 (2005)
[47] Batchman, T.E., McWright, G.M.: Mode coupling between dielectric and semiconductor planar waveguides. IEEE J. Quant. Electron. 18, 782–788 (1982)
[48] Carson, R.F., Batchman, T.E.: Multimode phenomena in semiconductor-clad dielectric optical waveguide structures. Appl. Opt. 29, 2769–2780 (1990)
[49] Del Villar, I., Matias, I.R., Arregui, F.J., Achaerandio, M.: Nanodeposition of materials with complex refractive index in long-period fiber gratings. J. Lightwave Technol. 23, 4192–4199 (2005)
[50] Xu, M.Y.C., Alam, M.Z., Zilkie, A.J., Zeaiter, K., Aitchison, J.S.: Surface plasmon polaritons mediated by ITO at near infrared wavelength. In: Conference on Quantum Electronics and Laser Science (QELS) - Technical Digest Series (2008)
[51] Chopra, K.L., Das, S.R.: Thin Film Solar Cells. Thin Film Solar Cells. Plenum, New York (1983)
[52] Costellamo, J.E.: Handbook of Display Technology. Academic, New York (1992)
[53] Marks, R.S., Novoa, A., Konry, T., Krais, R., Cosnier, S.: Indium tin oxide-coated optical fiber tips for affinity electropolymerization. Materials Science and Engineering C 21, 189–194 (2002)
[54] Patel, N.G., Patel, P.D., Vaishnav, V.S.: Indium tin oxide (ITO) thin film gas sensor for detection of methanol at room temperature. Sensors and Actuators, B: Chemical 96, 180–189 (2003)
[55] Konry, T., Novoa, A., Cosnier, S., Marks, R.S.: Development of an "electroptode" immunosensor: Indium tin oxide-coated optical fiber tips conjugated with an electropolymerized thin film with conjugated cholera toxin B subunit. Anal. Chem. 75, 2633–2639 (2003)
[56] Salama, O., Herrmann, S., Tziknovsky, A., Piura, B., Meirovich, M., Trakht, I., Reed, B., Lobel, L.I., Marks, R.S.: Chemiluminescent optical fiber immunosensor for detection of autoantibodies to ovarian and breast cancer-associated antigens. Biosensors and Bioelectronics 22, 1508–1516 (2007)
[57] Luff, B.J., Wilkinson, J.S., Perrone, G.: Indium tin oxide overlayered waveguides for sensor applications. Appl. Opt. 36, 7066–7072 (1997)
[58] Cooper, P.R.: Refractive-index measurements of liquids used in conjunction with optical fibers. Appl. Opt. 22, 3070–3072 (1983)
[59] Daimon, M., Masumura, A.: Measurement of the refractive index of distilled water from the near-infrared region to the ultraviolet region. Appl. Opt. 46, 3811–3820 (2007)

[60] Lee, B., Roh, S., Park, J.: Current status of micro- and nano-structured optical fiber sensors. Optical Fiber Technology 15, 209–221 (2009)
[61] Zamarreño, C.R., Hernáez, M., Del Villar, I., Matías, I.R., Arregui, F.J.: Optical fiber pH sensor based on lossy-mode resonances by means of thin polymeric coatings Sensors and Actuators, B: Chemical. Sensors and Actuators, B: Chemical 155, 290–297 (2011)
[62] Goicoechea, J., Zamarreño, C.R., Matías, I.R., Arregui, F.J.: Optical fiber pH sensors based on layer-by-layer electrostatic self-assembled Neutral Red. Sensors and Actuators, B: Chemical 132, 305–311 (2008)
[63] Itano, K., Choi, J., Rubner, M.F.: Mechanism of the pH-induced discontinuous swelling/deswelling transitions of poly(allylamine hydrochloride)-Containing polyelectrolyte multilayer films. Macromolecules 38, 3450–3460 (2005)
[64] Chen, Z., Lu, C.: Humidity sensors: A review of materials and mechanisms. Sensor Letters 3, 274–295 (2005)
[65] Arregui, F.J., Ciaurriz, Z., Oneca, M., Matias, I.R.: An experimental study about hydrogels for the fabrication of optical fiber humidity sensors. Sensors and Actuators, B: Chemical 96, 165–172 (2003)
[66] Zamarreño, C.R., Hernaez, M., Del Villar, I., Matias, I.R., Arregui, F.J.: Tunable humidity sensor based on ITO-coated optical fiber. Sensors and Actuators, B: Chemical 146, 414–417 (2010)
[67] Hernaez, M., Zamarreño, C.R., Fernandez-Valdivielso, C., Del Villar, I., Arregui, F.J., Matias, I.R.: Agarose optical fibre humidity sensor based on electromagnetic resonance in the infra-red region. Physica Status Solidi (C) Current Topics in Solid State Physics 7, 2767–2769 (2010)
[68] Corres, J.M., Matías, I.R., Hernáez, J.M., Bravo, J., Arregui, F.J.: Optical fiber humidity sensors using nanostructured coatings of SiO2 nanoparticles. IEEE Sensors J. 8, 281–285 (2008)

Ultrasonic Thermometry for Temperature Profiling of Heated Materials

Ikuo Ihara, Takuya Tomomatsu, Manabu Takahashi, Akira Kosugi,
Iwao Matsuya, and Hiroyuki Yamada

Nagaoka University of Technology,
Nagaoka, Japan

Abstract. In the fields of materials science and engineering, there are growing demands for monitoring temperature and its distribution of heated materials. This is basically because temperature is one of important factors that dominate material properties and related characteristics such as mechanical, electrical and chemical behaviours. In general, temperature monitoring is required for not only the surface but also the inside of heated materials. In this work, a new ultrasonic method for monitoring temperature gradients of materials during heating or cooling is presented. The method consists of ultrasonic pulse-echo measurements and an inverse analysis for determining one-dimensional temperature distributions along the direction of ultrasound propagation either inside or on the surface of heated materials. To demonstrate the practical feasibility of the method, several experiments with heated materials have been made and successful results of internal temperature profiling are obtained. In addition, non-contact methods with a laser ultrasonic technique for monitoring surface temperature distributions of heated materials are proposed and their potentials are demonstrated. Thus, it is highly expected that the ultrasonic thermometry is a promising means for on-line temperature profiling of industrial materials processed at elevated temperatures.

1 Introduction

Temperature is one of the fundamental and important parameters in the fields of science and engineering. This is basically because material properties such as mechanical, electrical, and chemical characteristics are closely related to temperature and often show a strong temperature dependence. Therefore, measuring temperature and understanding its behaviour comprehensively are indispensable issues required to be able to succeed in basic research, development and fabrication of advanced materials and related products. In particular, for development and manufacturing of industrial materials, it is strongly required to monitor the temperature distribution and its transient variation of the material being processed at high temperatures because the temperature state in the material crucially influences the quality and productivity of final products. Thus, in-situ or

S.C. Mukhopadhyay et al. (Eds.): Advancement in Sensing Technology, SSMI 1, pp. 211–236.
springerlink.com

in-process monitoring technique for temperature distributions could be beneficial not only for basic research of materials but also for realizing an effective process control of materials manufacturing. It is often expected to evaluate either or both of internal and surface temperatures of heated materials, depending on application or objective because surface and internal temperatures are closely related to each other and sometimes independent of each other. Although conventional thermocouple techniques are widely used for temperature measurements, it is not always acceptable for obtaining a high spatial distribution of internal temperature because of difficulty in installing the probes into the material being processed. In addition, the thermocouple may not be appropriate for applying to real-time monitoring because of its relatively slow time-response or sensitivity in measurements. Furthermore, it is inconvenient for precise measurements of surface temperatures because of atmospheric effects and difficulty in installing the probe onto the material surface. An infrared radiation technique is well known as an alternative method for temperature measurement. Since this method enables noncontact measurements of the surface temperatures of materials, it may be convenient for on-line applications. In this method, however, accurate temperature measurements are often hindered by the different emissivity and reflection of infrared radiation from other heat sources. Such effects due to the emissivity and reflectivity result in the deterioration of measurement accuracy. To avoid such problem and improve the measurement accuracy in infrared radiation method, material surface is often required to be painted black, though it is a troublesome for practical applications. It should be noted that this technique does not allow internal temperature measurements.

Ultrasound, owing to its high sensitivity to temperature, is expected to be an alternative method for temperature measurements. Because of the advantages of ultrasonic measurements, such as non-invasiveness and faster responses, many works on the application of ultrasound to temperature estimations have been carried out extensively. In the early stages, Degertekin et al. [1] carried out temperature measurements of semiconductor wafers using Lamb waves, and Simon et al. [2] attempted to fabricate a temperature tomograph using an array sensor. Mizutani and co-workers [3][4], Kudo and coworkers [5][6], Huang et al.[7], Gulik et al. [8], Tsai et al.[9], Funakoshi et al.[10], Minamide et al.[11] and Ingleby et al. [12] extensively studied the measurements of temperature distributions in air using multiple sensors. Chen et al. [13], Balasubramainiam et al. [14], and Ishikawa and Mizutani [15] applied temperature measurement techniques using a delay line to industrial applications. Wang et al. [16] and Nishimura et al. [17] studied the relationship between temperature and surface acoustic wave velocity. Kashiwagura et al. [18] reported the temperature dependence of bulk waves. Matsuda et al. [19] reported the measurement of a uniform temperature by a laser ultrasound. In our previous works [20][21], a new ultrasonic thermometry which is an ultrasonic pulse echo method coupled with an inverse analysis was developed and applied to the measurements of internal temperature distributions of heated thick plates. It has been demonstrated in the

works that one-dimensional temperature distributions inside the materials being heated can be successfully determined by the ultrasonic inverse method coupled with a one-dimensional finite difference calculation [21]. The advantage of the method is that no information on the thermal boundary condition at the heating surface at which the thermal state is often unstable and measuring temperature is difficult to perform appropriately is required for inversion. It was also shown in the experiment using a heated steel plate [20][21] that the response time in the ultrasonic method is shorter than that in a method using thermocouples. It is noted that a so-called bulk wave such as longitudinal wave or shear wave is employed in the ultrasonic measurements. Since the velocity of a surface acoustic wave (SAW) propagating on a material surface also exhibits temperature dependence [16][17], the ultrasonic thermometry is also effective in surface temperature measurements [22] if SAW measurements on the surface of heated material are properly performed. One of the advantages of using the SAW in temperature measurements is that it can be applied to any material with a shiny or mirror-finished surface to which the infrared radiation technique cannot be applied. Thus, it has been shown that the ultrasonic thermometry with an appropriate wave type, bulk waves or surface wave, could be useful for monitoring both internal and surface temperature distributions of heated materials. In this paper, the principle of the ultrasonic thermometry and some experimental demonstrations to verify the validity and practicability of the method are presented. The demonstrations include internal temperature profiling for a thick steel plate and ceramic rod during heating or cooling, and surface temperature profiling for a heated aluminum plate. In the surface temperature profiling, a laser-ultrasonic technique providing non-contact ultrasonic measurements is effectively employed [23][24]. In addition, systematic errors which are closely related to measurements accuracy in the ultrasonic thermometry are quantitatively examined through numerical investigations.

2 Principle of Ultrasonic Thermometry

It is known that the velocity of ultrasonic wave propagating through a medium changes with the temperature of the medium. The principle of temperature measurement by ultrasound is based on the temperature dependence of the ultrasonic wave velocity. Assuming a one-dimensional temperature distribution in a medium, the transit time of an ultrasonic wave propagating in the direction of the temperature distribution can be given by

$$t_L = \int_0^L \frac{1}{v(T)} dx, \tag{1}$$

where L is the propagation distance of the ultrasonic wave and $v(T)$ is the ultrasonic velocity which is a function of temperature T. In general, the temperature dependence of the velocity depends on material properties and may

be expressed by a simple equation such as a linear or quadratic function for a certain temperature range such as between 20 °C and 200 °C for a steel [13]. When the medium is being heated, the temperature distribution in the medium can be given as a function of location x and time t. Such a temperature distribution $T(x, t)$ is subjected to the thermal boundary condition of the heated medium. Therefore, on the basis of equation (1), if an appropriate inverse analysis with a certain boundary condition is used, it could be possible to determine the temperature distribution from the transit time t_L measured for the heated medium. In fact, such ultrasonic determination of temperature distribution of a heated silicone rubber plate was demonstrated in our previous work [20]. It should be noted that the inverse method proposed in the former work does work properly as long as the boundary condition such as temperatures at both ends of the heated plate is held stable and known during the heating process. However, such thermal boundary condition is often unstable and unknown for materials being processed at high temperatures. In particular, the temperature of the surface being heated by contacting with a hot medium is extremely difficult to estimate. Therefore, it is required to develop an effective method to overcome such problem and to determine temperature profiles of heated materials quantitatively.

3 Quantitative Determination of Temperature Profiles

3.1 Inversion Method

As shown in Figure 1(a), we consider an internal temperature gradient in a material whose single side is uniformly heated. It is noted that cooling at the single side is also possible to consider. To investigate the temperature distribution of the material we consider a one-dimensional unsteady state heat conduction with a constant thermal diffusivity for making the analysis simple. Assuming that there is no heat source in the plate, the equation of heat conduction is given by [25]

$$\frac{\partial T}{\partial t} = \alpha \frac{\partial^2 T}{\partial x^2}, \tag{2}$$

where T is temperature, x is the distance from the heated surface, t is the elapsed time after the heating starts, and α is the thermal diffusivity. It is known that the temperature distribution can be estimated by solving equation (2) under a certain boundary condition. In actual heating processes, however, the thermal boundary condition at the heating surface is often unstable and unknown because of difficulty in measuring its transient change during heating. Because of little knowledge about the boundary condition on temperature, the temperature distribution inside the material is hardly determined from equation (2). This kind of problematic situation often occurs when the plate is heated by contacting with a very hot medium such as molten metals.

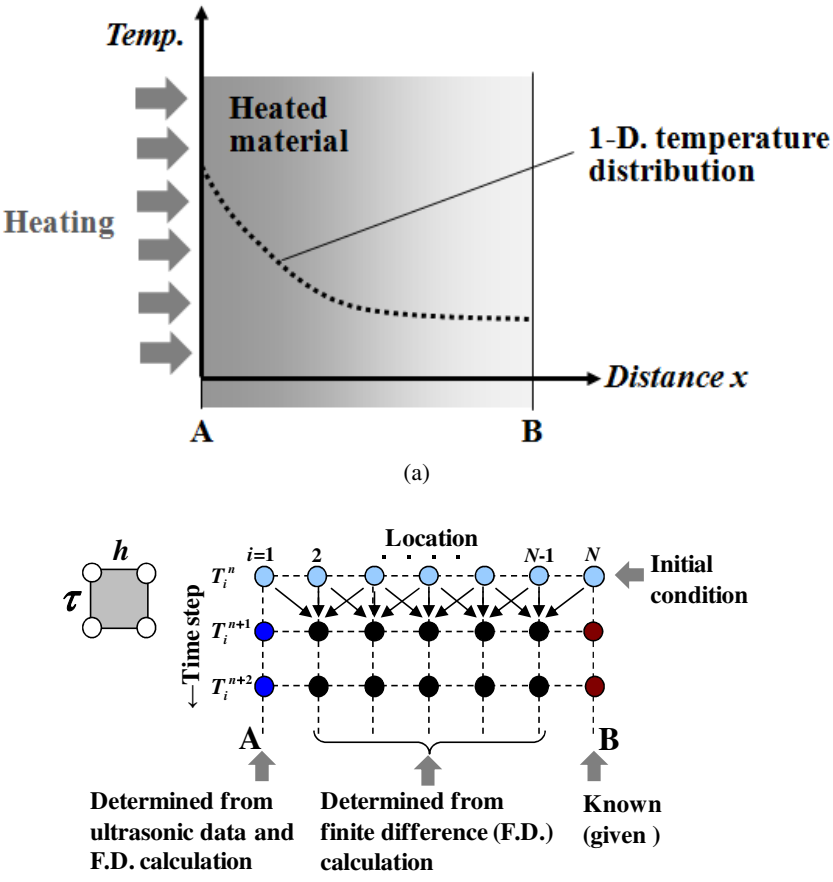

Fig. 1. Analysis model used for temperature distribution estimation: (a) Schematic of a single side heated material with a one-dimensional temperature distribution, (b) Schematic of staggered grids for a one-dimensional finite difference calculation analysis, for determining the temperature distribution of the material shown in (a) [21][22].

To overcome the problem, an effective method for determining the internal temperature distribution is developed [21][22]. The method consists of an ultrasonic pulse-echo measurement and an inverse analysis coupled with a one-dimensional finite difference calculation. A one-dimensional finite difference model composed of a large number of small elements and grids is used for analyzing the temperature distribution in x direction of a material as shown in Figure 1(b). We assume that the material has a uniform temperature T^n in x direction before heating starts. Considering that the heating of the single side of

the material is started at time n, the temperature of each grid point inside the material at time n+1 (that is a very short elapsed time after heating starts) can be given by [26]

$$T_i^{n+1} = T_i^n + r\left(T_{i+1}^n + T_{i-1}^n - 2T_i^n\right) \quad (i = 2, \cdots, N-1) \tag{3}$$

$$r = \frac{\alpha\tau}{h^2} \quad , \tag{4}$$

where N is the number of the grid point, i and n are indices corresponding to spatial coordinate and consecutive time, respectively. T_i^n is the temperature of each grid point i at time n. The coefficient r is called "the Von Neumann stability criterion" and should be taken to be less than 0.5 to be able to obtain appropriate and stable results in the finite difference analysis. τ is the time step and h is the interval between the grid points. We define i=1 as the heated surface that may be contacted with a hot medium and i=N as the other side that has no heat source. Since we can calculate the temperatures T_i^{n+1} (i=2, ⋯ , N-1) from equation (3), it is now required to obtain the temperatures at the both sides of the plate, T_1^{n+1} and T_N^{n+1}, so that the temperature distribution in x direction of the material could be fully determined. We can assumed that the temperature T_N^{n+1} may be able to be known or given because such temperature of a low temperature side can easily be obtained using any conventional technique such as a thermocouple or an infrared radiation. However, the temperature at the heated surface, T_1^{n+1}, is usually unknown because of difficulty in measuring it. Although the T_1^{n+1} is unknown unless the thermal boundary conditions at both ends of the plate are given, it is fortunately possible to estimate the T_1^{n+1} if a finite difference calculation is coupled with a transit time of ultrasound propagating through the material. Using a concept of trapezoidal integration, the transit time t_L given in equation (1) can be approximately calculated from

$$t_L = h\left(\frac{1}{v_1^{n+1}} + \frac{1}{v_N^{n+1}}\right) + 2h\sum_{i=2}^{N-1}\frac{1}{v_i^{n+1}} \quad . \tag{5}$$

From equation (5) and the relation between temperature and ultrasonic velocity, the temperature of the heated surface at time n+1, T_1^{n+1}, can be determine by

$$T_1^{n+1} = -\frac{1}{a\left\{\frac{t_L}{h} - \left(\frac{1}{v_N^{n+1}} + 2\sum_{i=2}^{N-1}\frac{1}{v_i^{n+1}}\right)\right\}} + \frac{b}{a}, \tag{6}$$

where t_L is the transit time of ultrasound measured in the x direction at the time n+1. It should be noted that equation (6) is derived under the assumption that the temperature dependence of ultrasonic velocity has a linear relation shown as follows:

$$v(T) = -aT + b \quad , \tag{7}$$

where a and b are constants determined experimentally. The velocity v_i^{n+1} at each grid point in equation (6) can be estimated from equation (7) since the temperature at each grid point can be obtained from equations (3) and (4). Therefore, the temperature of the heated surface at time n+1, T_1^{n+1}, can then be determined from equation (6) when the transit time t_L is given as a measured value with any experimental technique such as a pulse-echo measurement. Once the temperatures of all grid points in the material at the time n+1, T_1^{n+1},⋯, T_N^{n+1}, are determined, we can then determine the temperature distribution at next time n+2 in the same procedure using the transit time t_L measured at the time n+2. Thus, we can continuously obtain the temperature distribution as long as the ultrasonic measurement is being continued. The advantage of the proposed method is that no boundary condition at the heating surface is necessary. Figure 2 shows the flowchart for determining the temperature distribution. It should be noted in the method that the temperature dependence of the velocity depends on both material property and temperature range and does not always show a linear relation. For almost all the industrial materials, it has been experimentally verified that the temperature dependence may be expressed by a simple equation such as a linear or quadratic function for a certain temperature range such as less than several hundred degrees Celsius.

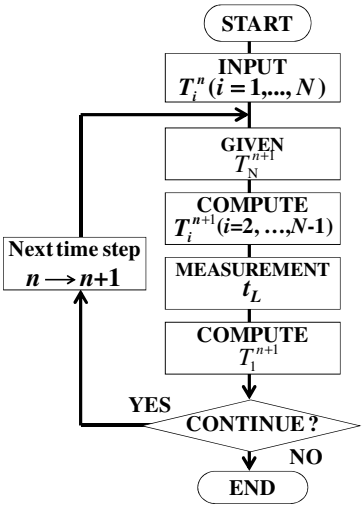

Fig. 2. Flowchart of the procedure for determining temperature distributions

The method for determining temperature profiles described above is available not only for internal temperature but also for surface temperature. Figure 3 shows the concept of the ultrasound thermometry we have proposed. Bulk wave such as a longitudinal or shear wave is used for profiling internal temperatures and SAW is used for surface temperature. The procedure for surface temperature profiling by SAW is described in [27], which is quite similar to that of the internal temperature profiling described in this section.

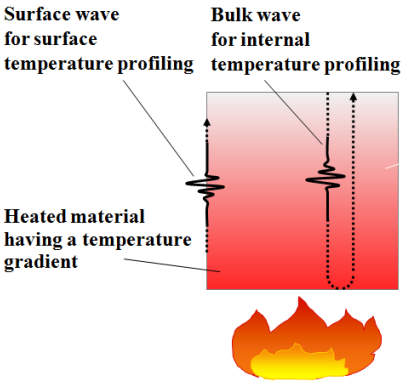

Fig. 3. Concept of the ultrasound thermometry proposed

3.2 Verification of Inversion Method

To verify the validity of the proposed inversion method, a sample model that is numerically given with known data is investigated by the proposed method [21]. We consider an artificial model for heating or cooling process of a steel plate of 30 mm thickness having a one-dimensional temperature distribution in the thickness direction. In the model, various temperature distributions calculated from equation (2) under certain heat conditions are given. Typically, the following two cases are used: (i) increasing in the internal temperature of the plate while the temperatures of heated and non-heated surfaces, T_1 and T_N, are held constant to 100 °C and 26 °C, respectively, (ii) decreasing in the internal temperature while the temperature of the heated surface T_1 is suddenly cooled down from 100 °C to 30 °C. The duration of the heating is 3 s and then the cooling is performed for 2 s. In the verification of the inversion method, such temperature distributions obtained numerically in advance are used as the objectives to be searched. At first, the variations of the transit time of ultrasonic wave propagating through the steel plate during the heating and cooling are calculated from the given temperature distributions and then used for the inversion analysis to determine the temperature distribution and its variation. In the inversion, $v(T)$=-0.691T+5920.5 m/s for the temperature dependence of longitudinal velocity of the steel and T_N=26 °C for the temperature of the non-heated surface are employed as known information. It should be noted that the temperature dependence of the velocity was obtained experimentally for temperature range between 20 °C and 250 °C. Figure 4 shows the variation in internal temperature distribution with elapsed time after heating starts. It is clearly demonstrated that the results determined by the inversion agree very well with the true ones which are the temperature distributions calculated in advance. Thus, it is verified that the proposed inversion method can properly determine the temperature distribution from the transit time of ultrasonic wave. The value of thermal diffusivity for the steel used in the calculation is 11.8×10^{-6} m^2/s. It is noted that the heating and cooling conditions used here are

just used for verifying the validity of the inversion method and have no relation to actual situations. The systematic errors in the temperature estimation due to the deviations in the given data such as the temperature dependence of velocity and thermal diffusivity will be examined in Section 5.

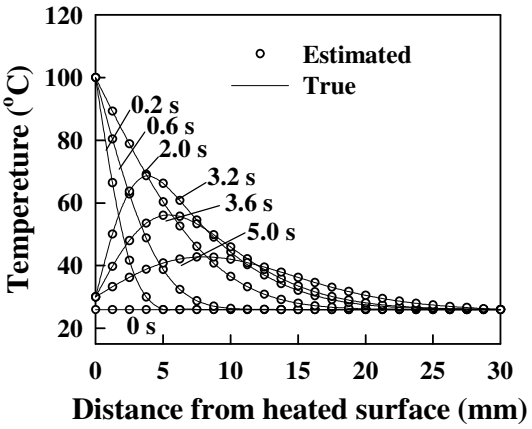

Fig. 4. Comparison of true and estimated temperature distributions during heating and cooling processes. Numbers in the figure denote elapsed time after heating starts [21]

4 Experiments and Results

4.1 Temperature Profiling during Heating and Cooling

To examine the feasibility of the proposed ultrasonic thermometry, internal temperature gradients of a thick steel plate are measured during heating and cooling [28]. Figure 5 shows a schematic diagram of the experimental setup used. This system provides not only ultrasonic pulse-echo measurements but also temperature distribution measurements using thermocouples for comparison purpose. A steel plate (JIS type: SKD61) of 30 mm thickness is used as a specimen. At first, the bottom surface of the plate is heated by contacting with a heater of 200 ºC for a period of 100 s, and then the surface is cooled by water. A longitudinal ultrasonic transducer of 2 MHz is installed on the top surface of the steel for making pulse-echo measurements. To obtain a reference value of the temperature distribution inside the plate, five thermocouples, TC1-TC5, are inserted into the plate. In addition, an infrared radiation camera is used to measure the temperature at the top surface of the plate. The surface temperatures during heating and cooling processes are used as known data in the inversion analysis. Ultrasonic pulse-echo measurements are being performed during heating and cooling, and ultrasonic echoes reflected from the bottom surface and temperatures

at each position are continuously acquired every 0.2 s with a PC based real-time acquisition system. The sampling rate of ultrasonic signal is 100 MHz. Signal fluctuation due to electrical noise in measurements is reduced by taking the average of ten acquired signals.

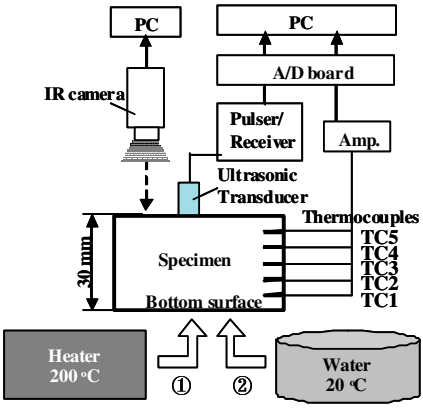

Fig. 5. Schematic of the experimental setup for ultrasonic temperature monitoring

Figure 6 shows ultrasonic echoes reflected from the bottom surface of the plate during heating. The transit time t_L through the plate can precisely be determined from the time delay between the first and second reflected echoes, by taking a cross-correlation between them. Figure 7 shows the variations of the transit time of the ultrasonic wave and temperature in the plate during heating and cooling. The temperature measured using the thermocouple TC1 which is installed at 5 mm from the bottom of the steel is shown in the figure. As expected, the temperature rapidly increases with elapsed time immediately after the contact of the heater, and then markedly decreases just after the water cooling starts. The transit time of ultrasonic wave is also significantly changed with the elapsed time as shown in Figure 7. The tendency of the variation of the transit time almost corresponds to that of the temperature. The transit time at each time step during the heating and cooling is used for the inverse analysis to determine the temperature distribution and its transient variation.

As mentioned in Section 3, the temperature dependence of ultrasonic velocity should be known as the prior information to be used for the inverse analysis. To obtain the relationship between the longitudinal velocity and temperature for the steel plate, pulse-echo measurements with a uniformly heated steel plate is performed using a high temperature ultrasonic transducer of 2 MHz at temperatures up to 100 ^{o}C. The measured temperature dependence of the ultrasonic velocity is shown in Figure 8. It is found that the change of the velocity is almost linear with temperature in this temperature range and therefore the

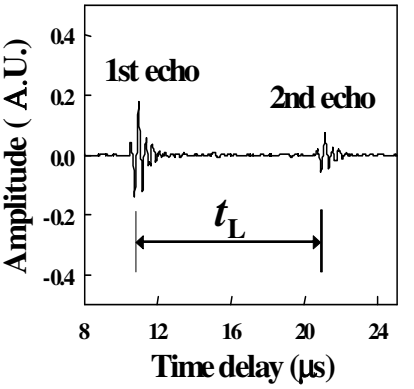

Fig. 6. Ultrasonic pulse echoes reflected from the bottom of the steel plate [28]

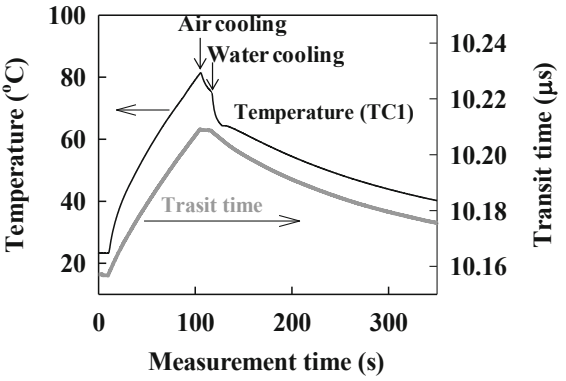

Fig. 7. Variations of the transit time of the ultrasonic wave and temperature in the steel plate during heating and cooling [28]

temperature dependence is approximately given by $v(T) = - 0.616T + 5933.7$ m/s. Using the transit time shown in Figure 7 and the temperature dependence of the ultrasonic velocity, the temperature distribution in the plate and its variation are estimated from the inversion procedure described in Section 3. In the estimation, the temperature of the steel before heating was measured to be 23.3 °C and used as the initial condition. In addition, the temperature of the top surface of the steel plate is being measured using an infrared radiation camera and used as a known value in the inversion.

The estimated temperature distributions are shown in Figure 9, where the numbers shown in the figure denotes the elapsed time after the heating starts. It can be seen that the temperature profile estimated ultrasonically and its variation agree with those measured using thermocouples within a margin of error of plus or

minus 5 °C. Thus, we can see that the proposed ultrasonic thermometry does work properly. It is noted that it takes about 20 ms to calculate a temperature profile from the measured ultrasonic data at each time step, which may be fast enough to make a real-time monitoring.

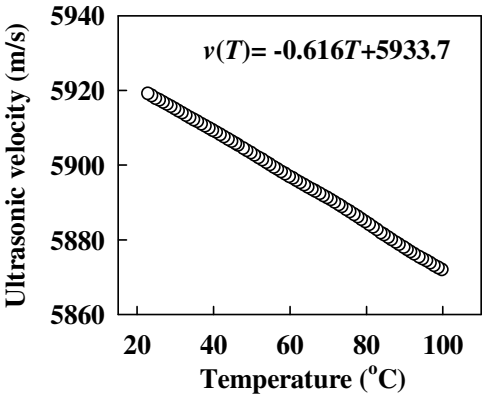

Fig. 8. Temperature dependence of the ultrasonic velocity in the steel plate used [28]

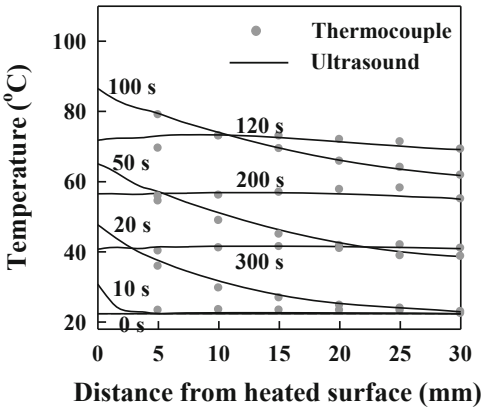

Fig. 9. Variations in temperature profile in the steel plate with elapsed time [28]

Because the heating or cooling rate of the steel plate in the experiment above is rather slow, it is important to check if the proposed thermometry is capable of temperature monitoring for higher heating or cooling rate. We then apply the ultrasonic thermometry to a temperature monitoring in which the bottom surface of a steel plate is quickly heated up to more than 200 °C by contacting with molten aluminum at 600 °C [21]. It is highly expected to realize a sudden and significant change in temperature rise in the heated steel plate. Ultrasonic pulse-echo measurements are performed during the heating, and ultrasonic echoes reflected

from the bottom surface of the steel are continuously acquired every 0.2 s with a PC based real-time acquisition system. Figure 10 shows the variations of reference temperatures with elapsed time after heating starts, measured using thermocouples at different locations in the plate, where TC1 is measured at 5 mm from the bottom surface, TC6 is at the top surface, and TC7 is for the molten aluminum. As we expected, the temperatures start to rise just after the contact of the molten aluminum and increase with the elapsed time. The rising rate becomes higher in the vicinity of the heated surface. The variation in the transit time of the ultrasound through the steel plate is also shown in Figure 10. The temperature of the aluminum, TC7, gradually decreases with the elapsed time because of solidification of the aluminum after the contact with the steel plate while the temperatures in the steel increases because of heating by the hot aluminum. We can clearly see from the behaviour of temperature rising in each location, TC1 to TC6 that there exists a significant temperature gradient in the steel plate. Corresponding to the temperature rising in the plate, we can also see a drastic increase in the transit time of ultrasound. It is interesting that the rising point of the transit time is slightly earlier (about 1.5 s) than the point at which the temperature TC1 starts to rise. This reveals that the ultrasonic technique has a higher sensitivity to temperature change than the conventional thermocouple technique. The transit time at each elapsed time is used for estimating the temperature distribution through the inversion procedure described in Section 3. In the estimation, the temperature of the steel before heating was measured to be 18.7 ^{o}C and used as the initial condition. The temperature of the top surface, TC6, measured using the thermocouple is also used as a known value. Figure 11 shows the temperature distributions estimated for 1.1 s, 6.1 s, 50.0 s and 100.0 s after the heating starts, where the ultrasonically estimated temperatures are compared with those measured using thermocouples. It can be seen that both temperature distributions determined from ultrasound and thermocouples show a similar tendency. We can also see that there are certain discrepancies between ultrasound and thermocouples in the early stage of heating (within about 6 s after the heating starts), while there is a good agreement between them as the time proceeds. Although the reason for the discrepancy is not clear at this moment, it should be noted that the thermocouple does not always provide an accurate measurement for a quick variation in temperature gradient which occurs in the early stage of heating because of its relatively slow time-response in measuring temperature. In contrast, the ultrasonic thermometry may give a proper measurement result because of its faster time-response to temperature change as shown in Figure 10. It is also important that the ultrasonic thermometry enables us to monitor a transient variation in internal temperature profile of heated materials without any thermal boundary condition at heating surface. These features in the ultrasonic thermometry could be practical advantages in industrial process monitoring. It is noted that this method has been applied to a rapid cooling process monitoring of a steel plate and its usefulness is successfully demonstrated. The detail will be published soon.

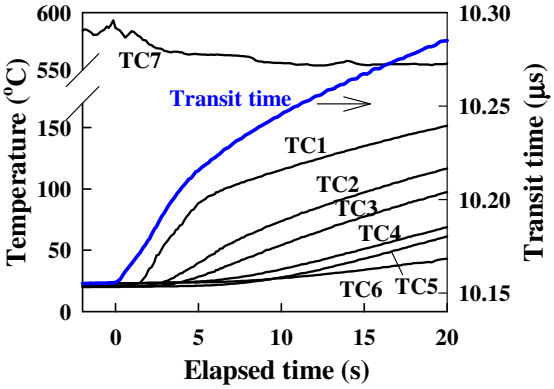

Fig. 10. Variations of the transit time of the ultrasonic wave and reference temperatures in the steel plate being heated by contacting with molten aluminum at 600 °C [21]

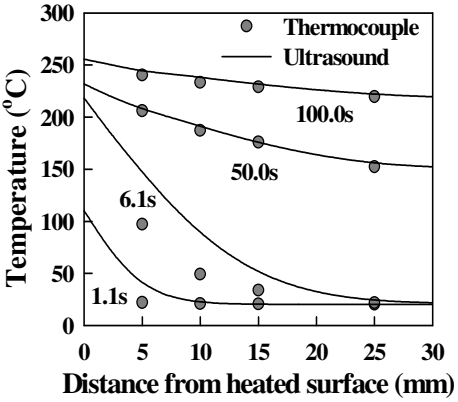

Fig. 11. Comparison between temperature profiles determined by the ultrasonic thermometry and using conventional thermocouples [21]

4.2 Temperature Profiling of Ceramic Material

Ceramics, because of their unique characteristics, have become important and indispensable materials in modern industrial fields. The special character of ceramic materials gives rise to many applications in materials science, electrical engineering, chemical engineering and mechanical engineering. In particular, advanced ceramics with extremely high heat resistant property can be used for many high temperature applications for which metals and polymers are unsuitable. For such high temperature applications, it is often required to know internal temperature of heated ceramics. In sintering or moulding process for ceramics, not only temperature but also its distribution inside the heated ceramics is strongly required to be measured because such temperature distribution plays an important

role affecting the quality of final products of the process, due to the temperature dependence of materials properties of ceramics. Thus, in-situ or in-process monitoring of the internal temperature distribution for heated ceramics is quite beneficial not only for making progress in basic research but also for realizing an effective process control of advanced ceramic materials. In this section, the applicability of the ultrasonic thermometry to ceramics monitoring is demonstrated [29]. In the monitoring, we use shear wave rather than longitudinal wave for the ultrasonic measurements because it is expected that the use of shear wave improves the accuracy in determining temperature due to the fact that the velocity of shear wave is roughly two times slower than that of longitudinal wave.

Figure 12 shows a schematic diagram of the experimental setup used. This system provides not only ultrasonic pulse-echo measurements but also temperature distribution measurements using an infrared camera, so that we can verify the validity of the ultrasonically determined temperature distribution by comparing with that measured using the infrared camera. An alumina rod of 14 mm diameter and 25 mm length is used as a specimen. It should be noted that the surface temperature of the rod measured using the infrared camera is identical to the internal temperature because the Biot number, Bi, which is a dimensionless number used in non-steady-state heat transfer calculations is estimated to be about 0.001 for the alumina and is small enough to ensure that there exists no difference between the internal and surface temperatures for the heated alumina in the temperature range up to a few hundred degrees Celsius. The top surface of the alumina rod is being heated by a heater and pulse-echo measurements are performed using a shear wave ultrasonic transducer of 2 MHz for high temperature-use (Japan probe Co.), during the heating. As mentioned above, the use of shear wave allows us to improve the accuracy in pulse-echo measurements due to the relatively slow velocity in wave propagation. Ultrasonic pulse-echoes reflected from the top surface are continuously acquired every 0.2 s with a PC based real-time acquisition system. The sampling rate of ultrasonic signal is 100 MHz. Signal fluctuation due to electrical noise in measurements is reduced by taking the average of ten ultrasonic signals. The transit time of the ultrasonic wave propagating through the alumina rod can precisely be determined from the time delay between the first and second reflected echoes by taking a cross-correlation between them. The variation in the transit time during the heating is shown in Figure 13. We can see a significant increase in the transit time due to the heating. The transit time at each elapsed time is used for the inverse analysis [21] described in Section 3 to determine the temperature distribution. The estimated temperature distributions are shown in Figure 14, where the numbers shown in the figure denote the elapsed time after the heating starts. It is noted that the temperature dependence of the ultrasonic velocity, $v(T) = - 0.9576T + 5953.3$ m/s for the alumina rod and the initial temperature of the rod before heating, 24 ^{o}C, are used in the estimation. It can be seen in Figure 14 that the temperature distributions estimated ultrasonically almost agree with those measured using the infrared camera, while there are small discrepancies between them in the vicinity of heating surface. Although the reason for the discrepancy is not clear at this moment, we can see that the ultrasonic method does work properly. It is noted that it takes about 20 ms to calculate a temperature distribution at each time step from the measured ultrasonic data, which may be fast enough to make a real-time monitoring.

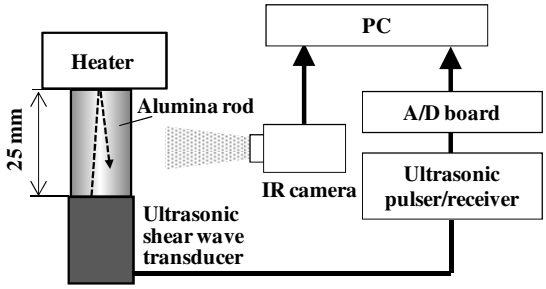

Fig. 12. Schematic diagram of the experimental setup for the temperature profiling of an alumina rod [29]

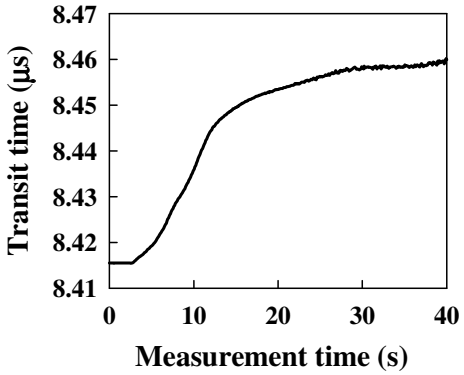

Fig. 13. Variation in the transit time of ultrasonic shear wave in the alumina rod during heating [29]

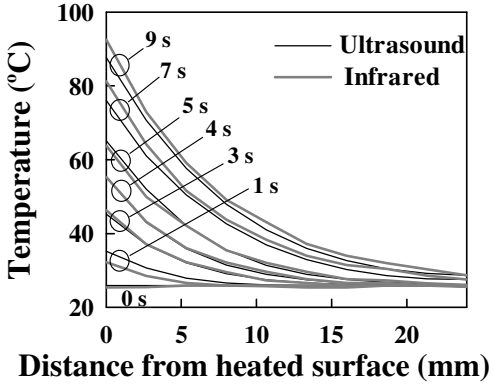

Fig. 14. Variations in the temperature profiles of the alumina rod during heating [29]

4.3 Surface Temperature Profiling by Laser Ultrasound

Surface temperature measurements of heated materials are often required for many industrial applications because the surface temperature reflects the state of internal temperature and therefore, could be a useful diagnositic parameter. It is known that infrared radiation techniques are widely used for measuring the temperature distribution and its variation on a material surface, because of its simplicity and sophisticated ability in non-contact measurements. This technique, however, does not allow to measure internal temperatures of heated materials. In addition, in this method accurate temperature measurements are often hindered by the different emissivities and reflections of infrared radiation from other heat sources. Such influences due to emissivity and reflectivity result in the deterioration of measurement accuracy. Thus, conventional methods including thermocouples as well as the infrared radiations have not always been satisfactory, therefore, development of an alternative method is required for some applications.

4.3.1 One-Dimensional Measurement

In this section, quantitative evaluations of one-dimensional and two-dimensional temperature distributions on a material surface using a SAW which is an ultrasonic wave propagating along a material surface are presented. The principle of the method is based on the temperature dependence of the velocity of the SAW. An effective method consisting of SAW velocity measurements and an inverse analysis coupled with a one-dimensional finite difference calculation is developed to determine the surface temperature distribution quantitatively [22][27]. It is noted that the inverse analysis is similar to that described in Section 3.1. Because conventional contact type ultrasonic transducers are not suitable for high temperature applications owing to the limitation of the Curie point of the piezoelectric elements used in the transducers, non-contact methods are indispensably necessary for measuring SAWs of heated materials. In this work, a laser-ultrasound technique that enables non-contact ultrasonic pulse-echo measurements is employed. The advantage of using the laser-ultrasound technique is that both surface waves and bulk waves such as longitudinal or shear waves can be measured in non-contact configuration. Figure 15 shows a schematic of the laser-ultrasonic system used for non-contact monitoring of SAWs on a heated plate [22]. This system provides simultaneous measurements of the SAWs and the surface temperatures, where the surface temperatures are measured using an infrared radiation camera and used for comparing with ultrasonically estimated temperatures. In the experiment, an aluminum plate of 30 mm thickness is used for a specimen. Two SAWs, SAW1 and SAW2, are generated at positions A and B, respectively, using a pulsed laser generator (Nd:YAG, λ=1064 nm, energy 200 mJ/pulse, pulse width 5 ns) with a polarizing beam splitter, and detected at position C using a laser interferometer based on photorefractive two-wave mixing (Nd:YAG, λ=532 nm, energy 200 mW) [23][24]. Such SAW measurements are continuously performed, while the bottom surface of the plate is heated by

contacting with a heater of 300 ºC. The SAW echoes are acquired every 0.1 s with a PC-based real-time acquisition system. The sampling rate of the ultrasonic signal is 100 MHz. From the difference in time delay between the SAW1 and SAW2 signals, the transit time t_L of the SAW propagating from A to B can be determined. The propagation distance is set to be 50 mm. The transit time t_L is precisely calculated by taking the cross-correlation of the measured SAW1 and SAW2 signals during the heating, and then used for the inverse analysis to determine the one-dimensional surface temperature distribution between A and B. To obtain the reference value of the surface temperature distribution of the plate, an infrared radiation camera is used.

Figure 16 shows the estimated surface temperature distributions for the aluminum plate and their variations with the elapsed time after the heating starts, where the ultrasonically estimated results are compared with those measured using the infrared radiation camera. It is noted that the temperature dependence of the ultrasonic velocity, $v(T) = - 0.7560T + 2981.7$ m/s, the initial temperature of the aluminum plate before heating, 23.5 ^{o}C, and the following values: α=96.8×10^{-6} m^2/s, τ=0.3 s, h=10 mm are used in the estimation. It can be seen from Figure 16 that both temperature distributions determined by the ultrasonic method and the infrared radiation camera almost agree with each other. Although it is probable that the measured values by the infrared radiation camera contain some measurement errors due to an uncertainty of the emissivity and reflectivity of infrared radiation, the good agreement between the temperatures by the ultrasound and infrared radiation reveals that the non-contact ultrasound method does work properly. It is found in the experiment that a relatively large fluctuation of the estimated temperature occurs at point A which is near the heating area. The fluctuation is about ±5 ^{o}C around the value measured by the infrared radiation camera. The standard deviation of the fluctuation is found to be about 2.1 ^{o}C [30].

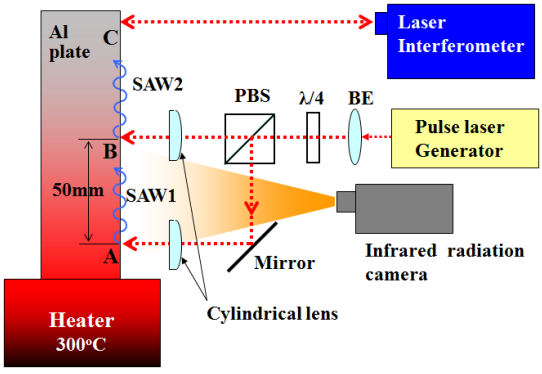

Fig. 15. Schematic of the laser-ultrasonic system used for non-contact monitoring of SAWs on a heated plate [22]

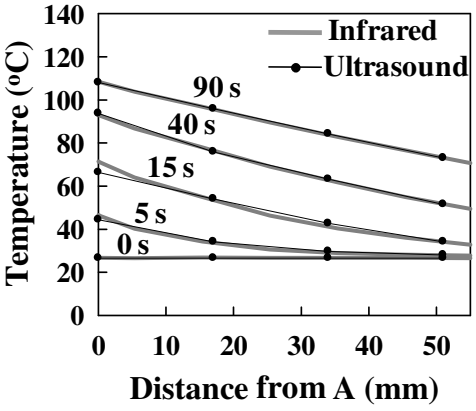

Fig. 16. Estimated surface temperature distributions for the heated aluminum plate and their variations with the elapsed time after the heating starts [22]

4.3.2 Two-Dimensional Measurement

Because it is quite attractive to measure two-dimensional surface temperature distributions in a certain area rather than the one-dimensional distribution such as described in paragraph 4.3.1, an area mapping of surface temperature distribution is attempted [27]. As illustrated in Figure 17, the irradiation point by the pulsed laser generator is sequentially scanned from point A_1 to A_{13} so that thirteen SAWs (SAW_1, …, SAW_{13}) are generated at those irradiated points and propagate toward point B at which each SAW is detected by the laser interferometer [23][24]. Thus, a series of one dimensional SAW measurements are performed within the area of a square on a material surface. Each SAW measured in each propagation route (A_1-B, A_2-B, …, A_{13}-B) is used for the inverse analysis to determine the surface temperature distribution along the route. The surface temperature distributions determined for those routes are then combined for constructing surface temperature distribution in the square. It is noted here that the configuration that the laser interferometer is fixed and the pulsed laser is scanned, is quite effective for conducting two-dimensional measurements of SAWs in a certain area. This is because the alignment between the laser beam by the laser interferometer and the material surface is crucially important in the SAW detections and even a minute misalignment causes problems in detecting the SAW; therefore, any minute displacement of the detection position by the laser interferometer should be avoided and the scanning of the laser beam is quite difficult to perform. On the other hand, the scanning of the irradiation position by the pulsed laser generator does not affect the SAW generation significantly. Thus, the pulsed laser scanning shown in Figure 17 is appropriate for conducting two-dimensional measurements of SAWs.

To demonstrate the feasibility of the area mapping of surface temperature, an experiment is curried out. An aluminum plate of 30 mm thickness is used for a specimen. As shown in Figure 17, the left side of the plate is heated by a heater of 300 ºC and then SAWs are generated at different positions from A_1 to A_{13} on the surface consecutively by pulsed laser scanning irradiation (Nd:YAG, λ=1064 nm, energy 200 mJ/pulse, pulse width 3 ns) using a two-dimensional galvanometer scanner, and each SAW is detected at position B using a laser interferometer mentioned above. By this scanning method, SAWs propagating along different routes are measured within the square of 60 mm x 60 mm. The irradiation interval of the pulsed laser is taken to be 10 mm. Since the pulsed laser scanning from A_1 to A_{13} is completed within 1 s, the scanning is repetitively performed every 1 s. The transit time of each SAW is precisely determined by taking the cross-correlation of the detected signal of SAW during the heating, and then used for the inverse analysis [22] to determine the one-dimensional surface temperature distribution in each propagation route (A_1-B, A_2-B, …, A_{13}-B). It is noted that the temperature dependence of the SAW velocity of the aluminum, $v(T)$=- 0.7560T + 2981.7 m/s, and the following values: α=96.8×10^{-6} m^2/s, τ=0.3 s, and h=10 mm are used for the inverse analysis. The obtained thirteen temperature distributions are combined together to construct the two-dimensional surface temperature distribution of the square at the transient moment. An interpolation method is employed for constructing the two-dimensional distribution. Figure 18 shows the estimated surface temperature distributions and their variations with the elapsed time after heating starts, where the ultrasonically estimated results (left) are compared with those measured using the infrared camera (right). It can be seen that both temperature distributions determined by the ultrasonic method and the infrared camera almost agree with each other.

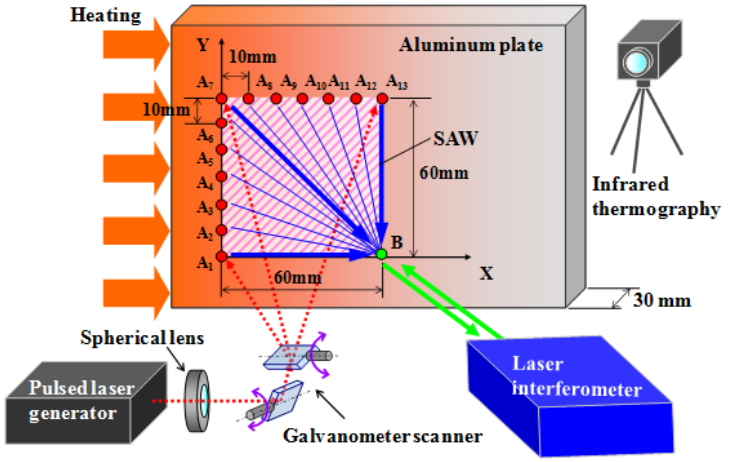

Fig. 17. Schematic of SAWs generations at points A_1 to A_{13} by a pulsed laser scanning and SAWs detections at point B. SAWs in the area of the square, A_1-A_7-A_{13}-B, on the surface of the heated plate are measured to obtain the surface temperature distribution in the square [27].

It should be noted that the proposed method with a pulsed laser scanning is properly applicable to a simple heat conduction state producing an approximately one-dimensional surface temperature distribution similar to that demonstrated in this work. When the method is applied to a complicated temperature distribution on a heated material surface, an inclination of the SAW propagation direction to the predetermined direction should be carefully taken into consideration. This is because the SAW does not always propagate straight along the predetermined direction, owing to the anisotropic effect in wave propagation caused by the complicated temperature distribution. To avoid such problem in monitoring complicated temperature distributions, it is recommended to use the simplified scanning method [31] by which there is little influence from such complicated temperature state.

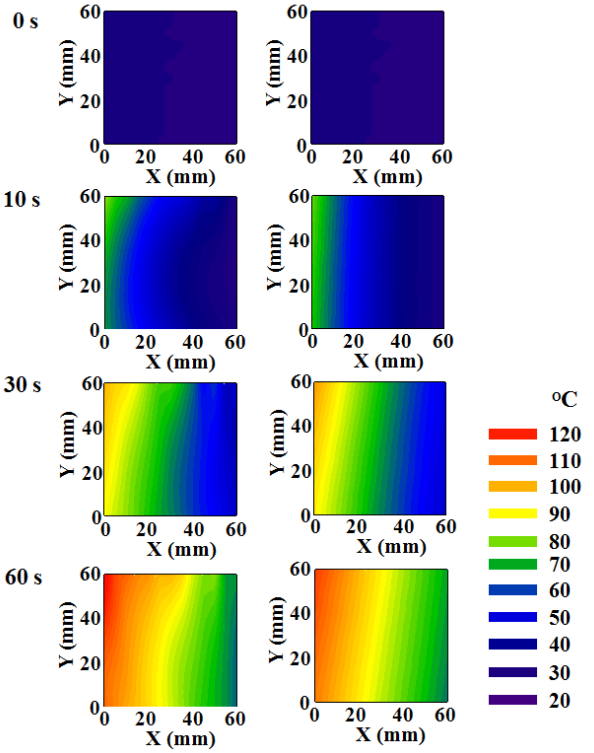

Fig. 18. Variations in surface temperature distribution of an aluminum plate with heating time, estimated by ultrasound (left) and infrared radiation (right) [27]

5 Accuracy

It is demonstrated in Section 4 that the high potential of the ultrasonic thermometry for measuring temperature profiles of inside or surface of heated

materials. However, there has been little information about the accuracy of the estimated results by the method. For the practical application of the method, it is indispensable to know the measurement accuracy of the method. In general, there are two kinds of error factors affecting the accuracy in the temperature estimation: a random error due to the statistical fluctuation in measuring the transit time of ultrasound, and systematic errors due to the deviations from the true values used in the analysis. The influence of these error factors on the accuracy in surface temperature estimation has been examined quantitatively [30]. Since the temperature dependence of SAW velocity and the thermal diffusivity coefficient used in the inverse analysis seem to be important factors affecting the systematic errors, their influences on the temperature estimation are investigated through the numerical evaluations for a heated aluminum plate having a one-dimensional temperature distribution [30].

Influence of the Temperature Dependence of SAW Velocity

It can be seen from equations (6) and (7) that coefficients a and b should be dominant factors affecting the estimated temperature, T_1^{n+1}, which normally shows the largest deviation in the temperature estimation [30]. Those coefficients, a and b, are the gradient and intercept of a linear equation showing the relationship between temperature and SAW velocity, respectively. The influences of errors in those coefficients on the temperature estimation are examined here. To avoid any influences due to experimental uncertainty in the estimation, numerical investigations of the temperature estimation are performed for a single-side heated aluminum plate model having a one-dimensional temperature on the surface, similar to that shown in Figure 15. The surface temperature distribution and its transient variation of the aluminum plate model are numerically estimated by a finite difference calculation with boundary conditions of the second kind [32] so that a numerical model that appropriately imitates a real heated aluminum plate can artificially be prepared. The inverse analysis described in Section 3 is then applied to the numerical model to estimate surface temperature distributions by the ultrasonic method. In the analysis, two coefficients in equation (7), a and b, are systematically changed around their correct values so that the influences of the deviations in the two values on the temperature estimation are quantitatively investigated. The results are shown in Figure 19. As we expected, the influence of the deviation in each coefficient increases with the increases in temperature and therefore, systematic errors become larger in the vicinity of heated area. It is also interesting to note in Figure 19 that a few percent errors in each coefficient gives a deviation of a few degrees Celsius in the estimated temperature near the heated area, and the deviation increases with elapsed time. It can be seen from Figure 19(a) and (b) that the influence due to the error in the intercept b is similar to that due to the gradient a, but they have an opposite tendency.

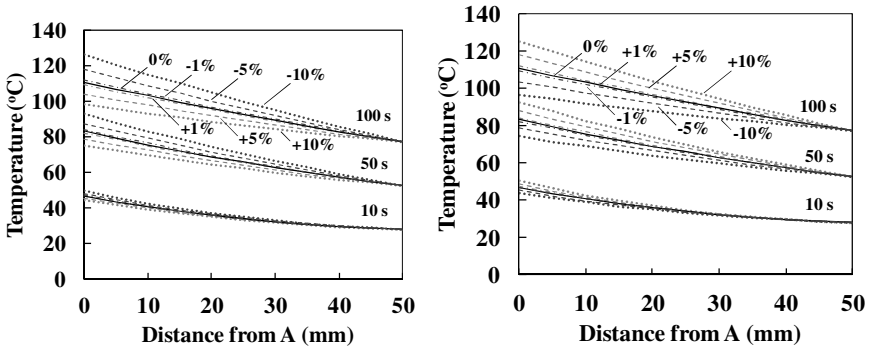

Fig. 19. Influence of the temperature dependence of SAW velocity on the estimated temperature distribution, where A denotes the point near heated area, as shown in Figure 15 and numbers, 10 s, 50 s and 100 s denote the elapsed time after heating starts. (a) Influence of the deviation in gradient *a*. (b) Influence of the deviation in intercept *b* [30].

Influence of Thermal Diffusivity

It can also be seen from equations (2) - (6) that thermal diffusivity is also another factor that may affect the temperature estimation. It is known that the value of thermal diffusivity depends on the type of material used and changes with temperature. It is necessary to examine the influence of the deviation in thermal diffusivity in the ultrasonic thermometry because the temperature dependence of thermal diffusivity is neglected for simplicity in the present analysis. Actually, the value of thermal diffusivity at room temperature was used for the inverse analysis in this work. Using the same numerical model as used in the investigation for the temperature dependence of SAW velocity, surface temperature distributions are estimated by the inverse analysis with different values of thermal diffusivity in order to examine the influence of uncertainty in thermal diffusivity. The following three values are used in the analysis: 9.68×10^{-5}, 8.37×10^{-5}, and 7.36×10^{-5} m^2/s. It is noted that these values correspond to thermal diffusivities at 27, 327, and 527 ^oC for aluminum. The estimated temperature distributions with the different values of thermal diffusivity are shown in Figure 20. It is found that no significant influence of thermal diffusivity on the estimated results is observed in spite of the fact that an inappropriate value, such as 7.36×10^{-5} m^2/s, that should be used for an extremely high temperature (527 ^oC) is employed in the analysis. Thus, it is found that the temperature dependence of thermal diffusivity does not affect the accuracy in the temperature estimation and therefore, is not a crucial factor in the ultrasonic thermometry.

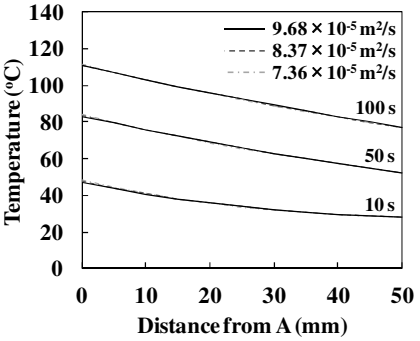

Fig. 20. Influence of thermal diffusivity coefficient of the aluminum on the estimated temperature distribution. It is noted that three lines for temperature distributions estimated from different values of thermal diffusivity are almost overlapped. Numbers, 10 s, 50 s and 100 s denote the elapsed time after heating starts [30].

6 Conclusion

A new ultrasonic thermometry for monitoring temperature distributions of heated materials is presented. This method consists of ultrasonic pulse-echo measurements and an inverse analysis for determining one-dimensional temperature distributions along the direction of ultrasound propagation. The practicability of the method is demonstrated through experiments with a steel plate, alumina rod and aluminum plate. Although the present ultrasonic thermometry is not always better than other conventional methods such as an infrared radiation and thermocouples methods, its distinct characteristics are quite attractive to many practical situations in material science and engineering. One of the advantages of the ultrasonic thermometry is that not only surface temperatures but also internal temperatures can noninvasively be profiled. Although further study is necessary to improve the robustness and accuracy in measurements, it is highly expected that the method will be a useful means for the in-situ or on-line monitoring of the transient temperature variation of the material being processed at high temperatures. There are ongoing attempts by the authors to make non-contact internal temperature profiling of a moving or rotating objectives at elevated temperatures. The demonstrative results will be reported soon.

Acknowledgments. Financial supports by JSMS KAKENHI, a Grant-In-Aid for Scientific Research (B22360304) and Grant-in-Aid for challenging Exploratory Research (23656454) are greatly appreciated. This work is partially supported by Toyota Motor Co.

References

[1] Degertekin, F.L., Pei, J., Khuri-Yakub, B.T., Saraswat, K.C.: In-situ acoustic temperature tomography of semiconductor wafers. Applied Physics Letters 64, 1338–1040 (1994)

[2] Simon, C., Van Baren, P., Ebbini, E.: Two-dimensional temperature estimation using diagnostic ultrasound. IEEE Transactions on Ultrasonics, Ferroelectrics and Frequency Control 45(4), 1088–1099 (1998)
[3] Mizutani, K., Funakoshi, A., Nagai, K., Harakawa, K.: Acoustic measurement of temperature distribution in a room using a small number of transducers. Japanese Journal of Applied Physics 38, 3131–3134 (1999)
[4] Mizutani, K., Kawabe, S., Saito, I., Masuyama, H.: Measurement of temperature distribution using acoustic reflector. Japanese Journal of Applied Physics 45, 4516–4520 (2006)
[5] Kudo, K., Mizutani, K., Akagami, T., Murayama, R.: Temperature distribution in a rectangular space measured by a small number of transducers and reconstructed from reflected sounds. Japanese Journal of Applied Physics 42, 3189–3193 (2003)
[6] Kudo, K., Mizutani, K.: Temperature measurement using acoustic reflectors. Japanese Journal of Applied Physics 43, 3095–3098 (2004)
[7] Huang, K.N., Huang, C.F., Li, Y.C., Young, M.S.: High precision fast ultrasonic thermometer based on measurement of the speed of sound in air. Review of Scientific Instruments 73, 4022–4027 (2002)
[8] Gulik, G.-J.S., Wijers, J.G., Keurentjes, J.T.F.: Measurement of 2D-temperature distributions in a pervaporation membrane module using ultrasonic computer tomography and comparison with computational fluid dynamics calculations. Journal of Membrane Science 204, 111–124 (2002)
[9] Tsai, W.-Y., Chen, H.-C., Liao, T.-L.: An ultrasonic air temperature measurement system with self-correction function for humidity. Measurement Science Technology 16, 548–555 (2005)
[10] Funakoshi, A., Mizutani, K., Nagai, K., Harakawa, K., Yokyama, T.: Temperature distribution in circular space reconstructed from sampling data at unequal intervals in small numbers using acoustic computerized tomography (A-CT). Japanese Journal of Applied Physics 39, 3107–3111 (2000)
[11] Minamide, A., Mizutani, K., Wakatsuki, N.: Temperature distribution measurement using reflection with acoustic computerized tomography. Japanese Journal of Applied Physics 47, 3967–3969 (2008)
[12] Ingleby, P., Wright, M.D.: Ultrasonic imaging in air using fan-beam tomography and electrostatic transducers. Ultrasonics 40, 507–511 (2002)
[13] Chen, T.-F., Nguyen, K.-T., Wen, S.-S., Jen, C.-K.: Temperature measurement of polymer extrusion by ultrasonic techniques. Measurement Science and Technology 10, 139–145 (1999)
[14] Balasubramainiam, K., Shah, V.V., Costley, R.D., Boudreaux, G., Singh, J.P.: High temperature ultrasonic sensor for the simultaneous measurement of viscosity and temperature of melts. Review of Scientific Instruments 70, 4618–4623 (1999)
[15] Ishikawa, E., Mizutani, K.: Temperature measurement using a dual frequency acoustic delay line oscillator. Japanese Journal of Applied Physics 42, 5372–5373 (2003)
[16] Wang, S., Harada, J., Uda, S.: A wireless SAW temperature sensor using langasite as substrate material for high temperature applications. Japanese Journal of Applied Physics 42, 6124–6127 (2003)
[17] Nishimura, K., Shigekawa, N., Yokoyama, H., Hohkawa, K.: Temperature dependence of surface acoustic wave characteristics of GaN layers on sapphire substrates. Japanese Journal of Applied Physics 44, L564–L565 (2005)

[18] Kashiwagura, N., Akita, M., Kamioka, H.: Ultrasonic study of machinable ceramic over temperature range from room temperature to 1000°C. Japanese Journal of Applied Physics 44, 4339–4341 (2005)
[19] Matsuda, Y., Nakano, H., Nagai, S., Yamanaka, K.: Precise sound velocity measurement using laser ultrasound and its application for temperature measurement in semiconductor processing (in Japanese). Journal of the Japanese Society for Non-destructive Inspection 57, 204–209 (2008)
[20] Takahashi, M., Ihara, I.: Ultrasonic monitoring of internal temperature distribution in a heated material. Japanese Journal of Applied Physics 47, 3894–3898 (2008)
[21] Ihara, I., Takahashi, M.: Non-invasive monitoring of temperature distribution inside materials with ultrasound inversion method. International Journal of Intelligent Systems Technologies and Applications 7(1), 80–91 (2009)
[22] Takahashi, M., Ihara, I.: Quantitative evaluation of one-dimensional temperature distribution on material surface using surface acoustic wave. Japanese Journal of Applied Physics 48, 07GB04 (2009)
[23] Pouet, B.F., Ing, R.K., Krishnaswamy, S., Royer, D.: Het- erodyne interferometer with two-wave mixing in photorefractive crystals for ultrasound detection on rough surfaces. Applied Physics Letters 69, 3782–3784 (1996)
[24] Pouet, B.F., Breugnot, S., Clémenceau, P.: Robust laser-ultrasonic interferemeter based on random quadrature demodulation. In: Thompson, D.O., Chimenti, D.E. (eds.) Review of Quantitative Nondestructive Evaluation, vol. 25, pp. 233–239. AIP (2006)
[25] Meyers, G.E.: Analytical Methods in Conduction Heat Transfer, p. 10. McGraw-Hill, NY (1971)
[26] Press, W., Teukolsky, S., Vetterling, W., Flannery, B.: NUMERICAL RECIPES in C++, p. 849. Cambridge University Press, NY (2003)
[27] Yamada, H., Kosugi, A., Ihara, I.: Non-contact monitoring of surface temperature distribution by laser ultrasound scanning. Japanese Journal of Applied Physics 50, 07HC06 (2011)
[28] Ihara, I., Takahashi, M., Yamada, H.: New ultrasonic methodology for determining temperature gradient and its application to heated materials monitoring. In: Büyüköztürk, O., et al. (eds.) Nondestructive Testing of Materials and Structures. RILEM, vol. 6. RILEM (in print, 2012)
[29] Ihara, I., Tomomatsu, T.: In-situ measurement of internal temperature distribution of sintered materials using ultrasonic technique. In: IOP Conf. Series: Materials Science and Engineering, vol. 18, p. 022008 (2011)
[30] Kosugi, A., Ihara, I., Matsuya, I.: Accuracy Evaluation of Surface Temperature Profiling by a Laser Ultrasonic Method. Japanese Journal of Applied Physics (in print, 2012)
[31] Kosugi, A., Ihara, I.: A simple method for profiling surface temperature distributions by laser-ultrasound. Journal of Solid Mechanics and Materials Engineering 5(12), 705–708 (2011)
[32] Ozisik, M.N.: Basic Heat Transfer, p. 28. McGraw-Hill, Kogakusha (1977)

Non-invasive Measurement of Blood Components
Sensors for an In-Vivo Haemoglobin Measurement

J. Kraitl, D. Klinger, D. Fricke, U. Timm, and H. Ewald

University of Rostock,
Rostock, Germany

Abstract. This paper reports about fundamentals, simulations and measurements of optical absorption characteristics of whole blood and human tissues. A sensor system to measure blood components as haemoglobin is presented and corresponding results of in-vitro and in-vivo measurements. As basic technology NIR-spectroscopy and Photoplethysmography (PPG) is used for these non-invasive optical measurements. The characteristic absorption coefficient of blood in the visible and NIR region is well known and is mainly influenced by the different haemoglobin derivates. This fact is used to calculate the optical absorbability characteristics of blood which is yielding information about blood components as arterial oxygen saturation (SpO2), haemoglobin (Hb), carboxy-haemoglobin (CoHb) and met-haemoglobin. The measured PPG time signals and the ratio between the peak to peak pulse amplitudes are used for a calculation of these parameters. Haemoglobin is the main component of red blood cells. The primary function of Haemoglobin is the transport of oxygen from the lungs to the tissue and carbon dioxide back to the lungs. The Haemoglobin concentration in human blood is an important parameter in evaluating the physiological status of an individual and an essential parameter in every blood count. In currently standards, invasive methods are used to measure the Haemoglobin concentration, whereby blood is taken from the patient and subsequently analysed. Apart from the discomfort of drawing blood samples, an added disadvantage of this method is the delay between the blood collection and its analysis, which does not allow real time patient monitoring in critical situations. A non-invasive method allows pain free continuous on-line patient monitoring with minimum risk of infection and facilitates real time data monitoring allowing immediate clinical reaction to the measured data. The newly developed optical sensor systems uses up to five wavelengths in the range of 600 nm to 1400 nm for a measurement of the haemoglobin concentration, oxygen saturation and pulse. This non-invasive multi-spectral measurement method was tested with prototype-devices based on radiation of monochromatic light emitted by laser diodes and by using light emitting diodes (LED) through an area of skin on the finger. The sensors assembled in this investigation are fully integrated into wearable finger clips.

S.C. Mukhopadhyay et al. (Eds.): Advancement in Sensing Technology, SSMI 1, pp. 237–262.
springerlink.com

1 Introduction

Since the near infrared light was found to penetrate a great depth into biological tissues, near infrared spectroscopy has been developed into a non-invasive method for biomedical sensing and clinical diagnosis [1][2]. Oximetry is well known as typical example of a near-infrared application in clinic and can be used to non-invasive measure the oxygen saturation of human blood in-vivo [2]. The Haemoglobin concentration in human blood is also an important parameter to evaluate the physiological condition and the capability of oxygen transportation in blood. With this information anaemia (a low haemoglobin level) and polycythaemia vera (a high haemoglobin level) can be diagnosed and monitored. It is also possible to observe imminent postoperative bleedings and autologous retransfusions. Currently, invasive methods are used to measure the Haemoglobin concentration. For this purpose blood is taken and analysed. A disadvantage of this method is the delay between the blood collection and its analysis, which does not permit real-time patient monitoring in critical situations. A non-invasive method allows pain free online patient monitoring with minimum risk of infection and facilitates real time data monitoring allowing immediate clinical reaction to the measured data. It is well known that pulsatile changes of blood volume in tissue can be observed by measuring the transmission or reflection of light through it. This diagnostic method is called Photoplethysmography (PPG). The newly developed optical sensors system uses up to five wavelengths in the range of 600nm to 1400nm for the measurement of the haemoglobin concentration, oxygen saturation and pulse. For in-vitro tests and measurements a hemodynamic blood flow model has been developed which allows spectrometer measurements and the validation of the new sensors. A study to measure hypoxia showed that the sensitivity of the systems for measurement of SpO2 levels was accurate. In clinical measurements the ability to measure the haemoglobin content of blood in-vivo were proved and demonstrated.

2 Theoretical Aspects of HB-Measurements

The absorption and scattering of whole blood in the visible and near infrared range is dominated by the red blood cells, the different haemoglobin derivates and the blood plasma that consists mainly of water [3][4]. From the physiological point of view, the human skin and finger-tissue is particularly heterogeneous and therefore optically complicated, as shown in Figure 1. The radiation transport equation (1) can be regarded as the mathematical basis of tissue optics for the description of light-tissue interaction and the related phenomena [5][6].

$$\left(\frac{1}{c_n}\frac{\partial}{\partial t}+\vec{s}\tilde{N}\right)L(\vec{r},\vec{s},t)=-(\mu_a+\mu_s)L(\vec{r},\vec{s},t)+\mu_s\int_{4\pi}P(\vec{s},\vec{s}')L(\vec{r},\vec{s}',t)d\Omega'+Q(\vec{r},\vec{s},t) \qquad (1)$$

With $L(\vec{r},\vec{s},t)$ Radiance intensity of light at position $\vec{r}$ in direction $\vec{s}$ at time t

$c_n = \frac{c_0}{n}$	Velocity of light in tissue with index-of-refraction n
$(\vec{s},\vec{s}')$	Unit vector direction $\vec{s}$ and scattered direction $\vec{s}'$
$d\Omega' = \sin\upsilon'\partial\upsilon'\partial\varphi'$	Element of solid angle
$S(\vec{r},t)$	Energy intensity of the light source
$Q(\vec{r},\vec{s},t) = \frac{\partial S(\vec{r},t)}{\partial\Omega}$	Source term

Description of light-tissue interactions using the transport theory requires first to solve Eq.1. Because of difficulties to obtain exact solutions for biological tissue, several approximations have been made for the representations of $P(\vec{s},\vec{s}')$ and $L(\vec{r},\vec{s},t)$.

The pulsatile optical signal which is caused by the arterial blood flow in tissue [7] was detected and normalized with the non-pulsatile optical signal. This is necessary to eliminate the influence of the optical property changes of the venous blood and the bloodless tissue, and even the difference of tissue optical properties among patients (Figure 1).

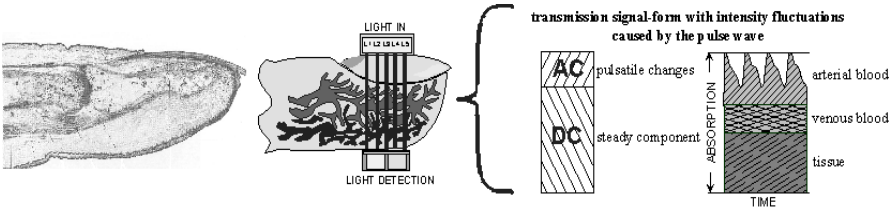

Fig. 1. Human fingertip [8] and principle of measurement

Beside the measurements of oxygenated (HbO_2) and reduced haemoglobin (HHb) for the calculation of oxygen saturation in the arterial blood (SpO_2), the noninvasive measurement of the haemoglobin concentration is a main objective of our application. Up to day the measurement of the haemoglobin concentration in blood needs an invasive method in clinical practice. The absorption and scattering of blood is influenced mainly by the total haemoglobin concentration and the amount of red blood cells (RBC's) as typical scatters. The light scattering behavior of biological tissue is a function of many variables such as the in-homogeneities in the refractive index as a result of the presence of blood vessels, blood cells, cell membranes and collagen structures within the tissue, which cause light scattering, i.e. change of the direction of photon propagation. The absorption-coefficient μ_a (in mm^{-1}), the scattering-coefficient μ_s (in mm^{-1}) and the so called phase-function $P(\vec{s},\vec{s}')$ are parameters necessary for the calculation of optical properties in turbid mediums like blood. The phase-function describes the probability of scattering for a photon traveling in direction $\vec{s}$ to be refracted in

direction $\vec{s}'$. Mathematical calculations can be simplified by using the anisotropy-factor $g = E(\cos(\vec{s}, \vec{s}'))$ instead of the phase-function and the reduced scattering-coefficient $\mu'_s = \mu_s(1- g)$ instead of the scattering-coefficient. To take the influence of light scattering into account, we assume that the measuring volume is composed of tissue (v^{Tissue} tissue volume, μ_a^{Tissue}, $\mu'_s{}^{Tissue}$ absorption and scattering coefficient tissue), arterial blood (v^{art} arterial blood volume, μ_a^{art}, $\mu'_s{}^{art}$ absorption and reduced scattering coefficient arterial blood), and venous blood (v^{ven} venous blood volume, μ_a^{ven}, $\mu'_s{}^{ven}$ absorption and reduced scattering coefficient venous blood). The model assumes further that the measuring volume can be considered as a homogeneous distribution of scatters and absorbers of the components mentioned [9]. Therefore, the Equations (2) to (6) are given in the following form for a human finger:

$$\mu_a^{Finger}(\lambda) = v^{artBlood}\mu_a^{artBlood}(\lambda) + v^{venBlood}\mu_a^{venBlood}(\lambda) + [1-(v^{artBlood} + v^{venBlood})]\mu_a^{Tissue}(\lambda) \quad (2)$$

$$\mu_a^{artBlood}(\lambda) = HSaO_2\mu_a^{HbO_2}(\lambda) + H(1-SaO_2)\mu_a^{HHb}(\lambda) + (1-H)\mu_a^{Plasma}(\lambda) \quad (3)$$

$$\mu_a^{venBlood}(\lambda) = HSvO_2\mu_a^{HbO_2}(\lambda) + H(1-SvO_2)\mu_a^{HHb}(\lambda) + (1-H)\mu_a^{Plasma}(\lambda) \quad (4)$$

and

$$\mu_s'^{Finger}(\lambda) = v^{Blood}\mu_s'^{Blood}(\lambda) + v^{Tissue}\mu_s'^{Tissue}(\lambda) \quad (5)$$

$$\mu_s'^{artBlood}(\lambda) = \mu_s'^{venBlood}(\lambda) = \mu_s'^{Blood}(\lambda) = f(H)\mu_s'^{Hb}(\lambda) \quad (6)$$

with H [0…1] = haematocrit (volume of red blood cells in whole blood)
v [0…1] = normalized volume

Our measurement method evaluates the PPG signal waveforms of peaks, troughs, steady averages, and pulsatile averages caused by the arterial blood volume shift $\Delta v(t)$ in the finger tissue [10]. With the assumption that $v^{artBlood} = v^{artBlood}(t)$ and $\Delta\mu_a = \Delta v\mu_a^{artBlood}$, follows Equation (7).

$$R = \frac{\Delta I}{I} = \frac{I(t+\Delta t) - I(t)}{I(t)} \approx \frac{\Delta\mu_a(\lambda)}{I}\frac{dI}{dt} = -\Delta\mu_a(\lambda)r \quad (7)$$

I = Intensity of light after interaction with the tissue

A multi-wavelength measurement with λ_k ($k = 1...K$) results in the following Equation:

$$(R_1, \cdots, R_K)^T = A(x_1, x_2, x_3)^T \quad (8)$$

with $(x_1, x_2, x_3) = \Delta vr(HSaO_2, H(1-SaO_2), 1-H)$ and $A = \begin{pmatrix} \mu_{a,1}^{HbO_2} & \mu_{a,1}^{HHb} & \mu_{a,1}^{Plasma} \\ \vdots & \vdots & \vdots \\ \mu_{a,K}^{HbO_2} & \mu_{a,K}^{HHb} & \mu_{a,K}^{Plasma} \end{pmatrix}$

With the mathematical model described before the measured PPG signals has been qualitatively analyzed by calculation of R_K-factors for each wavelength. But finally caused by the overwhelming nonlinear effects of tissue scattering a calibration of the PPG measurements has to be derived empirically by intensive statistical regression of the measurements obtained from volunteers and a hemodynamic blood tube model [10].

3 Simulation and Phantom-Models

3.1 Simulations of Tissue

Virtual modeling of turbid media, like biological tissue, and the description of photon transport in this media can lead to a better understanding of photonic processes and enables the effective development and optimization of optical systems.

In contrast to the analytical description of light-tissue-interaction with the already described radiation transport equation (1) a numerical method called Monte Carlo simulation or Monte Carlo ray tracing, provides considerable advantages like greater flexibility during model development and higher accuracy of the results [5][11]. Due to the stochastic nature of this method, the accuracy depends on the number of samples and thus on the number of simulated photons. Therefore the efficiency of this method has been improved in the last years by fast development of high-performance computational resources at an affordable price.

With the Monte-Carlo simulation (MC) it is possible to trace photons step by step through a turbid medium. A large quantity of the traced photons with their resulting paths in the medium results in a realistic mapping of the propagation of light in the target tissue. The medium itself is described by the optical parameters scattering coefficient μ_s, absorption coefficient μ_a, the anisotropy coefficient g and the index of refraction n. The tracing process of the photons can be described by few steps [12][13]. In a first step the photon flux is defined and the start position of the photon is assigned by its cartesian coordinates. The photon moves towards the direction of the tissue and hits the first surface. Due to the difference in the refractive index, only a certain amount of flux is transmitted through the surface which is described by the Fresnel's equations [14]. A further step describes the path length of the photon between two events like absorption and scattering. This path length must be chosen carefully in order to guarantee realistic photon paths on the one hand and to avoid an unnecessary reduction of the simulation speed on the other hand. This path length is randomly sampled by an exponential distribution which depends on absorption coefficient μ_a and scattering coefficient μ_s, however the mean free path length of the photon-tissue interaction is given by $1/(\mu_s+\mu_a)$. After moving the photon the described distance a decision is made for absorption, scattering and the new scattering direction. In the case of absorption the current photon energy E_{photon} is reduced by $\Delta E_{photon}=E_{photon}*\mu_a/(\mu_s+\mu_a)$.

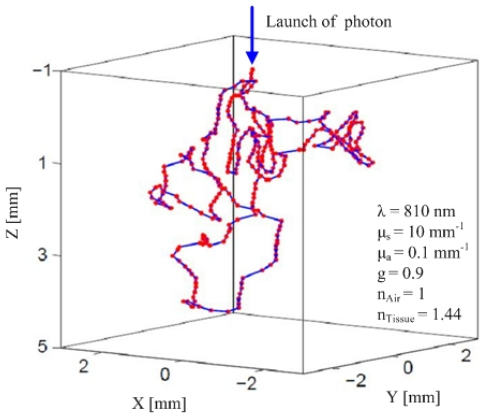

Fig. 2. Single photon path from Monte Carlo simulation

Dots mark the points of scattering and absorption events during the ray trace. Lines show the distributed free path length of the photon between the scattering and absorption events.

The Henyey-Greenstein phase function describes the probability of the polar deflection angle after each scattering event. The event depends on anisotropy coefficient g, which is equal to the mean cosine of scattering angle and variates between forward scattering g=1, isotropic scattering g=0 and back scattering g=-1. The tracing of the photon ends by total absorption on a certain layer or detector or by reaching a predefined cut-off-energy. In this case a new photon trace is started. In conclusion the relationship between absorption, scattering and mean free path length are displayed as a single photon path in Figure 2.

The simulations of light-tissue interactions were performed with the optic software ASAP® (Breault Research). ASAP® includes functions for simulations of geometric- and physical-optical properties and delivers complete 3D-models of optical and mechanical systems. In addition the Monte-Carlo simulation is already implemented in the software.

Besides the simulation of multi-layered tissue models, ASAP® in our case is used to simulate cuvettes and blood transporting tubing's of our blood flow model. The results of the simulations provide important information such as optical path lengths, penetration depths and internal distributions of the energy in the target tissues. Furthermore the simulations supplement the analysis of real measurements.

As already mentioned above, the basic model for simulations consists of a virtual volume which is described by his optical properties. Basically it's possible to model arbitrary complex systems. In the case of human tissue excessive complex models are counterproductive under certain circumstances for at leas two reasons. Wavelength dependent optical parameters for tissue sub structures as hair follicles, sweat glands and pacinian corpuscles are limited available. These sub systems have only small contribution to the whole system and can be easier described in the context of a functional layer, like tissue layers. Consequently simple models consists

only of one single tissue layer where all specific different optical properties are reduced to only one u_s, u_a, g and n. More complex systems like the following in figure 3 and figure 4 consist of up to five functional isolated tissue layers.

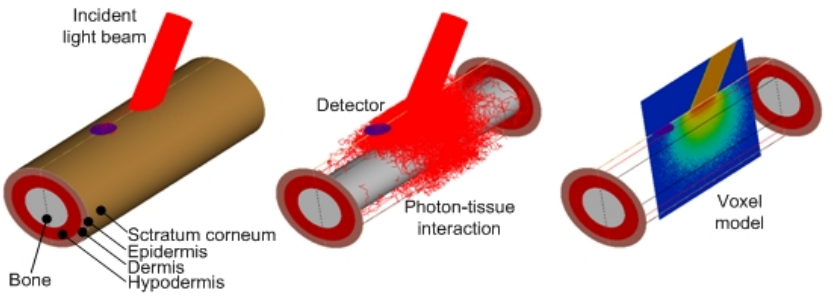

Fig. 3. Simulation of finger-model with ASAP®

The finger-model consists of the main layers stratum corneum, epidermis, dermis, hypodermis and bone. The light is obliquely incident on the stratum corneum surface and penetrates the first layer. Inside the finger model the photons are scattered and absorbed, according to the predefined optical tissue parameters μ_a, μ_s, g and the refraction index n. A Voxel-model allows the visualization of the irradiance.

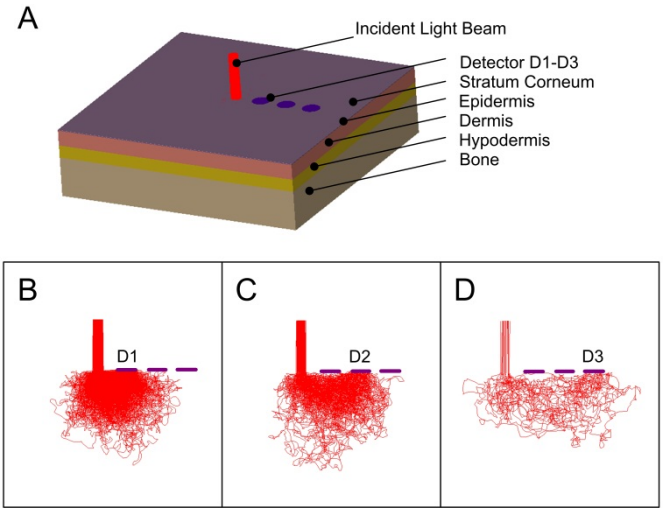

Fig. 4. Simulation of five layer tissue model with ASAP® **A:** Five layer tissue model consisting of the layers stratum corneum, epidermis, dermis, hypodermis and bone. Three detectors are positioned in different radial distances from the incident light beam. **B, C and D:** Lateral view of the tissue model from A with Detectors D1-D3. Displayed are only the rays corresponding to the detector.

The tissue model is implemented as a section of a human finger. The first layer in this model represents the stratum corneum. This outer layer, about 20 µm thin, consists of dead cells and forms a barrier to protect underlying tissue from environmental influences. The epidermis is the subsequent layer, about 80 µm thin, and consists of living cells. It regulates the amount of water released from the tissue and contains high amounts of light absorbing melanin pigments. Below this layer is the dermis located. It is mainly connective tissue based on collagen fibers with continuous blood perfusion. Therefore the light scattering and absorption in this layer is dominated by haemoglobin. The dermal scattering results primarily from the collagen fibers. The next layer is named hypodermis and is used basically for fat storage. The center of the model consists of bone. In the present case a section of the intermediate phalanges is modeled. For plethysmography like simulations a model of the distal phalanges is required.

3.2 Integrating-Sphere Measurement System

For simulations of biological tissues wavelength dependent optical parameters especially the scattering- and absorptions coefficients are required as inputs. Those parameters can be partially gained from various publications and literature [4][15][16][17][18]. Due to the variation of composition of biological tissues it should be noted that there are also deviations in the published data. Optical parameters for tissues containing different scenarios for quantitative compositions, like haemoglobin (Hb), carboxy-haemoglobin (CoHb) and arterial oxygen saturation (SpO2), are rarely incomplete or not available.

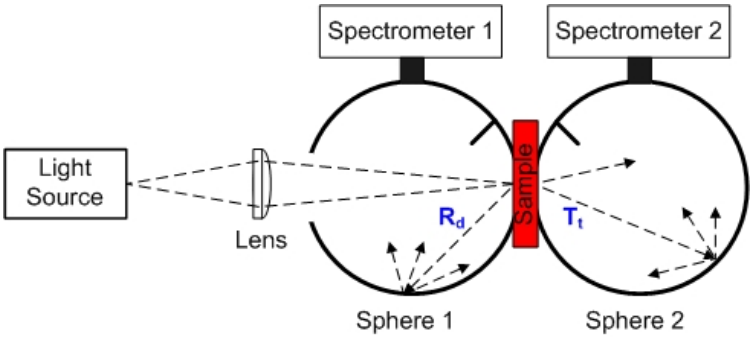

Fig. 5. Double integrating sphere system

The system consists of two integrating spheres with the blood sample between. The light of a halogen wide band light source is focused on the sample. Two fiber coupled spectrometers detecting the reflected and transmitted light. The data are acquired and post processed. The inverse adding-doubling method is used to calculate the scattering and absorption coefficients out of R_d and T_t.

The measurements of optical properties of tissue are made in the classical manner with an integrating sphere setup. This measuring system illuminates a tissue sample with light and detects the reflected and transmitted parts of light separately. In a further step this data are used to calculate the absorption and scattering μ_a and μ_s. For the integration of the reflected and transmitted light R_d and T_t, integrating spheres are used. Those hollow spheres have several input and output ports and a high reflection coating on the inner side. The coating material is adjusted to the wavelength range for the measurements and can be divided into barium sulfate ($BaSO_4$) and polytetrafluoroethylene (PTFE) for application in the visible and near-infrared region and gold coatings for the measurements in the near and far-infrared spectral region.

The integration of the light in the sphere is achieved by a high number of reflections. Basically it is possible to carry out the measurement of R_d and T_t with one sphere. A system based on two spheres has the advantage to measure R_d and T_t simultaneously without changing the setup and therefore reduces measurement artifacts due to undesired position changes of the sample. Therefore a double sphere setup also reduces the measuring time.

The detection of the integrated light depends on the used light source. Narrow band light sources allow the detection with photomultipliers or photodiodes and hence connect the illumination with high spectral irradiance and sensitive detection. The use of lock-in technique can increase the signal-to-noise ratio additionally. In order to acquire optical properties over a wide spectral range at once, light sources like halogen lamps in combination with spectrometers are used. Therefore optical parameters from visible or near-infrared spectrum can be recorded in a single step.

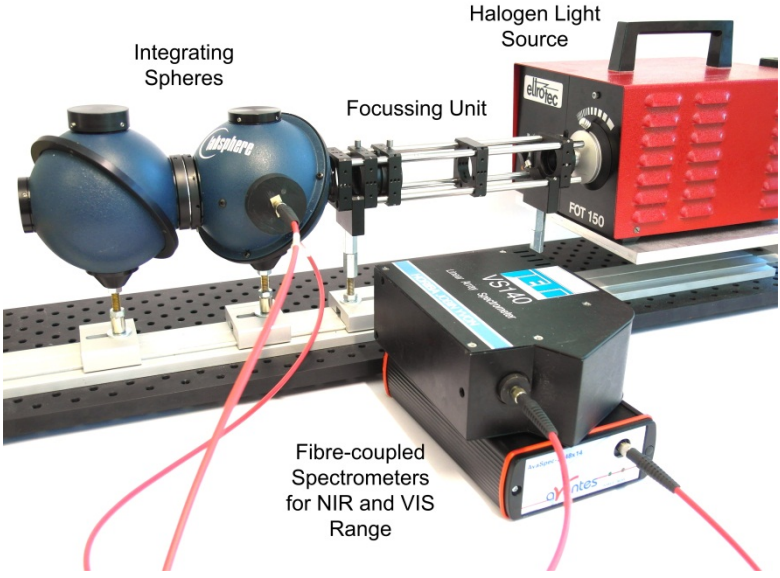

Fig. 6. Double integrating sphere setup

The labor measurement setup consists of two 4" integrating spheres (SphereOptics GmbH) with a Spectraflect® coating which is optimized for visible and near-infrared region. As a light source a modified 150W FOT150 halogen lamp (Eltrotec) is used. The light is focused over a system of pinholes and a plano-convex lens on the sample. The sample itself is fixed in a cuvette and placed between the spheres. Depending on the wavelength range and the sample, the thickness of the cuvettes ranges between 0.5 mm and 2 mm. Saline is used to reduce the mismatch of index of refraction between tissue and cuvette.

The integrated fraction of R_d and T_t is guided from the sphere ports through a fibre to the fibre coupled spectrometers. The spectrometer Avaspec covers a wavelength range from 370 nm - 920 nm with an optical resolution of 0.5 nm, while the VS 140 NIR spectrometer (HORIBA Scientific) covers a wavelength range from 800 m - 1700nm with an optical resolution of 7 nm. A diffuse reflectance standard (Spectralon®, LabSphere) is used for the calibration of the setup.

The calculation of the absorption and scattering coefficients μ_a and μ_s out of R_d and T_t is performed by the iterative algorithm named inverse adding-doubling method (IAD) [6]. This numerical method is based on the solution of the radiation transport equation for plane-parallel layers and considers the aspect of the inverse scattering problem. In a first step of the solution, the optical parameters for a thin sample layer are estimated. Through the solution of the one dimensional radiation transport equation R_d and T_t are calculated and compared with the measured values. In the case they are not corresponding, μ_a and μ_s varies until they match. In a second step the sample thickness is doubled and the procedure from step number one is repeated until the final sample thickness is reached. The „adding" involves in the calculation of μ_a and μ_s inhomogeneous media with internal reflections between the different tissue layers due to differences in the index of refraction.

Double integrating spheres combined with an inverse adding–doubling algorithm produce accurate values of μ_a and μ_s. Furthermore the presented setup can be expanded to measure also the anisotropy g if the collimated transmission is measured at some distance from the sample through a hole in the second sphere.

3.3 Optical Tissue Phantoms

The development and calibration of optical plethysmography systems require references with stable scattering and absorption properties [19]. The transmission and reflection measurements with human tissues show, in contrast to the required standard, considerable volatility in time. There are multiple reasons for this: thickness changes because of volume changes in the arteries, hydration status, difference in chromospheres concentrations, and oxygenation of the blood, temperature and perfusion status. The required calibration standards, named tissue phantoms, imitate the optical properties of human tissue and are characterized, contrary to human tissue, by time constant absorption and scattering and guarantee therefore repeatable measurements.

For the design of tissue phantoms it is recommended to look at the scattering and absorption separately. The scattering in human tissue is caused by mismatch of index of refraction between nuclei of the cells, cell organelles and the cell walls. This scattering can be reproduced by isolated microspheres with given diameters and index of refraction [20]. The absorption in tissue phantoms is realised by dyes, ideally with no scattering properties [21]. Because most of the dyes absorb in a narrow-band, the peak wavelength must be adjusted to the desired measurement wavelength. The carrier material for the dye and scattering particles has also ideally no absorption and scattering properties.

Tissue phantoms can be basically subdivide in tow categories: liquid phantoms and solid phantoms [22]. Liquid phantoms, like the fat emulsion infusion Intralipid, have the advantage that the detector can be moved also inside the phantom. The main disadvantage of liquid phantoms is the missing possibility to create complex shapes like multi layer systems. Furthermore the additives in the liquid can deposit over the time and change therefore the optical properties. However solid state phantoms are more complex in the processing but keep the optical properties stable over time.

A typical base material for solid state phantoms is epoxy resin or silicone gel. Due to the diameter within the lower µm range and similar refractive index to cellular structures, quartz microspheres are the ideal material choice for high forward anisotropic scattering imitations. Another, much cheaper scattering material is titanium dioxide but the nano-sized particles of this powder reducing the forward scattering characteristic. Common dyes for phantoms in the visible spectral range are Trypan blue and India ink. Pro-Jet 900 NP [23] is used for phantoms in the near-infrared region.

The manufacturing process of solid phantom can be described by the following steps. In the first stage a suitable quantity of scattering particles and absorbing dyes is mixed properly with the base material epoxy resin and placed in an ultrasonic bath for an ideal seperation of the particles. In a further step the hardener is added in a prescribed ratio and the suspension is mixed again. The bubbles in the liquid can be eliminated effective by placing the suspension in a vacuum chamber. In the last step the suspension is cast into shape and hardens at room temperature or elevated temperature.

The measurement of the optical properties of the finished phantom is performed with the already described integrating sphere system.

4 Haemodynamic Blood Flow Model

An artificial blood flow model (BFM) based on the human circulatory system was developed to allow a controlled variation of the blood parameter as total haemoglobin concentration (ctHb), oxyhaemoglobin (O2Hb), carboxyhaemoglobin (COHb) and methaemoglobin (MetHb). For this reason the optical properties of the blood were observed continuously by spectrometer measurements to determine the absorption, transmission and scattering properties of human whole blood in a wavelength range from 400 to 1700 nm and to test new noninvasive measurement systems.

4.1 Structure of the Model

For all measurements donor erythrocyte concentrates were used. The concentration of haemoglobin was changed by adding fixed amounts of blood plasma to the erythrocyte concentrate. Blood circulation and predetermined oxygen state were adjusted with an extra-corporal circulation unit. The blood was gently stirred and kept flowing through the blood tubes and the specially designed cuvettes (for spectrometric measurements). The blood temperature was kept constant at 37 °C via a tube heating mechanism and a separate water circulation through the Oxygenator.

The following blood parameters were varied by using the blood flow model:

- total haemoglobin (ΔctHb)
- oxyhaemoglobin (ΔO_2Hb)
- carboxyhaemoglobin (ΔCOHb)
- deoxyhaemoglobin ((ΔHHb)
- temperature (ΔT)
- flowrate (ΔQ)
- kind of fumigation (N_2-CO, N_2, compressed air)
- flowrate of fumigation

The model enables a defined circulation of app. 250 ml of human blood. The peristaltic blood pump has a maximum rotation speed of 250 rpm (Q: 0 to 200 ml/min).

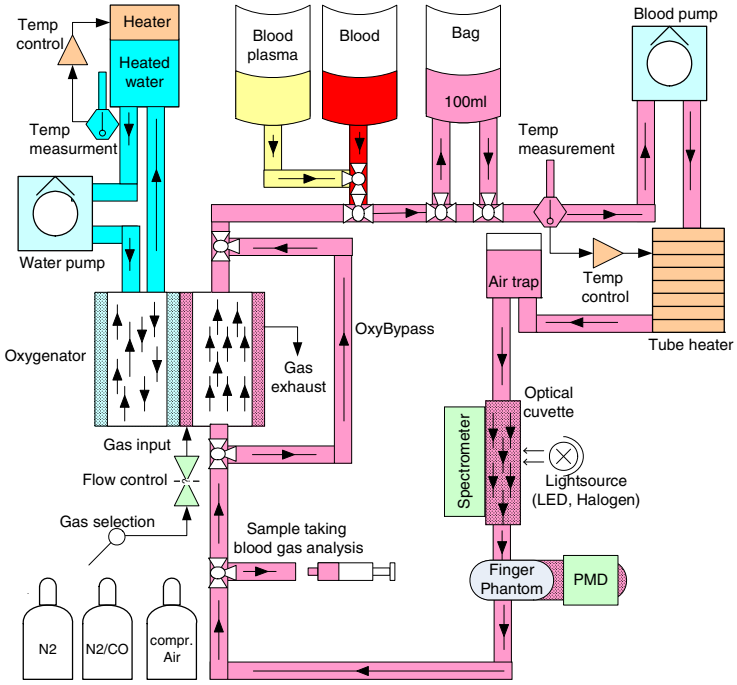

Fig. 7. Structure of the blood flow model

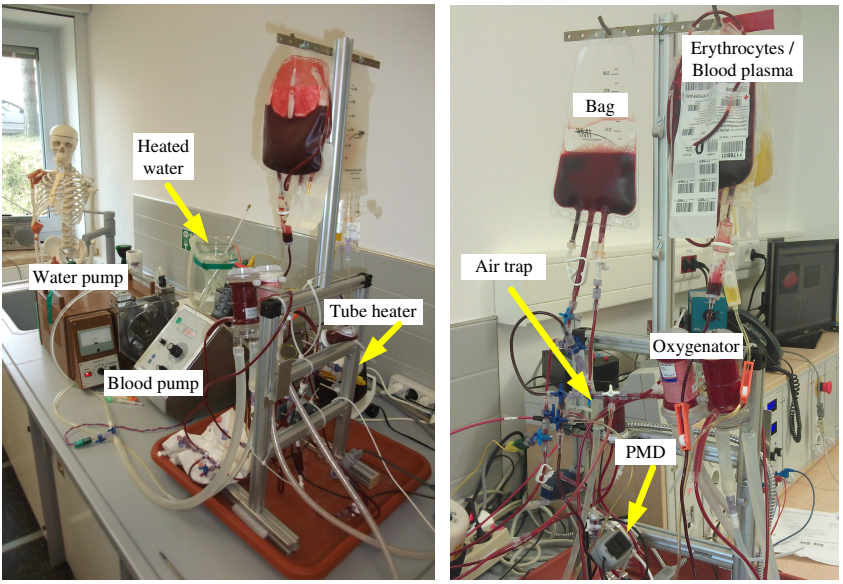

Fig. 8. Set up blood stream model

To avoid bubbles in the circuit an air trap was installed. To change the oxygen saturation a hollow fibre was used. Diverse gas molecules were transferred to the haemoglobin via the membrane surface. Nitrogen was used for desaturation and compressed air for oxygenation. The gas support enables flow rates of up to 5 l/min. The donated blood stored in blood banks was warmed up to 37°C before filled in the circulatory.

An additional bag in the bypass of the oxygenator were used to stabilize the system after changing the blood parameters so that defined conditions of the system could be hold for a while. Next to the optical cuvettes is port located for the extraction of blood samples for reference measurements with external devices as a BGA.

4.2 Optical Measurement System

To determine the optical properties of the blood components two grid spectrometer were used. With these spectrometers it is feasible to cover an area from 370nm to 1700 nm to obtain transmission data of whole blood for the comparison with literature data [10,24,25]

The blood mixture circulates in an artificial circuit with optical cuvettes. Different thicknesses of the cuvettes (0.5, 1, 2 and 3 mm) were realized to extend the dynamic area of the spectrometer. In figure 4 the first double layer cuvette is shown.

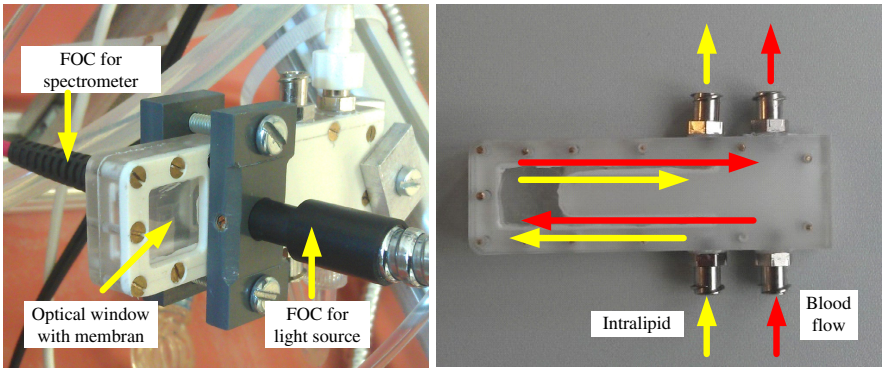

Fig. 9. Double layer optical cuvette (finger phantom) with membrane

This cuvette contains of two channels, one for the blood flow and one for intralipid to simulate human tissue. An optical window with a flexible membrane was used to generate PPG signals.

As light source different lamps where used, a wolfram halogen lamp with an interface to a fibre optical cable and a diameter of 6 mm. In the wavelength area below 700 nm an additional white LED power lamp (15W) was used. In opposite to the light sources the transmitted light was coupled in a 600 µm FOC with SMA interface which ends in a spectrometer.

4.3 Results

In first measurements the transmission spectra of water was determined to verify the measurement system and compare the results of the model with literature data [26].

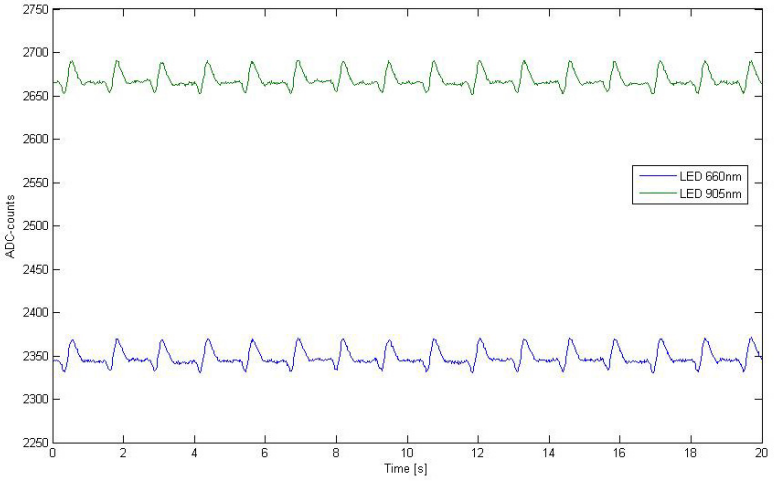

Fig. 10. Plethysmographical signals measured with the PMD

Figure 10 shows the plethysmographical signals of the finger phantom with blood and intralipid inside. The peristaltic blood pump was driven at 30 rpm (that corresponds to a heart rate of app. 60 bpm). The pressure of the blood pump was adjusted in a way to avoid a destruction of the erythrocytes (haemolysis).

Figure 11 shows the LED signals (660 nm, 905 nm) of the PMD on the finger phantom during the deoxygenation process in the blood flow model. The haemoglobin concentration was fixed at 5.3 mmol/l and proven by measurements with the blood gas analyzer (BGA). The tube heater and the additional water cycle maintain the blood temperature at app. 37°C.

For the complete oxygenation the compressed air was used to reach an oxygenation of 96 % O_2Hb. The deoxygenation was started with the pure nitrogen gas in periods of some minutes. The oxyhaemoglobin could be reduced to different levels and kept constant for a while to build up the system.

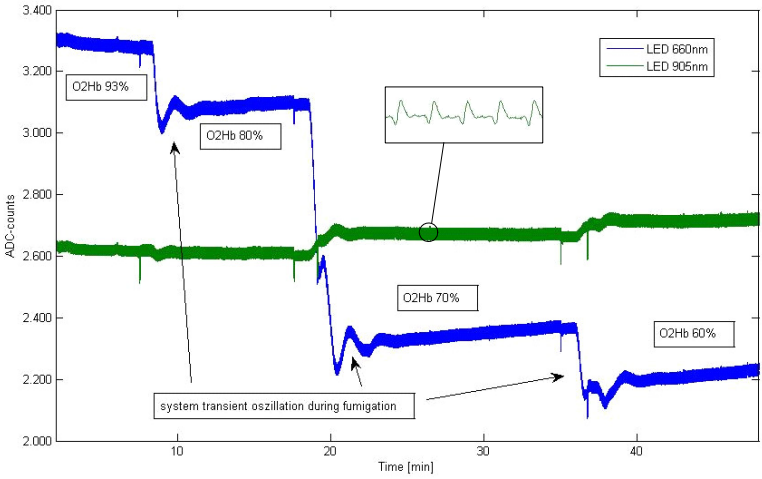

Fig. 11. PMD LED signals during deoxygenating in the blood model

The curves offer the measuring effect of deoxygenated blood by 660 nm and the contrary effect by 905 nm.

In figure 12 different O2Hb in the spectrum are displayed. In this diagram the oxyhaemoglobin values of 95%, 82% und 71 % are shown.

Figure 13 shows the absorption spectra of a blood solution with different COHb values (left) and MetHb values (right) through a 0.5 mm cuvette.

With the presented blood flow model different levels of total haemoglobin, oxyhaemoglobin, deoxyhaemoglobin, carboxyhaemoglobin and methaemoglobin could be realized. With the optical measurement system and the developed cuvettes the dynamic range of the spectrometer could be adapted to new measurement conditions.

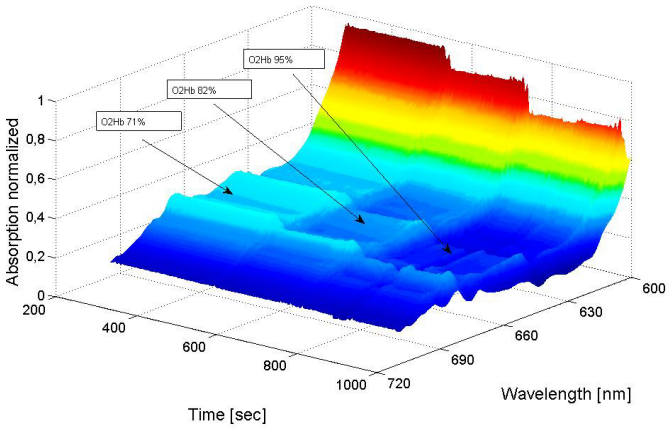

Fig. 12. Absorption spectrum blood on BFM

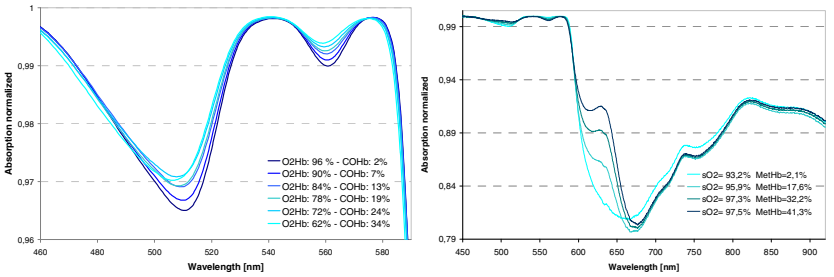

Fig. 13. Spectrum of different COHb and MetHb

First prototypes of non-invasive sensors were tested and PPG-signals could be generated, recorded and analysed on the model. Also calibration procedures for the prototypes are possible on the BFM.

5 Non-invasive HB-Measurement Method

The new developed non-invasive sensor systems allow a continuous measurement of the haemoglobin concentration, oxygen saturation and pulse which is based on a pulse-photometric measurement method. Thereby an area of skin on the fingertip is trans-illuminated by light which is emitted by Laser-diodes or LEDs in the range from 600nm - 1400nm. The objective of the photometric devices described here is the non-invasive continuous measurement of heart circulation patterns and light absorbent blood components in the blood of the human finger. The arteries contain more blood during the systolic phase of the heart than during the diastolic phase, due to an increased diameter of the arteries during the systolic phase. This effect occurs only in arteries but normally not in veins. For this reason the absorbance of light in tissues with arteries increases during systole because the

amount of haemoglobin (absorber) is higher and the light passes through a longer optical path length in the arteries. These intensity changes are the so called PPG-waves. The time varying part allows the differentiation between the absorbance due to venous blood and bloodless tissue (DC part) and that due to the pulsatile component of the total absorbance (AC part). Upon interaction with the tissue the transmitted light is detected non-invasively by photo diodes. Suitable wavelengths derived from measurements with the blood stream model were selected for the analyses of relative haemoglobin concentration change and SpO_2 measurement. During the measurement of haemoglobin the absorption should not depend on the oxygen saturation. The principle of measurement is based on the fact of a substantial absorption/transmission difference of light in red and near infrared region between oxygenated (HbO_2) and reduced haemoglobin (HHb) and blood plasma (optical mainly water). HHb is optically much denser to the red light (600 to 750 nm) than HbO_2, whereas the reverse is true in the near infrared region (900 to 1000 nm), even to a lesser degree. We selected suitable wavelengths to analyse the SpO_2 and relative haemoglobin concentration change for our application. Four of the five laser diodes of the newly developed laser based Photometric I device (PMD I) emits light in the range of wavelengths between 600 – 1000 nm (670, 808, 905 and 980 nm). This is the therapeutic window region, in which the blood absorption is dominated by the haemoglobin derivatives. An additionally 1300 nm laser diode is integrated, At this wavelength the absorption of water is dominant. For a calculation of haemoglobin, the wavelengths are chosen to suit the absorbance peaks of water in blood where the two components of blood have differing amounts of water (980 nm, 1310 nm). To find a value corresponding to an isosbestic point for absorbance of oxy-haemoglobin and deoxy-haemoglobin, a wavelength of 808 nm is chosen. A second relationship for the measurement and correction of oxygen saturation is calculated with the 670 nm (absorbance of deoxy-haemoglobin greatly exceeds the absorbance of oxy-haemoglobin) and 905 nm (absorbance of oxy-haemoglobin greatly exceeds the absorbance of deoxy-haemoglobin) transmission signals. Additionally we developed a LED based Photometric II device (PMD II) which operates three LEDs as optical light sources with center wavelengths of 670 nm, 810 nm and 1300 nm.

6 Measurement Devices

The Photometric I device PMD I (Figure 14) is basically a main box of electronic components, a light probe and a Laptop or PC for display and data storing [27]. The probe is attached to the patient's body usually the finger. Red to Near Infrared light is transmitted sequentially through the body tissue via fast –switching laser diodes and special driver electronics. The transmitted light is picked up with two suitably positioned photodiodes. Inside the measurement device the laser diodes are integrated together with the required control electronics. The main unit electronics consists of the components required for signal amplification, digitalization, and triggering of the laser diodes, which operate in a time-multiplex pulse mode. The sample frequency of the system is about 7 kHz. After mean value calculation and subtraction of the dark-current inside the main unit, the transfer of the five photocurrents is achieved with a sample rate of about 120 Hz each. The laser light is transmitted to a special optical transmission head by means of optical

fibers inside the sensor probe. Two Photo-detectors are also contained in the sensor head together with the required pre-amplifiers; the sensor signals detected here will be processed inside the measurement device.

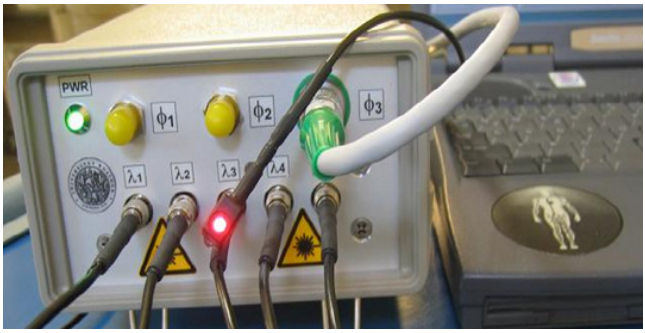

Fig. 14. PMD I front panel with fibre optics and transmission head

Figure 14 shows a photo of the PMD I device and the fiber optical sensor head used to transfer the laser light into the finger tissue. To detect the transmission signals of lasers 1 to 4 (670 nm to 980 nm) a Silicon Photodiode is used with a spectral sensitivity of 400 nm to 1150 nm. To detect the 1310 nm transmission signal an InGaAs-Photodiode is required with a spectral sensitivity of 1000 nm to 1700 nm. The application software is programmed in LabView (Figure 15).

Fig. 15. PMD I Software Frontpanel for Hb measurement

The second sensor system Photometric device II (PMD II) being developed consists of hardware modules including appropriate light sources and receivers, a microcontroller and a wireless interface [28]. Figure 16 shows a functional block diagram of the PMD II device.

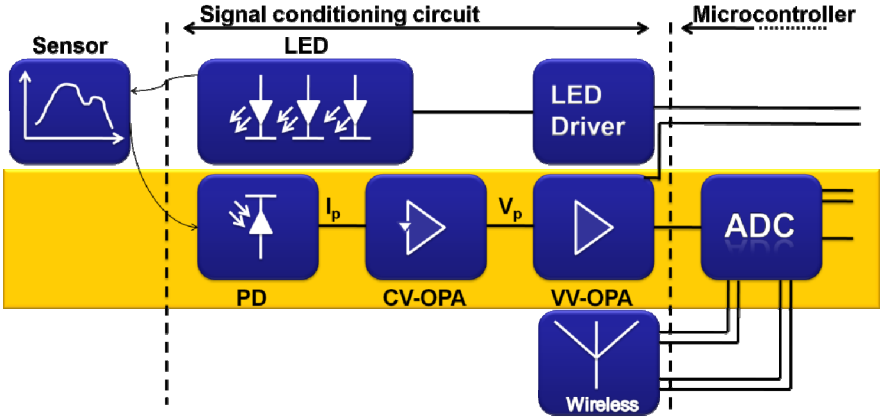

Fig. 16. PMD II: block diagram

The sensor system is low powered from a battery. A key component allows low power wireless operation, is the low power microcontroller MSP430F1611. This enables software controlled and time multiplexed operation of the light sources and receiver channels. The mean value is calculated and dark current subtracted in software, and the data is transmitted via serial USB or the wireless Bluetooth or ZigBee interface. The light sources, three LEDs, with centre wavelengths of 670nm, 810nm and 1300nm are installed in the upper part of the clip. The pulsed LED currents are controlled by the microcontroller, which allows a change of the light source intensity. To detect the transmission signals an Indium Gallium Arsenide/Indium-Phosphor photodiode was chosen. With a spectral range of 400nm-1700nm a measurement at all three used wavelengths is feasible. All components of the sensor system are chosen to guarantee low power consumption.

Fig. 17. High performance Hb-Sensor (PMD II) from Bluepoint Medical GmbH

Figure 17 shows the newly developed HB-Sensor OxyTrue Hb^{TM}. The prototype software runs on a touch screen PC.

Fig. 18. PMD II PC with Display and storage software

With the developed application software programmed in LabVIEW^{TM} it is possible to handle, analyze and store the data (Figure 18).

7 Application and Results with Prototypes

The PMD I and PMD II Prototype-devices was tested in-vitro with the blood stream model and in-vivo on volunteers and patients.

7.1 In-Vitro Results with the Prototypes

Figure 19 and Figure 20 show results measured with the PMD I and compared with the BGA reference values for two in-vitro measurements with the blood stream model. At first the oxygen level of the blood variants from 100% to 3% and the haemoglobin concentration remains constant at 88g/l. During the second measurement (Figure 20) the haemoglobin concentration was changed from 206 g/l to 50 g/l with a constant oxygen saturation of 97 %. Figure 19 shows that the measured and calculated coefficient for haemoglobin concentration was not affected by the different blood spectra for HHb and HbO_2. We found a non-linear relationship between the haemoglobin concentration and the calculated R coefficients measured with the PMD I. As expected, the oxygenation state of the blood was found to have no discernible effect on light attenuation at the 808 nm and 1310 nm wavelength, confirming that these wavelengths are isosbestic for HHb and HbO_2. After an empirically derived partial least-squares (PLS) calibration and statistical regression of the PMD I measurements the application is able to measure the Hb and sO_2 value in whole blood very well.

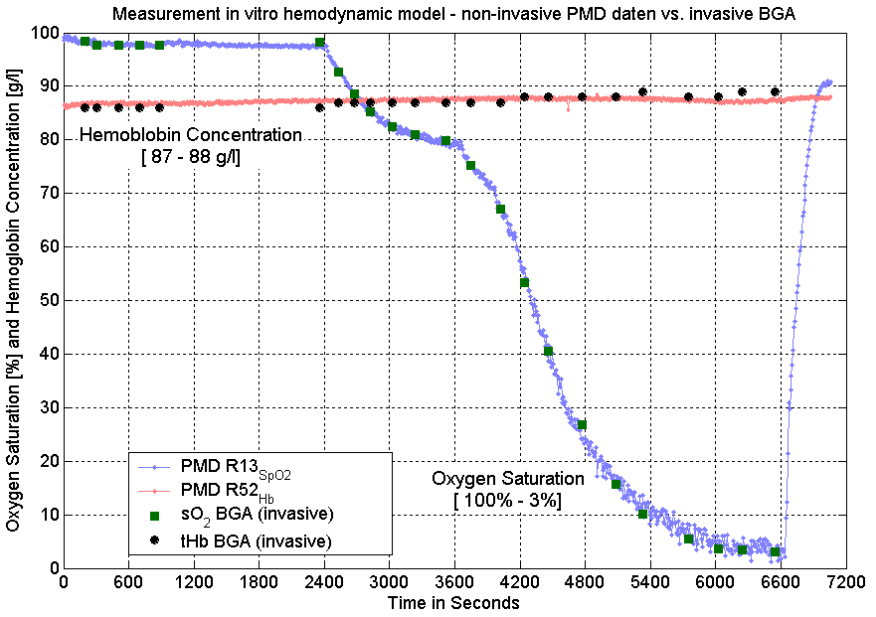

Fig. 19. Measurement of sO_2 and Hb with the PMD I through a blood tube of an in-vitro model

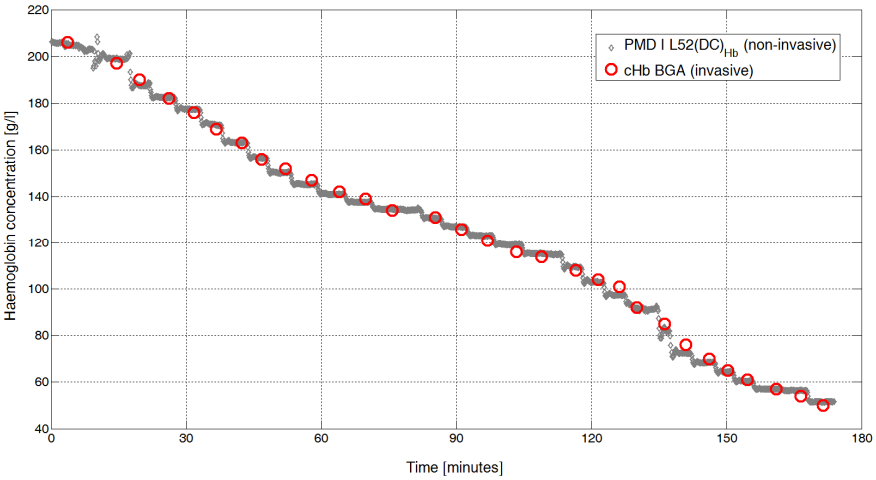

Fig. 20. Non-invasive measurement of HB (206g/l to 50g/l) with the PMD I in-vitro

7.2 In-Vivo Measurements

After a good correspondence between in-vitro experimental results with a blood tube system and our mathematic model, we used the PMD I to measure the arterial blood oxygenation and haemoglobin concentration for studies with healthy subjects. Previous measurements of the transmission signals of the five wavelengths had shown an apparent variation of the arterial pulse during in-vivo measurements. The signal quality was sufficient to analyze the signal components and to calculate relative attenuation coefficients of the arterial blood. With regard to the components at 1300 nm an evaluation of the relative portions of haemoglobin and water in the blood is feasible. The in-vivo measurement technique requires a pulse signal for the calculation of the relative attenuation coefficients. Vasoconstriction at the extremities can be a problem, as it decreases the signal amplitude, and therefore the signal to noise ratio. A small signal amplitude tends to give inaccurate results. The PMD sensors have therefore, a minimum signal amplitude below which no value for the calculated coefficient is displayed. The lower limit for the pulse amplitude with the 1300 nm laser or LED is in the order of 0.2% of the measured intensity. This may be a limitation when using the system on various patient groups (vascular disease, Raynaud's phenomenon, shock etc.). The non-invasive measurement method for haemoglobin and arterial oxygenic saturation described in this paper might be applicable for clinical applications where an invasive method is undesirable or inconvenient. One particular application could be the monitoring of patients vital signs in Critical Care Medicine or Anesthesia. Another application might be in the monitoring of patients who are undergoing surgery, were presumably the loss of blood during surgery would produce a change of haemoglobin concentration. It may also be a useful tool during dialysis sessions for the monitoring of haemodialysis patients with end stage renal failure. By using a dialyser (haemofilter) the patient has dialysat (prevailing water) distracted. This deferral means a fluid reduction for the patient during the ultra filtration. The change in blood volume involves a change of the haemoglobin status. It is necessary to compute a correction factor and the influence against deferrals in the arterial oxygen saturation for a photometric non-invasive measurement of haemoglobin. During a hypoxia-study the device sensitivity was validated for SpO_2. The pulsatile changes in the intensity observed with the PMD were caused by changes in arterial blood volume. It has thereby been assumed that the arterial blood volume fluctuations do not introduce pulsatile changes of the venous (and capillary blood) volume fraction. The PPG signal intensity of the 670nm and 905 nm wavelength from PMD I is used to compute the SpO_2 value. Figure 21 shows a measurement during a hypoxia study for one subject. The arterial oxygen saturation was reduced to about 75%. Thereby the recorded data of the photometric device PMD was compared with the data of a blood-gas-analysis BGA from the A. radialis (arterial oxygenic saturation - SpO_2 in percent). The results for 4 subjects showed a high sensitivity and high reproducibility for all measurements with the photometric device.

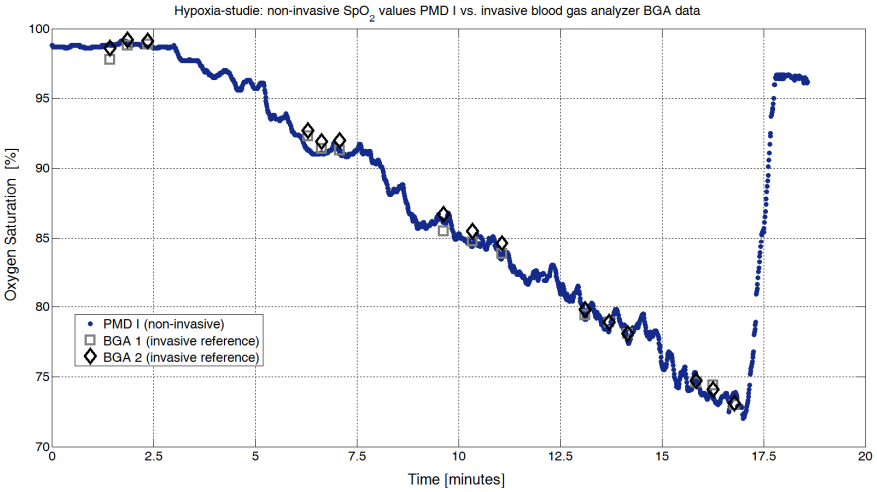

Fig. 21. SpO2 PMD I, compared with invasive BGA

A study with n=43 adult healthy male and female volunteers (range 19 - 60 years, 15 women and 28 men) was performed to test the ability of PMD I to measure the haemoglobin content non-invasive. The third or fourth finger of the left hand was connected with the PMD I sensor. The photometric measurements spanning 3 to 5 minutes for each subject and were stored using the PMD I system. After that the data was analyzed and the PMD I R_{Hb} coefficient was computed for each subject. A HemoCue™ haemoglobin device (HemoCue AB, Sweden) was used for invasive reference measurements. This system provides reliable quantitative haemoglobin results with the same performance as a large haematology analyser. A drop of capillary blood was taken from the same fingertip used for the photometric measurements for each volunteer, and analyzed with the HemoCue™ device. The Figure 22 shows the results of the non-invasive photometric measurements vs. the invasive measured haemoglobin values (131 measurements). In this study, we achieved good results with our application for a non-invasive haemoglobin determination. For this study the squared correlation coefficient is 0.918.

The example is too small to represent the variability in the population. Therefore the whole data set of 43 volunteers is not sufficient by itself to further evaluate the effects of patient-to-patient variation on the measurement method. The potential of this photometric method to measure the non-invasive haemoglobin in-vivo were proved with a good result. Future work will involve further clinical studies, which allows an extensive statistical analysis of these measurements.

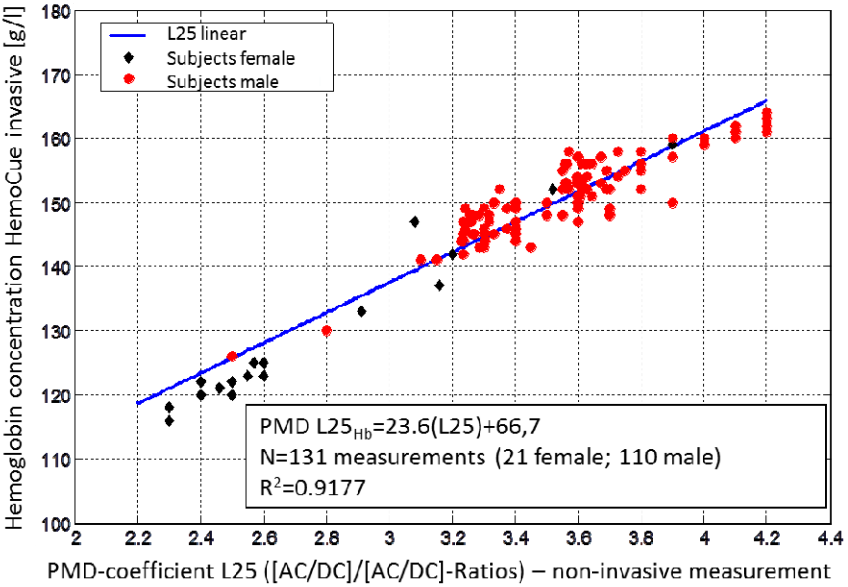

Fig. 22. Non-invasive PMD I HB coefficient vs. invasive HemoCue (R=0.95)

8 Conclusions

In this paper a multi-wavelength photometric measurement method that provides non-invasive in-vivo spectral measurements in human blood and tissue as well as the monitoring of heart circulation patterns has been described. A newly developed laser based PMD I and a LED based PMD II device has been introduced that is able to measure PPG-signals continuously at different wavelengths from 600 nm up to 1400 nm. The fact that the absorption-coefficients μ_a and scattering-coefficients μ_s for blood differ at difference wavelengths has been exploited and is used for calculation of the optical absorbability characteristics of human blood yielding information on the blood composition. A trial study to measure hypoxia showed that the sensitivity of the PMD I system for measurement of SpO2 levels was precise. In the first clinical measurements of the new measurement system, the potential to measure the haemoglobin content of blood in-vivo were proved and demonstrated. What could not be determined so fare in a first approach is a measurement with a large group of patients and volunteers. Future work will involve further clinical studies with this measurement method. A main aspect is the test of the optimized hardware system (PMD II) and a further evaluation of suitable statistical on-line analysis algorithms for the blood components. Future work in frame of the so called project PHOTOSENS includes the investigation and development of motion tolerant PPG measurement during low perfusion, the noninvasive measurement of carboxy-haemoglobin and the noninvasive determination of tissue dehydration.

Acknowledgment. This work was conducted within the framework of the project PHOTOSENS and has been funded with financial support from the Ministry of Economics, Labor and Tourism of the State Mecklenburg-Western Pomerania, Germany. A large part of this work was realized in close cooperation with our industrial partner bluepoint MEDICAL GmbH, Selmsdorf in Germany.

References

[1] Wukitsch, M.W., Petterson, M.T., Tobler, D.R., Prologe, J.A.: pulse oximetry: analysis of theory, technology, and practice. J. Clin. Monit. 4, 290–301 (1988)
[2] Ahrens, T., Rutherford, K.: Essentials of Oxygenation: Implication for Clinical Practice. Jones & Bartlett Pub. (1993)
[3] Roberts, V.C.: Photoplethysmography – Fundamental aspects of the optical properties of blood in motion. Trans. Inst. Meas. Control 4, 101–106 (1982)
[4] Roggan, A., Friebel, M., Dörschel, K., Hahn, A., Müller, G.: Optical properties of circulating human blood in the wavelength range 400-2500 nm. J. Biomed. Opt. 4, 36–46 (1999)
[5] Prahl, S.A., Keijzer, M., Jacques, S.L., Welch, A.J.: A Monte Carlo model of light propagation in tissue. In: Proc. SPIE IS, 6th edn., vol. 5 (1989)
[6] Prahl, S.A.: Inverse adding-doubling program. Oregon Medical Laser Center, St. Vincent Hospital (2011)
[7] Kamal, A.A.R., Hatness, J.B., Irving, G., Means, A.J.: Skin photoplethysmography – a review. Comput. Methods Programs Biomed. 28, 257–269 (1989)
[8] Schmidt, H.M., Lanz, U.: Chirurgische Anatomie der Hand. Stuttgart, Hippokrates, Verlag (1992)
[9] Niemz, M.H.: Laser-Tissue Interactions – Fundamentals and Applications. IEEE Journal of Quantum Electronics QE-32, 1717–1722 (1996)
[10] Kraitl, J.: Die nichtinvasive Bestimmung der Hämoglobinkonzentration im Blut mittels Pulsphotometrie. MBV Verlag, Berlin (2007) ISBN 3-86664-361-6
[11] Wang, L., Jacques, S.L., Zheng, L.: MCML-Monte Carlo modeling of light transport in multi-layered tissues. Computer Methods and Programs in Biomedicine 47, 131–146 (1995)
[12] Veach, E., Guibas, L.J.: Robust monte carlo methods for light transport simulation. Stanford University, Stanford (1998)
[13] Sobol, I.M.: A Primer for the Monte Carlo Method. CRC Press, Boca Raton (1994)
[14] Born, M., Wolf: Principles of Optics: Electromagnetic Theory of Propagation, Interference and Diffraction of Light, 6th (corrected) (edn.) Pergamon Press, New York (1986)
[15] Yaroslavsky, A.N., Yaroslavsky, I.V., Goldbach, T., Schwarzmaier, H.J.: The optical properties of blood in the near infrared spectral range, in Optical Diagnostics of Living Cells and biofluids. In: Proc. SPIE, Int. Soc. Opt. Eng., vol. 2678, p. 314 (1996)
[16] Tuchin, V.: Tissue Optics - Light Scattering Methods and Instruments for Medical Diagnosis, 2nd edn., pp. 145–191. SPIE (2007)
[17] Bashkatov, A.N., Genina, É.A., Kochubey, V.I., Tuchin, V.V.: Optical Properties of the Subcutaneous Adipose Tissue in the Spectral Range 400 – 2500 nm. Text 99, 868–874 (2005)

[18] Troy, T.L., Thennadil, S.N.: Optical properties of human skin in the near infrared wavelength range of 1000 to 2200 nm. J. Biomed. Opt. 6, 167 (2001)
[19] Weininger, S.A.: Prototype device for standardized calibration of pulse oximeters II. Journal of Clinical Monitoring and Computing (2002)
[20] Firbank, M., Oda, M., Delpy, D.T.: An improved design for a stable and reproducible phantom material for use in near-infrared spectroscopy and imaging. Physics in Medicine and Biology 40, 955–961 (1995)
[21] Lualdi, M., Colombo, A., Farina, B., Tomatis, S., Marchesini, R.: A phantom with tissue-like optical properties in the visible and near infrared for use in photomedicine. Lasers Surg. Med. 28, 237–243 (2001) doi: 10.1002/lsm.1044
[22] Firbank, M.: A design for a stable and reproducible phantom for use in near infrared imaging and spectroscopy. Physics in Medicine and Biology 38, 847–853 (1993)
[23] Koh, P.H., Elwell, C.E., Delpy, D.T.: Development of a dynamic test phantom for optical topography. Adv. Exp. Med. Biol. 645, 141–146 (2009)
[24] Roggan, A., Friebel., M., et al.: Optical Properties of circulating human blood. BIOS Europe (1997)
[25] Kraitl, J.: Optisches Monitoring für die in-vitro –Messung der Hämoglobin Konzentration und der Sauerstoffsättigung. In: BMT 2006, Zürich, Schweiz (2006)
[26] Fricke, D., Koroll, H., Kraitl, J., Ewald, H.: Blood flow model for noninvasive diagnostics. In: Proceedings of IEEE GCC Conferenc and Exhibition, Dubai, UAE, pp. S.343–S.346 (2011) ISBN 978-1-62284-118-2
[27] Kraitl, J., Ewald, H., Gehring, H.: An optical device to measure blood components by a photoplethysmographic method. J. Opt. A.: Pure Appl. Opt. 7, 318–324 (2005)
[28] Kraitl, J., Timm, U., Lewis, E., Ewald, H.: Optical sensor technology for a noninvasive continuous monitoring of blood components. In: BIOS, SPIE Photonics West, San Francisco, CA, USA (2006)

Homeland Security and Cloud: Challenges and On-Going Developments

M. Fazio, M. Paone, A. Puliafito, and M. Villari

University of Messina, Contrada Di Dio 98166 Sant'Agata - Messina
{mfazio,mpaone,apuliafito,mvillari}@unime.it

Abstract. In this chapter we deal with the Homeland Security issue, which is a very crucial topic for all over the world. We specifically focus on how to benefit from cloud computing to prevent and face off terrorism attacks. To show and discuss such benefits, we analyse a specific scenario for HS, that is the Transport of Dangerous Goods. We introduce the concept of "Concurrent" transport, that describes the contemporary movement of goods through different modes in a specific geographical area in a given time interval. Spatial and temporal constrains allow to analyze the global *Societal Risk* of the transport in that area and to highlight the requirements of the Homeland Security activities. We present a new Cloud architecture specifically designed for supporting Homeland Security, both in terms of prevention and management of dangerous situations. It offers world wide services for the cooperation of governments and organizations involved in disaster prevention and/or rescue through the creation of federations. It also guarantees a capillary interaction with the environment along with different and heterogeneous sensing infrastructures, in order to collect massive information for detection, planning, and management activities against terrorism.

1 Introduction

Enforcing security of citizens is becoming crucial for all world-wide Governments and Public Institutions, which are strongly working for implementing new solutions to improve what is commonly referred as Homeland Security (HS) [23][22][26]]. In the digital era, the use of electronic devices and social medias is determining an increasing of the complexity in managing preventions against terrorists and their malevolent behaviors. Terrorists are able to exploit the ICT (Information and Communication Technology) for selecting sensible targets, organizing their activities and coordinating criminal actions. For example, social networks such as Facebook and Twitter have been designed for helping people to get in touch and share data. However, they are becoming also a way for accomplishing bad intents, since they allow to exchange information over wide geographical areas, without any control or super-visioning.

S.C. Mukhopadhyay et al. (Eds.): Advancement in Sensing Technology, SSMI 1, pp. 263–282.
springerlink.com

In this chapter we deal with HS and explain how it can take advantages from an ICT Cloud based infrastructure and services. We believe that Cloud computing may help HS offering a flexible support for organizing and managing heterogeneous systems, providing huge amount of processing, storing and sensing resources. These systems have to react to unusual behaviors in order to promptly detect dangerous activities. As highlighted in [1], the US Government Certification and Accreditation (C&A), together with the Department of Homeland Security (DHS) and NIST, are helping agencies to efficiently acquire Cloud computing capabilities for mitigating threats. In fact, Cloud computing may help Departments of Defense in reducing the risks of attacks by minimizing the probability that Dangerous Situations occur in a specific time and place, hence reducing the vulnerability to terrorism. In worst situations, i.e. when an attack takes place, Cloud computing can be also useful to efficiently manage the disaster, minimizing damages and speeding up recovering. All these tasks can be summarized as the effort necessary for minimizing the *Societal Risk*.

In order to limit the Societal Risk, Cloud should provide a communication infrastructure helpful to integrate efforts and resources of different organizations involved in the disaster prevention and/or rescue, giving a concrete support for a common planning of all the activities against terrorism. Cloud should offer a very flexible architecture providing benefits in terms of availability, security and dependability. For this purpose, we can also consider the capability of heterogeneous Clouds to collaborate each other for increasing their productivity and efficiency. Cooperating Clouds have to form a federation, where virtual resources and services are shared.

To better explain the impact of the Cloud technology in fighting terrorism, in our discussion we refer to a specific case of study, that is the Transportation of Dangerous Goods (TDG), although our considerations can be easily applied to a whichever HS scenario. We present a new Cloud architecture, called HSCloud, which has been specifically designed to support HS activities. It is able to reduce vulnerabilities to terrorism by coupling activities of monitoring and detection with advanced features in the treatment, filtering and provisioning of collected data. In particular, it allows to accomplish the following main tasks:

- collecting data from heterogeneous sensing devices spread over sensible geographical areas;
- managing data in order to offer a common representation of information;
- providing a platform for developing algorithms aimed at HS;
- offering a web-based interface for an easy interaction with the Cloud.

The chapter is organized as follows: next section provides basic concepts on Homeland Security, focusing on Transport of Dangerous Goods (TDGs). Section *Risk Evaluation* aims at the Investigation of Risk, an important argumentation for describing metrics and equations helpful for evaluating hazardous of human activities. Then the chapter will introduce cloud computing

principles, and how HS may benefit from cloud. Our HSCloud infrastructure completes the dissertation where more design and implementation details are presented. At the end *Conclusions* closes the chapter.

2 Background

In [30], the authors presented a survey on incidents that are related to HS and Defense such as terrors, cyber-attacks and disasters. They provided an overview on existing projects from the department of Homeland Security and Defense of the US government; it highlights the great interest on such a topic.

The book of Chen et al. [16] describes how the terrorism informatics represents the umbrella gathering huge amounts of information from varied and multiple sources and in numerous different languages. These terrorism-related information are used for international and HS related applications. The Terror Informatics is the interdisciplinary and comprehensive assessment where techniques of Knowledge Management and Data Mining for HS help to reduce world-wide threats.

The work [20] provides several practices for HS modeling, simulation and analysis (MS&A). This work is useful for understanding how to characterize a software stack robust to attacks. This is an important issue, which needs to be faced up all the times the IT systems are exploited for preventing Security attacks.

The US FBI has recently reported the following list [2] of hot matters that should be addressed for HS in the next future: **Terrorism**, **Espionage**, **Proliferation**, **Economic Espionage**, **Targeting the National Information Infrastructure**, **Perception Management** and **Foreign Intelligence Activities**.

Our work focus on Terrorism [2] and provides a technological solution for reducing vulnerabilities of countries and minimizing damaging effects of attacks. In our idea, all private companies, military or public departments, civilian organizations operating in HS should merge their efforts, resources and strategies to create a complete and efficient shield against terroristic attacks. These activities are based on a capillary monitoring of buildings, streets, vehicles and human behaviors, in order to detect sensible targets or malicious intents. Information coming from several monitoring infrastructures can be correlated in order to provide an in depth knowledge of the environment and a solid base for developing the HS intelligence.

In the next section, we discuss of a specific and strategic scenario for HS, that is the Transportation of Dangerous Goods (TDGs) [24] over multimodal ways (such as freeways, railways, air routes and sea routes). However, the presented solution can be easily generalized and similar conclusions on the strategic combination of cloud and HS can be done also for different HS scenarios.

3 Transportation of Dangerous Goods (TDGs)

Goods can be moved by using different types of transports and they can change transport mode during the transfer from the origin to the destination. Transport system can be roughly classified in:

- Air transport: it implies a management of three-dimensional areas, where the prevention of terrorist attacks is crucial, since rescue activities for saving human lives are very hard;
- Surface transport: it covers two-dimensional areas over the surface of the earth. Its complexity comes from concurrencies in the following ways:
  - land transport by road and rail;
  - maritime transport;
  - pipelines, which represent fixed infrastructures for continuous transfer of goods, such as natural gas, water or ammonia.

For our purposes we need to consider the concurrent movement of goods through different routes. We want to analyze the global movement of goods along different routes in the same geographical area in a given time interval. Thus, we extend theIntermodal transport mode [3] in *Concurrent transport*, which includes spatial and time features in the issue of goods delivery.

Most of the times, people are not aware about the danger related to TDGs. Indeed, dangerous goods can cause terrible disaster due to their congenital high potential risk. An accident may produce uncontrollable effects, especially in highly populated areas or during popular events. So, terrorist attacks increase the hazard of TDGs of hundreds of times.

An analysis of the state of the art shows a great interest on the TDGs. This is demonstrated by the existence of many solutions, projects and business products falling in this area, as discussed in the next section.

3.1 The State of the Art on TDGs

The analysis of Concurrent transport is a very complex problem involving economical, legislative and technological aspects. The European Agreement Concerning the International Carriage of Dangerous Goods by Road (Accord Dangereuses Route: ADR [4]) describes in detail which are the dangerous substances and how to transport them by road. In particular, the initiative aims to increase the safety of international movement of dangerous goods by surface transport, contributing to the protection of the environment, preventing pollution resulting from possible accidents, facilitating transport operations and promoting international trade. Transport of Dangerous materials by sea is regulated through the IMDG Code (International Maritime Dangerous Goods Code [5]). The IMDG Code is intended to protect crew members and to prevent marine pollution in the safe transportation of dangerous materials by vessel. Transport of Dangerous Goods by air should be compliant with

the requirements established by the *Dangerous Goods Panel* of ICAO (International Civil Aviation Organization [6]) and codified in Annex 18 to the ICAO Technical Instructions. In practice, the industry uses the Dangerous Goods Regulations issued by the association IATA (International Air Transport Association) that contains all the requirements dictated by the ICAO Technical Instructions, making them even tougher.

Dangerous good transportation gather great attention also from the research community and business companies. The main goal is to provide a framework for goods monitoring and activities planning, in order to prevent disaster and to manage activities if accidents occur.

MITRA [12] is a research project funded by the European Commission with the objective to prototype a new operational system based on regional responsibilities for the monitoring of dangerous goods transportation in Europe. It provides a real-time knowledge of position and contents of dangerous goods through the European Geostationary Navigation Overlay Service (EGNOS), that is a satellite based augmentation system developed by the European Space Agency, the European Commission and EUROCONTROL. In case of dangerous situations, GSM communications allow to alert the Security Control Centre, which is responsible to prevent accidents, manage crisis and enable quick intervention.

SMARTFREIGHT [13] is a European research project, partly funded by the European Commission under the 7^{th} Framework Program (7FP). The overall objective of SMARTFREIGHT is to address new traffic management measures towards individual freight vehicles by using open ICT services, with an emphasis on the interoperability between traffic management and freight distribution systems, and an integrated heterogeneous wireless communication infrastructure within the framework of CALM (Communication Access for Land Mobiles)

In [29], the authors propose a complete monitoring and tracking solution for truck fleets. The system exploits battery-powered environmental sensors (temperature, humidity, pressure, gas concentration and ionizing radiation levels), connected by a ZigBee-based Wireless Sensor Network. Collected data is then sent from the vehicle to a remote server via a GPRS link. The GPS positioning system is integrated by the use of an Inertial Navigation System, which guarantees a precise estimate of the position also when the GPS signal is weak or temporarily lost.

The solution proposed in [31] aims to improve the security of maritime container transport of dangerous goods by the real-time monitoring of container state. This system uses micro-sensor technologies and radio frequency communication technology to obtain the dangerous goods condition inside containers, as well as automatic positioning in the cargo hold. Information on the state of dangerous goods are transmitted to the shore monitoring center on land through INMARSAT stations.

4 Our Idea of Cloud Computing for TDG

By comparing the different solutions for dangerous goods existing in literature, we have identified the following common goals:

1. monitoring of the TDG infrastructures, which includes the localization and tracking of freight transportation and the analysis of goods state according to several types of information (temperature, pressure, gas detection,...);
2. data collection and elaboration, to correlate all the information coming from the monitoring activity;
3. HS Intelligence services, to implements policies for both disaster prevention and emergency management.

Cloud computing can offers several benefits in carrying out these HS activities and we are going to explain how.

With reference to the first item, that is the monitoring activity, existing solutions differ a lot in terms of sensor technologies, communication infrastructures, design of the system organization and software support. Companies operating in the monitoring of dangerous goods have to use specific technologies that depend on several factors: the type of dangerous goods that are tracked, their geographical position and route, mode of transport, legislation of the country and so on. International Regulations define standard procedures for the treatment of dangerous goods. However, from a technological point of view, they do not provide any specification with reference to the monitoring infrastructure installation. The result is that, usually, there is not compatibility between different monitoring systems managed by organizations or companies, both in terms of hardware and software. Another important point is related to the transportation solution adopted. Each solution focuses on a specific method of transportation (such as ship, truck, airplane or railways) and the concept of *concurrent* service is not faced at all. However, the aggregation of information from *concurrent* ways can be extremely useful to predict terrorist attacks. Furthermore, in case of attacks, the management of different types of way out from the disaster area can save human lives. A world wide solution is still missing. Recent events have shown the importance of collaboration among different countries to fight against terrorism. So, we imagine a future HS system where efforts will integrate activities along the roads, highways, railways, harbors and airports at once. The integration will also include activities provided by different operators inside the same country and among different countries. Cloud Computing represents the *GLUE* to integrate and homogenize such heterogeneous systems. Governments are responsible to enforce the use of such *GLUE*. By using the concept of virtualization, Cloud computing is able to abstract hardware

and software resources and, thus, guarantee an high level of interoperability among different physical infrastructures involved in the HS activities.

The monitoring activity causes a massive collection of data, which need to be organized and processed in order to provide an integrated knowledge of the context. The context knowledge is the base to build up strategies for the National Security level. High amount of data means more efficient services, but implies high requirements in terms of processing power and storage space. However, the demands of resources vary significantly depending on several parameters, such as the geographical area, traffic, and so on. The distributed nature of Cloud computing guarantees high availability of computational and storage resources as services, which can be dynamically adapted to specific needs of the system. Concurrent transport of dangerous goods is characterized by specific constrains, which need guarantees on the quality of the informative services (e.g. reaction time to an event occurrence, synchronization of activities, trust in using third party support,...). The high flexibility of the Cloud in dynamic configuration, management and optimization of resources and services allows to respond effectively to the quality of service requirements of the system.

HS Intelligence services correlate information on the environment, goods, carriers and freight operators, and determine the best routes for goods transfer. Routes are evaluated according to the probability of dangerous events, that is the risk assessment of the routes. So, risk investigation is a basic problem that has to be addressed in TDG scenarios. In the next sections we describe some issues on risk investigation and discuss how they can be faced in designing HS solutions. The Cloud offers a very innovative approach to develop HS services through a software platform, where resources and context information are accessible through well-defined interfaces. This approach allows to implement new services without any knowledge of physical infrastructures and software architecture, making the HS intelligence development easier and flexible.

Another important feature offered by the Cloud technology is its ability to manage a federation of several clouds. Thus, we consider the Cloud environment as a constellation of hundreds of independent, heterogeneous, private/hybrid Clouds able to interact, maintaining separated their own domains and the specific administration policies. This requirement is particularly important in the HS area, because actors that interact to improve their HS do not intend to disclose their valuable owned data.

To exploit the benefits of the Cloud in reducing vulnerability to terrorist attacks, we have designed HSCloud, that is a new Cloud architecture for HS. It is able to set up a federation of heterogeneous systems that cooperate to prevent and manage dangerous events and disasters, by minimizing damages and recovery efforts. We will present HSCloud in detail in the next sections.

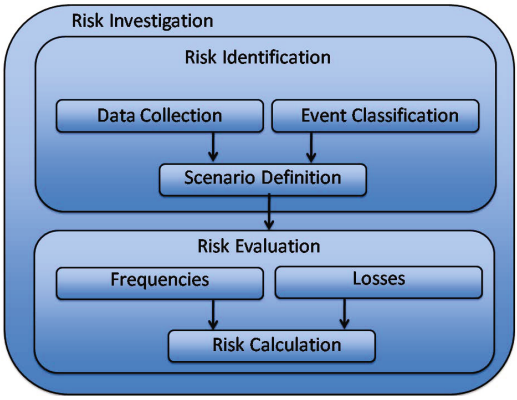

Fig. 1. Risk Investigation activities

5 Risk Evaluation

Risk is the potential that a chosen action or activity leads to a loss. This concept implies that each choice has influence on the outcome. Almost any human intent carries some risk, but some are much more relevant than others. We face risks in many human activities characterized by an *hazard* as well economics investments, building infrastructures and transport of people and/or goods. With the term of *hazard* we mean every risky condition, which can potentially cause harm, like human injury or death, damage to the environment, damage to physical assets and loss of production.

The Risk Investigation is a way for evaluating the hazard of an activity and Figure 1 shows how it is possible to perform it. The first step is characterized by two independent tasks:

1) Data Collection, for gathering all the necessary information useful to characterize the context. The specific data types depend on the environment and/or activities. For example, in TDG, data types include the physical geography of the area under interest, routes, exchange nodes, goods properties, carrier details and so on.

2) Event Classification, for specifying which events cause loss and the impact of the loss. In our scenario, damaging events include accidents, explosions, delays and so on.

The second step of the Risk Evaluation aims to merge information on data and events in order to clearly define the scenario where the activity will be carried out. The formal description of the scenario allows to perform the evaluation of the risk.

Risk R can be analytically defined as follows:

$$R = F * L \tag{1}$$

where F is the Frequency of the risk occurrences (that is the probability that a risk might become concrete) expressed as the number of events per time unit and L is a dimensionless number for measuring the intensity of the loss (that is the effect of a risk occurrence).

In the Risk Evaluation assessment, it is possible to identify three typologies of risk:

- Individual Risk (IR): as defined by AIChE/CCPS[7], it represents the probability that an average unprotected person, permanently present at a certain location, is killed in a period of one year due to an accident resulting from a hazardous activity.
- Societal Risk (SR): it is a measure of risk for a group of people. It is most expressed in terms of the frequency distribution of multiple casualty events (F/N curve, described later).
- Environmental Risk (ER): it represents the potential threat of adverse effects on living organisms and environment by effluents, emissions, wastes, resource depletion, etc., arising out of an organization's activities.

Since our work focuses on concurrent transports considering the global movement of goods, we have to evaluate situations having the potential to harm many people and, hence, the cumulative effects of risks. So, the best way to quantified risk is to evaluate the *Societal Risk*.

In order to evaluate acceptable Risks for human beings, we measure risks in terms of mortality rate. High risky conditions are characterized by:

$$10^{-2} deaths/person - year \tag{2}$$

and the low risky conditions are characterized by:

$$10^{-6} deaths/person - year \tag{3}$$

Figure 2 shows as example, the SRs of two dangerous chemical substances, *ammonia* and *clorine* [11], in a F/N graph, where F is the frequency of outcomes occurrences and N is the number of outcomes. Both curves have an acceptable risk degree. However, clorine has an higher level of explosion effects respect to the ammonia. Thus, these goods should not share the same route during their transport, in order to avoid to increase the risk level of the ammonia to the level of the clorine.

In concurrent transports, the total risk T(called group-risk) is evaluated as the sum of the risks of concurrent activities [21]. It can be expressed as follows:

$$T_{SR} = \sum_{i=1}^{n} SR_i \tag{4}$$

where n represents the number of concurrent activities. In TDG, if we consider the concurrent transport of ammonia, clorine and other dangerous

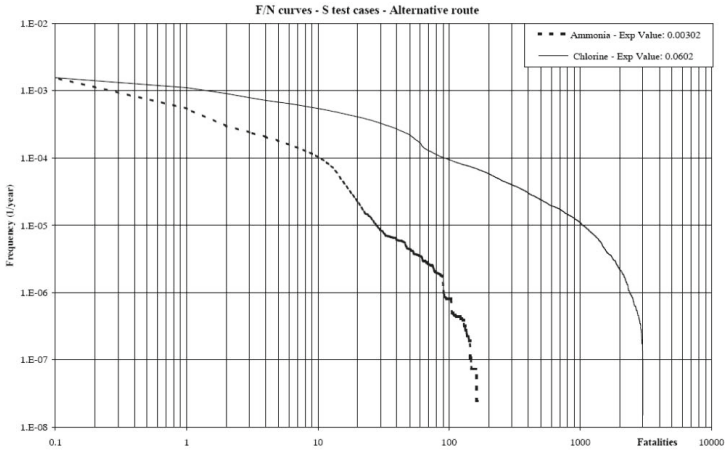

Fig. 2. Example of Societal Risk of the substances ammonia and chlorine for a road tunnel [11]

substances over the same geographical area, independently from the transportation mode, the overlapping of effects brings to a very high global risk, which can causes devastating outcomes.

Only an inter-operable Cloud system (Clouds of the Highway Operator along with the Railway Operator and Maritime Operator) might reveal the risk, reduce the vulnerability of a geographical area and shift back/down the T_{SR}.

6 Briefly on Clouds

Cloud Computing is a very challenging technology that many generally considered as one of the more challenging topic in the IT world, although it is not always fully clear what its potentialities are and which are all the involved implications. Ian Foster describes Cloud Computing as a large-scale distributed computing paradigm that is driven by economies of scale, in which a pool of abstracted, virtualized, dynamically-scalable, managed computing power, storage, platforms, and services are delivered on demand to external customers over the Internet [19]. Until now, such trend has brought the steady rising of hundreds of independent, heterogeneous Cloud providers managed by private subjects yielding various services to their clients.

Cloud services in HS,according to the NIST formalization [8], are offered at three different levels:

- *SaaS in HS*: it represents the capability given to consumers of accessing provider's applications running on a Cloud infrastructure. In the HS case, SaaS may represent the web service interface used to access information and activities available in the system.

- *PaaS in HS*: it makes consumers able to deploy their own applications onto the Cloud infrastructure using programming languages and tools supported by PaaS Cloud providers. The plethora of applications already developed for HS may convey on the Cloud, in order to increase their degree of accessibility and availability.
- *IaaS in HS*: it provides consumers with computation, storage, networks data transfer and other computing resources. Consumers are able to deploy and run arbitrary software, which can include operating systems and applications. In the HS context, IaaS ensures high elasticity in the usage of available resources, thus determining higher efficiency to all the HS activities, shielding attacks and efficiently managing crisis conditions.

ICT developers are exploring to improve the economy of scale, the efficiency of their systems and, also, to reduce power consumptions and CO2 emissions. In order to provide a flexible use of resources, Cloud computing makes wide use of virtualization, allowing to treat traditional hardware resources like a pool of virtual ones. In addition, virtualization enables resources migration, regardless of the underlying physical infrastructure. Using virtualization and aggregation techniques, Cloud computing offers its available resource *as a Service* rather than as physical product.

6.1 The State of the Art on Cloud and Sensing Technologies

In [15] the authors present a framework that provides a semantic overlay of underlying Cloud-based Internet of Things. The framework they propose introduces the concept of sensor-as-a-service (SenaaS) to address the connectivity issue with various types of sensor nodes. They employ enhanced semantic access polices to ensure access to only authorized parties.

In [25], the authors describe the *Integration Controller interaction Architecture (*IICiA), which enables users to easily collect, access, process, visualize, archive, share and search large amounts of sensor data from different applications. The architecture should support complete sensor data life cycle from data collection to the backend decision support system. They characterize the Cloud technology by using a Service Oriented Architecture (SOA).

In [27] the authors present a model for Smart Grid data management based on specific characteristics of Cloud computing, such as distributed data management for real-time data gathering, parallel processing for real-time information retrieval, and ubiquitous access. They gather the requirements by utilizing REST based APIs to collect and analyze set of data from well-known smart grid use cases.

The authors in [18] present a platform, called ubiquitous Cloud, to exploit Cloud facilities. They propose adaptive services to manage ubiquitous resources, which are able to dynamically adapt their behaviors to requirements and contexts of the ubiquitous computing. To facilitate the management of ubiquitous service resources, their paper presents a platform called ubiquitous Cloud.

The authors in [32] proposed an infrastructure, called Sensor-Cloud, which can manage virtual sensors on the Cloud. It virtualizes physical sensors as virtual sensors and dynamically provides grouped virtual sensors the users need them.

Since the Cloud paradigm is used in many application areas, we want to exploit its features to specifically address issues related to HS in TDGs.

6.2 The CLoud-Enabled Virtual EnviRonment (CLEVER)

The CLoud-Enabled Virtual EnviRonment (CLEVER) is a Cloud middleware [28] which aims to develop a Virtual Infrastructure Manager (VIM) for the administration of private Clouds infrastructures. Its main capability is to setup an overlay network useful for allowing the interaction of several federated Clouds spread all over the Internet.

CLEVER was originally conceived as part of the IaaS level [28] for implementing the Virtual Infrastructure Management (VIM) layer. In general, a VIM manages the physical resource of a datacenter (i.e., a cluster of machines), interacting with end-users, providing them Accounting, Service Level Agreements (SLAs), Billings, etc. It dynamically creates and executes Virtual Machines (VMs) on the CLEVER hosts, considering their workload, data location and several other parameters.

CLEVER has been designed to support horizontal federation. The concept of federation has always had both political and historical implications: the term refers, in fact, to a type of system organization characterized by a joining of partially "self-governing" entities united by a "central government". In a federation, each self-governing status of the component entities is typically independent and may not be altered by a unilateral decision of the "central government". The components of a federation are in some sense "sovereign" with a certain degree of autonomy from the "central government": this is why a federation can be intended as more than a mere loose alliance of independent entities. The choice of using XMPP for the CLEVER module communication has been made thinking about the possibility to support in the future also interdomain communication between different CLEVER administrative domains. The interdomain communication is the base for the horizontal federation.

To meet the requirements of sensing environments, we have extended the VIM functionalities of CLEVER in the SensCLEVER middleware, in order to manage physical resources of sensing infrastructures. There, we have added new capabilities for exposing specific services for sensing resource management, hiding underneath technologies. This has meant the definition of new PaaS functionalities in our middleware (i.e., data filtering and aggregation, on-demand messages, etc.).

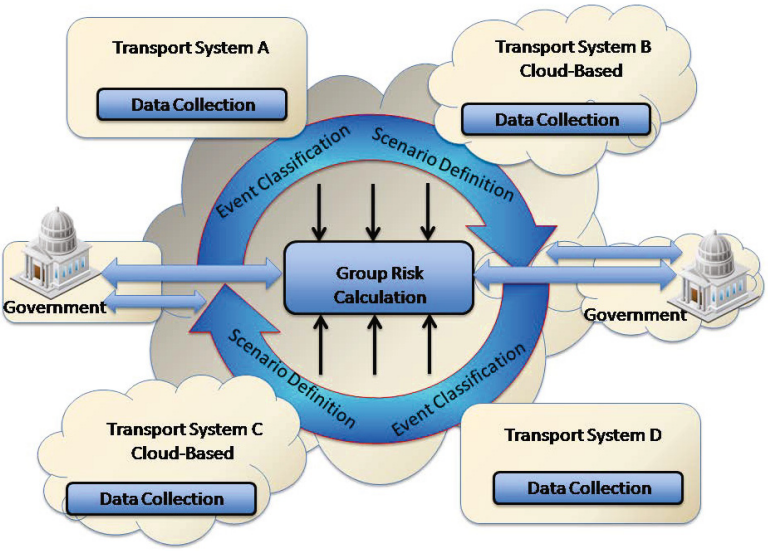

Fig. 3. Cloud-based Risk Investigation

7 Risk Investigation in the Cloud

Figure 1 shows the main functionalities for Risk Investigation in TDGs. A leader organization responsible for risk investigation coordinates efforts over each task in order to provide the risk calculation. The cooperation of the different entities involved is based on a rigid hierarchical organization, where higher elements are responsible for the lower. In a Cloud environment, thanks to its distributed paradigm, the architectural organization of work can be redesigned. All the organizations, institutions and companies involved in risk investigation are organized in a federation. Each of them has a specific role and responsibilities and gives its contribution to the federation, according to a flat organization model of tasks. This approach improves the flexibility of the whole system, where competences and activities are independent from each other.

As shown in Figure 3, Transport Systems are responsible to provide Data Collection through their monitoring infrastructures to the cloud. At the same time, other organizations, such as governments or other institutions for HS, provide services for the Scenario Definition. However, each organization specifies properties of the scenario according to different parameters (geographical area, legislation, HS policies,...). Risk Calculation is performed through the elaboration of risks models through Cloud virtual resources. All these contributions are orchestrated within the Cloud in order to offer seamless services.

8 The HSCloud Architecture

Figure 4 shows the HSCloud architecture based on the SensCLEVER middleware, which extends the CLEVER middleware with sensing functionalities at the IaaS and PaaS layers.

To provide an effective integration among the services offered by Transport Systems, we need to recur to the virtualization of sensing infrastructures, i.e. abstracting each framework for secure goods transportation and provide it with a common interface toward the Cloud system. To this aim, we introduce the Virtual Pervasive Element (VPE) in the HSCloud infrastructure. In SensCLEVER, a VPE represents the peripheral element necessary to endure the interaction between Sensing Infrastructures and the other Cloud services. It is able to gather information from the specific sensing infrastructure and transfer them into the Cloud federation in JSON or XML formats to a remote Data Base Management System (DBMS) application.

The Data Manger module has mainly two tasks. First, it provides advanced features on data, as well filtering and data retrieval. Second, it acts as a manager element, which coordinates and supervises monitoring activities, by wondering and comparing responses from different components in the monitoring environment. This task allows to improve the efficiency and robustness of monitoring systems, since it allows to integrate different kind of information over the controlled area and to detect misbehaviors in a subsets of monitoring nodes. Communications among nodes in the SensCLEVER system is based on the XMPP protocol [9], which was born to drive the communications in heterogeneous instant messaging systems conveying any type of data.

On top of SensCLEVER, specific algorithms for supporting HS activities have been included at the PaaS layer. The Risk Investigation module elaborates data coming from the Data Manger module through CDMI API and accesses other Cloud resources through OCCI API. Then, it offers information on risks to the modules for the prevention and the management of attacks and disasters. About the first issue, the prevention activity in TDGs can be mainly organized in the detection module, to identifies misbehaviors or malicious initiatives, and the planning module, to improve the security of transports according to clever policies of forwarding. The management activity aims to orchestrate efforts of rescue squads and redirect traffic whenever a dangerous event occurs.

The SaaS exposes the interfaces to access services for HS. Different profiles are conceived in order to allow the HSCloud users to give different types of contributions. In fact, we can have actors belonging to Governments, having more departments relaying on differentiate contexts (Security Dep, Environment Dep, Military Dep, etc.) business enterprises, up to research centers. They can provide different contributions in HSCloud that we can classify as

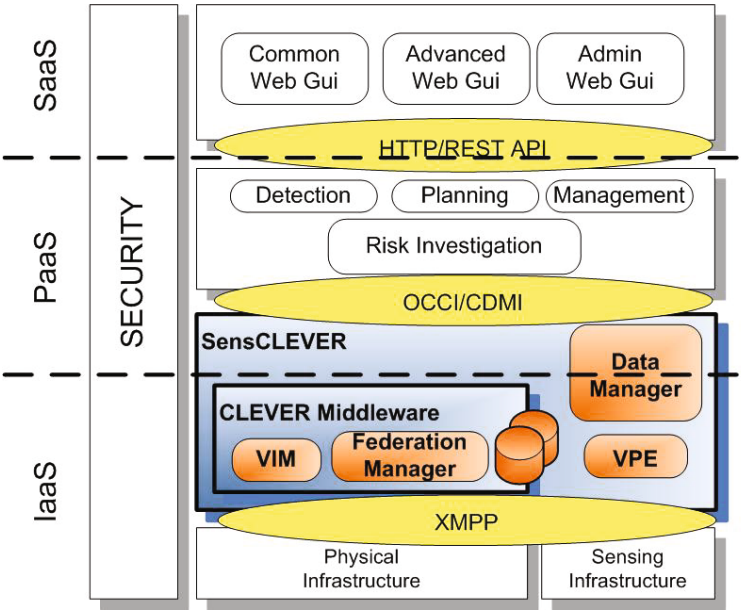

Fig. 4. Architecture of HSCloud

passive, active and hybrid. With the term *passive,* we mean actors that have a low level of trustiness on Clouds and can only achieve data from Cloud. *Active* actors are those that fully adopt and use Cloud technologies, transferring their software and hardware resources into the Cloud. *Hybrid* contributors are actors knowing Cloud, using such technology internally in their IT systems, but that partially use external Cloud technologies.

On the left side of Figure 4, we have included the security block. One of the main concern in using Clouds is related to security and the problem increases in our scenario since it deals with Public National Security rules. XMPP has natively some fundamental security mechanisms for guaranteeing, the confidentiality of communications, message integrity verification among the parties and non repudiation of messages senders. However additional mechanism can be developed.

9 System Prototype

This sections describes a prototype of a cloud based service for tracking trucks inside a city. It has been implemented by the University of Messina together with the City Council of Messina for improving services of the local public transport. On each truck, a Linux box equipped with a GPS, a HSDPA

communication device and Ultrasonic Range Finders (in the front and rear parts of the vehicles) is installed. In particular, the SRF10 Ultrasonic Range Finders used in the prototype allow to make measurements of distance in a range of up to 6 meters and they can be useful to estimate information on traffic. The Linux box hosts Contiki [17], an Operating System designed for sensors and embedded systems. It allows to give a uniform platform for interact with heterogeneous devices on board. The box acquires realtime information on the geographical position, speed and acceleration of trucks, and data from the Range Finders. Then, it sends them towards the Cloud through the HSDPA interface.

Behind the HSDPA provider hotspots, a SensCLEVER host implements the VPE module, to virtualize the mobile infrastructure for trucks monitoring. We have developed a runtime system to collect and represent sensor data as meta-data implementing the SWE specifications [14]. The SWE framework enables the discovery, exchanging and processing of sensor observations, through a set of XML-based languages and interface specifications, such as the Sensor Observation Service (SOS). Furthermore, languages for the description of sensed data, such as the Sensor Model Language (SensorML) and Observations and Measurements (O&M), provide a means to integrate data from heterogeneous sources in a standard format accessible from Cloud users. In our prototype, we made reference to the SOS standard to supports the functionalities for the description of sensors and observations, setting new observations and gathering measurements from the monitoring infrastructure. The SOS agent makes use of the SensorML standard, for describing sensors, sensor systems and sensed data, and the O&M standard, for modeling sensor observations.

The DBMS in SensCLEVER has been designed as a main module with several plugins, in order to support different types of database. In our prototype, we have developed a plugin for the Sedna native XML database [10]. Sedna natively supports XML data schemata (as well as SWE standards). Even, it is open-source, allows to create incremental backup copies of a database and supports ACID transactions. Sedna dynamically generates the descriptive schema from any type of data and maintains them by using an incremental approach. This solution makes the storage of information on the monitored environment very flexible. Thanks to the XPath and XQuery capabilities of Sedna, the system easily retrieves information from the database formatting them according to the SOS specification.

Figure 5 shows data on trucks belonging to the monitored fleet on a Google Map available through the HSCloud Web portal.

Statistics on traffic evolutions are elaborated by the Data Manager of the SensCLEVER middleware. In Figure 6, we draw, as example, the mean trucks' speed during one day.

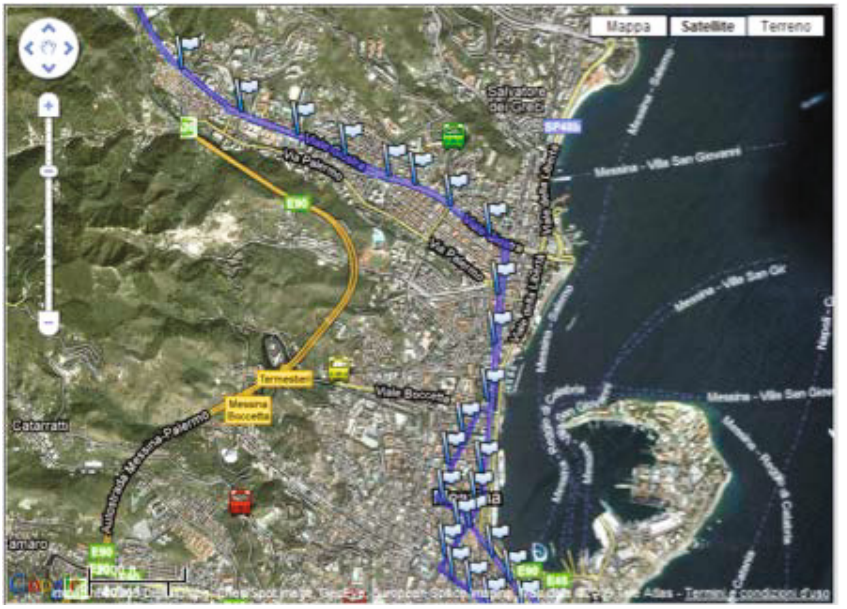

Fig. 5. A Shapshot of google Map

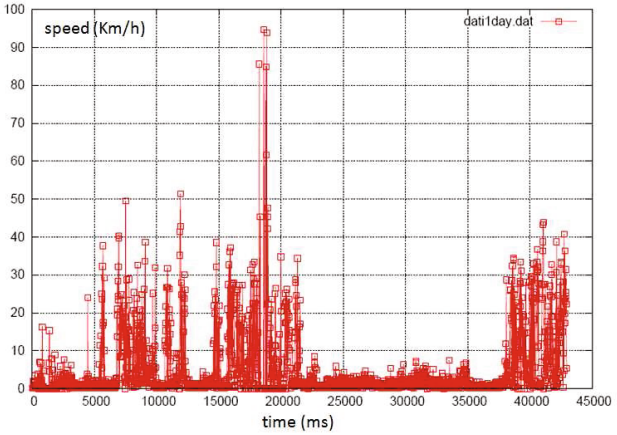

Fig. 6. A one-day traffic of city of Messina automatically captured by a truck during its work

10 Conclusions

In this chapter we have presented a Cloud-based architecture able to deal with Homeland security problems, called HSCloud. To show the main features of HSCloud, we have analyzed a specific use case, that is a TDGs scenario. We

have discussed current solution for security in TDGs highlighting limitations and drawbacks. Then we have explained how Cloud computing can improve the world wide security against terrorist attacks. According with all these considerations, we have presented the main features of HSCloud, describing in detail its working core, that is a Cloud middleware called SensCLEVER. The virtualization techniques implemented in SensCLEVER for integrating sensing infrastructures in a Cloud environment guarantees efficient and secure services at the infrastructure, platform and application layers. In the next future, we will improve SensCLEVER by including additional features related to information filtering according to users profile. Furthermore, we intend to implement methods to execute remote control of the sensing infrastructure.

References

1. Federal Cloud Computing Strategy (December 2011), http://www.theresearchpedia.com/sites/default/files/FederalCloudComputingStrategy.pdf
2. National Security Threat List (April 2011), http://www.wright.edu/rsp/Security/T1threat/Nstl.html
3. Multimodal Transport Handbook, UNCTAD 1996 (2002), http://unctad.org/en/docs/c3em20d2_en.pdf
4. Accord Dangereuses Route (March 2012), http://www.unece.org/trans/danger/publi/adr/adr_e.html
5. International Maritime Dangerous Goods Code (March 2012), http://www.imo.org/Pages/home.aspx
6. ICAO: Dangerous Goods (March 2012), http://www.icao.int/safety/DangerousGoods/Pages/default.aspx
7. AIChE/CCPS, Guideline for chemical process quantitative risk analysis, 2nd edn., New York (2000)
8. NIST Cloud Computing Reference Architecture (December 2011), http://www.nist.gov/customcf/get_pdf.cfm?pub_id=909505
9. The Extensible Messaging and Presence Protocol (XMPP) protocol, http://tools.ietf.org/html/rfc3920
10. Sedna, Native XML Database System (December 2011), http://modis.ispras.ru/sedna/
11. Transport of dangerous goods through road tunnels. quantitative risk assessment model (version 3.60), reference manual. In: OECD/PIARC/EU, CDROM (2003)
12. MITRA: Monitoring and intervention for the transportation of dangerous goods (2004-2006), http://www.mitraproject.info/
13. SMARTFREIGHT project, FP7-216353 (2009), http://www.smartfreight.info//
14. Sensor Web Enablement (2011), http://www.opengeospatial.org/standards

15. Alam, S., Chowdhury, M., Noll, J.: Senaas: An event-driven sensor virtualization approach for internet of things cloud. In: 2010 IEEE International Conference on Networked Embedded Systems for Enterprise Applications (NESEA), pp. 1–6 (2010), 10.1109/NESEA.2010.5678060
16. Chen, H., Reid, E., Sinai, J., Silke, A., Ganor, B.: Terrorism Informatics: Knowledge Management and Data Mining for Homeland Security, 1st edn. Springer Publishing Company (2008) (incorporated)
17. Dunkels, A., Grnvall, B., Voigt, T.: Contiki - a lightweight and flexible operating system for tiny networked sensors. In: Proceedings of the 29th Annual IEEE International Conference on Local Computer Networks, LCN 2004 (2004)
18. Egami, K., Matsumoto, S., Nakamura, M.: Ubiquitous cloud: Managing service resources for adaptive ubiquitous computing. In: 2011 IEEE International Conference on Pervasive Computing and Communications Workshops (PERCOM Workshops), pp. 123–128 (2011), doi:10.1109/PERCOMW.2011.5766853
19. Foster, I., Zhao, Y., Raicu, I., Lu, S.: Cloud Computing and Grid Computing 360-Degree Compared. In: Grid Computing Environments Workshop, GCE 2008, pp. 1–10 (2008)
20. Jain, S., McLean, C.R.: Recommended practices for homeland security modeling and simulation. In: Winter Simulation Conference, WSC 2009, pp. 2879–2890 (2009), http://dl.acm.org/citation.cfm?id=1995456.1995848
21. Jonkman, S.: An overview of quantitative risk measures for loss of life and economic damage. Journal of Hazardous Materials 99(1), 1–30 (2003), http://linkinghub.elsevier.com/retrieve/pii/S0304389402002832
22. Koyuncugil, A., Ozgulbas, N.: Surveillance Technologies and Early Warning Systems: Data Mining Applications for Risk Detection. In: Premier Reference Source. IGI Global (2010), http://books.google.com/books?id=l4Ir1nvyURIC
23. Mortimer, D.: Homeland security public safety dive teams: how technology can help. In: Proceedings of MTS/IEEE, OCEANS, vol. 1, pp. 178–183 (2005), doi:10.1109/OCEANS.2005.1639758
24. Ortner, M., Nehorai, A., Jeremic, A.: Biochemical transport modeling and bayesian source estimation in realistic environments. IEEE Transactions on Signal Processing 55(6), 2520–2532 (2007), doi:10.1109/TSP.2006.890924
25. Rajesh, V., Gnanasekar, J., Ponmagal, R., Anbalagan, P.: Integration of wireless sensor network with cloud. In: 2010 International Conference on Recent Trends in Information, Telecommunication and Computing (ITC), pp. 321–323 (2010), doi:10.1109/ITC.2010.88
26. Reddick, C.: Homeland security preparedness and information systems: strategies for managing public policy. Information Science Reference (2010), http://books.google.com/books?id=NaT_Fob6lBIC
27. Rusitschka, S., Eger, K., Gerdes, C.: Smart grid data cloud: A model for utilizing cloud computing in the smart grid domain. In: 2010 First IEEE International Conference on Smart Grid Communications (SmartGridComm), pp. 483–488 (2010), doi:10.1109/SMARTGRID.2010.5622089
28. Tusa, F., Paone, M., Villari, M., Puliafito., A.: CLEVER: A Cloud-Enabled Virtual Environment. In: 15th IEEE Symposium on Computers and Communications Computing and Communications, ISCC 2010, Riccione (2010)

29. Valente, F., Zacheo, G., Losito, P., Camarda, P.: A telecommunications framework for real-time monitoring of dangerous goods transport. In: 2009 9th International Conference on Intelligent Transport Systems Telecommunications (ITST), pp. 13–18 (2009)
30. Yim, K., You, I.: It issues on homeland security and defense. In: ARES, pp. 374–385 (2011)
31. Yingjun, Z., Shengwei, X., Peng, X., Xinquan, W.: Shipping containers of dangerous goods condition monitoring system based on wireless sensor network. In: 2010 6th International Conference on Networked Computing (INC), pp. 1–3 (2010)
32. Yuriyama, M., Kushida, T.: Sensor-cloud infrastructure - physical sensor management with virtualized sensors on cloud computing. In: 2010 13th International Conference on Network-Based Information Systems (NBiS), pp. 1–8 (2010), doi:10.1109/NBiS.2010.32

Formulation, Characterization and LPG-Sensing Properties of CuO-Doped ZnO Thick Film Resistor

M.K. Deore[1], V.B. Gaikwad[2], R.M. Chaudhari, N.U. Patil[2], P.D. Hire[2], S.B. Deshmukh[2], G.E. Patil[2], V.G. Wagh[2], and G.H. Jain[2,*]

[1] Dept. of Physics, Arts, Science and Commerce College, Ozar (Mig), India-422 206
[2] Materials Research Lab., K.T.H.M. College, Nashik, India
gotanjain@rediffmail.com

Abstract. Formulation, characterization and sensing properties of pure and CuO-doped ZnO thick films were studied by preparing thick films using the screen printing technique on glass substrate. The pure AR grade powder of the Copper chloride was added at the various concentrations (1, 3, 5, 7and 9 wt. %) into the pure AR grade powder of the Zinc oxide. The powders of different compositions were sintered at 1000^{o}C for 12 h. The Copper chloride ($CuCl_2$) transforms into Copper oxide upon heating. The structural properties of the pure and CuO-ZnO composite materials was analyzed by the X-ray diffractogram and it shows the polycrystalline nature. The films were fired at temperature 550^{o}C for 30 min. The surface morphology of the films was analyzed using SEM analyzer. The final composition of each film was determined by EDAX analysis. The gas response, selectivity, response and recovery time of the sensor were measured and presented. The 5 wt. % CuO- doped ZnO film showed highest response and selectivity to LPG than other gases.

1 Introduction

Semiconductor gas sensors based on metal oxides has been used extensively to detect toxic and inflammable gases. The focus of this paper is on semiconductor based gas sensors. A wide range of gas sensors are developed using metal oxide semiconductors (MOS) because of its advantageous features like sensitivity to the ambient conditions, low material cost, easy processing and simplicity in fabrication. The most commonly used n-type MOS for gas sensors are based on SnO_2 [1], TiO_2 [2], ZnO [3-5], Fe_2O_3 [6], In_2O_3 [7], CeO_2 [8], and WO_3 [9] and are known for their changes in electrical conductivity when exposed to test gases. At elevated temperatures (100^{o}C–600^{o}C); these materials show large variations of electrical conductivity in response to the presence of traces of reactive gases in air. Gas

* Corresponding author.

S.C. Mukhopadhyay et al. (Eds.): Advancement in Sensing Technology, SSMI 1, pp. 283–298.
springerlink.com

sensors based on MOS in thick-film form, have been developed for detection and control of gases such as: CO [10], O_2[11], NH_3[11],NO_2[12], Ethanol [13], H_2S [14] and LPG [15], etc.

Metal and non-metal catalysts [16] were added / incorporated to improve the sensitivity and selectivity of the sensors. Most of the gas sensors developed are doped with noble metals like Pt., Pd, etc. which are expensive. However, low cost metals or metal oxides are generally doped to achieve higher sensitivity and selectivity. For example, a low cost metal such as Sb has been doped in SnO_2 based thick-films to achieve higher sensitivity for H_2 and CO sensing [17]. Among various dopants, CuO is an outstanding promoter in enhancing the catalytic activity and gas sensing properties MOS. In the present work, CuO dopant used for doping in the base material (ZnO) to enhance the gas response and selectivity. The CuO-doping reduce the electrical conductivity of ZnO and the reduced conductivity of ZnO was proposed to be responsible for the increase of the gas sensitivity of ZnO–CuO composite by increasing the current through p–n junction [18].

Among the n-type semi conducting oxides, ZnO is one of the metal oxide semi conducting material having wurtzite structure, with a direct large-band gap of about 3.37eV at low temperature and 3.30eV at room temperature [19]. It is sensitive to many gases at moderate temperature. ZnO is one of the most widely applied oxide-gas sensor. ZnO gas sensing materials owe to their high chemical stability, low cost, and good flexibility in fabrication. ZnO sensor elements have been fabricated in various forms such as single crystal [20], sinter pellet, thin film [21], and thick film [22].

Liquefied Petroleum Gas (LPG) is highly inflammable gas. It is widely utilized in industrial and domestic fields as fuel. It is potentially hazardous and explosion accidents might cause when it is leaked out by mistake. It is referred also as town or cooking gas. Cooking gas consists chiefly of butane (55-vol %) [23], It is a colourless and odourless gas. It is usually mixed with compounds of sulphur (methyl mercaptan and ethyl mercaptan) having foul smell, so that its leakage can be noticed easily. It has been reported that, at the concentration up to noticeable leakage, it is very much more than the lower explosive limit (LEL) of the gas in air. So there is a great demand and emerged challenges for monitoring it for the purpose of control and safety applications in domestic and industrial fields.

The aim of the present work is to study ZnO thick films gas sensor with CuO as additives, which could be able to detect the LPG gas. CuO in ZnO is outstanding in promoting the sensing properties to LPG in air.

2 Experimental

2.1 Preparation of Functional Material

The pure (99.9%) AR grade Zinc oxide powder was ball milled to ensure the sufficiently fine particle size. The fine powder was sintered at 1000^{o}C for 12 h in air and reground. The reground powder of Zinc oxide and Copper chloride

($CuCl_2$) were mixed mechanochemically to obtain CuO-doped ZnO powders in various weight percentages such as 1, 3, 5, 7, and 9 wt. %. The prepared composite powders were sintered at 1000°C for 12 h in air ambience and ball milled to ensure sufficiently fine particle size.

2.2 Preparation of Thick Films

The thixotropic paste was formulated by mixing the fine powder of functional material with a solution of ethyl cellulose (a temporary binder) in a mixture of organic solvents such as butyl cellulose, butyl carbitol acetate and terpineol, etc. The ratio of the inorganic to organic part was kept at 75:25 in formulating the paste. This paste was screen-printed [24, 25], on a glass substrate in a desired pattern (1.5cm X 0.5cm). The thickness of the film was observed to be 65 µm to 75 µm. The films were dried under infrared radiation for 45 minutes to remove the organic vehicle and then fired at a temperature of 550°C for 30 min, constant firing for 30 minutes at the peak temperature and then to attain the room temperature in a muffle furnace.

2.3 Details of Gas Sensing System

The sensing performance of the sensors was examined using a 'static gas sensing system' [26], shown in Figure1, there was electrical feeds through the base plate. The heater was fixed on the base plate to heat the sample under test up to required

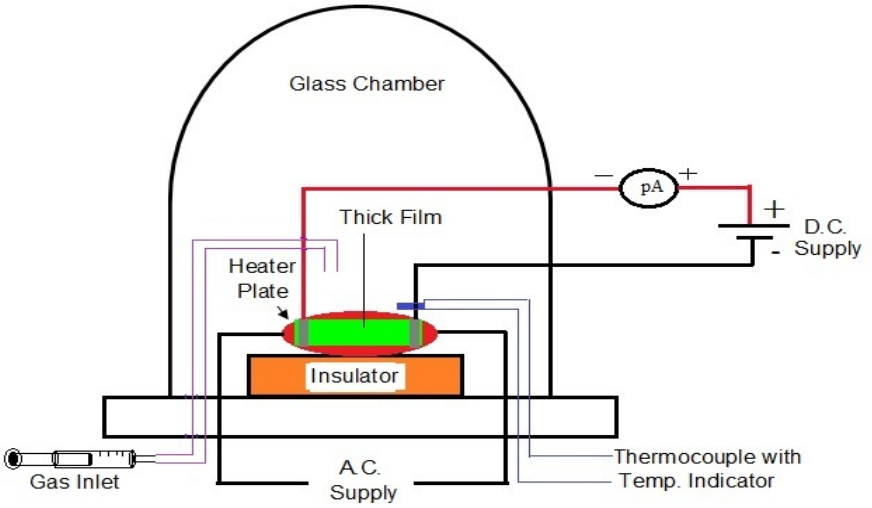

Fig. 1. Block diagram of gas sensing unit

operating temperatures. The current passing through the heating element was monitored using a relay operated with an electronic circuit with adjustable ON-OFF time intervals. A Cr-Al thermocouple was used to sense the operating temperature of the sensor. The output of the thermocouple was connected to a digital temperature indicator. A gas inlet valve was fitted at one of the ports of the base plate. The required gas concentration inside the static system was achieved by injecting a known volume of a test gas using a gas-injecting syringe. Aluminium electrodes were used to provide a proper ohmic contact. A constant DC voltage was applied to the sensor, and a digital Pico ammeter measured the current. The air was allowed to pass into the glass chamber after every gas exposure cycle.

3 Characterizations

3.1 Physical Characterization

3.1.1 X-Ray Diffraction

The crystalline structure of the films was analyzed with X-ray diffractogram in the 20-80^{O}(2θ) range using Cukα radiation. Figure 2, shows the XRD pattern of undoped ZnO and CuO-doped ZnO composite material with different doping concentrations. The observed diffraction peaks correspond to the hexagonal wurtzite structure of ZnO (JCPDS 76-0704) and monoclinic phase of CuO(JCPDS 22-1107) and thus confirming polycrystalline nature. The higher peak intensities of an XRD pattern are due to the better crystallinity. There are no prominent peaks of CuO are observed in the XRD pattern of 1 and 3 wt.% CuO doped ZnO, due to the smaller wt %.of CuO-in comparison with ZnO. The XRD pattern of 5,7, and 9 wt. % CuO-doping, presents traces of CuO as a secondary phase (insoluble ZnO).These peaks are related to complex reactions involving the production of Cu → Cu_2O → CuO during calcinations in air.The average crystallite size was calculated from XRD pattern using following Debye Scherer's formula [27].

$$D = \frac{0.9\lambda}{\beta \cos\theta} \tag{1}$$

Where D is Average crystallite size, β is Broadening of the diffraction line measured at half-maximum intensity (FWHM), λ is-Wavelength of the X- ray radiation and θ is Bragg's angle.

It has been also observed that in all cases, undoped- ZnO and CuO- doped ZnO phase has preferred orientation in (101) planes are of maximum intensity. The peak intensity of planes (101) was decreased with increase in dopant concentration. The crystallite size calculated by Debye Scherer's of pure ZnO was in the range of in 27 -36nm while for the doped Zno was in the range of 13-35nm. It has been observed that the increased dopant concentration decreases crystallite size. Slightly broadening of diffraction lines may be attributed to small crystalline effects or chemical heterogeneity of the samples [28].

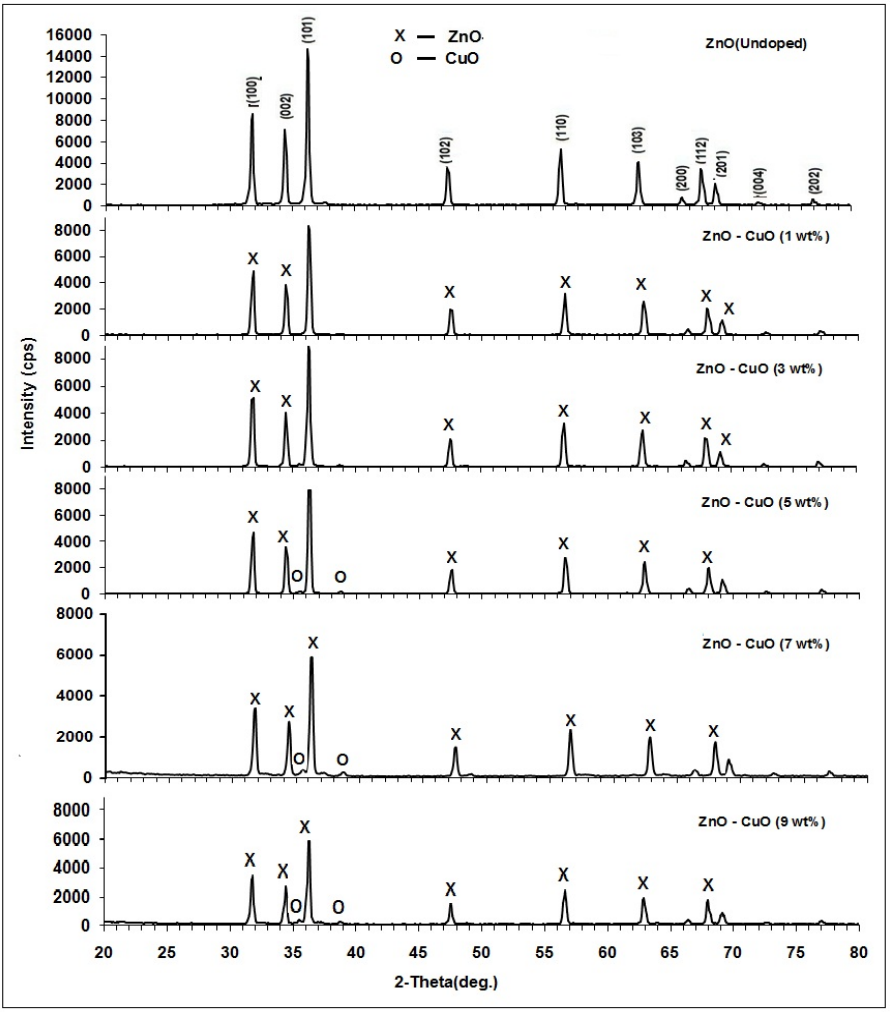

Fig. 2. XRD patterns of undoped-ZnO and CuO- doped ZnO

3.1.2 Microstructural Analysis

It is well known that gas-sensing properties of metal oxide thick films strongly depend on its morphological features. A high surface area facilitates the chemisorption process by increasing the adsorption and desorption rates [29, 30].The surface morphology and chemical composition of the films were analyzed using a scanning electron microscope [SEM model JEOL 6300 (LA) Germany] coupled with an energy dispersive spectrometer (EDS JEOL,JED-2300, Germany).

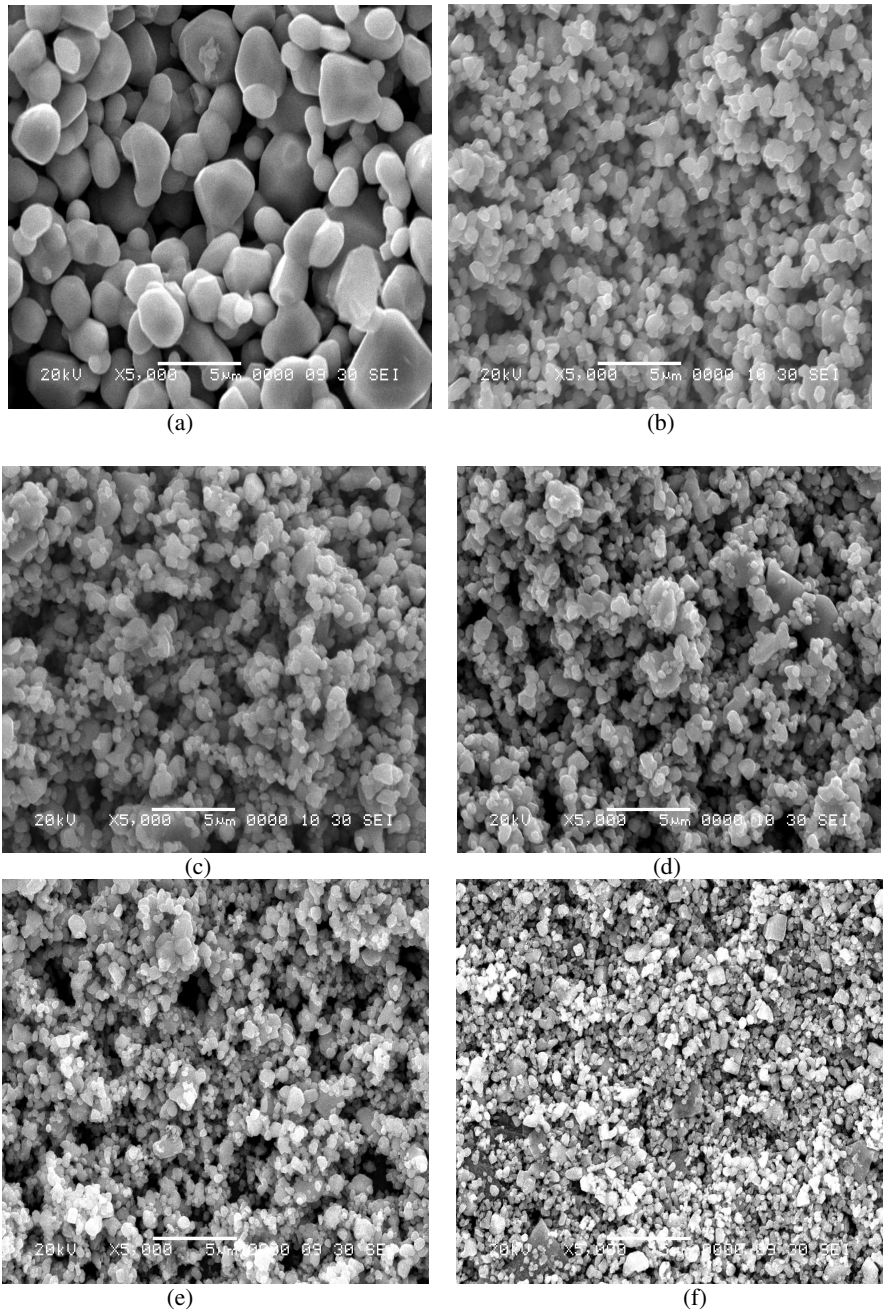

Fig. 3. SEM images of (a)undoped-ZnO and (b)1wt.% (c)3wt.% (d)5w.% (e)7wt.% (f)9wt.% CuO-doped ZnO thick films

Figure 3(a-f), shows the surface morphology of thick films of undoped- ZnO and CuO- doped ZnO with different wt. %. Figure 3(a), shows the micrograph of undoped- ZnO thick film. It showed that the micrograph is nearly uniform with negligible open porosity. Figure 3(d), shows the micrograph of 5 wt. % CuO- doped ZnO thick film which was most sensitive. It showed that the grain size decreases giving large effective surface area. The larger surface area gives more response to react with the target gas. The film seems to be highly porous for oxygen adsorption.

3.1.3 Elemental Analysis

The chemical composition of the films were analyzed using a scanning electron microscope [SEM model JEOL 6300 (LA) Germany] coupled with an energy dispersive spectrometer (EDS JEOL, JED-2300, Germany).

Table 1. Quantative elemental analysis of undoped and doped- ZnO films

Elements	At. Wt. % CuO doped ZnO films				
	1wt. %	**3wt. %**	**5wt. %**	**7wt. %**	**9wt. %**
O	41.46	41.87	39.91	43.90	43.91
Zn	58.27	57.81	59.92	55.72	0.38
Cu	0.27	0.33	0.17	0.38	55.72
Total	100	100	100	100	100

Table1, shows the composition of the film doped at different level. The wt.% of Zn and O in each sample was observed to be non-stoichiometric. The all ZnO film was observed to be oxygen deficient. But the film 5wt.% of CuO-doped is more than others. The deficiency or excess of the constituent material results in distorted band structure with corresponding decrease in conductivity.

The higher response may be attributed to the optimum porosity and largest effective surface area available to react with the gas. The response could also be attributed to the adsorption–desorption type of sensing mechanism. The amount of oxygen adsorbed on the surface would depend on the number of Cu misfits to adsorb the oxygen, which in turn would oxidize the exposed gas. When the optimum amount of Cu (5 wt. %) is incorporated on the surface of the ZnO film, Cu species would be distributed uniformly throughout the surface of the film. As a result the initial resistance of the film is high, this amount would also be sufficient to promote the catalytic reaction effectively, and the overall change in the resistance on the exposure of LPG leading to an increase in the gas response. When the amount of Cu on the surface of the film is less than the optimum, the surface dispersion may be poor and the sensitivity of the film was observed to be decreased since the amount may not be sufficient to promote the reaction more effectively. On the other hand, as the amount of Cu on the surface is more than the optimum, the Cu atoms would distribute more densely. Therefore, the initial resistance of the film would decrease and the overall change in the resistance on the exposure of LPG would be smaller leading to lower response.

3.2 *Electrical Characterizations*

3.2.1 Electrical Conductivity of the Films

The conductivity of thick films at constant temperature was calculated using the relation,

$$\sigma = \frac{l}{(R \times b \times t)}\left(\frac{1}{(\Omega - m)}\right) \quad (2)$$

Where R = Resistance of thick film sample at constant temperature
t = thickness of the thick film sample
l = length of the thick film sample
b = breadth of the thick film sample.

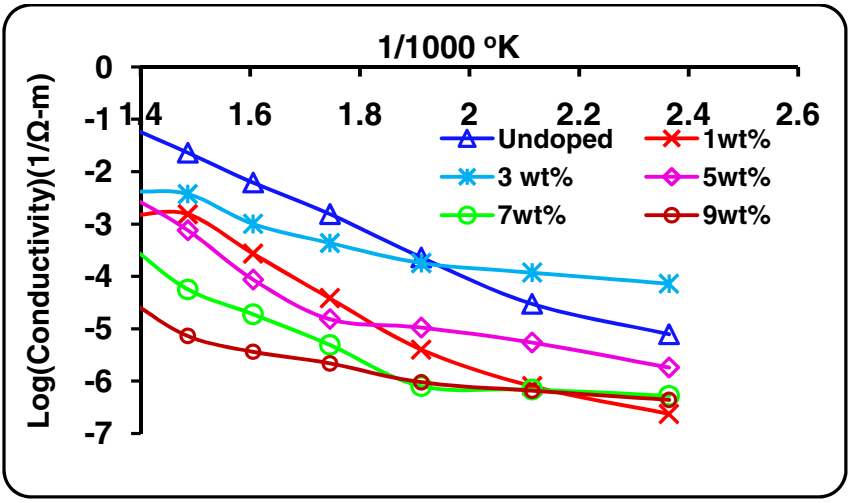

Fig. 4. Variation in conductivity of undoped and CuO- doped ZnO films

Figure4, shows the temperature dependence of conductivity of pure and CuO-doped ZnO thick films in air ambience. It is clear from graph that the conductivity of these films goes on increasing with increase in temperature, indicating negative temperature coefficient (NTC) of resistance and semi-conducting nature of the film. It was observed that the conductivity of doped films decreased with the increased dopant concentration.

The electrical conductivity of ZnO films was decreased by doping CuO indicating the acceptor like behaviour of the CuO dopant. The four co-ordinated Zn^{2+}, Cu^{1+} and Cu^{2+} cations have ionic radii of 0.06, 0.06 and 0.057nm respectively[31], with stable electronic configuration, Zn^{2+} ($3d^{10}$), Cu^{2+}($3d^{9}$) and Cu^{1}($3d^{10}$). Diffusion at high firing temperature may lead defect reactions in which Cu^{2+} cations substitute Zn^{2+} cations in the wurtzite unit cell of ZnO. The stability

of the coulomb forces of the interactions between the acceptor defect ($Cu^{1+}_{Zn)}$ and intrinsic ZnO donors (Zn_i or V_o) may occur by capture of an electron from the lattice.

West et al.[32]proposed an interesting model of an associate donor-acceptor for Cu_{Zn} where,

$$[Cu^{+}_{Zn}(3d^{10})]^{-} + Zn^{+}_{i}(5s^{1}) \rightarrow \{[Cu^{+}_{Zn}(3d^{10})] - Zn^{+}_{i}(4S^{1})\}^{1\,0} \quad (3)$$

or Kroger and Vink notations,

$$Cu^{\bullet}_{zn} + Zn^{\bullet}_{i} \rightarrow [Cu_{Zn} - Zn_i]^{\times} \quad (4)$$

According to the model, the creation of complex defects $[Cu_{Zn}$- $Zn_i]^x$into ZnO/ZnO interface may contribute to increased barrier height. The presence of these types of defects compensates for n-type conductivity of ZnO, giving rise to n-type ZnO: Cu. Thus, the conductivity decreases [33].

The decrease in film conductivity can also be explained in terms of electron trapping by Cu 3d hole states of Cu^{2+}. The copper dopant after oxygen annealing in the ZnO films can be in the form of copper oxide. CuO (Cu^{2+}) has a Cu 3*d*9 4*s*0 O 2*p*6 valence band configuration (neglecting hybridization) and may therefore trap electrons with the Cu 3*d* hole state. So conductivity is decreased [34].

4 Gas Sensing Performances

4.1 Gas Sensing Performance of Pure and CuO-Doped ZnO Thick Film

The gas sensing performance of undoped and CuO doped ZnO thick films were studied by using static measurement system. The conductance of thick film was measured by means of conventional circuitry by applying constant voltage and measuring the current by Pico ammeter as a function of temperature in air as well as in H_2S, LPG, CO_2, NH_3, Cl_2, and Ethanol gas atmosphere. The operating temperature was varied at the interval of 50^oC. From the measured conductance in air as well as in gas atmosphere, the gas response was determined at particular operating temperature using the equation.

The gas response(s) is defined as the ratio of change in conductance in gas to air to the original conductance in air given by Eq.5[35]

$$S = \frac{(G_g - G_a)}{G_a} \quad (5)$$

Where G_a= conductance of sensor in air.
G_g = Conductance of sensor in gas.

The undoped ZnO thick film fired at 550^oC was observed to be poor response for sensing of pollutant and toxic gases. It has been observed that the increased sensitive and selective of gas sensor is by using dopants[36].

The gas sensing properties of the thick films was initiated to study the gas sensing performance of doped films, the optimization of operating temperature of film sample for test gases. The repeatability and reproducibility study of the films. On the basis of measured data, the gas response, selectivity, response and recovery time of thick film for a fixed gas concentration and also the response of thick film with variation of gas concentration at optimum operating temperature is studied.

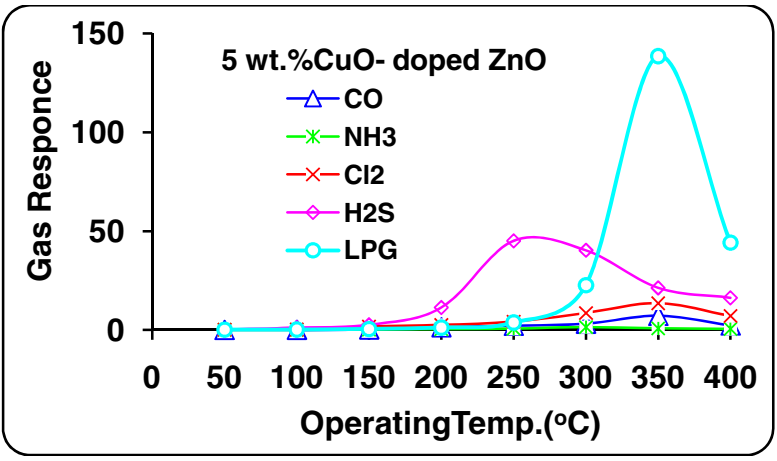

Fig. 5 (a). Variation in gas response of 5wt. % CuO- doped ZnO thick film

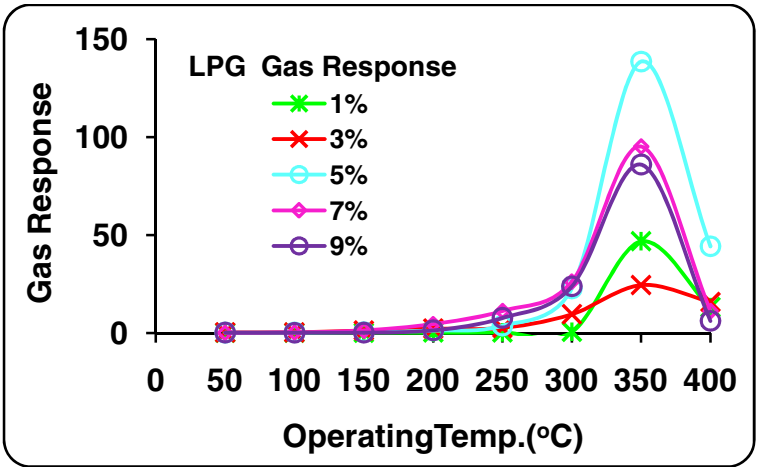

Fig. 5(b). Variation in LPG response of CuO- doped ZnO thick films

Figure 5(a), shows, the variation in gas response of CO_2, Cl_2, NH_3, H_2S and LPG as a function of operating temperature ranging from 50°C to 400°C for the film doped with 5wt. % CuO. It shows that the film gives the highest response to LPG gas (1000) at 350°C. It has been observed from the graph that the gas response increases with increase in temperature up to 350°C and then decreases with further increase in operating temperature. Thus, it is clear from the graph that the 350°C is the optimum temperature for film composition to LPG.

Figure 5(b), shows the variation in LPG response of CuO- doped ZnO thick films at different doping concentrations (1,3,5, 7, and 9 wt. %) as the function of operating temperatures ranging from 50°C to 400°C.It has been observer from graph that as compared to other doped ZnO films the 5wt. % doped film gives the highest response to LPG. It has been observed from the graph that as level of additives (CuO) increases, the response increases up-to the optimum level of additives and after optimum level it decrease.

4.2 Effect of Gas Concentrations on Gas Response of ZnO Thick Film

Figure 6, shows the variation in LPG response with gas concentrations of 5wt. % CuO- doped ZnO thick film. The gas response was observed to have increased continuously by increasing the gas concentration up to 1000 ppm. The response was highest for 1000 ppm of LPG. If the gas concentration increases above 1000 ppm, the monolayer of the gas molecules formed on the surface could cover the whole surface of the film. The excess gas molecules would remain idle and would not reach the surface active sites of the film. So, the response at higher concentrations of the gas was not expected to increase in large extent. Thus, the active region of the film is up to 1000 ppm.

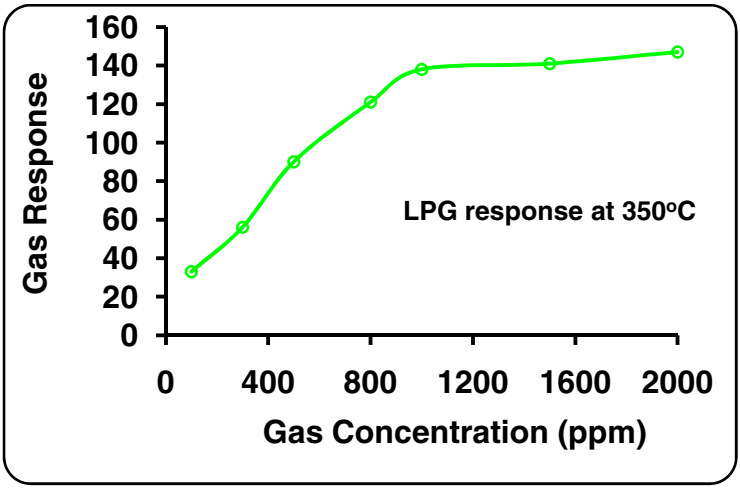

Fig. 6. Variation in LPG response with gas concentration for of 5 wt. % CuO- doped ZnO thick film

4.3 Selectivity of 5 wt. % CuO-Doped ZnO Film

The selectivity is the ability of a sensor to respond to certain gas in the presence of other gases. Percentage selectivity [37, 38] of one gas over the other is defined as the ratio of maximum response of other gas to the maximum response to the target gas at the optimum temperature.

$$\% \text{ Selectivity} = \frac{S_{gas}}{S_{target\ gas}} \times 100 \tag{6}$$

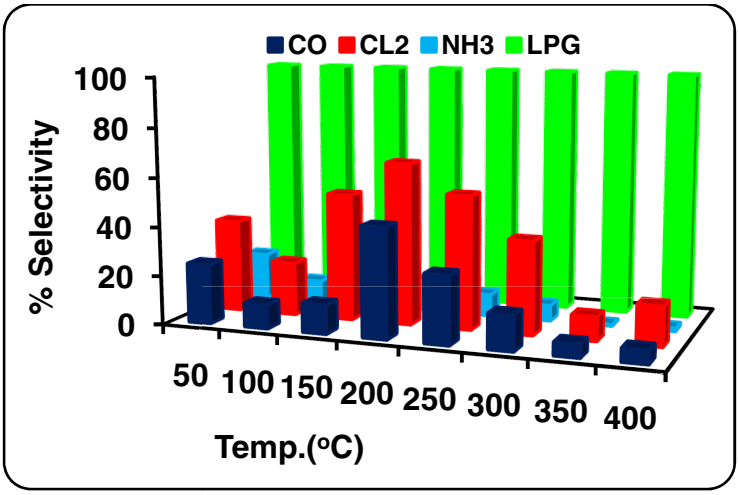

Fig. 7. Selectivity of 5wt.% CuO- doped ZnO film for different gases against LPG (1000 ppm)

The bar diagram in Figure6, indicating percentage selectivity of 5wt. % CuO-doped ZnO film and operated at different temperatures for various gases. It is clear from the bar diagram that the doped thick film is more selective to LPG against the other gases viz: CO, NH_3, and H_2.

4.4 Response and Recovery Time of 5wt. % CuO- Doped ZnO Thick Film

The response/recovery time is an important parameter, used for characterizing sensors. It is defined as the time required to reach 90 % of the final change in voltage or resistance, when the gas is turned on or off, respectively.

Figure 8, depicts the variation of LPG response of 5 wt. % CuO- doped ZnO film with time at 350°C. It has been observed that the film shows quick response (~10 s) to LPG(1000 ppm) while the recovery time was fast (~16s). The quick

response may be due to faster oxidation of gas. Its high volatility explains its quick response and fast recovery to its initial chemical status. The negligible quantity of the surface reaction products and their high volatility explain the quick response to LPG and fast recovery to its initial chemical status.

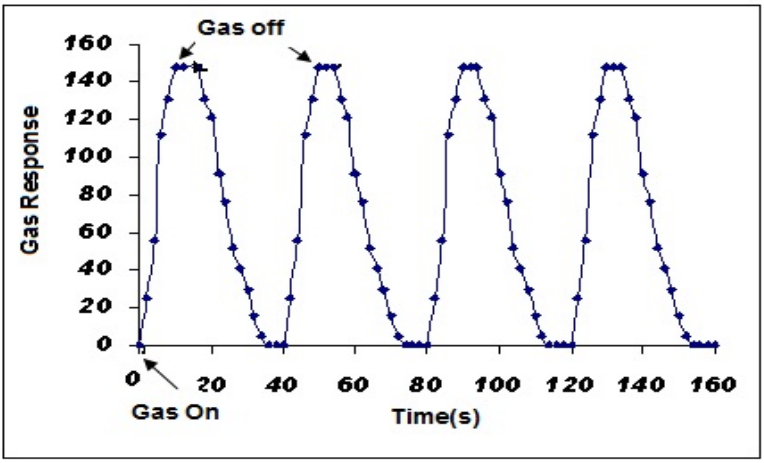

Fig. 8. Response transients of the 5wt. % CuO- doped ZnO film

5 Discussion

5.1 Gas Sensing Mechanism of CuO- Doped ZnO Thick Film Resistor as a LPG Sensor

Gas sensing mechanism of semiconducting gas sensors is based on the surface reaction of semiconducting oxide. In air, molecular oxygen is chemisorbed in the form of O_2^- ,O^-, O^{2-} depending on the operating temperature and depletes electron from the surface of these materials leading to reduction of conductivity [39].

The LPG is a complex gas and the main constituents of LPG are methane, propane, butane, etc.[40,41], where propane and butane dominate. Upon exposure, LPG molecules oxidized with the adsorbed oxygen ions. For butane and propane, the activation of the C–H bond is the first crucial step in all oxidation reactions [42, 43] once the first bond is broken, sequential reactions to carbon dioxide and water are relatively facile. The proposed reactions in the present study are given as:

$$C_4H_{10} + 13O^- \rightarrow 4CO_2 + 5H_2O + 13e^- \quad (7)$$

$$C_4H_{10} + \frac{13}{2}O_2^- \rightarrow 4CO_2 + 5H_2O + \frac{13}{2}e^- \quad (8)$$

$$C_4H_{10} + 13O^{2-} \rightarrow 4CO_2 + 5H_2O + 26e^- \quad (9)$$

$$C_3H_8 + 10O^- \rightarrow 3CO_2 + 4H_2O + 10e^- \quad (10)$$

$$C_3H_8 + 5O^- \rightarrow 3CO_2 + 4H_2O + 10e^- \quad (11)$$

$$C_3H_8 + 10O^{2-} \rightarrow 3CO_2 + 4H_2O + 20e^- \quad (12)$$

This results in evolving oxygen as electrically neutral atoms trapping behind the negative charges (electrons). Upon exposure, the energy released in decomposition of LPG molecules, would be sufficient for trapped electrons to jump into the conduction band of activated ZnO, resulting in increase in the conductivity of the film.

It is evident from the proposed reaction schemes that a large number of electrons are released upon LPG exposure to ZnO surface particularly in the presence of O_2^- which is responsible for increase in conductivity. Thus, generated electrons contribute to a sudden increase in conductance of the thick film.

6 Conclusion

Pure ZnO thick films does not response to LPG but CuO(5 wt. %) doped ZnO thick film showed highest response to LPG at 350°C.The sensitivity increases in proportion to the test gas concentration. The film has good selectivity to LPG against NH_3, Ethanol, and CO at 350°C. The thick film showed very rapid response and quick recovery to LPG. Over long exposure to LPG, it was observed that the thick film exhibited a good stability and repeatability as gas sensor with consistent pattern and response magnitude.

Acknowledgements. The author (MKD) is grateful to B.C.U.D., University of Pune, and U.G.C., New Delhi, for financial assistance to this project and very much thankful to The Sarchitnis, M.V.Prasraksamaj, Nashik, Principal, K.T.H.M.College, Nashik and Principal, Arts, Science and Commerce, College, Ozar (Mig) and Nandgaon for his keen interest in this project.

References

[1] Olvera, M.L., Asomoza, R.: SnO_2 and SnO_2, Pt thin films used as gas sensors. Sens. Actuators B: Chem. 45, 49–53 (1997)

[2] Sharma, R.K., Bhatnagar, M.C., Sharma, G.L.: Mechanism of highly sensitive and fast response Cr doped TiO_2 oxygen gas sensor. Sens. Actuators B: Chem. 45, 209–215 (1997)

[3] Chiorino, F.A., Tsubota, S., Haruta, M.: An IR study of CO-sensing mechanism on Au/ZnO, Sens. Actuators B: Chem. 24-25, 540–543 (1995)

[4] Bott, B., Jones, T.A., Mann, B.: The detection and measurement of CO using ZnO single crystals. Sensors and Actuators 5, 65–73 (1984)
[5] Jones, A., Jones, T.A., Mann, B., Firth, J.G.: The effect of the physical form of the oxide on the conductivity changes produced by CH_4, CO and H_2O on ZnO. Sensors and Actuators 5, 65–73 (1984)
[6] Lee, E.T., Jang, G.E., Kim, C.K., Yoon, D.H.: Fabrication and gas sensing properties of Fe2O3 thin film prepared by plasma enhanced chemical vapor deposition (PECVD). Sens. Actuators B: Chem. 77, 221–227 (2001)
[7] Kim, S.R., Hong, H.K., Kwon, C.H., Yun, D.H., Lee, K., Sung, Y.K.: Ozone sensing properties of In_2O_3-based semiconductor thick films. Sens. Actuators B: Chem. 66, 59–62 (2000)
[8] Bene, R., Perczel, I.V., Meyer, F.A., Fleisher, M.M.H.: Chemical reactions in the detection of acetone and NO by a CeO_2 thin film. Sens. Actuators B: Chem. 71, 36–41 (2000)
[9] Bender, F., Kim, C., Mlsna, T., Vetelino, J.F.: Characterzation of a WO_3 thin film chlorine sensor. Sens. Actuators B: Chem. 77, 281–286 (2001)
[10] Lin, H.M., Tzeng, S., Hsiau, P., Tsai, W.: Electrode effects on gas sensing properties of nanocrystalline zinc oxide. Nanostructure. Mater. 10, 465–477 (1998)
[11] Rao, G., Rao, D.: Gas sensitivity of ZnO based thick film sensor to NH_3 at room temperature. Sens. Actuators B 23, 181–186 (1999)
[12] Rao, B.B.: Zinc oxide ceramic semiconductor gas sensor for ethanol vapours. Mater. Chem. Phy. 64, 62–65 (2000)
[13] Tamaki, J., Maekawa, T., Miura, N., Yamazoe, N.: Cuo–SnO_2 element for highly sensitive and selective detection of H_2S. Sens. Actuators B 9, 197–203 (1992)
[14] Yamazoe, N.: New approaches for improving semiconductor gas sensors. Sens. Actuators B 5, 7–19 (1991)
[15] Dayan, N., Sainkar, S., Karekar, R., Aiyer, R.: Formulation and characterization of ZnO:Sb thick-film gas sensors. Thin Solid Films 325, 254–258 (1998)
[16] Göpel, W., Schierbaum, K.D.: SnO_2 Sensors-Current Status and Future Prospects. Sens. Actuat. B 26, 1–12 (1995)
[17] Bagnall, D.M., Chen, Y.F., Zhu, Z., Yao, T., Koyama, S., Shen, M.Y., Goto, T.: Appl. Phys. Lett. 70, 2230 (1997)
[18] Batzill, M., Diebold, U.: Phys. Chem. Chem. Phys. 9, 2307 (2007)
[19] Sahay, P.P., Tewari, S., Jha, S., Shamsuddin, M.: Sprayed ZnO thin films for ethanol sensor. J. Mater. Sci. 40, 4791–4793 (2005)
[20] Rao, B.B.: Zinc oxide ceramic semi-conductor gas sensor for ethanol vapours. Mater. Chem. Phys. 64, 62–65 (2000)
[21] Feng, P., Wan, Q., Wang, T.H.: Contact-controlled sensing properties of flowerlike ZnOH.Mexiner, metal oxide sensor. Sensors and Actuators B 33, 198–202 (1996)
[22] Patil, D.R., Patil, L.A., Jain, G.H., Wagh, M.S., Patil, S.A.: Surface activated ZnO thick film resistors for LPG gas sensing. Sensors & Transducers 74, 874–663 (2006)
[23] Batzill, M., Diebold, U.: Phys. Chem. Chem. Phys. 9, 2307–2318 (2007)
[24] Gaikwad, V.B., Deore, M.K., Khanna, P.K., Kajale, D.D., Shinde, S.D., Chavan, D.N., Jain, G.H.: Studies on Gas Sensing Performance of Pure and Nano- Ag Doped ZnO Thick Film Resistors. In: Mukhopadhyay, S.C., Gupta, G.S., Huang, R.Y.-M. (eds.) Recent Advances in Sensing Technology. LNEE, vol. 49, pp. 293–307. Springer, Heidelberg (2009)

[25] Deore, M.K., Gaikwad, V.B., Pawar, N.K., Kajale, D.D., Shinde, S.D., Jain, G.H.: Preparation and study the Electrical, Structural and Gas Sensing Properties of ZnO Thick Film Resistor. Sensor and Transducers Journal 119(8), 160–173 (2010)
[26] Deore, M.K., Gaikwad, V.B., Pawar, N.K., Shinde, S.D., Jain, G.H.: Effect of Ni dopping on gas Gas Sensing Properties of ZnO Thick Film Resistor. Sensor and Transducers Journal 122(11), 143–157 (2010)
[27] Cullity, B. D.: Elements of X-ray diffraction, 2 edn. Addison Wesley (1978)
[28] Roy Morrison, S.: Mechanism of semiconductor gas sensor operation. Sens. Actuators 11, 283–287 (1987)
[29] Kupriyanov, L.Y.: Semiconductor Sens. in Physico-Chemical Studies. Elsevier, Amsterdam (1996)
[30] Puchert, M.K., Hartmann, A., Lamb, R.N.: J. Mater. Res. 11(10), 2463–2469 (1996)
[31] Chiang, Y.M., Birnie, D., Kingery, W.D.: Physical Ceramics: Principle for Ceramics Science and Engineering. MIT Series. John Wiley and Sons. Inc. (1997)
[32] West, C., Robbins, D.J., Dean, P.J., Hays, W.: Physica B+C 116, 492–499 (1983)
[33] Bellini, J.V., Morelli, M.R., Kiminami, G.A.: Journal of Materials science: Materials in Electronics 13, 485–489 (2002)
[34] Puchert, M.K., Hartmann, A., Lamb, R.N.: J. Mater. Res. 11(10), 2463–2469 (1996)
[35] Jain, G.H., Gaikwad, V.B., Patil, L.A.: Studies on gas sensing performance of$(Ba_{0.8}Sr_{0.2})$ $(Sn_{0.8}Ti_{0.2})O_3$ thick film resistors. Sens. Actuators 122, 605–612 (2007)
[36] Yamazoe, N., Kurokawa, Y., Seiyama, T.: Effects of additives on semiconductorgas sensors. Sens. Actuators 4, 283–289 (1983)
[37] Jain, G.H., Patil, L.A., Wagh, M.S., Patil, D.R., Patil, S.A., Amalnerkar, D.P.: Surface modified $BaTiO_3$ thick film resistors as H_2S gas sensors. Sens. Actuators 117, 159–165 (2006)
[38] Patil, D.R., Patil, L.A., Amalnerkar, D.P.: Ethanol gas sensing properties of Al_2O_3-dopped ZnO thick film resistors. Bull. Mater. Sci. 30(6), 553–559 (2007)
[39] Kim, Y.H., Kawamura, H., Nawata, M.: Journal of Materials Science 32(6), 1665–1670 (1997)
[40] Srivastava, A., Rashmi, K.J., Srivastava, A.K., Lakshmikumar, S.T.: Study of structural and microstructural properties of SnO_2 powder for LPG and CNG gas sensors. Material Chemistry and Physics 97, 85–90 (2006)
[41] Mishra, V.N., Agarwal, R.P.: Sensitivity, response and recovery time of SnO_2 based thick film sensor array for H_2, CO, CH_4, and LPG. Microelectronics Journal 29, 861–874 (1998)
[42] Burch, R., Crittle, D.J., Hayes, M.J.: C–H bond activation in hydrocarbon oxidation on heterogeneous catalysts. Catalysis Today 47, 2299 (1999)
[43] Kohl, D.: Surface processes in the detection of reducing gases with SnO_2-based Devices. Sensors and Actuators B 18, 71–113 (1989)

Synthesis of Cu-Doped SnO_2 Thin Films by Spray Pyrolysis for Gas Sensor Application

G.E. Patil[1], D.D. Kajale[1], S.D. Shinde[1], V.G. Wagh[2], V.B. Gaikwad[1], and G.H. Jain[1,*]

[1] Materials Research Lab., KTHM College, Nashik 422 002, India
[2] V.N. Naik Arts, Commerce and Science College, Nashik 422 002, India
gotanjain@rediffmail.com

Abstract. Pure and Cu-doped SnO_2 thin films have been prepared by a simple and inexpensive technique namely spray pyrolysis. Films were prepared from an aqueous solution of tin chloride pentahydrate on ultrasonically cleaned glass substrates at temperature of 350°C. Doping is achieved by adding a small amount of copper chloride to the starting solution which is mixed thoroughly prior to spraying. The goal of this work is to study the influence of doping (Cu) with different wt% (1-5 wt% Cu) on the structural, optical, and gas sensing properties of Cu-doped SnO_2 films. The crystallite size with pyramid type nanostructures was found to increase with increasing Cu content in the SnO_2 films. Gas sensing characteristics were investigated for different target gases such as carbon monoxide, ammonia, H_2S and ethanol. The films with 3% Cu content showed high response and excellent selectivity for H_2S compared to other gases at room temperature. These results have been correlated with the surface chemistry and crystallite size effect resulting from Cu doping in the SnO_2 thin films.

Keywords: Cu-doped SnO_2 thin films, spray pyrolysis, gas sensor.

1 Introduction

The growing demand of fast accurate and low cost air quality analysis techniques for environmental monitoring, automotive applications, air conditioning in airplanes, spacecrafts and houses, sensors networks, in domestic and industrial environments, is tailoring the research toward new materials and techniques to solve the problems related to the commercial sensors. Metal-oxide semiconducting layers are the most promising conductometric chemical sensors among solid-state devices, due to their low dimension, price and power consumption.

The sensing properties of the material are based on reactions between semiconductor and gases in the atmosphere. These reactions produce changes in the semiconductor electrical properties. There are many possible kinds of reactions, in semiconductor gas sensors the more common reaction that leads to changes in the conductivity is the adsorption of gases on its surface.

* Corresponding author.

S.C. Mukhopadhyay et al. (Eds.): Advancement in Sensing Technology, SSMI 1, pp. 299–311.
springerlink.com

Metal oxide, especially tin oxide (SnO_2) is one of the most significant and well-known n-type nanomaterial semiconductors with large band gap (3.6 eV) [1]. Owing to their distinctive electronic, physical, optical, chemical, and catalytic properties, it has been extensively employed in flat-panel displays, transparent conducting electrodes, solar cells, sensors, and rechargeable Li-ion batteries [2].

The attention in tin oxide is revealed due to the naturally stoichiometric apparent conducting oxide containing high transparency in visible region and high reflectivity in infra-red region. Further, the electrical resistance of SnO_2 is small compared to other semiconductor nanomaterials [3]. It is normally monitored that increasing the surface/bulk or surface to volume ratio by decreasing the particle size of SnO_2 aggregated nanoparticles is vital for attaining high sensitivity in sensors [4]. One of the most significant routes to modify the features of the nanostructured materials is the introduced of doped materials in the parent system. It has been revealed that several dopants (Cr, Cd, Mn, Al, Mg, Cu, Fe) can escort to enhance the surface area of SnO_2 nanostructure. These dopants alleviated the surface and promote the decrease in size as well as change the shapes. To acquire the maximum benefit of the properties of metal ions doped SnO_2 nanomaterial, a number of techniques have been introduced for the efficient preparation of metal doped SnO_2 nanostructured materials. Few of them are mechanical alloying [5], condensed vapor deposition [6], sol–gel method [7], solvo-thermal method [8], spray pyrolysis [9], gel-combustion method [10], and physical vapor deposition [11].

In this work, Cu-doped SnO_2 pyramids were prepared by spray pyrolysis technique. This method has several advantages such as very easy to handle and cost effective as well accurate control the stoichiometry. Optical, electrical and chemical properties of tin-oxide are of huge significance from the scientific aspect. Doped nanostructured oxide has a large band-gap which in its non-stoichiometric form exhibits non-insulating nature. Non-stoichiometry, mainly oxygen vacancies, makes it conducting nature. The formation energy of oxygen vacancies and tin interstitials in SnO_2 is very low and thus these defects form eagerly, resulting in the experimental elevated conductivity of doped SnO_2 [12]. Electrical and gas sensing properties can further be enhanced by extrinsic dopants. There are many reports in the literature that highlight the gas sensing properties of pure and doped tin oxide ceramics using nanostructured SnO_2 [13]. For the reason of environmental aspect using reliable chemical routes, various efforts [14, 15] have been made to establish simple, easy, economical, consistent, and reliable sensors have been organized. Semiconductor doped nanostructure sensors, due to their many meticulous advantages over the conventional chemical methods, such as high response, low charge, and portability, are widely employed for the detection of contaminated or toxic pollutants, chemical process control, and monitoring of air/water contamination in the environment [16].

For semiconductor nanostructured materials, doping is an excellent application to confirm the optical and electrical properties, improve the progress of frequent electronic and optoelectronic devices. Cu-doped SnO_2 nanostructured material permit very sensitive transduction of the surface interactions into modify in the

chemical properties. The significant prospect is to appearance a variety of structural morphologies offers different vision of modification of the toxic chemical sensing possessions. Cu-doped SnO_2 nanostructure (pyramids) has been used to fabricate a simple and efficient chemical sensor and assessed the chemical sensing performance considering H_2S at room conditions.

2 Experimental Procedure for Preparation of Pure and Cu-Doped SnO_2 Thin Films

The spray pyrolysis method consists of spraying a solution on a heated substrate. The apparatus needed to carry out the chemical spray process, a device to atomize the spray solution and a substrate heater. The various process parameters in the film deposition are listed in Table 1.

The spray solution was prepared by taking ($SnCl_4.2H_2O$) as a source material. As ($SnCl_4.2H_2O$) dissolves in distilled water at room temperature, water was taken as solvent. For Cu-doping $CuCl_2$ is used as a source material. The home made spray unit used in the present experiments operates via a partial vacuum path at the mouth of the spray nozzle; the concentration of the solution prepared by the solvent should be such that the nozzle could at least draw it. A typical value of solution concentration is 0.075 M was used in this work. A considerable amount 20 ml of spray solution was taken in the precursor solution reservoir fitted up with the spray gun. An ultrasonically cleaned substrate was put on the susceptor of the heater. The distance between the tip of the nozzle and surface of the substrate was 28 cm. Before supplying the compressed air the heater was kept for sometime so that the substrate and the reactor wall attain the requisite temperature. The substrate temperature, was to be kept at a level slightly higher than the required substrate temperature because at the onset of spraying a slight fall of temperature would take place. The temperature of a substrate was controlled by controlling the heater power. When compressed air is passed through pressure regulator at a constant pressure, fine droplets were produced and sprayed where film was deposited on the heated substrate. Thus the SnO_2 films with different Cu content of: 0 wt %, 1wt %, 3wt % and 5wt % were obtained and were refered to as C1, C2, C3 and C4, respectively.

Table 1. Process parameters for the spray deposition of the films

Spray parameters	**Optimum value**
Nozzle	Glass
Nozzle–substrate distance	28cm
$SnCl_4.5H_2O$ and $CuCl_2$ solution concentration	0.075 M
Solvent	Distilled water
Solution flow rate	5 ml/min
Carrier gas	Compressed air
Substrate temperature	300 °C

X-ray diffraction was taken for pure and Cu-doped samples by an X-ray diffractometer (Bruker D 8 Advance, France). The diffraction scan was recorded within 20 to 80° using CuK_α radiation (k = 0.154056 nm). The crystallite size in the direction perpendicular to the substrate was determined from the peak width of the corresponding reflection by the Scherrer's formula. The surface morphology of the films was analyzed using high resolution field emission scanning electron microscopy (FESEM Hitachi-S-3400, Japan) with FESEM. An optical absorption study was carried out using UV-visible spectrophotometer (SHIMADZU UV-2450, Japan) in the wavelength range 300-700 nm. The gas sensing properties of thin films were studied using static gas sensing unit.

3 Results and Discussion

3.1 X-Ray Diffraction Analysis

Fig. 1 shows the X-ray diffraction patterns for pure and Cu-doped SnO_2 thin films. The characteristic peaks were identified from JCPDS cards and these are at 2θ = 26.6, 33.8, 37.9, 51.8, 54.7, 61.9 and 65.9° having (h k l) values of (110), (101), (200), (211), (220), (310) and (301), respectively. In both cases the tetragonal rutile-type SnO_2 phase is observed and the peak positions of the films are found to be in good agreement with JCPD data card 41-1445. It can be noted that no shift in the SnO_2 peak positions or any Cu phase (i.e., Cu oxides or ternary compounds with Cu) is observed due to the doping procedure. This observation leads to the conclusion that doping of SnO_2 with CuO has occurred.

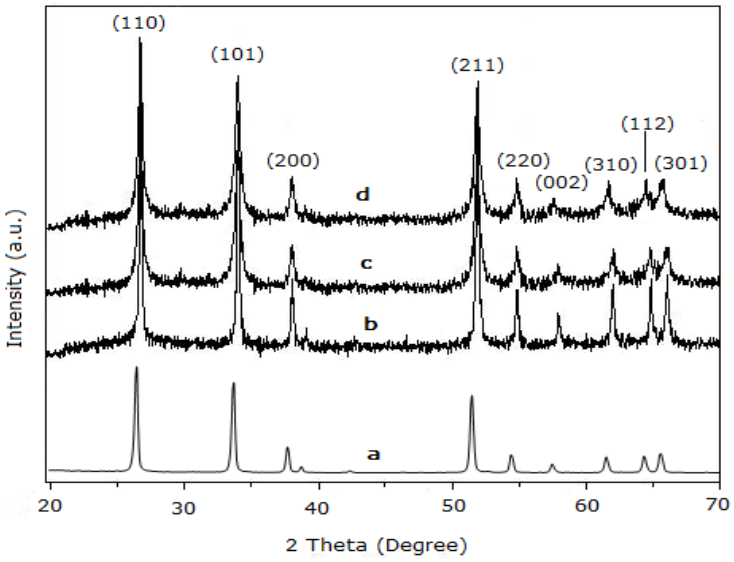

Fig. 1. XRD spectra for pure and Cu-doped SnO_2 thin films; (a) Pure, (b) 1 wt% Cu-doped, (c) 3 wt% Cu-doped and (d) 5 wt% Cu-doped SnO_2 thin films

There are two possible doping mechanisms of SnO_2 with CuO: a) substitutional and b) interstitial.

a) In the case of substitutional doping some Sn^{4+} ions are replaced with Cu^{2+} (Equation 1) based on the comparable radii of Sn^{4+} and Cu^{2+} (0.69 Å and 0.73 Å, respectively). The oxygen-ion vacancies ($V_o^{\cdot}$) created by substitutional doping of Sn^{4+} with Cu^{2+} are charge compensated by electron holes (h), if the sample is annealed in air. The electron holes compensate the Cu_{Sn}'' point defect charge and are required for the site balance (Equation 2).

b) In the second case Cu^{2+} ions can occupy the interstitial sites of the SnO_2 lattice (Equation 3), inducing an increase of the concentration of tin ion vacancies (V_{Sn}'''').

Substitutional:

$$CuO \xrightarrow{SnO_2} Cu_{Sn}'' + O^x_o + V_o^{\cdot\cdot} \quad (1)$$

$$CuO + 1/2\ O_2 \xrightarrow{SnO_2} Cu_{Sn}'' + 2O^x_o + 2h \quad (2)$$

Interstitial:

$$2CuO \xrightarrow{SnO_2} Cu_i'' + 2O^x_o + V_{Sn}'''' \quad (3)$$

The average crystallite size for pure and Cu-doped samples was calculated using the Debye- Scherrer formula [17]:

$$D = 0.9\lambda / \beta\cos\theta \quad (4)$$

Where D is the crystallite size (nm), λ the radiation wavelength (0.15406 nm for CuKα), β the full-width at half maximum height FWHM of the X-ray line (radians), and θ is the diffraction peak angle. The average grain size D is found to be in the range 25-80 nm for pure SnO_2 and Cu-doped SnO_2. The XRD results confirm that the grains have a nanometer size.

The crystallite sizes at different crystallographic planes and d spacing for different doping concentration of Cu is tabulated in Table 8.2. A negligible change of d-spacing is observed for Cu-doping. The grain sizes of the crystallites are changed unsystematically depending on both crystallographic axes and doping concentrations as well. Since grain size involved so many physical parameters such as, substrate temperature, spray rate, growth atmosphere, concentration of the solutions etc., therefore, it is difficult to maintain uniform crystallite size; henceforth unsystematic variation of the grain size is not unrealistic.

3.2 Surface Morphology of the Films by FESEM

Fig. 2 shows the FESEM images of SnO_2 and Cu-doped samples. It is observed that the surface of the pure SnO_2 thin film is inhomogeneous and the dense nanoparticles formed surface. With the Cu-doping, particle shape alters to pyramid

type nanostructures. Also from Fig. 2(b-d) the grain size increase as Cu-doping % increases. This suggests that Cu acts as an agent to alters the morphology and to improve the grain size.

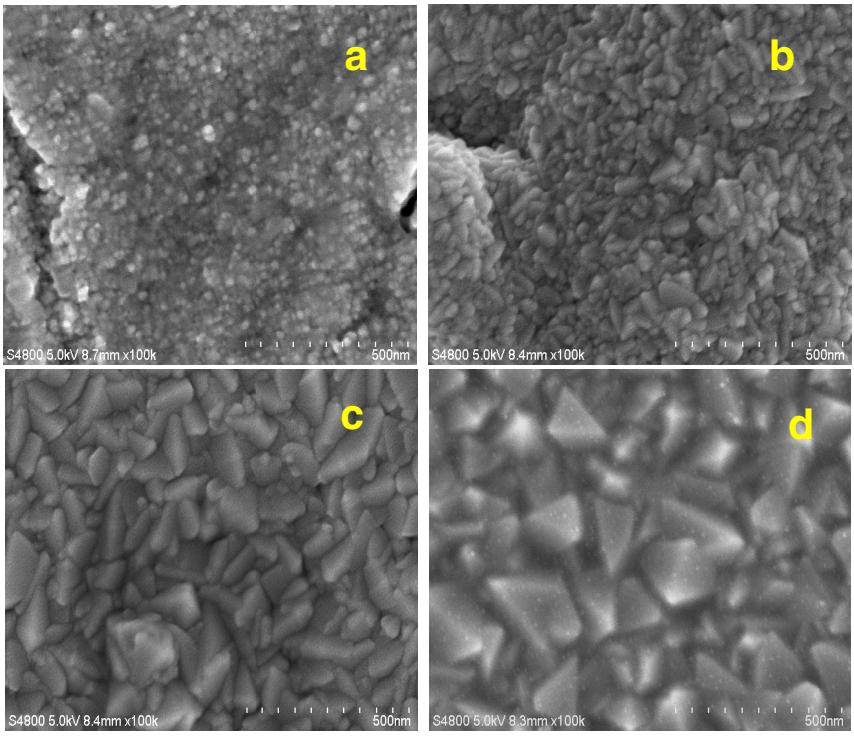

Fig. 2. FESEM images of (a) pure SnO_2, (b) 1% Cu-doped SnO_2, (c) 3% Cu-doped SnO_2 and (d) 5% Cu-doped SnO_2 thin films

3.3 Optical Properties of Pure and Cu-Doped SnO_2 Thin Films by UV-Vis Spectroscopy

The optical absorption spectra of pure and Cu doped SnO_2 thin films were accomplished by using UV–visible spectrophotometer in the visible range (200–700 nm). UV-visible absorption is a method in which the outer electrons of atoms or molecules absorb radiant energy and undergo transitions to high energy levels. In this method, the spectrum obtained due to optical absorption can be analyzed to obtain the energy band gap of the semiconductor. The optical absorption measurement was carried out at ambient conditions.

The optical band gap energy (Eg) of the film can be obtained by plotting $(\alpha h\nu)^2$ verses hν and extrapolating the straight line portion of this plot to the energy axis. The linear dependence of $(\alpha h\nu)^2$ to hν indicates that the films are direct transition type semiconductors. The photon energy at the point where $(\alpha h\nu)^2$ is zero is band gap energy, Eg. Table 2 gives the optical band gap values obtained by extrapolating the linear portion of the plots of $(\alpha h\nu)^2$ versus (hν) to $\alpha = 0$. These plots are given in Fig. 3 for the films deposited at different % of Cu content. It is seen that the increase in the optical band gap of the films with the increasing Cu (but 5% of Cu has band gap lower than other samples). This means that doping of Cu in SnO_2 thin films also affects the band gap of the film. Fig. 4 shows the effect of Cu doping on band gap of SnO_2 thin films.

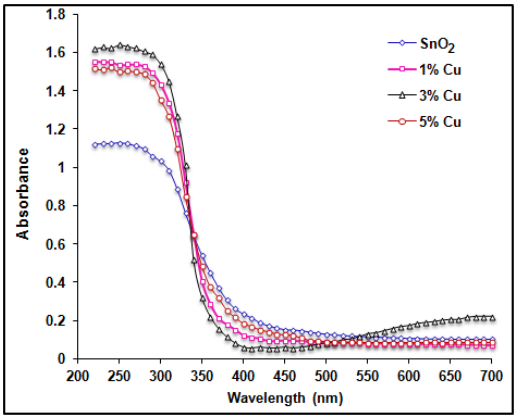

Fig. 3. UV-visible absorption spectra recorded for pure SnO_2 film and Cu-doped SnO_2 thin films

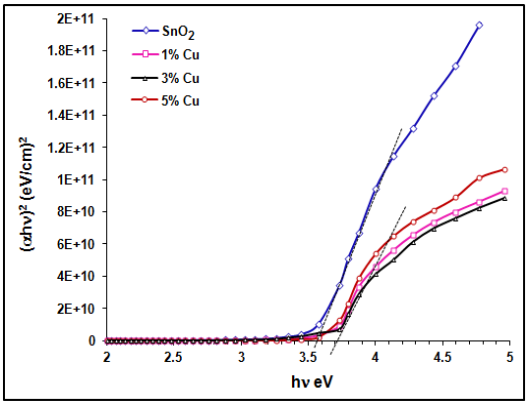

Fig. 4. Plot of the $(\alpha h\nu)^2$ vs photon energy (hν) for pure and Cu-doped SnO_2 thin films

Table 2. Band gap energy, crystallite size and nature of grains of pure and Cu-doped SnO_2 thin films

Doping concentration of Cu (wt.%)	Crystallite Size from XRD	Nature of grains from FESEM	Band gap (eV)
Pure SnO2	30.66	Spherical	3.56
1% Cu	42.22	Pyramidal	3.68
3% Cu	52.66	Pyramidal	3.70
5% Cu	85.44	Pyramidal	3.64

3.4 Gas Sensing Performance of Pure and Cu-Doped SnO_2 Thin Films

The gas response studies of pure and Cu doped SnO_2 thin films at different operating temperatures and gas concentrations were performed in the gas sensing assembly described elsewhere [18].

3.4.1 Variation of H_2S Gas Response of Pure and Cu-Doped SnO_2 with Operating Temperature

The thin film oxide semiconductor gas sensors are well explored. The gas response depends on factors, such as morphology, dopants and their concentrations, thickness of film and operating temperatures. We tested response for pure SnO_2

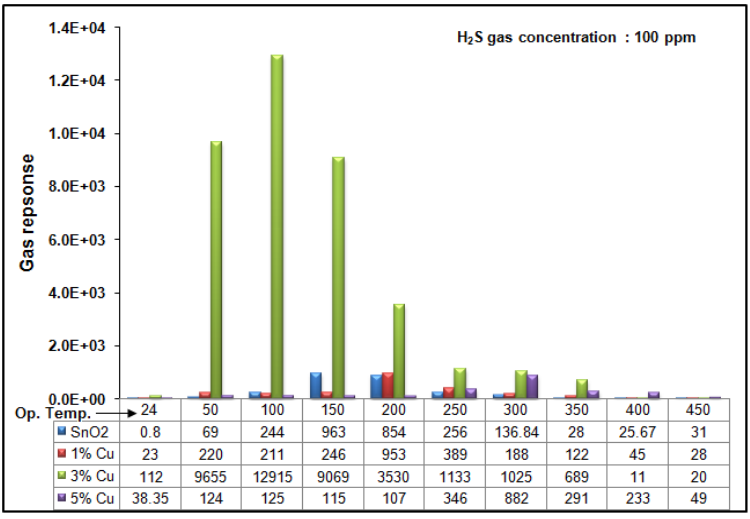

Fig. 5. Gas response at different operating temperature for the pure SnO_2 film and Cu-doped SnO_2 thin films

and modified by Cu doped SnO_2 towards various reducing and oxidizing gases, such as H_2S, H_2, CO_2, CO, liquid petroleum gas, Cl_2, NH_3 and ethanol vapors. The pure and Cu-doped thin films have been tested for 100 ppm H_2S gas concentration at temperatures between 50 and 450 ^oC. We observed that low response for the above gas by pure SnO_2 films than Cu doped SnO_2 films. However, for Cu doped SnO_2 thin films with 3 wt% concentrations remarkable response towards H_2S gas is observed at 100 ^oC operating temperature. It is found that in comparison to 1 wt% and 5 wt%, the 3 wt % Cu shows highest response towards H_2S gas and hence we carried out the detailed gas response studies of this composition.

The gas sensing mechanism of Cu-doped SnO_2 to H_2S could be divided into two parts, as (1), (2), (3) and (4) follows:

$$½\, O_2 + e^- \rightarrow O^- \tag{5}$$

$$3O^- + H_2S \rightarrow H_2O + SO_2 + 3e^- \tag{6}$$

$$CuO + H_2S \rightarrow CuS + H_2O \tag{7}$$

$$2CuS + 3O_2 \rightarrow 2CuO + 2SO_2 \tag{8}$$

Equation (5) and (6) reveal the normal sensing mechanism of the SnO_2 material caused by the supply and consumption of adsorbed oxygen. (7) and (8) show the p–n junction theory which has been commonly accepted [19]. In the later mechanism, the p-type semiconducting CuO transforms to metallic CuS when the H_2S gas is introduced and the p–n junction between CuO and SnO_2 is disrupted. Therefore, the resistance of the thin films is dramatically decreased by the H_2S gas due to the disappearance of the CuO semiconducting region and p–n junction. If the reducing atmosphere is removed, the CuO region recurs and the p–n junction is reconstructed again, leading to the recovery of the film resistance [20-22]. Thus in summary, when a Cu-doped SnO_2 thin film responses to H_2S gas, both mechanisms make contributions to the whole response and reactions of (5), (6), (7) and (8) are in progress simultaneously.

Another contribution to high response could be due to doping of Cu^{2+} ions onto Sn^{4+} site leads to the creation of oxygen vacancies to retain charge neutrality. Increased oxygen deficiency has been earlier reported to enhance the gas sensing properties of nanostructured SnO_2 [23].

3.4.2 Selectivity of Pure and Cu-Doped SnO_2 Thin Films for Various Gases

The gas response of 3wt % Cu doped thin film towards 100 ppm of various test gases (except H_2S) at 100 ^oC is shown in Fig. 6. From Fig. 5 and 6 significantly high response (S = 12915) reveals its remarkable selectivity towards hydrogen sulfide gas at low operating temperature of 100 ^oC. In comparison, it shows marginal response towards LPG (S = 6.96) and other test gases.

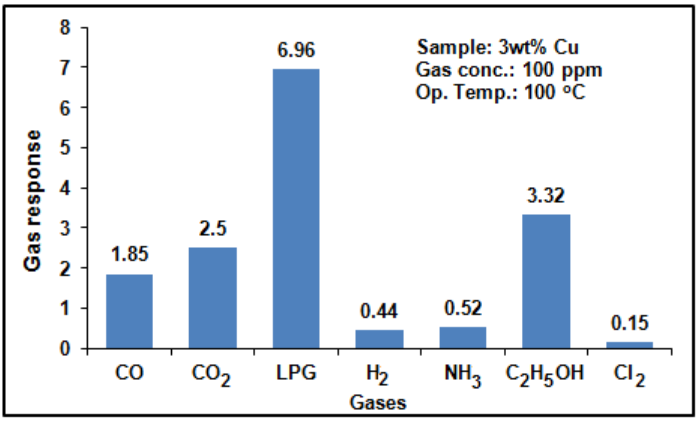

Fig. 6. Selectivity to various gases

3.4.3 Gas Response at Room Temperature

The histogram (Fig. 7) clearly displays the dependence of response on Cu content at room temperature. It is observed that 3 wt% Cu doped SnO_2 film show their highest response at room temperature.

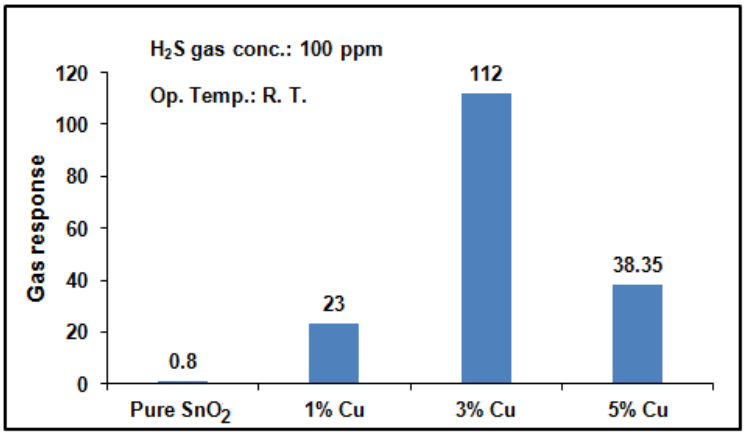

Fig. 7. Gas response at room temperature for the pure SnO_2 film and Cu-doped SnO_2 thin films

3.4.4 Variation in Gas Response with H_2S Gas Concentration

Fig. 8 represents the sensing characteristics of the 3 wt% Cu-doped SnO_2 thin film as a function of H_2S gas concentration at operating temperature 100 °C. It is observed in the figure that the response increases gradually in the lower concentration region of H_2S, while it increases rapidly at higher concentrations of H_2S. For

a low concentration (1-50 ppm), there is a smaller surface coverage of H_2S molecules on the film and hence the surface reaction proceeds slowly. On an increase in gas concentration to 70 ppm, the surface reaction increases due to a larger surface coverage of H_2S molecules, resulting in a rapid increase in response. On a further increase in gas concentration to 100 ppm, the surface coverage of H_2S molecules on the film begins to attain saturation which leads to a gradual increase in response.

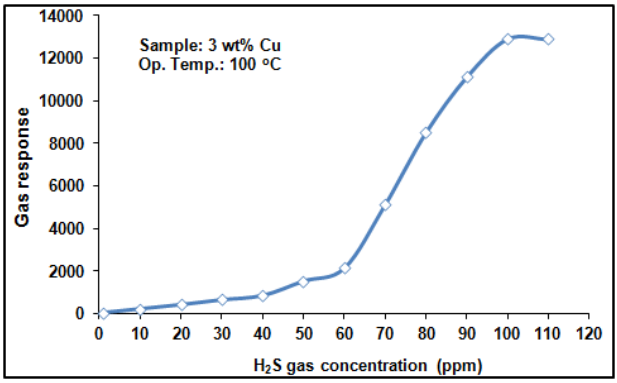

Fig. 8. Sensing characteristics of the 3 wt% Cu-doped SnO_2 thin film as a function of H_2S gas concentration

3.4.5 Response and Recovery Time

The response and recovery time of 3 wt% Cu doped SnO_2 thin film for 100 ppm of H_2S at 100 °C is shown in Fig. 9. It is observed that thin film sensor attains maximum response to H_2S gas within 24 s and recovery is achieved within 30 s. It is indicating its potential as a sensor material for the commercial application.

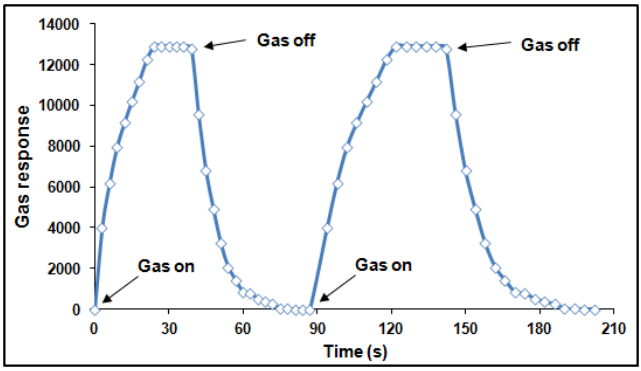

Fig. 9. Response and recovery time of 3 wt% Cu doped SnO_2 thin film for 100 ppm of H_2S at 100 °C

4 Conclusions

i) The uniform thin films of pure and Cu-doped SnO_2 were deposited on glass substrate by spray pyrolysis technique.
ii) Thin films were characterized by using XRD, FESEM and UV-visible spectroscopy techniques.
iii) Tetragonal rutile-type SnO_2 phases are observed in XRD spectra of all samples and the peak positions of the films are found to be in good agreement with standard JCPD data.
iv) The average crystallite size increases as Cu doping % increases.
v) FESEM image of pure SnO_2 thin film showed the dense nano-particles formed on the surface while with the Cu-doping, particle shape alters to pyramid-type nanostructures.
vi) The band gap energy values obtained for Cu doped thin films are higher than pure SnO_2 thin film.
vii) The 3 wt% Cu doped SnO_2 thin film exhibits highest response and selectivity towards H_2S gas at operating temperature 100 ^oC and also sharp response and fast recovery time.
viii) Thus, it can be assumed that the pyramid type Cu-doped SnO_2 thin films deposited using surfactant have a potential to become a good H_2S gas sensing material.

Acknowledgements. Authors are thankful to Principal, KTHM College, Nashik and Principal, Arts, Commerce & Science College, Nandgaon for providing laboratory facilities. One of the authors (G. E. Patil) is highly grateful to Department of Science and Technology, New Delhi for its support through INSPIRE fellowship.

References

1. Li, P.G., Guo, X., Wang, X.F., Tang, W.H.: Facile route to straight SnO_2 nanowires and their optical properties. Journal of Alloys and Compounds 479, 74–77 (2009)
2. Wang, C., Li, J., Zhang, Y., Wei, Y., Liu, J.: The influence of phosphate on crystal grain growth of nanosized SnO_2. Journal of Alloys and Compounds 493, 64–69 (2010)
3. Batzill, M., Diebold, U.: The surface and materials science of tin oxide. Prog. Surf. Sci. 79, 47–154 (2005)
4. Fang, L.M., Zu, X.T., Li, Z.J., Zhu, S., Liu, C.M., Zhou, W.L., Wang, L.M.: Synthesis and characteristics of Fe^{3+}-doped SnO_2 nanoparticles via sol–gel-calcination or sol–gel-hydrothermal route. Journal of Alloys and Compounds 454, 261–267 (2008)
5. Azam, A., Ahmed Arham, S., Shahnawaze Ansari, M., Muhamed Shafeeq, M., Naqvi Arham, S.: Study of electrical properties of nickel doped SnO_2 ceramic nanoparticles. Journal of Alloys and Compounds 506, 237–242 (2010)
6. Huh, M., Kim, S., Ahn, J., Park, J., Kim, B.: Oxidation of nanophase tin particles. Nanostructured Materials 11, 211–220
7. Zhang, J., Gao, L.: Synthesis and characterization of nanocrystalline tin oxide by sol-gel method. Journal of Solid State Chemistry 177(4-5), 1425–1430 (2004)

8. Liu, Y., Yang, F., Yang, X.: Size-controlled synthesis and characterization of quantum-size SnO_2 nanocrystallites by a solvothermal route Colloids and Surfaces A. Physicochemical and Engineering Aspects 312, 219–225 (2008)
9. Shinde, S.D., Patil, G.E., Kajale, D.D., Gaikwad, V.B., Jain, G.H.: Synthesis of ZnO nanorods by spray pyrolysis for H_2S gas sensor. Journal of Alloys and Compounds 528, 109–114 (2012)
10. Fraigi, L., Lamas, D.G., Reca, N.E.W.: Novel method to prepare nanocrystalline SnO_2 powders by a gel-combustion process. Nanostructured Materials 11, 311–318 (1999)
11. Davazoglou, D.: Optical properties of SnO_2 thin films grown by atmospheric pressure chemical vapour deposition oxiding $SnCl_4$. Thin Solid Films 302, 204–213 (1997)
12. Zhang, H., Hu, C., He, X., Hong, L., Du, G., Zhang, Y.: Pt support of multidimensional active sites and radial channels formed by SnO_2 flower-like crystals for methanol and ethanol oxidation. Journal of Power Sources 196, 4499–4505 (2011)
13. Tan, E.T.H., Ho, G.W., Wong, A.S.W., Kawi, S., Wee, A.T.S.: Gas sensing properties of tin oxide nanostructures synthesized via a solid-state reaction method. Nanotechnology 19, 255706 (2008)
14. Yang, M., Wang, D.J., Peng, L., Zhao, Q.D., Lin, Y.H., Wei, X.: Surface photocurrent gas sensor with properties dependent on $Ru(dcbpy)_2(NCS)_2$-sensitized ZnO nanoparticles. Sensors and Actuators B 117(1), 80–85 (2006)
15. Jain, G.H., Patil, L.A., Gaikwad, V.B.: Studies on gas sensing performance of $(Ba_{0.8}Sr_{0.2})(Sn_{0.8}Ti_{0.2})O_3$ thick film resistors. Sensors and Actuators B 122(2), 605–612 (2007)
16. Patil, G.E., Kajale, D.D., Gaikwad, V.B., Jain, G.H.: Nanocrystalline tin oxide thin film as a low level H_2S gas sensor. International Journal of Nanoscience 10(4), 1–5 (2011)
17. Culity, B.D.: Elements of X-ray Diffraction, p. 262. Addision–Wesley Publishing Co., Inc. (1667)
18. Jain, G.H., Patil Ganesh, E., Kajale, D.D., Gaikwad, V.B.: Cr_2O_3-doped BaTiO3 as an Ammonia Gas Sensor. In: Mukhopadhyay, S.C., Lay-Ekuakille, A., Fuchs, A. (eds.) New Developments and Applications in Sensing Technology. LNEE, vol. 83, pp. 157–167. Springer, Heidelberg (2011)
19. Patil Ganesh, E., Jain, G.H.: Nanocrystalline $CdSnO_3$ thin film as highly sensitive ethanol sensor. In: Proceedings of 5th International Conference on Sensing Technology ICST 2011, pp. 249–252 (2012), doi:978-1-4577-0168-9
20. Pawar, N.K., Kajale, D.D., Patil, G.E., Shinde, S.D., Gaikwad, V.B., Jain, G.H.: Gas Sensing Characteristics of Pure and ZnO-modified Fe_2O_3 Thick Films. In: Mukhopadhyay, S.C., Lay-Ekuakille, A., Fuchs, A. (eds.) New Developments and Applications in Sensing Technology. LNEE, vol. 83, pp. 123–132. Springer, Heidelberg (2011)
21. Choudhary, V.A., Mulla, I.S., Vijaymohan, K.: Comparative studies of doped and surface modified tin oxide towards hydrogen sensing: synergistic effects of Pd and Ru. Sensors and Actuators B 50, 45–51 (1998)
22. Kong, X., Li, Y.: High sensitivity of CuO modified SnO_2 nanoribbons to H2S at room temperature. Sensors and Actuators B 105, 449–453 (2005)
23. Wang, B., Zhu, L.F., Yang, Y.H., Xu, N.S., Yang, G.W.: Fabrication of a SnO_2 nanowire gas sensor and sensor performance for hydrogen. J. Phys. Chem. C 112, 6643–6647 (2008)

Nanocystalline In_2O_3 Thick Film Sensor

D.N. Chavan[1], R.H. Bari[2], G.E. Patil[3], D.D. Kajale[3], V.B. Gaikwad[3], D.V. Ahire[3], and G.H. Jain[3,*]

[1] Department of Chemistry, Arts, Commerce and Science College, Lasalgaon 422 306 India
[2] Department of Physics, GMD Arts, KRN Commerce and MD Science College, Jamner 424 206 India
[3] Materials Research Lab., KTHM College, Nashik 422 002 India
gotanjain@rediffmail.com

Abstract. The nanocrystalline powder of In_2O_3 with cubic structure prepared by a simple hydrothermal decomposition route. The structure and crystal phase of the powder was characterized by X-ray diffraction (XRD), microstructure by Transmission Electron Microscopy (TEM). The results indicated that the indium oxide was cubic with range size 28.5- 65.8 nm. Gas sensing properties of the nanocrystalline In_2O_3 thick film sensor were tested for various gases in air at static state. The tested results showed that the sensor based on In_2O_3 nanocrystals exhibited high response towards H_2S gas (40 ppm) at an operating temperature 100°C. The selectivity of the sensor elements for H_2S gas against different gases was studied. The results on response and recovery time were also discussed.

Keywords: nanocrystalline In_2O_3, H_2S gas sensor, sensitivity, selectivity, response time.

1 Introduction

Gas sensors have been used for industrial process control, for the detection of toxic environmental pollutants, in human health and for the prevention of hazardous gas leaks, which comes from the manufacturing processes [1]. Though there are different types of gas sensors that have been used to detect several inflammable, toxic and odorless gases, the gas sensors based on metal-oxide are playing an important role in the detection of toxic pollutants and the control of industrial processes. Hydrogen sulphide (H_2S) detection is nowadays a very important target for different processes such as coal or natural gas manufacturing. This gas can be very dangerous for human bodies when its concentration is greater than 250 ppm. Monitoring and controlling of H_2S is crucial in laboratories and industrial areas. Semiconductor gas sensors in the forms of thin or thick films, based on metal oxides like SnO_2, WO_3 and p-n heterojunctions have been widely reported in the literature for H_2S detection [2].

* Corresponding author.

S.C. Mukhopadhyay et al. (Eds.): Advancement in Sensing Technology, SSMI 1, pp. 313–322.
springerlink.com

Gas sensitivity, selectivity and durability are the most important sensor properties. It is well known that sensing mechanism is based on the surface reaction of the particles with the exposed gas (adsorption and desorption of the test gas). As the adsorption is a surface effect, one of the most important factors to change the sensitivity of the sensor material is the surface area. It is well known that the response of gas sensors can also be improved by decreasing the particle size of the gas-sensing material in order to increase the number of oxygen sites on its surface. So the nano sized materials are desirable to enhance the gas sensing properties of semiconducting oxides. In nano sized materials a large fraction of the atoms are present at the surface and consequently, the surface properties turn out to be foremost. The use of nano sized materials in gas sensors is arousing attention in the scientific community [3].

Indium oxide (In_2O_3) belongs to the class of wide-band gap metal oxides, which has a wide application in preparing transparent conducting windows [4].moreover, this oxide has been shown to be a promising material for semiconductor gas sensors [18,19]. As a gas sensing material, In_2O_3 has been extensively applied to detect O_3, NO_2 and CO etc. [5].

Nanocrystalline metal oxide powders for sensing applications have been produced by several methods, such as sol–gel processing [6], thermal hydrolysis [7], spray pyrolysis [8], micro emulsion [9], reactive magnetron sputtering [10], metallorganic laser photolysis [12] etc. However, the operation of conventional semiconductor gas sensors at elevated temperatures, typically in the range of 200-500^oC is their major drawback. Obviously it would be desirable for many applications if the sensor could operate at low temperatures. However, the working temperature for these H_2S gas sensors is 200^oC and 400^oC [13]. Also, they have along response time and recovery time for a few ppm H_2S gas. About the detection of dilute H_2S less than 1 ppm thin film or thick film sensors using CuO- SnO_2 [14] have been reported to show excellent performance. Indium oxide offers a new advantage in designing metal oxide-based gas sensors, linked with an essential difference in electro- physical and chemical properties between SnO_2 and In_2O_3. As a gas- sensing material, In_2O_3 has been extensively applied to detect O_3, NO_2 and CO. However, there are no reports on H_2S sensing properties of bulk In_2O_3 ceramics.

In this paper, nanocrystalline In_2O_3 powder prepared by simple hydrothermal decomposition route has been reported. Their gas-sensing property to hydrogen sulphide gas (H_2S) was investigated. The results revealed that nanocrystalline In_2O_3 sensor was very promising for detection of low concentration up to 40 ppm of H_2S gas at an operating temperature 100^oC.

2 Experimental

2.1 Synthesis of In_2O_3 Nanocrystalline Powder

All the chemicals used in this work are of AR grade (>99.9%). In a typical experiment of synthesis, the precursor $In(OH)_3$ was prepared by a simple hydrothermal

reaction. $InCl_3.4H_2O$ was used as a raw material without further purification. In a typical synthesis, 0.305g $InCl_3.4H_2O$ was dissolved in 25 ml distilled water, aqueous solution of indium chloride salt stirred for 30 min. and added into a Teflon- lined stainless autoclave of 40 ml capacity with proper quantity of sodium dodecyl benzene sulfonate as a surfactant. The autoclave was sealed and heated at 250°C for 24 h, then allowed to cool to room temperature. The precipitate was poured out into a tube for centrifugal separating, washing, drying at 105°C for 3 h. In_2O_3 nanocrystals can be gained by sintering the dried precursor at 600°C for 1 h. According to the reaction, In_2O_3 nanocrystals may be formed as follows:

$$In^{3+} + OH^- \rightarrow In(OH)_3 \quad (1)$$

$$2\ In(OH)_3 \rightarrow In_2O_3 + 3H_2O\ (g) \quad (2)$$

2.2 Preparation of Nanocrystalline In_2O_3 Sensor (Thick Films)

The thixotropic paste was formulated by mixing the sintered nanocrystalline In_2O_3 powder with a solution of ethyl cellulose (a temporary binder) in a mixture of organic solvents such as butyl cellulose, butyl carbital acetate and terpineol etc. The weight ratio of the inorganic to organic part was kept at 75:25 in formulating the paste. This paste was screen printed on a glass substrate in a desired pattern [15-16]. The sensitivity of the sensors increases with the sensor porosity as well as with thickness of the sensor [17]. The sensor was dried under IR lamp at 80°C for 1 h and fired at 550°C for 30 min. Silver contacts are made for electrical measurements.

2.3 Operating Principle of Gas Sensor

Since long it has been known that adsorption of reducing gas molecules results in decrease in electrical resistance of oxide material [18]. The In_2O_3 materials are characteristically n-type semiconductor due to non-stoichiometry associated with oxygen vacancy and/or metal excess which acts as donor states thus providing conduction electrons. However, the overall surface resistance of such films is generally influenced by chemisorptions (chemical adsorption) of oxygen from air on the surface and at the grain boundaries. The chemisorbed oxygen traps conduction electrons and remains as negatively charged species (O_2^-, O^- or O^{2-} depending on temperature.) on the surface [19]. The process results in an increase of surface resistance. In presence of reducing gases the trapped electrons are released due to the reaction between the gas molecules and negatively charged chemisorbed oxygen species resulting in decreasing in resistance of the materials. When the gas is removed from the sensor environment, the resistance again increases and the material recovered to original resistance.

2.4 Thickness Measurements

The thickness of the sensor was measured by using the Taylor-Hobson (Talystep, UK) system and was observed in the range from 40 to 50 μm. The reproducibility of the sensors' thickness was achieved by maintaining the proper rheology and thixotropy of the paste.

2.5 Details of Gas Sensing Unit

The sensing performance of the sensor was examined using a 'static gas sensing system' [20]. There were electrical feeds through the base plate. The heater was fixed on the base plate to heat the sample under test up to required operating temperatures. The current passing through the heating element was monitored using a relay operated with an electronic circuit with adjustable ON-OFF time intervals. A Cr-Al thermocouple was used to sense the operating temperature of the sensor. The output of the thermocouple was connected to a digital temperature indicator. A gas inlet valve was fitted at one of the ports of the base plate. The required gas concentration inside the static system was achieved by injecting a known volume of a test gas using a gas-injecting syringe. A constant voltage was applied to the sensor, and the current was measured by a digital picoammeter. The air was allowed to pass into the glass chamber after every gas exposure cycle.

3 Characterizations

3.1 Structural Analysis

Fig. 1 depicts that the XRD pattern of sintered nanocrystalline In_2O_3 powder. The structure of sintered nanocrystalline In_2O_3 powder was examined using X-ray diffractogram (XRD) BRUKER D8 EVA model, a= 10.118 with CuKα radiation (wavelength, λ = 1.5418 Á). The XRD pattern confirmed that the sintered nanocrystalline In_2O_3 powder prepared by hydrothermal reaction was cubic structure, all the diffraction peaks indexed according to the (JCPDS Card No. 44–1087, a=10.118 nm), All the observed peaks in figure are matched well with (JCPDS Card No. 44 - 1087) reported data of In_2O_3.

The average grain size was calculated according to Debye- Scherer's equation, it was observed to be 24.5 nm, provided in Eq. (3).

$$D = 0.9\lambda / \beta COS\theta \tag{3}$$

where β is the full width at half-maximum intensity (in radians) of a peak at an angle θ; K is a constant, depending on the line shape profile; λ is the wavelength of the X-ray source.

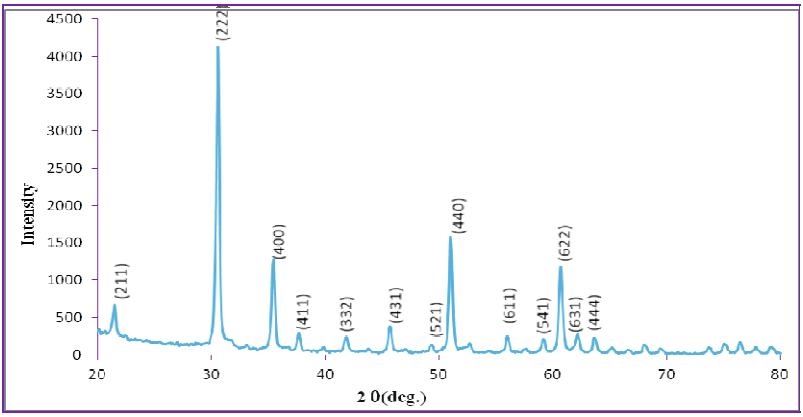

Fig. 1. XRD pattern of nanocrystalline In_2O_3

3.2 Microstructural Analysis

Fig. 2 shows TEM images of nanocrystalline In_2O_3 displayed cubic form morphology, and the average particle size around 43.9 nm was the same as the result from the XRD peak broadening. The crystallographic form of the prepared product of nanocrystalline In_2O_3 by hydrothermal process is rectangular with perfect crystallization and fine dispersion with range size of 28.5- 65.8 nm.

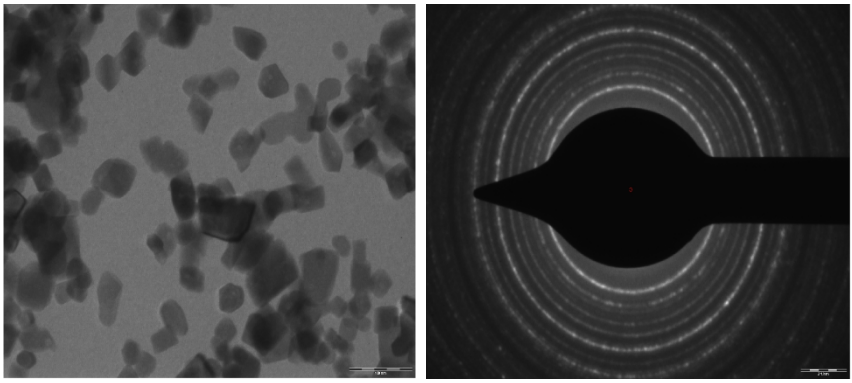

Fig. 2. Transmission electron micrograph of In_2O_3 with corresponding SAED pattern

4 Electrical Properties

4.1 I-V Characteristics

Fig. 3 shows the I-V characteristics of nanocrystalline In_2O_3 sensor at room temperature. I-V Characteristics are observed to be symmetrical in nature, indicating the ohmic nature of silver contact.

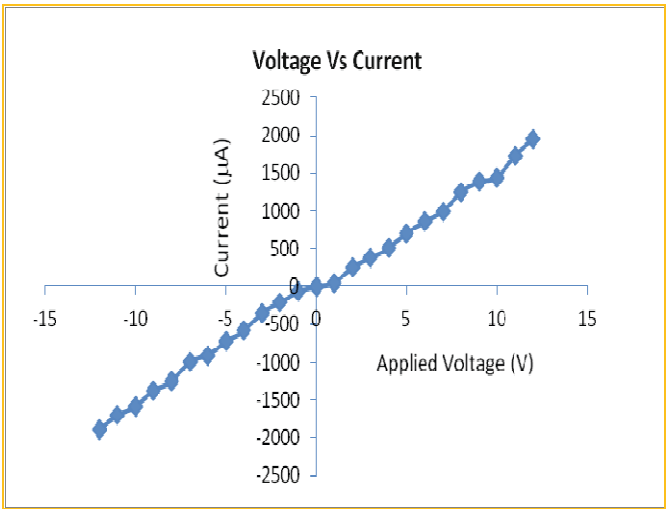

Fig. 3. I-V Characteristics of nanocrystalline In_2O_3 sensor

4.2 Electrical Conductivity

The electrical conductivity of nanocrystalline In_2O_3 sensor in air ambience was studied. The electrical conductivity of this sensor goes on increasing with increase in temperature, indicating negative temperature coefficient (NTC) of resistance. This shows the semi conducting nature of the sensor.

5 Gas Response of Nanocrystalline In_2O_3 Sensor

5.1 Gas Response with Operating Temperature

Gas response of a sensor was defined as the ratio of the change in conductance of a sample on exposure to the test gas to the conductance in air [38].

$$\text{Gas response} = \left| \frac{Gg - Ga}{Ga} \right| = \left| \frac{\triangle G}{Ga} \right| \quad (4)$$

where Ga = conductance of sensor in air, Gg = Conductance of sensor in gas, ΔG = change in conductance.

Fig. 4 shows the variation in the gas response of H_2S (40 ppm) with operating temperatures ranging from 50 °C to 450 °C.

It is noted from the graph that gas response increases with increasing temperature, and attains a maximum at 100°C, and decreases with further increase in operating temperature.

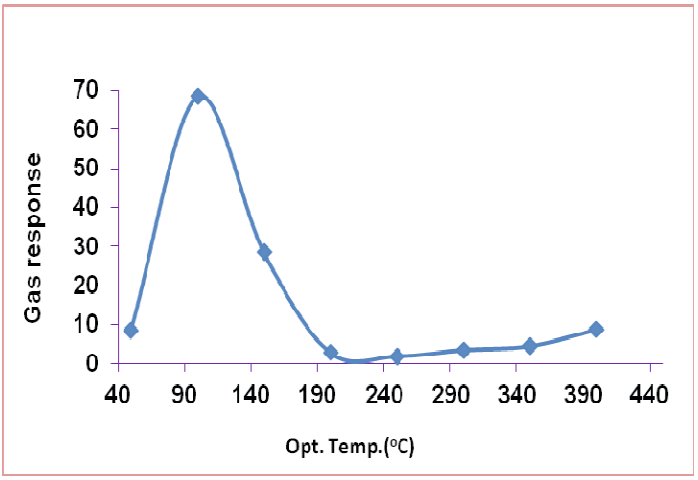

Fig. 4. Variations of H_2S gas response of nanocrystalline In_2O_3 sensor with operating temperature

5.2 Selectivity of Nanocrystalline In_2O_3 Sensor

Selectivity is defined as the ability of sensor to respond to a certain gas in the presence of other gases. Selectivity is another important parameter of a gas sensor .The sensor must have rather high selectivity for its application. Nanocrystalline In_2O_3 sensor is examined for ten different gases as a detecting gas to characterize the gas sensing properties of nanocrystalline In_2O_3, (synthesized by hydrothermal decomposition route) at different operating temperatures and the results are shown in figure 4. The bar diagram indicating selectivity of nanocrystalline In_2O_3 sensor at an operating temperature 100°C to H_2S gas (40 ppm) against the other gases. The sensor is the most selective to H_2S gas against the other gases.

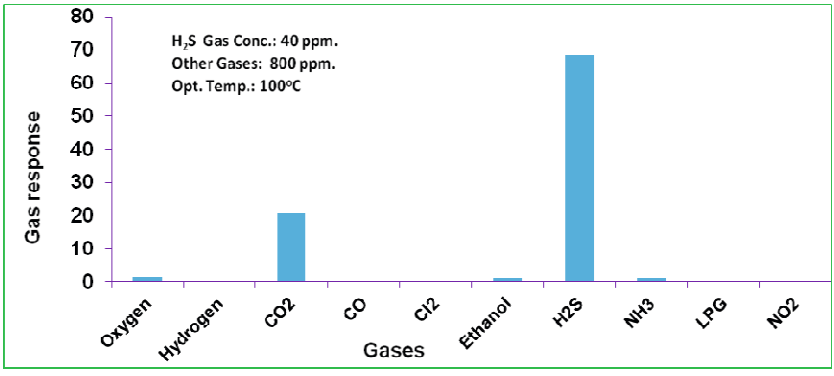

Fig. 5. Selectivity of nanocrystalline In_2O_3 sensor

5.3 Response and Recovery Time

Response and recovery time are the basic parameters of the gas sensors. Which are defined as the time taken for the sensor to attain 90% of maximum change in resistance on exposure to gas is the response time. The time taken by the sensor to get back 90% of the original resistance is the recovery time [21].The 90% response and recovery time were attained within 8s and 15s respectively. The very short response time is the important features of the nanocrystalline In_2O_3 sensor.

6 Discussions

The gas-sensing mechanism 0f In_2O_3-based sensors belong to the surface controlled type, that is, the resistance is controlled by the species and amount of chemisorbed oxygen on the surface. When O_2 is adsorbed on the sensor surface, it traps electrons from the conduction band of the sensor material to produce negatively charged chemisorbed oxygen such as O_2^-, O^- and O^{2-} which create a depletion layer at the surface of the individual particles and inter- granular regions. As a result, the concentration of electrons in the n-type In_2O_3 decreases and hence the electrical conductance of the material decreases. The oxygen adsorbed on the surface directly influences the conductance of the In_2O_3-based sensors. The amount of oxygen adsorbed on sensor surface depends on the operating temperature, particle size and specific surface area of sensor. The state of oxygen on the surface of nanocrystalline In_2O_3 sensor undergoes the following reaction,

$$O_2\ (gas) \leftrightarrow O_2\ (ads) \tag{5}$$

$$O_2^-\ (ads) + e^- \leftrightarrow O^{2-}\ (ads) \tag{6}$$

$$O^{2-}\ (ads) + e^- \leftrightarrow 2O^-\ (ads) \tag{7}$$

$$O^-\ (ads) + e^- \leftrightarrow O^{2-}\ (ads) \tag{8}$$

The oxygen species capture electrons from the material, which results in the concentration changes of holes or electrons in the nanocrystalline In_2O_3 semiconductor. When the nanocrystalline In_2O_3 sensor is exposed to H_2S gas, the reducing gases interacted with the chemisorbed oxygen, which exists in various forms such as $O2^-$, O^- and O^{2-} can takes place in different ways of reaction. The reducing gas readily reacts with the surface chemisorbed oxygen and thereby releasing electrons back to the conduction band and the electrical conductance of the semiconductor increases. It can be expressed in the following reaction

$$H_2S + 3\ O^{2-}\ (ads) \rightarrow H_2O\ (g) + SO_2\ (g) + 6e^- \tag{9}$$

As per earlier reports by many authors, the liberation of water saturates the surface and unless disrobed completely, affects the sensitivity of the surface. And hence, after each measurement, the chamber was flushed thoroughly and the sensor was heated to overcome the effect of humidity.

For the nanocrystalline In_2O_3 sensor, the low response at lower operating temperature can be attributed to the low thermal energy of the gas molecules, which is not enough to react with the surface adsorbed oxygen species. As a result, the reaction rate between them is essentially low and low response is observed [22-23]. On the other hand, the decrease in response after the optimum operating temperature may be due to the difficulty in exothermic gas adsorption at higher temperature [24]. Therefore the maximum gas response can just be observed at the right operating temperature.

7 Conclusions

Nanocrystalline powder of In_2O_3 with n-type semiconducting behavior has been prepared successfully by hydrothermal process. The phase composition analyzed by XRD. The nanocrystalline In_2O_3 was found to be non stoichiometric and oxygen deficient material. It showed negative temperature coefficient in nature. Nanocrystalline In_2O_3 sensor showed excellent response to H_2S gas (40 ppm) at an operating temperature 100^{o}C.The high response at lower operating temperature may be allied to largest lattice distortion, smaller particle size, highest surface activity and presence of grains with the cubic phase which results in stronger interaction between H_2S gas molecules and surface active sites. The quick response of the sensor could be attributed to larger oxygen deficiency on the surface of nano crystalline In_2O_3 sensor.

Acknowledgments. The authors are grateful to U.G.C., New Delhi for granting financial assistance to this project. The author (RHB) is very much thankful to the Principals, Arts, Commerce and Science College, Jamner and A.C.S. College Nandgaon for providing laboratory facilities.

References

1. Morrison, S.R.: Mechanism of semiconductor gas sensor operation. Sensors and Actuators 11, 283–287 (1987)
2. Wang, L., Kumar, R.V.: Thick film miniaturized HCl gas sensor. Sens. Actuators B 98, 196–203 (2004)
3. Jain, G.H., Patil, L.A.: CuO-doped BSST thick film resistors for ppb level H_2S gas sensing at room temperature. Sensors and Actuators B: Chemical 123, 246–253 (2007)
4. Zhao, M., Yang, X.F., He, S., Wang, L.: A rhodamine-based chromogenic and fluorescent chemosensor for copper ion in aqueous media. Sensors and Actuators B 135, 625–631 (2009)
5. Yamaura, H., Tamaki, J., Moriya, K., Miura, N., Yamazoe, N.: Selective CO Detection by Using Indium Oxide-Based Semiconductor Gas Sensor. J. Electrochem. Soc. 143, 136–139 (1996)
6. Shukla, S., Seal, S., Ludwig, L., Parish, C.: Nanocrystalline indium oxide doped tin oxide thin film as low temperature hydrogen sensor. Sens. Actuator B 97, 256–265 (2004)

7. Taurino, A.M., Epifani, M., Toccoli, T., Iannotta, S., Siciliano, P.: Innovative aspects in thin film technologies for nanostructured materials in gas sensor devices. Thin Solid Films 436, 52–63 (2003)
8. Epifani, M., Díaz, R., Arbiol, J., Comini, E., Sergent, N., Pagnier, T., Siciliano, P., Faglia, G., Morante, J.R.: Oxide nanocrystals from a low-temperature, self-limiting sol–gel transition in a coordinating environment: nanocrystal synthesis, processing of gas-sensing devices and application to organic com-pounds. Sens. Actuator B 126, 163–167 (2007)
9. Epifani, M., Díaz, R., Arbiol, J., Comini, E., Sergent, N., Pagnier, T., Siciliano, P., Faglia, G., Morante, J.R.: Nanocrystalline metal oxides from the injection of metal oxide sols in coordinating solutions: synthesis, characterization, thermal stabilization, device processing, and gas-sensing properties. Adv. Funct. Mater. 16, 1488–1498 (2006)
10. Korotcenkov, G., Boris, I., Cornet, A., Rodriguez, J., Cirera, A., Golovanov, V., Lychkovsky, Y., Karkotsky, G.: The influence of additives on gas sensing and structural properties of In_2O_3-based ceramics. Sens. Actuator B 120, 657–664 (2007)
11. Vomiero, A., Bianchi, S., Comini, E., Faglia, G., Ferroni, M., Poli, N., Sberveglieri, G.: In_2O_3 nanowires for gas sensors: morphology and sensing characterisation. Thin Solid Films 515, 8356–8359 (2007)
12. Neri, G., Bonavita, A., Micali, G., Rizzo, G., Galvagno, S., Niederberger, M., Pinna, N.: A highly sensitive oxygen sensor operating at room temperature based on platinum-doped In_2O_3 nanocrystals. Chem. Commun. 16, 6032–6034 (2005)
13. Francioso, L., Forleo, A., Capone, S., Epifani, M., Taurino, A.M., Siciliano, P.: Nanostructured In_2O_3–SnO_2 sol–gel thin film as material for NO_2 detection. Sens. Actuator B 114, 646–655 (2006)
14. Pawar, N.K., Kajale, D.D., Patil, G.E., Shinde, S.D., Gaikwad, V.B., Jain, G.H.: Gas Sensing Characteristics of Pure and ZnO-Modified Fe_2O_3 Thick Films. In: Mukhopadhyay, S.C., Lay-Ekuakille, A., Fuchs, A. (eds.) New Developments and Applications in Sensing Technology. LNEE, vol. 83, pp. 123–132. Springer, Heidelberg (2011)
15. Chavan, D.N., Gaikwad, V.B., Kajale, D.D., Patil, G.E., Jain, G.H.: Nano Ag-doped In_2O_3 thick film: A low temperature H_2S gas sensor. Journal of Sensors, Article ID 824215, 8 pages (2011), doi:10.1155/2011/824215
16. Jain, G.H., Gaikwad, V.B., Kajale, D.D., Chaudhari, R.M., Patil, R.L., Pawar, N.K., Deore, M.K., Shinde, S.D., Patil, L.A.: Gas sensing performance of pure and modified BST thick film resistor. Sensors and Transducers 90, 160–173 (2008)
17. Patil, G.E., Kajale, D.D., Shinde, S.D., Gaikwad, V.B., Jain, G.H.: Nanocrystalline Tin Oxide Thin Film as a Low Level H_2S Gas Sensor International Journal of Nanoscience 10, 1–5 (2011)
18. Oto, K., Shinobe, A., Manabe, M., Kakuuchi, H., Yoshida, Y., Nakahara, T.: New semiconductor type gas sensor for air quality control in automobile cabine. Sens. Actuator B 77, 525–528 (2001)
19. Iftimie, N., Rezlescu, E., Popa, P.D., Rezlescu, N.: Gas sensitivity of nanocrystalline nickel ferrite. J. of Optoelectronics and Advanced Materials 8, 1016–1018 (2006)
20. Maosong, T., Dai, G.R., Gao, D.S.: Surface modification of oxide thin film and its gas-sensing properties. App. Surf. Sci. 171, 226–230 (2001)
21. Kabayashi, T.M., Haruta, S.H., Nakane, M.: A selective CO sensing Ti-doped αFe_2O_3 with co-precipitated ultrafine particles of gold. Sens. Actuators B 13, 339–348 (1988)
22. Hu, Y., Tan, O.K., Cao, W., Zhu, W.: Fabrication and characterization of nano-sized $SrTiO_3$-based oxygen sensor for near room-temperature operation. Sensors 5, 825–832 (2005)

Author Index

Ahire, D.V. 313
Ahsant, Babak 69
Al-Shamma'a, A. 81
Arregui, Francisco J. 191

Babjak, Benjamin 43
Bari, R.H. 313
Barth, Eric J. 43
Berthold, M. 181
Blakey, R.T. 81
Bond, G. 81
Brunnader, R. 165

Chaudhari, R.M. 283
Chavan, D.N. 313
Chen, Chia-Pang 1, 23
Chen, Po-Tang 23
Chuang, Cheng-Long 1, 23

Del Villar, Ignacio 191
Deore, M.K. 283
Deshmukh, S.B. 283

Ewald, H. 237

Fazio, M. 263
Fricke, D. 237

Gaikwad, V.B. 283, 299, 313
Giouroudi, I. 121
Gooneratne, C.P. 121
Guth, U. 181

Hernáez, Miguel 191
Hire, P.D. 283

Hofacker, Mark 43
Holler, G. 165
Holmes, W.S. 93

Ihara, Ikuo 211
Ikezawa, S. 105
Inoue, Shin-ichiro 139

Jain, G.H. 283, 299, 313
Jiang, Joe-Air 1, 23

Kajale, D.D. 299, 313
Klinger, D. 237
Kosel, J. 121
Kosugi, Akira 211
Kraitl, J. 237

Ledeczi, Akos 43
Liu, Chun-Yi 23

Mason, A. 81
Matias, Ignacio R. 191
Matsuya, Iwao 211
Mukhopadhyay, S.C. 93

Paone, M. 263
Paramasivam, M. 181
Patil, G.E. 283, 299, 313
Patil, N.U. 283
Pedchenko, Alex 43
Puliafito, A. 263

Riedel, J. 181
Riley, S.G. 93
Rolph, C.E. 81

Sasum, U. 181
Shinde, S.D. 299
Shuk, P. 181
Szilvasi, Sandor 43

Takahashi, Manabu 211
Tashiro, Kunihisa 139
Timm, U. 237
Tomomatsu, Takuya 211
Tran, T.N. 181

Ueda, T. 105

Vashook, V. 181
Villari, M. 263
Viswanathan, Ramanarayanan 69
Volgyesi, Peter 43
Vonau, C. 181

Wagh, V.G. 283, 299
Wakamatsu, M. 105
Wakiwaka, Hiroyuki 139

Yamada, Hiroyuki 211

Zamarreño, Carlos R. 191
Zheng, Xiang-Yao 23
Zosel, J. 181